FLORIDA INTERNATIONAL UNIVERSITY

Miami, Florida

TRI-LEVEL HIERARCHICAL COORDINATED CONTROL OF A LARGE-SCALE ELECTRIC VEHICLE CHARGING IN THE SMART GRID

A dissertation submitted in partial fulfillment of the

requirements for the degree of

DOCTOR OF PHILOSOPHY

in

ELECTRICAL AND COMPUTER ENGINEERING

by

Tawfiq Masad Aljohani

2021

To: Dean John Volakis
College of Engineering and Computing

This dissertation, written by Tawfiq Masad Aljohani, and entitled Tri-level Hierarchical Coordinated Control of a Large-Scale Electric Vehicle Charging in the Smart Grid, having been approved in respect to style and intellectual contents, is referred to you for judgment.

We have read this dissertation and recommend that it be approved.

Ahmed Ibrahim

Xia Jin

Stavros V. Georgakopoulos

Ahmed Elsayed

Osama A. Mohammed, Major Professor

Date of Defense: March 26, 2021

The dissertation of Tawfiq Masad Aljohani is approved.

Dean John Volakis
College of Engineering and Computing

Andrés G. Gil
Vice President for Research and Economic Development
and Dean of the University Graduate School

Florida International University, 2021

DEDICATION

To the greatest father ever walked on this planet, my role-model, my best friend, and my dad Masad Salim Aljohani

To my wife's beloved mom Alshaikha Alnazzawi

Two great people left us early and unexpectedly

Words cannot express our love, pain, and gratitude

I ask ALMIGHTY ALLAH to rest your souls in Eden's Heavens

This work is only a small dedication to your memory

ACKNOWLEDGMENTS

First and foremost, I am grateful to ALMIGHTY ALLAH for all the blessings, guidance and protection he provided me throughout my life.

I would like to express my deep gratitude to Dr. Osama Mohammed for his extraordinary mentorship and guidance throughout my PhD studies. Dr. Mohammed welcomed me very graciously, offered me all the available resources to make me a productive and well-established researcher. I will forever remain grateful for the opportunity made available to me to work under a distinguished name like him. The thanks are also extended to Taibah University for providing me with a full scholarship to continue my higher education in my field.

A very special note of thanks is directed to my elder sibling, Mohammed Aljohani, of whom without his financial and emotional support, I would have never been able to continue my graduate studies at the United States.

Last, but certainly not least, I would like to express my deep love and gratefulness to my mother, Maysar Mahllawi, for being the best mother anyone could ever have in this life. Her strength, endless love, support, wisdom, and mercy have made me the man I am today. I also want to express my gratitude to my wife, Sarah, for being a very supportive and loving partner, and for taking care of our beloved girls, Haifa and Aljazzy, who are the most precious things to me in this world. I also extend my gratefulness to my siblings Khalid, Fahad, Basim, Nahla and Norah, for being the most wonderful family in this world. Words are insufficient to express my deep gratitude for their unconditional love, support,

and care. Finally, I feel grateful for every positive experience I had during my times doing my graduate degrees in the United States. I will forever consider Southern California and South Florida as my second home after Medina, Saudi Arabia, and will always be grateful for all the good people I met here, which made my experience an unforgettable one.

ABSTRACT OF THE DISSERTATION

TRI-LEVEL HIERARCHICAL COORDINATED CONTROL OF A LARGE-SCALE ELECTRIC VEHICLE CHARGING IN THE SMART GRID

by

Tawfiq M. Aljohani

Florida International University, 2021

Miami, Florida

Professor Osama A. Mohammed, Major Professor

Electric Vehicles (EVs) are considered one of humanity's greatest hopes to combat the climate change crises in light of their great potentials to reduce Greenhouse Gases (GHG) emissions from two main sources: the electric power industry and the fossil-based transportation sector. To help expedite the large-scale adoption of EVs on the roads, optimal solutions are needed to overcome the technical and operational barriers that face the electrical network. This is due to the introduction of significant load levels from EVs; a substantial number is expected during peak demand hours. This dissertation addresses the various interaction between different parts of the electrical system in a hierarchical optimization framework to ensure proper large-scale integration of electric vehicles; without harm to the grid or the user.

To achieve our goals of achieving optimum operation scenarios, we developed a tri-level centralized and decentralized optimization methodologies with smart coordination algorithms. This will ensure optimal decisions with the simplest required communication infrastructure. Specifically, information from the EVs' owners are collected by an aggregator located at the charging station. In a timely fashion, the aggregator sends the

most updated scheduling information to its assigned microgrid that ensures no violation occurs within its jurisdiction and establishes a pricing signal for each aggregator. The microgrid takes a decision based on the downstream input information from other aggregators attached to it and upstream input information from a system operator that provides additional energy if needed and update the microgrids based on the overall grid's operation. Additionally, we developed a two-stage optimization strategy to ensure proper EVs charging and discharging coordination considering voltage and reactive power control levels. The optimization strategy starts with the decomposition of the power distribution network into optimal partitions based on their voltage sensitivity levels, then solves a centralized energy coordination problem using mixed-integer linear programming. The optimization problem takes into consideration various aspects of the systems' operation that include reactive power compensation devices and active power curtailment of PV inverters. The developed solutions presented in this dissertations have been verified and tested experimentally.

TABLE OF CONTENTS

LIST OF TABLES

TABLE PAGE

LIST OF FIGURES

FIGURE PAGE

LIST OF ACRONYMS

ACRONYMS	DETAILS
AES	All Electric Ship
AGC	Automatic Generation Control
AIMD	Additive Increase - Multiplicative Decrease
BESS	Battery Energy Storage Station
BEV	Battery Electric Vehicle
COP	Conference of the Parties
CPP	Critical Peaking Pricing
DA	Day-Ahead
DDS	Data Distribution Service
DG	Distributed Generation
DSM	Demand-Side Management
DSO	Distribution System Operator
EMALS	Electromagnetic Aircraft Launch System
ERCOT	Electric Reliability Council of Texas

ESS	Energy Storage Systems
EV	Electric Vehicle
EVA	Electric Vehicle Aggregator
FLC	Fuzzy Logic Controller
FR	Frequency Regulation
G2V	Grid to Vehicle
HEV	Hybrid Electric Vehicle
ICE	Internal Combustion Engine
IEC	International Electrotechnical Commission
LA	Load Aggregator
LFC	Load Frequency Control
LSE	Load-Serving-Entity
LVAC	Low Voltage Alternative Current
LVDC	Low Voltage Direct Current
MMGA	Mathematical Morphology Gradient Algorithm
MTOU	Multi-Group Time-of-Use

MTOUCP	Multi-Group TOU with Critical Peaking
MOOP	Multi-Objective Optimization Problem
MVAC	Medium Voltage Alternative Current
MVDC	Medium Voltage Direct Current
NSGA	Non-dominated Sorting Genetic Algorithm
PEV	Plug-in Electric Vehicle
PF	Pareto Front
PHEV	Plug-in Hybrid Electric Vehicle
PL	Parking Lot
PO	Pareto Optimality
POC	Point of Charging
PV	Photo-Voltaic
PWM	Pulse Width Modulation
RT	Real-Time
SOC	State of Charge
TOU	Time-of-Use

V2B	Vehicle to Building
V2G	Vehicle to Grid
V2V	Vehicle to Vehicle

Chapter 1 Introduction

1.1 Motivation

The electrical energy system is currently witnessing profound and historical changes, propelled by the recent advancements in renewable energy technologies, transportation electrification and the rise of electric vehicles and power electronic applications. The ever-dreamed concept of smarter and cleaner energy networks is still far from the real implementation. The integration of the smart grid is much needed to spare humanity the consequences of climate change, of which the electric energy industry has been a significant player in its steadily worsening condition. Despite the growing efforts in the recent decades to contain greenhouse gas (GHG) emissions, with the inauguration of the Paris Accord and the Kyoto Protocol [1, 2], GHG emissions continue to grow more rapidly in recent years. Specifically, instead of witnessing a long-awaited decline in its release, GHG emissions have hit another high record by the end of 2019, with almost 37 billion tons of total carbon dioxide (CO_2) released to our atmosphere from the electric power industry solely. This amount of released toxic gases constitutes a 0.6% increase from 2018's emissions record [3]. Figure 1.1 shows the recent accumulated numbers in GHG emissions by sources. In addition to the power generation sector, the transportation sector has played a significant role in the global increase in GHG emissions. According to the center for climate and energy solutions [4], transportation is the number one emitter of CO_2 in the United States. Furthermore, both the power and transportation sectors account for almost 60% of the total CO_2 equivalent emissions. Figure 1.2

shows the daily CO_2 equivalent emission by sector. These catastrophic figures have strengthened the calls for the restructuring of both fields, of which electric vehicles comes as a common factor of interest between the two industries. Therefore, electric vehicles could be critical in the mankind's battling against the climate change crises. Figure 1.3 illustrates the future power grids as defined in the IEEE 1547.4 standard, with the potential role that the EVs could play in its operation [5].

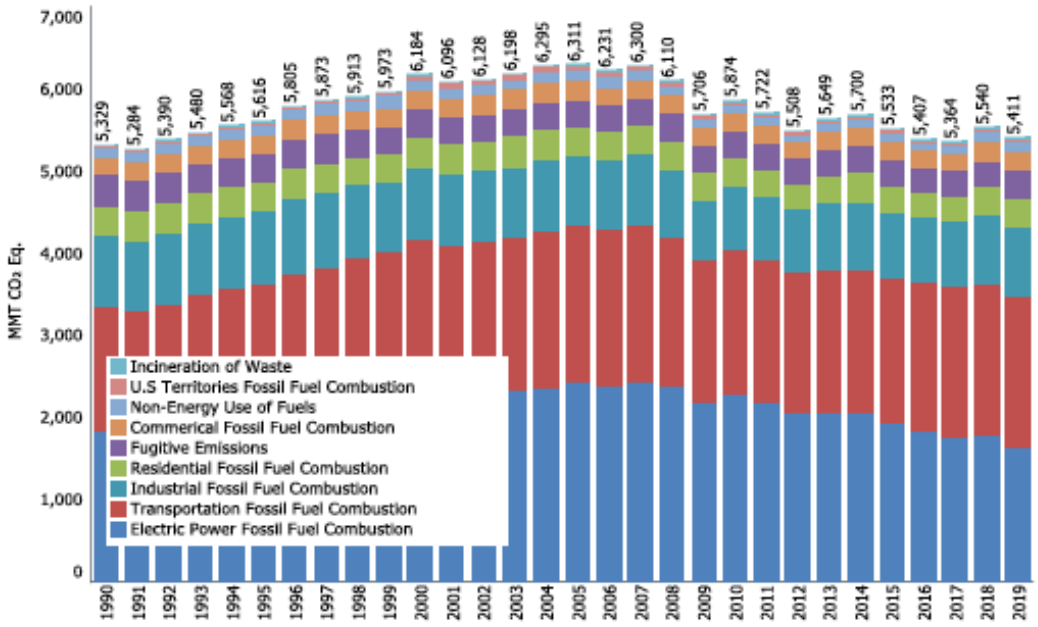

Figure 1-1 recent trends in the greenhouse gas emissions by sources [3]

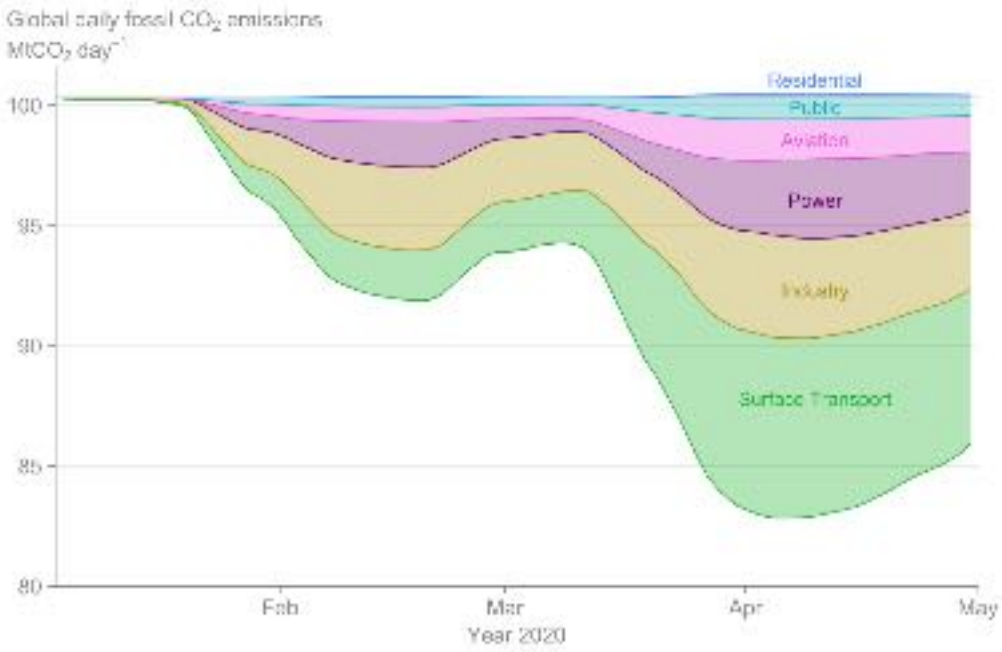

Figure 1-2 Global daily carbon dioxide emissions by sector [4]

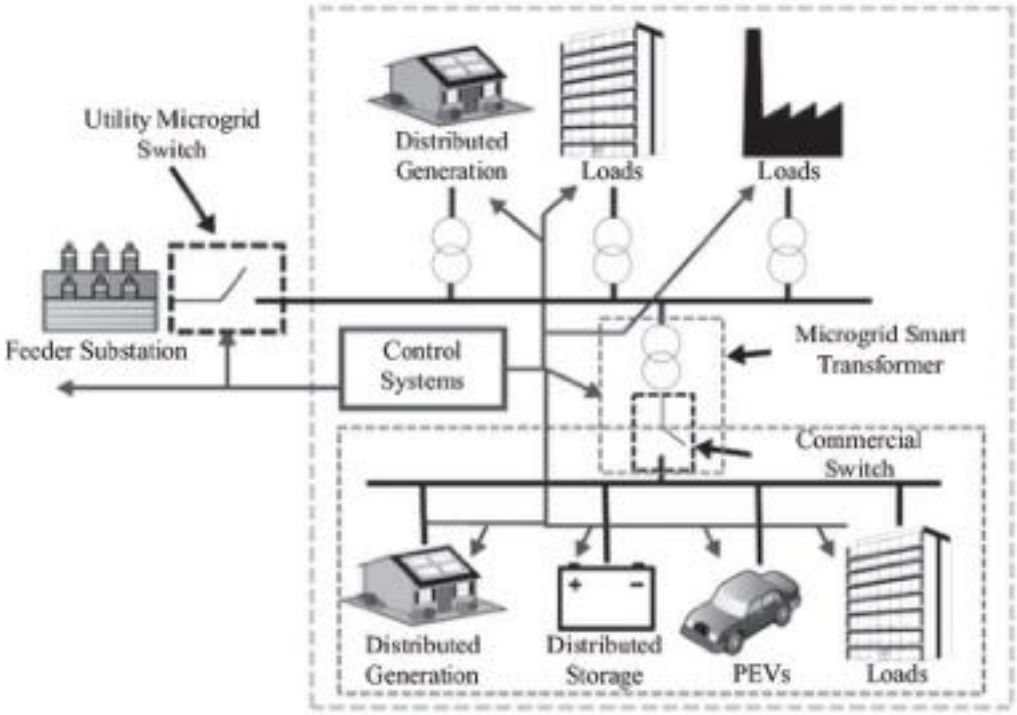

Figure 1-3 The IEEE 1547.4 definition of the future power grids [5].

There is no doubt that one of the major drivers to construct the smart grid is to meet the environmental goals and to accommodate a greater prominence on demand response programs and storage capabilities to modernize the ageing electrical infrastructure. Therefore, electric vehicles' support will grow substantially, as they are seen as mobile energy storage devices that could be exploited to upgrade the grid's operation. Such support to the grid could be utilized either as a form of energy source via vehicle to grid (V2G) or flexible loads by reaching agreements to delay charging to off-peak demand periods. Nevertheless, orchestrating the EVs interaction with the grid will be a challenging task. In addition to the many uncertainties involved in its integration process, several operational, technical, economic, and environmental hindrances complicate the large-scale adoption of EVs. An example is the fact that the power grids' ability to absorb the load of thousands of EVs on an already congested electrical network is another major obstacle that needs much attention to achieve optimal solutions to the planning and operation of the electrical networks.

1.2 Problem Statement

To ensure proper and safe operation of the power systems in light of the recent advancement in technologies with an eye on environmental concerns, many countries have started to increase their support for transportation electrification and adopt policies that foster its rapid integration. The role of researchers is to ensure feasible solutions to such integration in a way that does not alter the reliability nor does affordability of energy to the different categorize of consumers. A significant obstacle to reaching a milestone where EVs is considered as reliable and trusted as the internal combustion vehicles (ICV) is to allow safe

and timely available charging to EVs' owners without any service rejection due to the power grid's status. However, reaching such a goal will undoubtedly require significant restructuring of the current energy infrastructure to optimally manage and control the energy demand, considering the highly stochastic nature that EVs would introduce to the power grid. Successful implementation of optimal energy management and control in a timely and cost-effective manner is indispensable for large-scale adoption of EVs, ultimately contributing to reaching humanity's central goal to reduce the impact of climate change and preserve our planet for generations to come.

This dissertation research aims to provide solutions to some of the most challenging problems currently emerged in the arena of smart grid and electric vehicles load management and control. Mainly, we aims to pursue large-scale integration of EVs in a way that does not alter operational constraints of the energy infrastructure nor lead to an increase in energy tariffs on consumers. Moreover, the feasibility and robustness of such integration require smart optimization strategies that can alleviate as much as possible the expected large sums of infrastructure investment as well as the technical difficulties that will arise from the large-scale integration of EVs. Therefore, building smart, reliable and affordable charging systems is essential to facilitate the integration of large scale EVs in the next in the near future. The work presented here will provide solutions to make such integration possible in a practical and economical manner.

1.3 Literature Review

An important aspect of this dissertation is to investigate, utilize and implement various metaheuristic techniques for the purpose of deployment to the PEVs energy management and control. Recent years have witnessed growing attention on the metaheuristics and population-based techniques to solve various problems in power system operation and control. These modern approaches have been widely recognized to overwhelm the traditional gradient-based optimization methodologies that have been used for a long time [6]. The gradient-based approaches to reactive power planning and operation have many valid drawbacks and criticisms. One is that solving a large number of gradient variables requires intensive computations and tends to converge very slowly [7]. Another aspect of its drawback is that the gradient solution to the objective function is utilized as a search method is based on too many assumptions. for example, the active and reactive power are not directly influenced by voltage levels and phase Angles Θ [8]. This is unacceptable since Θ is considered one of the factors that determine the active power loss due to its link to the variation of the real power in the system. Therefore, the inconsistencies in formulating its mathematical representation lack adequate modeling accuracy, leading to repercussions in its search juncture.

On the other hand, metaheuristic approaches allow abstract-level description that provide non-specificity, which is useful for solving a wide range of problems that are presided over by the metaheuristics' upper-level strategies which influence greater search capabilities. They are based on utilizing search capabilities, mainly embodied as a form of memory, to be re-evaluated by successive iterations to steer their search process. This has helped to rapidly escalate its use in the literature to solve a variety of engineering and scientific-based, real-life problems. Many traditional and bio-inspired optimization algorithms have touched on different aspects of the ORPD problem in the literature, such as genetic algorithms (GA) [9, 10], particle swarm optimization (PSO) [11, 12, 13, 14], evolutionary programming (EP) [15], Tabu search

[16], dynamic programming (DP) [17], harmony search optimization (HSO) [18], gravitational search algorithm (GSA) [19, 20], and grey wolf optimizer (GWO) [21]. Some of these methodologies show superior performance in reaching a near-global optimum while greatly prevailing over the difficulty that arises due to the nonconvexity and nonlinearity nature of such problems.

The significant contribution of chapter three of this dissertation is to develop a hybridization of two naturally inspired metaheuristics techniques, particle swarm optimization (PSO) and artificial physics optimization (APO), then solve and optimize the complexity and nonlinearity of the ORPD problem and test it on various IEEE test systems to evaluate its search capacity. The PSO is an evolutionary metaheuristic algorithm that imitates the complex social behavior of flocking birds or fish schooling and was firstly introduced by Kennedy and Eberhard [22]. It utilizes a set of potential solutions (known as particles) to explore the search space, where every possible solution (or particle) modifies its position via the learning-by-experience concept from the history of its position and its neighboring particles. The use of PSO, either as a stand-alone or by hybridization with another metaheuristic methodology, has been extensively considered to solve complex problems in various engineering disciplines, including studies related to optimal reactive power dispatch. However, in this chapter, we present a new form of hybridization with the APO that has not been applied to the ORPD problem before. The APO is a probabilistic population-influenced algorithm inspired by physics-based swarm intelligence, also known as physicomimetics [23]. In APO, each solution is looked at as an individual that exhibits physical properties such as mass, force, velocity, and position. Derived mainly from Newton's second law, every particle (solution) can be optimized as the best solution based on the iterative relocations of the population, where a particle's movement is influenced by the force and inertia of other particles (possible solutions). Recent literature shows the powerful capabilities of APO in solving various kind of problems as a

stand-alone algorithm or when hybridized with other algorithms [24, 25, 26] and it exhibits solid search performance and fast convergence. Hybrid APO–PSO has been used in a previous study to solve dynamic power security analysis [25] but has never been applied to the ORPD problem nor to the microgrid energy management [26]. Our overall goal is to produce an intact algorithm that combines the global search capabilities of APO with the strong local exploratory search performance of PSO, while improving its convergence characteristics. The APO exhibits flexible and wide-range search features that enhance its global population diversity, adding a powerful searching-mixture when combined with PSO. After building the mathematical representation of each algorithm, we validate the performance of the hybridized algorithm on the IEEE 30, IEEE 57, and IEEE 118 bus test systems, and compare with the results of previously published reports using other methods to verify its capabilities.

The rise of microgrids with its dependence on intermittence renewable energy sources (RES) as well as stochastic EVs activities have underlined voltage stability and frequency control problems that must be carefully addressed for more safe and resilient operation. Specifically, uncoordinated large-scale integration of renewables sources, as well as rapid adoption of EVs with highly stochastic charging and discharging activities, will lead to detrimental consequences such as voltage collapse, power quality problems, frequency and stability oscillations, to name a few. Therefore, proper control and operation of microgrids are required to allow coordinated control mechanism while taking into consideration the heterogeneous mix of parameters corresponding to different attached power sources [27]. Research on microgrids operation and control has been widely considered in the literature. The authors of reference [28] analyzed various architecture, management and control in the microgrid paradigm, while the authors of reference [29] presented a survey on various research

that considered the integration of distributed energy resources with microgrids in different countries. Reference [30] investigated a decentralized energy control scheme for autonomous poly-generation microgrid topology to achieve proper management in case of malfunctioning of downstream parts. Besides, the authors of reference [31] presented a valuable review study on various hierarchical control schemes of microgrids on the primary, secondary, and tertiary control layers that aim to reduce the overall operation cost while improving the controllability and the reliability of microgrids.

Photovoltaic solar (PV) is one of the most advanced and reliable forms of renewable energy sources. However, the utilization of PV systems has yet to overcome many operational issues to be considered a thoroughly reliable and dispatchable source of energy for microgrids. The most critical issue with the consideration of PV systems is its intermittency throughout the day. Such shortages in the PV system's supply of energy could be compromised with increasing the level of energy transfer to the microgrid through EVs discharging, which is one of the main aspects this chapter is investigating. The work on PV systems is one of the widely considered research topics in the past decades. Optimization problems have been well-developed to investigate and verify the control of PV systems taking into consideration its stochastic nature such as in [32, 33]. The authors of reference [32] investigated the effect of changing cell's temperature and solar irradiance on the design of various DC-DC converter topologies which are widely used in PV systems. The authors of reference [33] developed a new topology scheme for a photovoltaic dc/dc converter which can drastically enhance the efficiency of a PV system by assessing the PV's module characteristics. The authors of reference [34] developed an

algorithm that offers dynamic distributed energy resources control that includes PV systems, small-scale wind turbines, controllable loads and energy storage devices. Studies on PV systems covered a wide range of applications, and literature are filled with so many great studies that investigate the use of PV systems for a more clean energy utilization.

Another side of consideration in this chapter is the relative impact of EVs integration on the hybrid microgrid operation. Reference [35] presents a linearization methodology to model real-time EVs activities on residential feeders based on the concept of Kirchhoff laws, nodal analysis, and modularity index. EVs offer high potentials to serve as mobile backup storage devices that can provide grid support to enhance its reliability as a means of smart grid application [36]. Reference [37] provides a Matlab-based Monte Carlo Simulation code that allows the incorporation of distributed energy resources (i.e., EVs) to assess the distribution network's reliability. Additionally, studies have covered the potentials of EVs in relevant frequency regulation and control. The authors of reference [38] developed an intelligent aggregator that synchronizes the charging and discharging activities of a group of EVs in order to regulate frequency by compensating for any potential power deficiency. Similarly, the authors of reference [39] developed a real-time dynamic decision-making framework based on Markov Decision Process (MDP) to allow intelligent frequency regulation by energy support from EVs. Reference [40] developed a multivariable generalized predictive controller to enable load frequency control in a standalone microgrid with V2G integration. The controller aims to allow sufficient energy exchange without causing frequency deficiency, considering possible load disturbances. Furthermore, the recent progressive policies that aim to reduce GHG

emissions from the transportation sector will result in a mass acquisition of EVs in the next few years [41], especially in regions where utilization of EV is expected to have a significant reduction of GHG emissions as a result of their weather and energy grid mixes [42]. Such rapid adoption of EVs on a large scale without proper coordination can result in phase imbalance, equipment fallout and degradation, increase active and reactive power losses, among many problems [43]. Therefore, careful consideration needs to be given to overcome the problems that may arise due to the intermittency and stochastic nature of the energy sources on the hybrid microgrids. Therefore, the utilization of a metaheuristic-based algorithm in this dissertation was deemed as a promising solution to solve the problem of PEVs integration on hybrid microgrids considering the intermittency of renewable energy sources.

Electric Vehicles, as storage devices, may have an impact on distribution feeder voltage and regulation. As the penetration level of such devices increases, reverse power flow on the distribution feeder leads to voltage rise and hence violations of voltage boundaries defined by American National Standards Institute (ANSI) [44, 45]. Many studies have been conducted on distribution feeders to assess the performance of commonly used voltage regulation schemes under reverse power flow. The simulation results in reference [45] show that the power quality of the system can be improved by suitable location selection of the photovoltaic (PV) system or storage devices. References [46, 47] provides a broad overview of the impacts of EVs on the system voltage stability and frequency. The introduction of local charging and discharging EVs to balance the loads negatively influences the efficiency of short-term load forecasting modules. Electric Vehicles characteristics are broken down into vehicle characteristics, charging characteristics, and when EVs are plugged in [48]. The impacts of EVs are determined through regional grid analysis based on the number of vehicles, vehicle demand profile, and

the effect that demand has on supply and demand. The study done in reference [48] does not come to any specific conclusions about optimal charging patterns or grid reliability, but it does suggest that work must be done to investigate further how EVs will impact the grid. Reference [49] provides detailed information on the distribution system modeling which provides a valuable resource for modeling and simulating distribution grid used in our study, the IEEE 34 bus feeder which released in 2003 by the IEEE power society [50]. References [51, 52] study the potentials of the EVs in the market and the virtues it makes by its connection to the local electrical grid. Also, the idea of charging the EVs considering renewable energy sources have been widely investigated, especially when current governmental policies, such as the 2014 Carbone Dioxide Standards of the Environmental Protection Agency (EPA), are currently forcing the power utilities to lessen the reliance on fossil fuels via adopting strict mandates such setting prohibited limit on the amount of gases released from their power plants [53]. Reference [54] addresses some of the technical and economic challenges during the process of designing a green recharge area for EVs with an overall goal to reduce costs and pollution connected to the charging process. Reference [55] provides modelling of a smart charging station for electric vehicles (EVs) for DC fast charging while ensuring minimum stress on the power grid. Furthermore, they analyzed a business model with that aim to provide a cost estimation for the deployment of charging facilities in a residential area. Reference [56] proposes a methodology aimed to allow the aggregated EV charging demand to be identified. Specifically, their methodology is based on an agent-based approach to calculate the EV charging demand in a given area. Their model simulates each EV driver in order to obtain the EV model characteristics, mobility needs, and charging processes required to reach its destination. Reference [57] presents EVs charging and discharging load model based on three tiers electricity rates to study the impact of the power flow of the distribution feeder considering EVs integration utilizing a probabilistic power flow model. Their model suggests that the

operational risk of the distribution network can be estimated and quantified for proper grid operation. Reference [58] provides an in-depth study about commanding the power flow conversion between the battery pack of the EVs and the load center of the power utilities, as they present a novel bidirectional converter to oversee the process of this critical power management.

Unlike traditional methodologies, reinforcement learning (RL) is an artificial intelligence technique that has been widely used in solving many scientific problems in recent years [59, 60]. The concept of Q-learning was first introduced in [61], and a Deep Q-learning Network (DQN) is an extension to it [62]. Applications of RL has been widely employed to perform studies related to EVs such as in proposing efficient smart charging algorithm [63], as well as energy management and control strategies for hybrid and pure electric vehicles [64, 65]. In addition to the battery's energy management, RL techniques and methodologies have covered a wide range of topics related to power and energy engineering, such as electricity market trading in smart grids [66], energy production scheduling [67], and multi-agent distributed energy management of a microgrid [68]. RL has been extensively investigated in the automotive industry in recent years. The authors of [64] employed RL to measure an adaptive optimal energy control strategy based on different driving schedules. They tested the learning ability of HEVs and verified via simulation the impact on fuel efficiency. They made comparisons of their developed strategy with results obtained previously utilizing Stochastic Dynamic Programming (SDP). Similarly, based on the Q-learning algorithm, the authors of [69] studied a predictive energy management framework for a parallel hybrid electric vehicle (HEV). Their results show significant reductions in both fuel consumption and computational time. Additionally, the authors in [70] tested the

capabilities of deep reinforcement learning to train autonomous, self-driving automobiles that are aware of other elements in their surroundings, such as pedestrians, other vehicles, etc. The probabilistic nature of driving patterns of EVs is modeled in many recent works of literature as a Markov decision process (MDP). In [71], researchers tested the behavioral response of the stochastic charging of an EV station using MDP methodology. In [72] MDP was utilized to model the impact of stochastic driving, parking, and charging patterns of EV loads on the local distribution grid. Range anxiety is one of the major obstacles in the EVs market. In addition to the automotive industry, RL has been a widely used technique in many fields of research in recent years, such as in robotic control [73, 74], computer systems applications [75, 76], image processing [77, 78], agent-learning systems [79], traffic improvement and coordination systems [80, 81], as well as wirelesses and communication networks [82, 83, 84].

Stochastic microgrid energy management and control has received considerable attention in recent years. References [85, 86] present mathematical microgrid energy control and prediction algorithms considering unforeseen stability issues and renewable energy fluctuations. The algorithms were tested and verified in a hardware-in-the-loop testbed that resembles a real hybrid microgrid system. Reference [87] utilizes reinforcement learning to develop a microgrid energy management framework with the customers acting as intelligent agents in a stochastic environment to issue decisions that maximize their utility functions. Reference [35] presents a revised linearization methodology to model the real-time EVs activities on residential feeders based on the concept of Kirchhoff laws, nodal analysis, and modularity index. Furthermore, it provides a methodology to distinguish between EVs and non-

EVs loads. References [88, 89, 90] present techno-economic studies that examine the relative impact of EVs integration on microgrids and distribution systems' hourly operation. It is widely evident that large-scale integration of EVs will be pivotal in restructuring future microgrids and distribution networks. Several works of literature discussed energy pricing schemes considering EVs' charging and discharging process. The authors in reference [91] presented a distributed EVs charging methodology and pricing models inspired by the control of Internet traffic congestion. The decision on real-time pricing is issued by the smart grid based on total supply from renewable and non-renewable sources. The authors in reference [92] developed a dynamic pricing scheme following a predictive charging strategy of EVs that considered reducing the carbon footprint. The pricing information is exchanged with the EVs via wireless communication based on predicted energy prices for the suggested charging period that aim to make the time of charging's price is at low-cost.

The proliferation of PEVs with uncoordinated charging and discharging may lead to significant damages to the grid's apparatus and introduce operational difficulties to overcome its charging demands, especially those during peak hours. Therefore, a necessity for proper coordination and control of the power grid is the meticulous incorporation of the PEVs scheduling in a way to make it contribute efficiently to the grid's operation; their exponential growth could also be seen as a golden opportunity to get rid of operational deficiencies and extend the lifespan of voltage and reactive power support devices. This is true, giving the detrimental impacts of renewable energy sources' intermittency on the operation of conventional voltage and reactive power compensation devices such as the on-line tap

changing transformer (OLTC) and shunt capacitor banks (CBs). Additionally, uncoordinated large-scale penetration of PEVs could significantly stress these devices and, therefore, contribute to unnecessarily extensive tap operations [93]. As a result, accounting for PEVs into the voltage-var optimization (VVO) of the PDNs should be recognized as a priority.

Regularly, the VVO problem deploys OLTC and voltage regulators (VRs) to regulate the voltage level across the PDNs, while considering CBs and other reactive power compensation devices (RPCs) such as dispersed energy sources (i.e. photovoltaic systems (PVs) inverter) for VAR support. Ideally, the problem of VVO has been investigated within the context of centralized control schemes, requiring massive communication infrastructure to promptly deal with thousands of equipment. In [94], the authors utilized a genetic algorithm (GA) to solve multiobjective voltage regulation control to reduce the system's losses and voltage fluctuations. Nevertheless, voltage control from generation resources was not incorporated into their formulation. Conversely, the authors of [95] developed an optimal voltage-var control scheme with the incorporation of large-scale distributed generators (DGs) to ensure adequate voltage regulation on the distribution level. However, their control scheme neglected the impact of OLTC and the prospect of active power curtailment (APC) on the voltage regulation problem. Besides, reference [96] presented an optimal voltage-var coordination scheme that considers day-ahead PV active and reactive power production to reduce OLTC tap operation, yet without including the effect of APC in the utilization of PV voltage support schemes. Moreover, one potential concern is that their day-ahead forecasting methodology could be adversely influenced by common margin errors usually inherited in the traditional forecasting techniques.

Additionally, PEVs were not accounted for in their VVO control scheme. In fact, literature that reports the utilization of PEVs in the VVO problem is still limited. Reference [97] has indeed considered PEVs in the distribution network's voltage regulation process, yet only in a centralized manner. It is clear that only a limited amount of literature has considered solving the VVO problem on a decentralized scale, with few considering the integration of PEVs. Therefore, more research should be performed to fill the gap in this area. Generally, solving for the VVO within the context of a decentralized framework requires some sort of decomposition methodologies to divide the distribution system into several subgroups. Furthermore, the accuracy of the decomposition technique plays a pivotal role in the realistic modeling of the information exchange among the divided subgroups of the network topology. Reference [98] presented a valuable study on the tradeoff of implementing various algorithms on the convergence speed for solving problems related to clustering-based decentralized optimization. The study indicates that strategies of low-coupling degrees may lead to an insignificant impact of one cluster over its neighboring subgroups. This emphasizes the potentiality of obtaining results that inaccurately represent a solution for highly complex and dynamical systems like the PDNs. Therefore, careful consideration must be advocated while designing decomposition methodologies that model efficiently the steady-state operation of the electrical systems. Recent literature has investigated various clustering methodologies applied to the power grids. References [99, 100] developed decomposing the large-scale power grids into subgroups based on spectral clustering. Specifically, reference [99] developed operationally constrained spectral clustering to identify intentional controlled partitioning of

wide areas of the power network to defend against cascading failures. The developed methodology allows system operators to constrain, without disconnection, branches against minimal power flow disruptions. The developed islanding technique was tested to reduce power grids that have the size of the United Kingdom's power network. Similarly, reference [100] defined the internal connectivity of the system's nodes via an undirected edge-weighted graph based on spectral clustering and developed solving the VVO problem with respect to the quality factor of each obtained partition, yet with no account for PEVs' integration. Other methodologies aimed for solving the VVO problem in a decentralized manner without incorporating the decomposition of the PDNs into subgroups. Reference [101] developed agent-based for reactive power compensation via DGs to regulate the voltage levels in a distributed manner with lower communication capabilities. However, no consideration of the active role of OLTC and VRs has been identified which does not provide the technical option for voltage regulation if reactive power outputs of the incorporated DGs are reached. On the other hand, reference [102] developed a voltage regulation scheme to account for parallel distribution networks with a strong assumption that VVO is performed considering only the OLTC device. While such assumption may yield valid results, it is a not recommended practice as it will increase operational stress on the OLTC and potentially forfeit its economical lifespan. Additionally, the solution might be infeasible giving that voltage boundaries of larger distribution systems may exceed the capability of the OLTC to solve the problem efficiently.

Several studies have studied the impact of the large adoption of PEVs without effective uncontrolled charging mechanism [103, 104, 105]. In this dissertation work, we aimed to test

the impact of the uncoordinated large-scale adoption of PEVs on the hourly operation of the power distribution grid. Specifically, we provided in chapter five of this dissertation dynamic modeling of the hourly impact of PEVs integration on the IEEE 34 bus system using the OpenDSS dynamic software of the Electric Power Research Institute (EPRI), considering different PEVs types and energy needs integrated throughout the whole day. Different testing scenarios were conducted and they are presented in detail in chapter five and in [103]. Our study in chapter five concludes that uncoordinated large-scale integration of the PEVs will definitely violate the system's voltage limits and lead to overloading condition and increased energy prices on all consumers connected to the distribution feeder. The authors of reference [104] provide extensive study on the impact of the integration of one million PEVs to the VACAR sub-region of the Southeast Electric Reliability Council (SERC). To achieve the purpose of testing the impact of modeling PEVs load of this size, the authors utilized the Oak Ridge Competitive Electrical Dispatch model to simulate the hourly dispatch of the power sources to meet this large loads. Furthermore, they consider various charging and discharging scenarios with different PEVs sizes, energy requirement and time of connectivity, and reach a conclusion that a typical-size residential power distribution feeder will not be able to withstand charging of PEVs for long hours without causing severe overloading and possibly outage. Reference [105] presents one of the earliest research literature that studies the impact of uncoordinated PEVs integration on the grid. Moreover, the author investigated the integration of 7.5 million PEVs and studied the impact of its integration on the technical, economical and operational aspect of the power grid. They reached a conclusion that unless PEVs load are

managed to delay large-scale charging of PEVs from peak hours to off-peak hours, substantial increase of the energy prices is almost certain in several areas of the US interconnected network. Furthermore, reference [105] is one of the first studies that emphasize the needs for energy management and coordination of PEVs that consider postponing PEVs charging demands to times where both energy prices and demand are lower. Additionally, reference [106] concludes that simple charging strategies yield peak demands in several time slots of the day, which require major investment to upgrade the system's overall generation and transmission capacities. Therefore, there is no doubt that proper energy management and control is needed to deal with the uncertainty of large-scale integration of PEVs. Several methodologies have been developed in the recent years to deal with the challenging task of accounting of PEVs load into the already-congested power grid. Reference [107] presents a two-step framework to coordinate the PEVs charging following a price-based coordination based on linear programming. The authors of reference [108] propose a methodology that account for the design of grid interfaced PEV charging systems incorporating stochastic renewable energy sources and storage units on the electrical infrastructure. Specifically, the authors utilize a linear programming-based framework to optimally choose designs that reduce the overall system's lifecycle cost.

1.4 Research Objectives

The main goal of this dissertation is to develop multi-level energy management, optimization and control methodologies that facilitate large-scale adoption of electric vehicles to the power grid. The optimization strategies developed here consider various operational

constraints and restrictions that cannot be avoided in typical power system operations. Such technical barriers include operating within permissible voltage, active and reactive power limits and frequency levels. It also includes unnecessary overloading of power distribution transformer and lines beyond their capacities. Another aspect is broadcasting real-time energy pricing that is summed with power production and grid operation costs. Additionally, the developed optimization strategies consider incorporating various power system components that are widely used and significantly impact the power system operation and dynamics, such as voltage compensation devices, renewable energy sources, EVs charging and discharging, and other non-EVs loads.

This research considers various interaction between different parts of the system in a hierarchical framework to ensure proper large-scale integration of electric vehicles. Both centralized and decentralized optimization methodologies were deployed together to ensure optimal decisions with the lowest required communication infrastructure. Specifically, information from the EVs' owners are collected by an aggregator located at the charging station. In a timely fashion, the aggregator sends the most updated scheduling information to its assigned microgrid that ensures no violation occurs within its jurisdiction and establishes a pricing signal for each aggregator to be dispatched for each EV. The microgrid takes a decision based on downstream input information from other aggregators attached to it and upstream input information from a system operator that provides additional energy if needed and updates the microgrids about the overall grid's operation.

The research in this dissertation also ensure that charging events does not cause any voltage, active and reactive power, and frequency levels deficiencies. Therefore, smart algorithms were designed to ensure that hybrid microgrid operation, including renewable energy sources and stochastic EVs charging and discharging events, never violates system levels. Additionally, two-stage optimization techniques were developed and deployed to ensure proper EVs charging and discharging coordination concerning the grid's real-time operation. At the first stage, a community-based particle swarm optimization algorithm was developed to decompose the power distribution grid into well-defined partitions based on their voltage sensitivity values with respect to changes in active and reactive power levels, respectively. After reaching an optimal decomposition, a centralized optimization technique was formulated with mixed-integer linear programming was run to obtain optimal coordination for the voltage and reactive power per partition while resolving the nonlinearity and nonconvexity of the electrical system via applied mathematical approximation . Such methodologies mainly aim to reach optimal large-scale EVs charging and discharging schedules without integrating extensive communication infrastructure.

Additionally, one of the main goals of this dissertation is to ensure the safe arrival of the EVs to their nearest charging stations at the lowest possible energy consumption. Therefore, a real-time, metadata-driven electric vehicle routing optimization algorithm was developed. The routing algorithm was based on the Double Deep Q-learning Network (DDQN) concept to learn the maximum travel policy of the EV as an agent. The policy model was trained to estimate the agent's optimal action per the obtained reward signals and Q-values, representing

the feasible routing options. The routes' modelling was achieved based on the dynamic Markov Chain Model (MCM), defining Markov's unit step as the vehicle's average energy consumption. Real-time driving data and road conditions such as traffic jams, road closures, number of stops, driving patterns and applicable driving restrictions were integrated via Google's API platform. The essence of this algorithm is to ensure that EVs can reach their final destination with the lowest possible energy consumption.

To sum up, the major contributions of this dissertation are as follow:

1. Developing a mathematical formulation that represents the real-time modeling of electric vehicles activities on the power distribution grid.
2. Designing an intelligent, metaheuristic-based vector-decoupled algorithm to properly manage the voltage, power, and frequency levels in hybrid microgrid via smart EVs charging and discharging.
3. Developing an intelligent, real-time data-driven routing algorithm based on Double Deep Q-learning Network to reach a destination with the lowest energy requirements.
4. Developing an intelligent, community-based detection to decompose the power distribution grid into well-established partitions based on nodes' sensitivity values to active and reactive power injection and absorption.
5. Designing and implementing a two-stage optimization technique to solve the voltage and reactive power optimization problem (VVO) with the integration of electric vehicle scheduling, active power curtailment of PV systems, and reactive power compensation devices.

6. Designing and implementing a tri-level hierarchical energy management system based on the Stackelberg model and real-time demand-inverse curve of various players in the energy market.

1.5 Organization of the Dissertation

This dissertation is composed of ten chapters.

- Chapter one provides introduction on general concepts related to the EVs and introduce the major contribution of this dissertation.
- Chapter two provides a revised linearization methodology to model the real-time EVs activities based on the concept of Kirchhoff laws, Nodal analysis, and Modularity index. Specifically, chapter two proposes modeling methodology and mathematical formulation based on the decomposition of the distribution feeder topology into clustering nodes while considering on-time demands and EVs activities. It presents a scalable and powerful tool that allows researchers to accurately model the grid's real-time dynamics at each specific node of the system. It also helps determine the voltage sensitivity and estimate potential operational deficiencies in reference to the active and reactive power conditions at different feeder spots. To verify our modeling strategy, we demonstrate it on the modified IEEE 34 node system to measure the impact on the system's voltage level for each hour of the day, which could provide an estimate for the operational needs of active and reactive power through proper EVs scheduling that is investigated in a later chapter of this dissertation.

- Chapter three presents a hybridization technique based on integrating particle swarm optimization (PSO) with artificial physics optimization (APO) to be used for energy management and control of hybrid microgrids considering large-scale integration of EVs. To ensure the effectiveness and robustness of the developed hybridization, this chapter tests it on one of the most investigated problems in the smart grid arena: the reactive power dispatch problem. The hybridized algorithm was tested on the IEEE 30, IEEE 57, and IEEE 118 bus test systems to solve both single and Multiobjective ORPD problems, considering three main aspects. These aspects include active power loss minimization, voltage deviation minimization, and voltage stability improvement. The results prove that the algorithm is highly effective and displays great consistency and robustness in solving both the single and Multiobjective functions while improving the convergence performance of the PSO. It also shows superiority when compared with results obtained from previously reported literature for solving the ORPD problem.
- Chapter four utilizes the hybrid algorithm discussed in chapter three to propose a metaheuristic-based vector-decoupled algorithm to balance the control and operation of hybrid microgrids in the presence of stochastic renewable energy sources and electric vehicles charging structure. The AC and DC parts of the microgrid are coupled via a bidirectional interlinking converter, with the AC side connected to a synchronous generator and portable AC loads, while the DC side is connected to a photovoltaic system and an electric vehicle charging system. The vector-decoupled control parameters of the bidirectional converter are tuned via hybridization of particle swarm

optimization and artificial physics optimization to properly ensure safe and efficient exchange of power within allowable voltage and frequency levels. The developed control algorithm ensures the stability of both voltage and frequency levels during the severe condition of islanding operation and high pulsed demands conditions, and the variability of renewable source production. The developed methodology is verified in a state-of-the-art hardware-in-the-loop testbed. The results show the robustness and effectiveness of the developed algorithm in managing the real and reactive power exchange between the AC and DC parts of the microgrid within safe and acceptable voltage and frequency levels.

- Chapter five provides dynamic modeling of large-scale charging and discharging integration of the EVs to assess their timely impact on the distribution grid. Four case scenarios were modeled here considering a 24-hour distribution system load data on the IEEE 34 bus feeder. The results show the level of charging and discharging allowed on this test system, during each hour of the day, before violating the system's limits. It also estimates the costs of charging throughout the day utilizing the time-of-use rates and the number of EVs to be charged on an hourly basis on each bus and provides hints on the best locations on the system to establish the charging infrastructure.
- In chapter six, a real-time, data-driven electric vehicle (EVs) routing optimization to achieve energy consumption minimization is developed. The developed framework utilizes the concept of Double Deep Q-learning Network (DDQN) in learning the maximum travel policy of the EV as an agent. The policy model is trained to estimate

the agent's optimal action per the obtained reward signals and Q-values, representing the feasible routing options. The agent's energy requirement on the road is assessed following Markov Chain Model (MCM), with Markov's unit step represented as the average energy consumption that considers the different driving patterns, the agent's surrounding environment, road conditions, and applicable restrictions. The framework offers a better exploration strategy, continuous learning ability, and the adoption of individual routing preferences. A real-time simulation in the python environment that considered real-life driving data from Google's API platform is performed. Results obtained for two geographically different drives show that the developed energy consumption minimization framework reduced the EVs' energy utilization to reach their intended destination by 5.89% and 11.82%, compared with Google's original developed routes. Both drives started at 4.30 PM on April 25th, 2019, in Los Angeles, California, and Miami, Florida, to reach EV's charging stations located six miles away from both of the starting locations.

- Chapter seven proposes a fair, real-time, demand-influenced dynamic pricing structure to accurately allocate more fairness to the billing strategy to reflect updated energy prices during the microgrids' real-time operation. This pricing structure comprises two pricing fractions; retail energy price that follows time-of-use (ToU) rates and congested energy price allocated solely for billing EVs charging events during congested timeslots. The developed methodology is implemented in a hierarchal multi-agent architecture with a stochastic energy management system that aims to provide a cost-

efficient microgrid operation. The inputs to the optimization problem are day-ahead PV forecast and stochastic EVs energy levels and connectivity times prediction models based on a discrete-time Markov chain. Moreover, a predictive model of daily load demand is also presented based on adaptive Artificial Neural Network (ANN). The models were develop based on historical data for Miami Dade County, South Florida. Through numerical simulations, we attest that the developed pricing structure achieves significant energy prices reduction when compared with results from previous well-established pricing policies.

- Chapter eight proposes a two-stage optimization strategy for solving the voltage-var optimization (VVO) problem considering large-scale, stochastic penetration of plug-in electric vehicles (PEVs) to unbalanced, 3-phase power distribution networks (PDN). The optimization strategy considers the prospect of forced active power curtailment (APC) at a minimized level, bidirectional PEVs activities, as well as relaxed tap operations of shunt capacitor banks (CBs), online tap changing transformer (OLTC), and voltage regulators (VRs) to achieve optimal economic gain while satisfying the VVO operational constraints. The first stage aims for the optimal decomposition of the PDN into well-defined, cross-checked smaller partitions via a developed community-based detection particle swarm optimization (CBDPSO) algorithm. The second stage incorporates a mixed-integer linear programming (MILP) formulation to solve the VVO problem per partition level while considering the nonlinearity and nonconvexity of the electrical system via applied mathematical approximation. This reduces the

complexity and computational burdens that usually arise in solving the problem on a larger scale. The developed two-stage strategy is tested on the modified IEEE 123 bus system with various case scenarios. Economical operation of the PDN is achieved during peak demand hours while maintaining a safe operation within the context of the VVO problem.

- Chapter nine proposes a tri-level, hierarchical energy management coordination considering large-scale integration of the PEVs. Specifically, the hierarchical framework is composed of two energy optimization problem formulation that oversee three layers of controls in the electrical infrastructure: a lower-level energy optimization problem that is based on the interaction of an aggregator and its assigned microgrid. The aggregator is located at the PEV's charging station, and its main duties is to collect in a decentralized manner the required information from the PEVs that would like to request connection to its station. Then and on a timely fashion, the aggregator sends the collected information to its assigned microgrid which run centralized energy management optimization problem to updates the energy prices signals for each charging stations based on the updated status of the grid. Moreover, for the microgrid to able to obtain efficient and accurate results that reflect the timely dynamic updates of the overall electrical interconnection, and to avoid any potential overlaps in peak demands in charging loads at other microgrid's location; the microgrid participates in an upper-level energy optimization problem with the system operator that oversee the complete generation and operation of the interconnected electrical system and other

important factors such as the system's overloading conditions and constraints. The main idea behind the formulation of the tri-level control is based on updating the grid's operation and issuing energy price signals for each station on the system based on continuously updated inverse-demand curve of each microgrid. This is because accurate representation of the dynamic pricing needs to reflect the updated demand on each part of the grid, including the peak and off-peak PEVs demands, and establish price signals based on the availability and scarcity of the generation level per microgrid. That is to say, the tri-level energy management and control aims to normalize the peak demand of the PEVs via influencing the charging behaviors of the PEVs by the dynamically issued energy price signals. The developed framework takes into consideration reducing the carbon emissions via the incorporation of the cap and trade market and renewable energy portfolio (RPS) standards into the upper-level energy optimization problem. The optimization strategy is formulated using mixed-integer quadratic programming (MIQP), with KKT approximation that aims to linearize the electrical energy constraints.

- Chapter ten gives conclusions of the dissertation's research. It also discusses the outcomes, and future recommendation in this research arena

Chapter 2 Mathematical Modeling of Voltage Drop and Grid Congestion Due to the Integration of Electric Vehicles on the Power Distribution Feeders

2.1 Introduction

In this chapter, we aim to provide mathematical interpretation and modeling of the EVs charging and discharging events, as well as the corresponding voltage sensitivity level that may emerge as results of EVs activities. Specifically, we present a revised linearization approach to model the voltage and power consumption at each node at the distribution feeder. Such modeling simplification and representation provides a relevant framework to dynamically model the EVs activities throughout the day, utilizing discretized time slots. The presented methodology aims to decompose the feeder into clustering nodes via the concept of modularity index, which allows precise estimation of the contribution of the EVs at each specific node of the system. This enables smarter load management and monetary control-policy following an actual real-time consumption estimation at each part of the system. This linearized approach can also serve as a tool to enable the modeling of other low-voltage activities such as demand response programs, on-site and low-scaled renewable energy sources, and microgrid control strategies, among others.

The rest of this chapter is organized as follows: section 2.2 presents the linearized methodology to estimate the EVs contribution at each node of the feeder, as well as provides an intuitive mathematical formulation based on the modularity index to estimate the voltage sensitivity with respect to the variation levels of active and reactive power because of EVs

activities. Section 2.3 presents a case study to verify the modeling approaches. Section 2.4 provides concluding remarks on the work of this chapter.

2.2 Modeling Methodology

Here, we assume a balanced low-voltage radial distribution feeder, as shown in Fig. 2.1. Since most distribution systems operate at low-voltage levels, we can give an intuitive assumption that the connected loads are purely resistive, since the resistive portion at the distribution feeder is usually much higher than the inductive portion. In a like manner, our second assumption is to neglect the modeling of the capacitive compensation devices, although they are frequently used as a way of voltage support to the distribution grid. Therefore, we assume that the distribution feeder operates close to unity. However, we neglect those assumptions in our modeling of the voltage sensitivity to properly estimate the reactive power needs of the grid according to the EVs activities. It should be noted that since the voltage level is a non-linear variable with the instantaneous active power, a linear approximation of the electrical feeder is required.

2.4.1 *Linear Approximation of a Decomposed Feeder Topology:*

As the electrical infrastructure is dynamic in nature, with its operation change from minute-to-minute, we discretize the 24-hour time horizon into discrete time slots, t, such that $t = \{1,2,\dots,T\}$. For the nth node on the feeder with an active power P_t^n at a specific time slot t, the load at that node could be represented as follows:

$$R_t^n = \frac{V_{nom}^2}{P_t^n} \qquad (2.1)$$

Where V_{nom} represents the nominal voltage of the distribution grid. The power from the EVs, during both charging and discharging scenarios, could be modeled as current source connected to the grid at the charging location. On the other hand, the power transformer could be modeled as a constant voltage source to properly estimate its overloading condition as a result of EVs contribution. Denoting the power of the EV at the nth node and time t as EV_t^n, the correspondent electrical current from each EVs could be found by:

$$I_t^n = \frac{EV_t^n}{V_{no}} \qquad (2.2)$$

Fig. 2.1 presents a clarified description of the distribution feeder with applying our so-forth assumptions. We can assume a linear representation of the feeder's circuit based on each node's correspondent consumption. Specifically, by inserting the proper resistive parameters of the line and properly setting the voltage of the node that resembles the power transformer as well as the assigned values of the current source, we can present a linear model to estimate the contribution levels of the EVs at each node of the feeder, utilizing the matrix analysis theory throughout the way. Let us break-up the feeder's topology into several segments representing the nodes that serve different customer classes, as shown in Fig. 2.2. By utilizing the basic concept of Kirchhoff's laws and nodal analysis, we can find the current at any node as a result of EVs charging or discharging as follows:

$$I_t^n = V_t^{in}\left(\frac{1}{R_{in}^n}\right) - V_t^{in}\left(\frac{1}{R_{in}^n} + \frac{1}{R_t^n} + \frac{1}{R_{out,1}^n} + \ldots\ldots + \frac{1}{R_{out,i}^n}\right) + V_t^{out,1}\left(\frac{1}{R_{out,1}^n}\right) + \ldots + V_t^{out,i}\left(\frac{1}{R_{out,i}^n}\right) \quad (2.3)$$

In case of no EVs charging or discharging event, equation (2.3) can be rewritten and presented as follows:

$$0 = V_t^{in}\left(\frac{1}{R_{in}^n}\right) - V_t^{in}\left(\frac{1}{R_{in}^n} + \frac{1}{R_t^n} + \frac{1}{R_{out,1}^n} + \ldots\ldots + \frac{1}{R_{out,i}^n}\right) + V_t^{out,1}\left(\frac{1}{R_{out,1}^n}\right) + \ldots + V_t^{out,i}\left(\frac{1}{R_{out,i}^n}\right) \quad (2.4)$$

Likewise, it should be noted that if we want to quantify the contribution of EVs activities at a node that is located directly following the transformer node, equation (2.3) can be rewritten as follows:

$$I_t^n - V_t^{Tr}\left(\frac{1}{R_{Tr}}\right) = -V_t^{in}\left(\frac{1}{R_{Tr}} + \frac{1}{R_{out,1}^n} + \ldots + \frac{1}{R_{out,i}^n} + \frac{1}{R_t^n}\right) + V_t^{out,1}\left(\frac{1}{R_{out,1}^n}\right) + \ldots + V_t^{out,i}\left(\frac{1}{R_{out,i}^n}\right) \quad (2.5)$$

Where V_t^{in} represent the voltage level at the node of connection at time slot t, while R_{in}^n and $R_{Out.i}^n$ are the downstream and upstream non-EVs loads (e.g. household loads) of the line in regard with the connection node placement on the feeder. V_t^{Tr} represents the voltage level of the power transformer at a given time slot t, which is modeled as constant voltage source as mentioned earlier. R_{Tr} represents the resistive parameter of the conductor that connect the

transformer with its following node. We also emphasize that if a node n is the last node on the feeder, then equation (2.3) could be rewritten as

$$I_t^n = V_t^{in}(\frac{1}{R_{in}^n}) - V_t^n\,(\frac{1}{R_{in}^n} + \frac{1}{R_t^n}) \qquad (2.6)$$

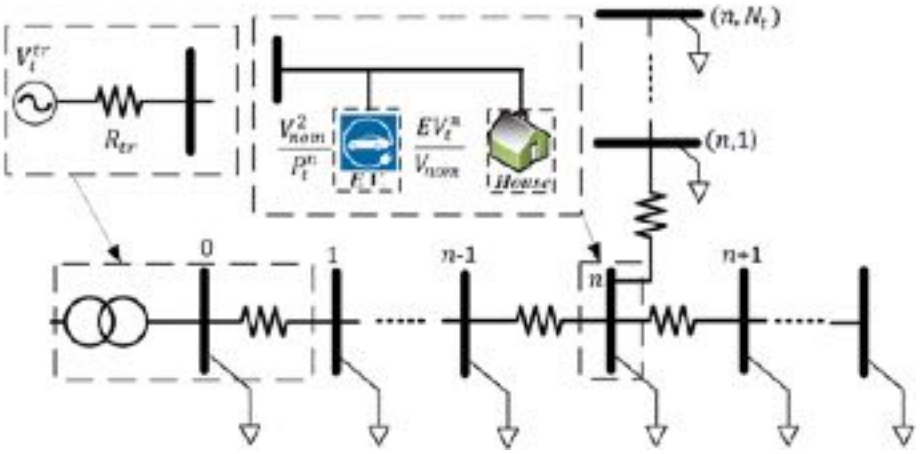

Figure 2-1 Illustration of a radial low-voltage distribution feeder

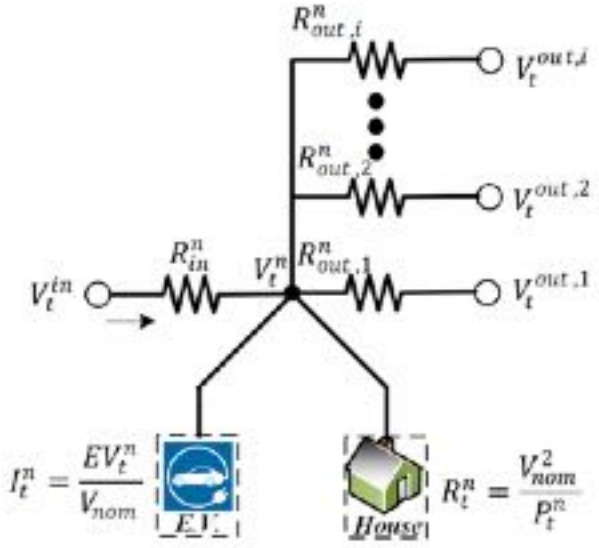

Figure 2-2 Description of EVs and non-EVs load calculation

As it may have been noted by now, we incurred N linear system equations and N voltage variables to be determined. Utilizing the concept of linear algebra and matrix analysis, we can

arrange the following mathematical expression to calculate the unknown voltages per each node of the feeder at a given time slot t, as follows

$$G_t V_t = I_t + V_t^{Tr}(\frac{1}{R_{Tr}}) \tag{2.7}$$

where G_t is the conductance matrix of the distribution feeder while V_t is a vector with the unknown voltages as its entries, to be calculated as follows:

$$V_t = [V_t^1, V_t^2, \ldots., V_t^n, \ldots., V_t^N]^T \tag{2.8}$$

where T stands for the transpose operator. Similarly, the contribution of the EVs charging and discharging is weighted by I_t which is the vector representation of the corresponding charging and discharging current values at each node during a given time slot t

$$I_t = [i_t^1, i_t^2, .., i_t^n, .., i_t^N]^T \tag{2.9}$$

It should be noted that the entry values are represented with a positive sign for the charging process on the relative entry, a negative sign for the discharging process, and zero when there is no EV connected to the node of interest. Lastly, V_t^{Tr} is a vector of the same dimension of I_t that has zero entries except with only one entry that represent the instantaneous time slot of interest that is filled with the voltage level of the power transformer at that time slot. It is represented as follows:

$$V_t^{Tr} = [-V_t^{Tr}, 0, \ldots, 0]^T \tag{2.10}$$

We want to bring to the reader's attention that the right-hand side of equation (2.7) is mathematically equal to the expression shown in equation (2.3). Furthermore, this expression allows us to distinguish the contribution to the grid operation for the current sources (the connected EVs) from the voltage source (the power transformer). Consequently, we can rewrite equation (2.7) following the EVs contribution during a slot, as follows:

$$G_t V_t = EV_t(\frac{1}{V_{no}}) + V_{Tr}(\frac{1}{R_{Tr}}) \tag{2.11}$$

where EV_t is a vector representation with entries that resemble the charging and discharging reference power at each node per a given time slot, with its sign as an indication of whether the activity is a charging or discharging event:

$$EV_t = [EV_t^1, EV_t^2, .., EV_t^n, .., EV_t^N]^T \tag{2.12}$$

Eventually, the unknown voltage levels of the grid for any time slot can be calculated by taking the inverse of the conductance coefficient matrix in equation (2.11), as follows:

$$V_t = G_t^{-1} EV_t(\frac{1}{V_{no}}) + G_t^{-1} V_t^{Tr}(\frac{1}{R_{Tr}}) \tag{2.13}$$

It should be noted that the impact of the EVs charging and discharging process on the voltage level of the feeder is essentially inferred from the first part of the right-hand side of equation (2.13), whereas the second part is dedicated to estimating the voltage level contributed from other non-EVs activities. This methodology allows proper modeling of smart scheduling of EVs charging and discharging throughout the 24-hour based on the condition of an electrical distribution feeder. However, to properly perform such modeling, we need to account for the

different parameters of the distribution feeder to properly model active and reactive power levels at each node. Thus, we include them in our next step of modeling the voltage sensitivity levels of the system, where we consider the unbalanced nature of the distribution grid at this point.

2.4.2 *Modularity Index Representation of the Voltage Sensitivity of the Decomposed Feeder*

We level up the modeling of the feeder to incorporate the voltage sensitivity as a result of the reactive power incurred on the feeder due to the charging and discharging process. We utilize the modularity index approach presented in [109, 110] to cross-check on the quality of the nodal partitioning and change of voltage levels across them as we aim to weight the difference between any connected nodes. The virtue of such modeling methodology lies in the ability to decompose the distribution feeder and identify the weakest nodes on the system, due to both the charging/discharging activities as well as the other non-EVs load consumption. For two nodes $i\ and\ j$, the modularity index, M, can be expressed as

$$M = \frac{1}{2w}\sum_{i}\sum_{j}\ (A_{ij} - \frac{\ell_i \ell_j}{2w}).\ \delta(i,j) \tag{2.14}$$

where A_{ij} is a matrix with entries that represent the correspondent weighted values of either active power-voltage or reactive power-voltage sensitivity values between two nodes at the feeder, described as follows:

$$A_{ij} = \begin{cases} 0 < a_{ij} \leq 1, if\ there\ is\ a\ link\ the\ nodes \\ 0, otherwise \end{cases} \tag{2.15}$$

while ℓ_i and ℓ_j represents the aggregated weighted values of all nodes connected to nodes $i\ and\ j$, $\delta(i,j)$ represents a connection factor that is labeled zero if there is no connection between nodes $i\ and\ j$, and assumed unity otherwise. The incremental changes in the values of active power (ΔP), reactive power ($\Delta\theta$), voltage (ΔV) and phase angle ($\Delta\delta$) due to the charging of EVs at a specific node during time slot t could be represented as follows:

$$\begin{bmatrix}\Delta\delta\\ \Delta V\end{bmatrix} = \begin{bmatrix}\mathfrak{s}_{\delta P} & \mathfrak{s}_{\delta\theta}\\ \mathfrak{s}_{VP} & \mathfrak{s}_{V\theta}\end{bmatrix}\begin{bmatrix}\Delta P\\ \Delta\theta\end{bmatrix} \tag{2.16}$$

where $\mathfrak{s}_{\delta P}, \mathfrak{s}_{\delta\theta}, \mathfrak{s}_{VP}, \mathfrak{s}_{V\theta}$ represent the sensitivity values of phase angel in regard with active power, phase angle in regard with reactive power, voltage corresponding to active power and reactive power levels, respectively. As an example, to fill out entries within matrix A_{ij}, we provide the way we calculate the sensitivity of the voltage corresponding to the change in reactive power level for the ij[th] entry of the matrix as follows:

$$A_{ij,t}^{V\theta} = \frac{\mathfrak{s}_{ij,t}^{V\theta} - \mathfrak{s}_{ji,t}^{V\theta}}{2} \tag{2.17}$$

where the variables of the nominator represent the weighted values of $\mathfrak{s}_{V\theta}$, considering (i,j) and(j,i) during a time slot t. The level of reactive power that can be injected at a given node is related to its level of voltage drop. Therefore, we can quantify such injection as follows:

$$\theta_t^n = \theta_{EV,t}^n - R_t^n \tag{2.18}$$

where θ_t^n is the aggregated level of reactive power at node n given its instantaneous total load, while $\theta_{EV,t}^n$ is the allowed permissible reactive power injection as a result of EVs charging

at the node during time slot t. Furthermore, we can extend the assessment of the reactive power status per each time slot for a large number of connected nodes, denoted by subsection R, as follows:

$$\mathfrak{s}_R = \sum_{i,j \in R} A_{ij}^{V\theta} \tag{2.19}$$

Finding the values for $\mathfrak{s}_R$ provides hints on the condition of different segments of the distribution feeder. Specifically, higher value means that due to its current voltage condition, subsection R of the feeder is more sensitive to the injection of the reactive power at a specific time slot. The level of required reactive power compensation in subsection R as a result of an incremental voltage change can be found as follows:

$$\theta_{required,t}^{i} = \sum_{i \in R} \frac{\Delta V_i}{\mathfrak{s}_{V\theta}} \tag{2.20}$$

where the formula expresses the incremental change in voltage level divided by the sensitivity of the voltage level as a result of the reactive power changes during time slot t at node i due to an EV activity. This provides the opportunity to quantify the required amount of reactive power we could assist to regulate the voltage level at the weakest area in the feeder by the mean of EVs discharging at the given node. Then, the voltage levels between nodes i and j could be updated according to the following formula:

$$V_R^i = V_i^0 + \sum_{j=1}^{n} \mathfrak{s}_{VP}^{ij} \Delta P + \sum_{j=1}^{n} \mathfrak{s}_{V\theta}^{ij} \Delta\theta \tag{2.21}$$

It should be noted that to properly identify the weak nodes on the system among possible tens or hundreds, we can merge the nodes that operates at the same voltage levels or

close to it and consider them as one unified node. Let us consider M_i^0 as the initial modularity index for node i. If the index for its following node is very close to node i, then we can treat the two nodes as a one merged node. This process continues iteratively until a limit is hit when the index of a node k is bigger than or equal to a predetermined level set by the tertiary operator, compared with the initial value of M_i^0. Once this condition reached, node k index serve as a starting point of comparison with the following node and the process continue so-forth. In addition, we present cost function as optimization goal to monetarize the charging events in regards with the voltage level deviation as follows:

$$min_{\theta,n} \ \sum_{n=1}^{N_T} |V_n - V_{Tr}| \tag{2.22}$$

A goal of formulating this global optimization problem is to strictly enforce monetary policy that penalize the charging activity of the EVs as a compensation to the level of voltage support needed at that point during a given time slot.

2.4.3 *Operational Constraints*

To govern a stochastic process such as charging and discharging amount of power into the grid in a probabilistic manner, a set of constraints must be placed to ensure safe and proper operation. We chose voltage limit as the critical factor not to be violated at any time

$$V_{min} \leqslant V_t^n \leqslant V_{max}, \forall \ n \in N_T \tag{2.23}$$

where V_t^n is the voltage level at the nth node at time slot t. Also, both charging and discharging rates must remain within a safe and permissible limit, as follows:

$$r^{n}_{charge,t} \leqslant r^{n}_{\max\_charge,t} \tag{2.24}$$

$$r^{n}_{discharge,t} \leqslant r^{n}_{\max\_discharge,t} \tag{2.25}$$

where $r^{n}_{charge,t}$ and $r^{n}_{discharge,t}$ are charging and discharging rates limits of the EVs level at the nth node at time slot t, which are set not to exceed certain predetermined limits. Similarly, we define the level of charging and discharging power at each node and any time slot as follows:

$$0 \leqslant EV^{i}_{charge} \leqslant EV^{i}_{\max\_charge,t} \tag{2.26}$$

$$0 \leqslant EV^{n}_{discharge,t} \leqslant EV^{i}_{\max\_discharge,t} \tag{2.27}$$

Therefore, the minimum and maximum allowed SOC levels per node which can be set up by the tertiary operator depending on the status of the feeder at each time slot must be strictly limited.

$$SOC^{Min}_{t} \leq SOC^{i}_{t} \leq SOC^{Max}_{t} \tag{2.28}$$

2.3 Case Study and Results

We assume that a node on the test system may diverge into countable finite number of nodes that represent residences. Parameters of the test system, the IEEE 34 bus system, is found in reference [111]. The socket rating for EVs in our simulation is assumed to be 3.3 and 7.6 kW. The arrival and departure times of the EVs are estimated based on truncated Gaussian probability distribution functions which allows us to indicate the voltage level of each node,

quantify the contribution of EVs activities more properly, and permit us to decompose the feeder into *N* zones for our second case scenario.

The decomposition allows us to indicate the voltage level of each zone on the feeder, which could be used to establish proper and real-time smart charging and discharging scheduling based on the status of each zone. Specifically, the solution to the voltage sensitivity model quantifies the active and reactive power boundary levels for each zone (e.g. the maximum allowed active power consumption and maximum allowed reactive power injection per each time slot). However, this chapter is only dedicated to the mathematical formulation of the electric vehicles on the distribution feeders and introduce the basis of utilizing the modularity index to decompose the distribution grid. Therefore, full analysis and detailed results for modeling the electric vehicles are illustrated in chapter 5 of this dissertation. Nevertheless, to illustrate the concept of using the modularity index in decomposing the distribution feeder, we provide in following subsection a case scenario considering the IEEE 34 bus system. A full detailed utilization of the modularity index in this dissertation are explained in detail in chapter 8, where we propose a community-based detection particle swarm optimization (CBDPSO) algorithm to decompose the power distribution grid into optimal partitions, considering the IEEE 123 bus system as application in that chapter.

2.4.1 *Decomposition of Zonal Areas Based on Modularity Index:*

Based on the modularity index estimation described in section 2 of this chapter, the distribution feeder could be decomposed into N zones with no overlap. We categorize the voltage condition at each node as either normal or abnormal nodes. The former labels the nodes

remaining within permissible voltage limits during the EVs activities, while the latter labels the nodes that violate the system's voltage limits otherwise. The voltage sensitivity level is performed according to equation 2.14. Based on our simulation results illustrated in detail in chapter 5 of this dissertation, we establish node 830 as the point of authority to control the voltage level at the test during the peak demand hours. This leading node could be updated to any other node based on the feeder's condition at other times. Assuming a responsible agent at each zone, the agent estimates its nodes instantaneous needs of real and reactive power and report the findings to the tertiary operator, which determines the scheduling of the EVs charging and discharging based on real-time feeder status. The updated voltage levels at each zonal section considering the sensitivity of the voltage concerning the active and reactive power are calculated from equation 2.19. The process is repeated iteratively at each time slot with corresponding charging and discharging scheduling for all decomposed parts until the abnormal voltage levels resume normality condition. Fig. 2.3 shows the overall decomposition of the feeder into optimal clusters to reduce the voltage variability during peak hours. As per the result, the modularity index reaches its highest value when there are six zonal nodes at the test feeder with a value of 0.45 instead of the originally established 34 nodes with an index of 0.20, as shown in Fig. 2.4. The system's optimized decomposition considers the accumulated levels of charging and discharging that could be carried out at each node of the feeder.

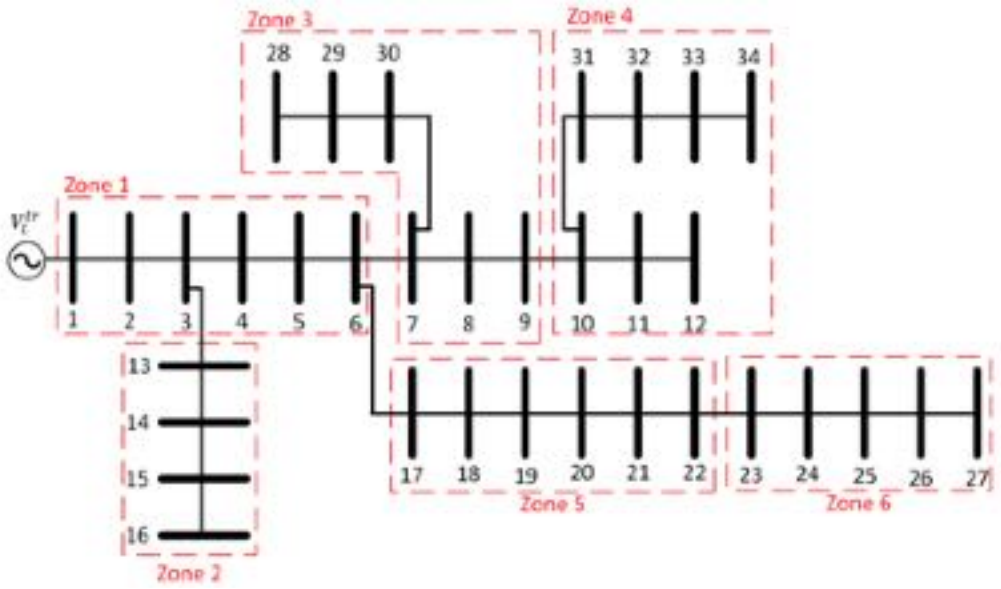

Figure 2-3 The decomposed feeder based on the concept of modularity index.

Upon clustering the feeder, the results show abnormal voltage levels as result of EVs activities during peak demand hours at zones 4, 5 and 6, while normal voltage operating condition at the rest of the zones. Therefore, after implementing an optimal scheduling strategy from the system operator in according with the level of severity, the process is repeated to ensure proper handling of any further over- and under-voltage issues at the grid. Fig. 2.5 shows the voltage sensitivity results at each node at the feeder based on the analysis described in our work. It should be noted that the sensitivity values are not constant and keep updating with respect with the operational condition of the grid. The greater the sensitivity value of a node the more prone it is to any changes on the system to sizeable EVs activities. Furthermore, results indicate that nodes with higher voltage-reactive power sensitivity are the ones that the operator should carefully plan their reactive power scheduling as level of voltage variations as they record severe voltage drops as consequences. Therefore, the nodes with the highest

reactive power absorption have high value representation in the sensitivity matrix in equation 2.14.

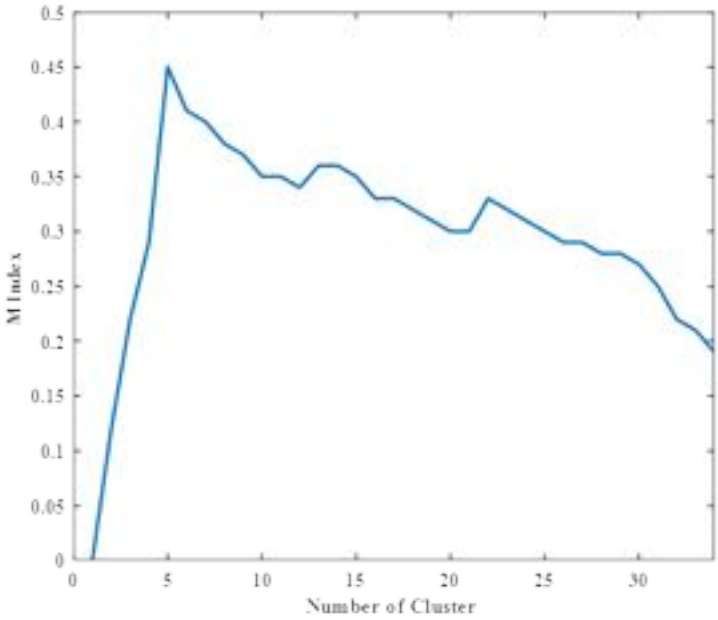

Figure 2-4 Results of modularity clustering versus number of nodes of the feeder

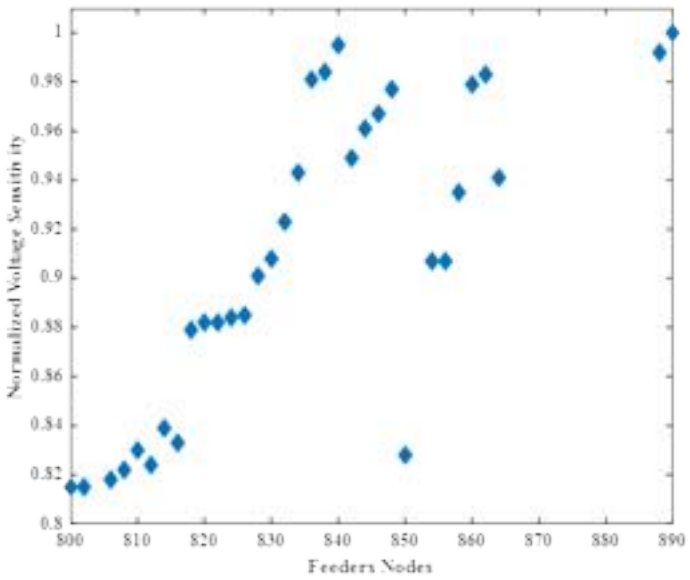

Figure 2-5 Normalized voltage sensitivity levels per each node

2.4 Conclusion

We presented in this chapter a methodology and mathematical formulation to properly estimate the dynamic contribution of the EVs activities on each node at the distribution feeder. The virtue of the presented modeling techniques lies in the ability to decompose the distribution feeder and identify the weakest nodes on the system, due to both the charging/discharging events as well as the other non-EVs load consumption. To validate our developed methodology, we modeled a case scenario to decompose the system into clustering zones and identify the sensitivity levels voltage and phase angels, each in reference to the allowable active and reactive power limits per each node on the system. Furthermore, upon using the modularity index to break-up to find the most optimal decomposition of the system, we do believe that decomposing the feeder into detailed topology offers great tool to the tertiary operator to identify on a timely manner the nodes with most deficiency in voltage levels and therefore dispatch a more accurate, timely-sensitive active and reactive power scheduling.

Chapter 3 Single and Multiobjective Optimal Reactive Power Dispatch Based on Hybrid Artificial Physics–Particle Swarm Optimization

3.1 Introduction

Optimal reactive power dispatch (ORPD) is an important problem in power system operation. The economy of grid operation has two main aspects to consider: active (Watt) and reactive (Var) power control problems. The Watt problem concerns regulating and controlling the output of the generation units to reduce the overall costs of production. The Var is considered a more complex problem due to the nature of control variables involved in its operation, where it focuses on different voltage control aspects of the grid components (i.e., tap-changing transformers, reactive compensators, etc.) to reduce the overall grid losses, and improve voltage balance. ORPD is considered a pivotal problem in this manner, which aims to solve highly constrained, nonconvex, and nonlinear optimization problems that possess both discrete and continuous control variables to achieve important goals, such as minimizing active power losses and voltage deviations, while improving the voltage stability index of the grid. These types of operational issues emerge due to the complexity arising in grid modernization. Specifically, the ORPD is essential to help maintain the voltage level in loading conditions by reducing the voltage deviation and power quality issues that emerge from the stochastic fluctuations of the power output. The latter due to the unpredictability of sources such as renewable energy and electric vehicle integration.

The significant contribution of this chapter is to develop a hybridization of two naturally inspired metaheuristics techniques, particle swarm optimization (PSO) and artificial physics optimization (APO), then solve and optimize the complexity and nonlinearity of the ORPD problem and test it on various IEEE test systems to evaluate its search capacity. Our overall goal is to produce an intact algorithm that combines the global search capabilities of APO with

the strong local exploratory search performance of PSO, while improving its convergence characteristics. The APO exhibits flexible and wide-range search features that enhance its global population diversity, adding a powerful searching-mixture when combined with PSO. After building the mathematical representation of each algorithm, we validate the performance of the hybridized algorithm on the IEEE 30, IEEE 57, and IEEE 118 bus test systems, and compare with the results of previously published reports using other methods to verify its capabilities.

This chapter is organized as follow: Section 3.2 provides mathematical modeling of the ORPD problem. Section 3.3 describes mathematical representations and framework of the APO, the PSO, and the hybrid APOPSO and its application to solve the ORPD problem. Section 3.4 provides an analysis of the results and compares them with the reported results in the literature. Section 3.5 concludes the chapter and provides suggestions for future studies to be carried out in this area.

3.2 Mathematical Formulation of the ORPD

The hybrid APOPSO algorithm developed in this chapter aims to individually and simultaneously minimize three main objectives in the ORPD problem subjected to equality and inequality constraints, namely, minimizing total active power loss, reducing voltage deviations, and improving voltage stability index (the L-index).

3.2.1. General Optimization Problem Formulation

The general mathematical formulation of an objective function can be expressed as

$$Min\ \widetilde{F}(\bar{x}, \bar{y}) \tag{3.1}$$

subject to

$$E(\bar{x}, \bar{y}) = 0 \tag{3.2}$$

$$I(\bar{x}, \bar{y}) \leq 0 \tag{3.3}$$

where F is the objective function to be minimized, E and I are nonlinear constraints represented as vectors that resemble both the independent (control) and dependent variables of the problem. Specifically, x is a vector containing the control variables of the ORPD which namely include the reactive power compensators G_c, dynamic tap-setting of transformers T, and voltage levels at generation units Vg. x can be expressed as

$$x = [V_{G_1} \ldots, V_{G_{N_g}}; Q_{C_1} \ldots, Q_{C_{N_C}}; T_1 \ldots, T_{N_T}] \tag{3.4}$$

y is a vector representing the dependent variables, which include slack generator $P_{G_{slack}}$, voltage levels at transmission lines V_L, reactive power from generation units Q_G, and the apparent power S_L. y can be expressed as

$$y = [P_{G_{slack}}; V_{L_1} \ldots, V_{L_{N_{Load}}}; Q_{G_1} \ldots, Q_{G_{N_g}}; S_{L_1} \ldots, S_{L_{N_{Tr}}}] \tag{3.5}$$

3.2.2. Single Optimization Function Formulation

3.2.2.1. Minimization of MW Losses Function

The fitness function formulated to reduce the overall MW losses in the system can be expressed as

$$OF_1 = P_{min} = \min [\sum_m^{NTL} G_m [V_i^2 + V_j^2 - 2 * V_i V_j \cos \emptyset_{ij}] \tag{3.6}$$

where N_{TL} is the number of transmission lines in the system, G_M is the conductance of the transmission lines between the i^{th} and the j^{th} buses, and $\emptyset_{ij}$ is the phase angle between buses i and j.

3.2.2.1. Minimization of Voltage Deviation

It is highly significant to record and notice all the voltage deviations across all the system's buses from reference points. This is done to ensure proper consideration of the voltage limits in optimal reactive power planning and operations, and not only as constraints, as bus voltages may operate at their maximum limits without invoking any violation yet leading to improper reactive power reserves that could cause outages and faults. The fitness function of voltage deviation minimization can be written as

$$OF_2 = \min \left[\sum_{I=1}^{N_{LB}} \left| V_{LK} - V_{LK}^{Desired} \right|\right]^2 + \sum_{I=1}^{Ng} Q_{GK} - Q_{KG}^{Lim} \,]^2 \qquad (3.7)$$

where V_{LK} is the load voltage at the k^{th} load bus, $V_{LK}^{Desired}$ is the desired load voltage at the k^{th} load bus that is usually set to be 1.0 pu, Q_{GK} is the reactive power from generators at the k^{th} load bus, Q_{KG}^{Lim} is the generator reactive power limit, while N_{LB} and N_g are the number of the load buses and generation units in the system, respectively.

3.2.2.3. Minimization of Voltage Stability Index

The L-index is utilized in this work as a metric indicator of voltage stability performance. This index is newly introduced and presented in [112]. It assesses the steady-state voltage levels for any node in the test system and provides highly consistent results compared to other voltage stability indices, e.g., voltage collapse prediction index (VCPI), equivalent node voltage collapse index (ENVCI), fast voltage stability index (FASI), etc. [113]. Such indices are crucial

factors to be considered in the planning and operation of an electrical network. L-index can be expressed as:

$$OF_3 = \min L_{max} \tag{3.8}$$

$$\text{where } L_{max} = \max [L_j];\ j = 1;\ N_{LB} \tag{3.9}$$

$$\text{and} \begin{cases} L_j = 1 - \sum_{i=1}^{N_{PV}} F_{j_i} \frac{V_i}{V_j} \\ F_{j_i} = -[Y_1]^{-1}[Y_2] \end{cases} \tag{3.10}$$

such that

$$L_{max} = \max [1 - \sum_{i=1}^{N_{PV}} - [Y_1]^{-1} [Y_2] \times \frac{V_i}{V_j}] \tag{3.11}$$

where N_{PV} is the number of the PV (generator type) buses in the system.

3.2.3. System Constraints (Independent and Dependent Variables)

3.2.3.1. Equality Constraints

Equality constraints of the ORPD are the usual nonlinear power flow equations which provide voltage levels and angles at each node in the test system, expressed as

$$0 = P_{G_i} - P_{D_i} - V_i \sum_{j-1}^{N_{Total\ Buses}} V_i\ [G_{ij} \cos[\emptyset_i - \emptyset_j] + B_{ij} \sin[\emptyset_i - \emptyset_j]] \tag{3.12}$$

where P_{Gi} and P_{Di} are the real power generation and demand at the system respectively while G_{ij} and B_{ij} are the real and imaginary entries of the bus admittance matrix corresponding with the i^{th} row and j^{th} column, for $i = 1, \ldots, N_{Totel\ buses}$.

$$0 = Q_{G_i} - Q_D - V_i \sum_{j-1}^{N_{Total\ bases}} V_j \left[G_{ij} \sin[\emptyset_i - \emptyset_j] + B_{ij} \sin\left[\emptyset_i - \emptyset_j\right]\right] \quad (3.13)$$

where Q_{Gi} and Q_{Di} are the reactive power generation and demand at the system respectively, for $i = 1, N_{Totel\ buses}$.

3.2.3.2. Inequality Constraints

It should be noted that both dependent and independent variables must operate within specific limits imposed on them to ensure proper operation. Therefore, we carefully consider both equality and inequality constraints in our modeling. The boundary of operation for the independent (control) variables applies to (i) the slack generator output limit, (ii) reactive power limit of the generation units, (iii) the load buses voltage limits, and (iv) the apparent power flow limit. These operational inequalities can be represented as

$$P_{G_{slack}}^{min} \leq P_{G_{slack}} \leq P_{G_{slack}}^{max} \quad (3.14)$$

$$Q_{G_i}^{min} \leq Q_{G_i} \leq Q_{G_i}^{max},\ i = 1, N_g \quad (3.15)$$

$$V_{L_i}^{min} \leq V_{L_i} \leq V_{L_i}^{max},\ i = 1, N_{LB} \quad (3.16)$$

$$\left|S_{L_i}\right| \leq S_{L_i}^{max},\ i = 1, N_{TL} \quad (3.17)$$

where N_g, N_{LB}, and N_{TL} are the numbers of generators, load buses, and transmission lines in the system. The dependent variables, such as (i) the generation unit voltage levels, (ii) reactive power compensators, (iii) the position of the tap transformers, are also operationally restricted and limited as follows:

$$V_{G_i}^{min} \leq V_{G_i} \leq V_{G_i}^{max},\ i = 1,\ N_g \tag{3.18}$$

$$Q_{C_i}^{min} \leq Q_{C_i} \leq Q_{C_i}^{max},\ i = 1,\ N_C \tag{3.19}$$

$$T_i^{min} \leq T_i \leq T_i^{max},\ i = 1,\ N_{RT} \tag{3.20}$$

where N_C and N_{RT} are the numbers of the compensator devices and regulating transformers, respectively.

3.2.4. Multiobjective Fitness Function

The previous fitness functions are incorporated into a multiobjective optimization function with penalty factors established to consider the dependent variables into the objective function minimization:

$$\text{MOF} = OF_1 + x_i\ OF_2 + \text{y}\ OF_3 = OF_1 + [\sum_{i=1}^{N_L} x_v\ [V_{L_i} - V_{L_i}^{min}]^2 + \sum_{i=1}^{N_G} x_g\ [Q_{G_i} - Q_{G_i}^{min}]^2] + x_f\ OF_3 \tag{3.21}$$

where x_v, x_g, and x_f are penalty factors incorporated to enforce the limits on the control variables to avoid any violation to the voltage deviation and stability index levels, assumed in this work to be 100. The limit values are defined as:

$$V_{L_i}^{min} = \begin{cases} V_{L_i}^{max},\ V_{L_i} > V_{L_i}^{max} \\ V_{L_i}^{min},\ V_{L_i} < V_{L_i}^{min} \end{cases} \tag{3.22}$$

$$Q_{G_i}^{min} = \begin{cases} Q_{G_i}^{max},\ Q_{G_i} > Q_{G_i}^{max} \\ Q_{G_i}^{min},\ Q_{G_i} < Q_{G_i}^{min} \end{cases} \tag{3.23}$$

3.3 Mathematical Framework of the Metaheuristic Algorithms

A thorough discussion on the APO and PSO algorithms and their hybridization is presented in this section.

3.3.1. Artificial Physics Optimization (APO)

APO, as a naturally inspired metaheuristic methodology, is well presented in [23, 114]. APO is based on the idea that an exerted force may result in either attractive or repulsive aggregation of physical entities (namely the particles or solutions) leading to a movement that represents the search to find local and global optima. Specifically, the process is based on three main observations: initializations, calculation of force, and motion of particles. At the initialization step, particles are sampled stochastically within a multidimensional decision space. The central presumption of APO is based on treating the particles (possible solutions) as physical entities that exhibit mass, position, and velocity, with the mathematical representation of the mass mapped as the fitness function. The mathematical representation of the mass (fitness) function is expressed as follow:

$$m_i = g\,[f(x_i)] \tag{3.24}$$

when $f(x) \in [-\infty, \infty]$, then;

$$\arctan[-f(x_1)] \in [\tfrac{-x}{2}, \tfrac{x}{2}], \text{ and } \tanh[-f(x_i)] \in [-I, I] \text{ with } \tanh(x_i) = \frac{e^{x} - e^{-x}}{e^{x} + e^{-x}} \tag{3.25}$$

Equations (3.24) and (3.25) can be mapped into the interval (0, 1) through an elementary transformation function. The mass functions can be rewritten as

$$m_i = e^{\frac{g\,[\,f(x_{best})-f\,(x_i)\,]}{f\,(x_{worst})-f\,(x_{best})}} \tag{3.26}$$

where the function $f\,(x_{best})$ is the objective function value at the position of the best received value for the individual (swarm particle), while $f\,(x_{worst})$ refers to the function value of the worst individual swarm reported:

$$\text{Best} = \text{avg}\,\{\min f\,(x_i),\ i\ \in S\,\} \tag{3.27}$$

$$\text{Worst} = \text{avg}\,\{\max \text{f}\,(x_i),\ i\ \in \text{S}\} \tag{3.28}$$

where S = {1; population of N agents}. Once each particle's mass is identified, a velocity vector will be produced. The inevitable changes in velocity in the iteration process are controlled by the level and amount of force exerted on the particle, which is the second stage of the algorithm; calculation of the force, which is based on the mass of the particle and its distance from its neighbors. The force exerted on a particle *i* via another particle *j* can be found via:

$$F_{ij,k} = \begin{cases} sgn\,(r_{ij}\,,k\,)\,G\,.\,(\,r_{ij}\,,k\,)\,.\frac{m_i m_j}{r_{ij}\,,\ k^2};\ \ if\ f\ (x_j) < f(x_i) \\ sgn\,(r_{ji}\,,\ k\,).G\,(\,r_{ji}\,,k\,)\ .\ \frac{m_i m_j}{r_{ij}\,,\ k^2};\ \ if\ f\ (x_j) \geq f(x_i) \end{cases} \tag{3.29}$$

$$r_{ij,k} = x_{j,k} - x_{i,k} \tag{3.30}$$

where $F_{ij,k}$ is the k^{th} force quantity enforced on particle *i* via particle *j* in their dimensions; $x_{i,k}$ and $x_{j,k}$ are the k^{th} dimension coordinates for the swarm particles *i* and *j*; $r_{ij,k}$ is the distance between these coordinates. Sgn(r) represents the signum function, while $G(r)$ denotes the

gravitational factor that follow the changes iteratively with $r_{ij,k}$. Both of them can be expressed as:

$$Sgn(r) = \begin{cases} 1 & if \quad r \geq 0 \\ -1 & if \quad r < 0 \end{cases} \tag{3.31}$$

$$G(r) = \begin{cases} g|r|^h & if \quad r \leq 1 \\ g|r|^q & if \quad r > 1 \end{cases} \tag{3.32}$$

Here, the g can be assumed as any value to provide simplicity and flexibility when experimenting. In our studies, we assumed these values based on studies presented in [113]. The total force exerted on all particles can be rewritten mathematically as:

$$F_{i,k} = \sum_{\substack{j=1 \\ i \neq j}}^{m} F_{ij\,,\;k} \;\; \forall\, i \neq best \tag{3.33}$$

The third stage is understanding the motion principles of the particles in the decision space, where the computed force is utilized to determine the velocity of the particles that are used to find (and then update iteratively) the respective positions of the particles. Such motions are set in either two- or three-dimensional space, in which particles can be locally spotted, and can be mathematically represented as

$$V_{i\,,k}\,(z+1) = \text{w}.\, V_{i,k}\,(t) + \beta \times {}^{F_{i,k}}\!/_{m_i} \tag{3.34}$$

$$x_{i,k}\,(t+1) = X_{i,k}(t) + V_{i,k}(\text{t} + 1) \tag{3.35}$$

where $V_{i,k}$ and $x_{i,k}$ are the k^{th} components of particle i's velocity and distance at iteration t. Beta is a uniformly distributed random number distributed on the interval (0, 1), while w is the user-specified inertia weight that can be iteratively updated, usually between 0.1 to 0.99. The inertia influences how two velocity values iteratively change. Larger values of w is a good indication of greater velocity changes, while small values is only used when we only want to

facilitate a local search. Each particle identifies the information of its neighbors, while the physical attractiveness/repulsiveness rule serves as the search strategy in this algorithm to guide the population to search within the region of a possible solution in accordance with their fitness function. The high accuracy and ability to map the particle's mass as a fitness function influence the whole optimization process, to which the relationship is proportionally related; the more accurately the objective function is designed, the bigger mass will be produced, which leads to a higher level of attractiveness, or in other words, more optimized searching strength, as particles will be naturally attracted to higher masses.

The iteration process in the APO leads to the updating of all particles' positions, and accordingly, the objective fitness function is adjusted to those new positions. Then, the fitness function identifies a new best individual and marks its position vector as the best solution. In this way, the second and third steps of the algorithm, force calculation and motion, are iteratively performed until a stopping criterion is achieved. Such criteria may be a predetermined number of executed iterations or reaching several successive iterations with no difference in the value of the best obtained particle position.

3.3.2. Particle Swarm Optimization (PSO)

PSO is a population-based, bio-inspired metaheuristic algorithm that was established by Kennedy and Eberhart in 1995 [22]. It is based on the concept of evolutionary computational method, where a system of study is started with an initial population of randomized solutions, updated iteratively in the process of searching for the local and global optima. The candidate solutions, known as particles, fly in the decision space with the velocity obtained in its previous best solutions, as well as its group's best results. Both the velocity and position of each particle are updated accordingly using the following mathematical formulas:

$$V_{ij}\ (t+1) = [\mathrm{W} \times\ V_{ij}(t)] + [C_1 + r_1 + [Pbest_{ij} - X_{ij}(t)]] + [C_2 + r_1 + [gbest_{ij} - X_{ij}(t)]] \tag{3.36}$$

$$X_{ij}\ (t+1) = X_{ij}(t) + \mathrm{C}\ V_{ij}(t+1) \tag{3.37}$$

Where $X_{ij}(t)$ and $V_{ij}(t)$ are vector representations in the solution space for both the velocity and position of particle *i*, while Pbest and gbest are the best individual and global optimal obtained solutions. The performance of PSO as a validated and well-proven metaheuristic technique is widely spread in the literature in different fields of study. This is due to its powerful searching capacity and premature convergence without the need to find local optimal. Fig. 3.1 shows the basic concept of the searching methodology and motion principle for particle *i* in PSO, where *V*(*t*), *Xm*, and *X* are three vectors describing the coordinates of the best solution in the decision space.

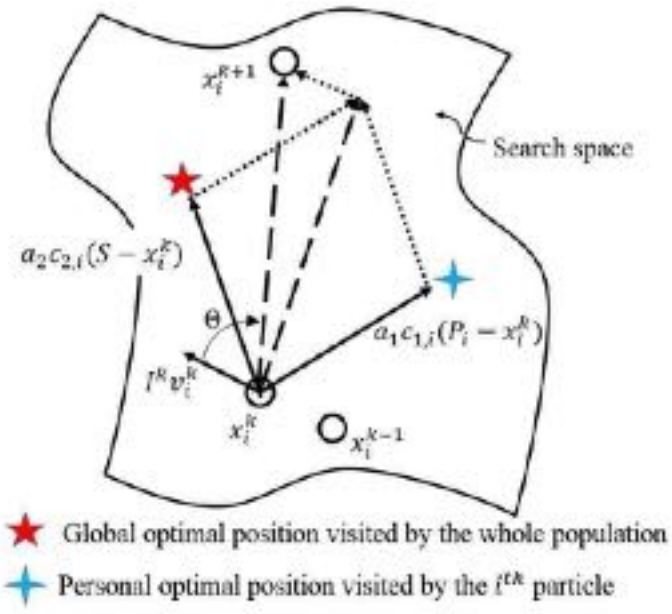

Figure 3-1 Criteria of the searching in the particle swarm optimization (PSO).

3.3.3. Hybridization of APO and PSO to Solve the ORPD Problem

The primary goal of establishing a hybridization of APO and PSO is to combine their individual strengths to form an optimized algorithm that utilizes the global search capabilities of APO with the strong local exploratory search performance of PSO, while improving its convergence performance. In other words, such hybridization aims to form a successful partnership among the local and global searching capabilities of the two algorithms to overcome any shortages each one may face if performed alone. Talbi et al. (2009) provide extensive analysis of the concept of integrating two metaheuristic techniques, which can be achieved on either lowly or highly heterogeneous integration [115, 116]. This work combines the two algorithms as a low-heterogeneity routine. Successful implementation of the hybridization requires modifying the particles' velocity and position equations, as follows:

$$v_{i,k}(t+1) = W \,.\, v_{i,k}(t) + \beta_1 - r_1 \,.\left[\frac{F_{i,k}(t)}{m_i}\right] + \beta_2 \,.\, r_2 \,.\left[g\ best - x_{i,k}(t)\right] \tag{3.38}$$

$$x_{i,k}(t+1) = x_{i,k}(t) + v_{i,k}(t+1) \tag{3.39}$$

In our developed APOPSO to solve the ORPD, we first define the dependent and control variables with their respective limits over a defined fitness function. Then, we randomly initialize the input values of the population (particles or swarms). Each particle represents a candidate solution. After the initialization step, we establish the best and worst values of the load flow and rank the obtained results. After that, the mass function given in Equation (3.26) will be assessed according to those results, and a force calculated using Equations (3.29) and (3.33) will be exerted on the particles, then their velocity and positions are updated based on Equations (3.36) and (3.37) and the distance between them according to (3.30), then ranking the newly produced results according to their fitness values. The process is repeated iteratively, and in each iteration, we check whether there is a violation that occurred at any level to ensure

proper operation within the limits. The iteration process stops updating the velocities and positions once an ending criterion is met. Fig. 3.2 shows the flowchart of the developed APOPSO algorithm. The pseudocode of the combined algorithm is as follows:

Step 1: Read and evaluate the input data [Tr, Qc, ….]. All values must be normalized in per unit system.

Step 2: 2.1: Define the independent (control) variables X within their specific boundary levels; 2.2: Define the dependent variables Y within their specific boundary levels; 2.3: Define the fitness function with its associated penalty factors.

Step 3: Generate an initial randomized population with N agents in the decision space. Specify the desired number of iterations to be performed. It should be noted that the initial positions of the population must be strictly within their boundary levels.

$$\text{POP}(0) = \begin{bmatrix} x_1(0) \\ x_2(0) \\ . \\ . \\ . \\ . \\ x_i(0) \\ . \\ . \\ x_N(0) \end{bmatrix} = \begin{bmatrix} x_1^1(0), \ldots\ldots\ldots., & x_1^d(0), \ldots\ldots\ldots., & x_1^n(0) \\ x_2^1(0), \ldots\ldots\ldots., & x_2^d(0), \ldots\ldots\ldots., & x_2^n(0) \\ & . & \\ & . & \\ & . & \\ & . & \\ x_i^1(0), \ldots\ldots\ldots.., & x_i^d(0), \ldots\ldots\ldots.., & x_i^n(0) \\ & . & \\ & . & \\ x_N^1(0), \ldots\ldots\ldots.., & x_N^d(0), \ldots\ldots\ldots.., & x_N^n(0) \end{bmatrix} \tag{3.40}$$

The initialized value of the k^{th} control parameter in an i^{th} particle (candidate solution) can be found using the following mathematical expression:

$$x_i^d(0) = x_{i,min}^d + rand\,.\,(x_{i,max}^d - x_{i,min}^d) \tag{3.41}$$

Rand is a number randomly allocated in the interval [0–1], while $x_{i,max}^d$ and $x_{i,min}^d$ are the boundary limits of the control variable *d*. The i^{th} particles corresponding to the optimal dispatch problem can be rearranged in a vector form as follows:

$$x_i = [\, x_i^1, x_i^2, \ldots\ldots, x_i^d, \ldots\ldots x_i^n \,] \tag{3.42}$$

$$n = N_G + N_T + N_C \tag{3.43}$$

At $i = 1, 2, \ldots\ldots; N$.

Step 4: Run the system's load flow to calculate the transmission line losses. Calculate the fitness values of all candidate solutions using the mass function. Select the minimally obtained result as best.

Step 5: Check if the control variables are within their boundary limits. If yes, proceed to step 6. If no, then penalize using the penalty function in Equation (3.21). The penalization is considered only for the multiobjective case studies.

Step 6: Evaluate the mass function's best and worst values using equation (3.26). Calculate the force based on $F_{i,k}$ as in Equation (3.33).

Step 7: Update the velocity and position of the particles according to the modified PSO Equations (3.38) and (3.39).

Step 8: Evaluate the fitness function by newly obtained population information. Check if the control variables are within their boundary limits. If yes, proceed to Step 9. If no, then penalize using the quadratic penalty function in Equation (3.21).

Step 9: Record the best fitness values and rank the best obtained solutions.

Step 10: Repeat Steps 4–9 until a stopping criterion is achieved.

Step 11: Print best results and end.

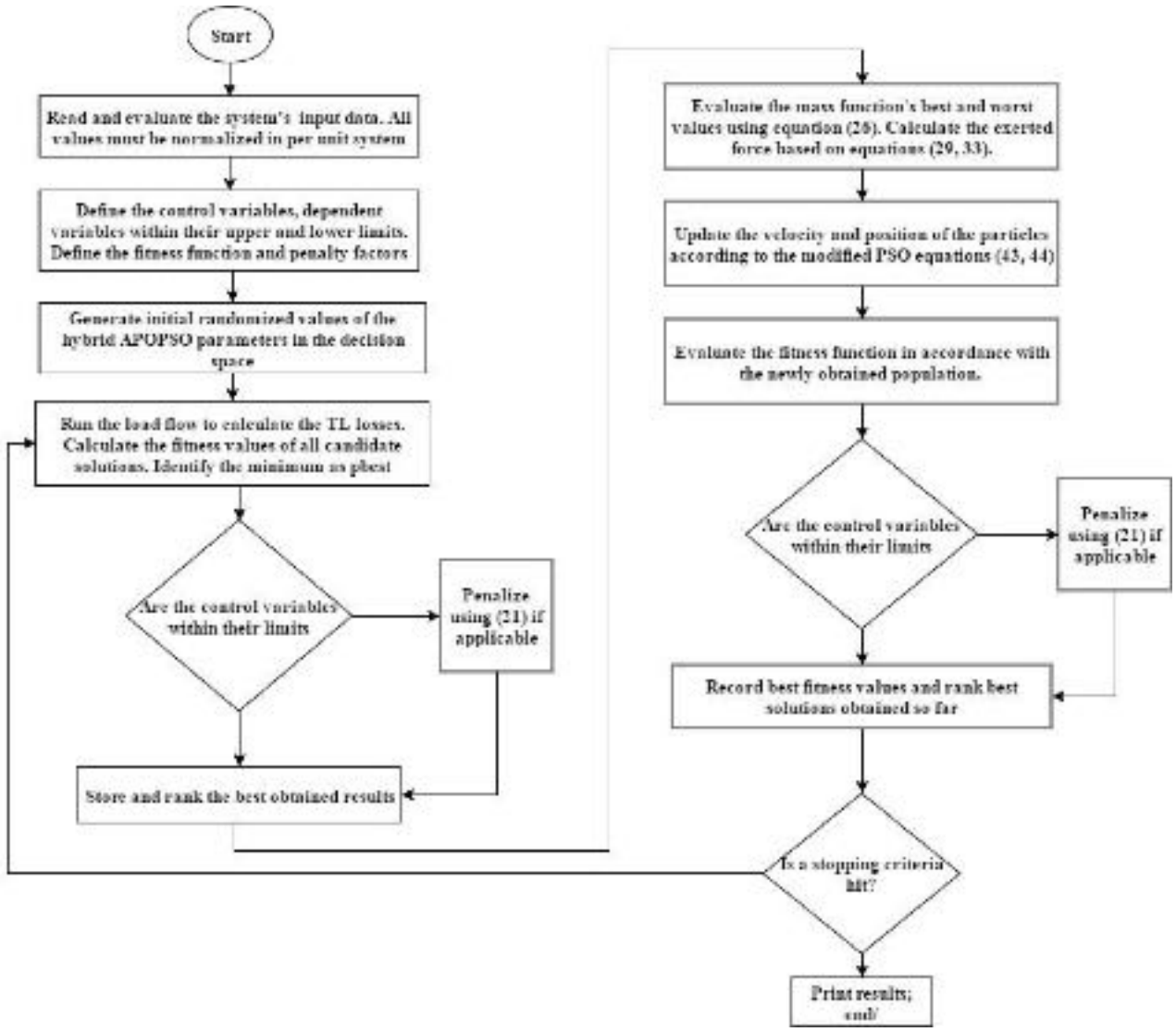

Figure 3-2 The developed algorithm to solve the optimal reactive power dispatch (ORPD) problem.

3.4 Simulation and Results

This section provides an analysis of the obtained results on the three (IEEE 30, IEEE 57, and IEEE 118) test systems to verify the capacity of the developed algorithm to solve the ORPD problem. Table 3.1 shows the parameters of the test systems used in our study. The test system's detailed line data and parameters can be found in [117, 118, 119]. The results were obtained utilizing a developed Matlab code that was run in an i7 Core, 3 GHz, 16 GB RAM

computer with Matlab 2018-b . For each test system, the main outcomes to be recorded is the influence of the algorithm on the minimization of the MW losses, the minimization of the voltage deviation, and the voltage stability index (VSI) improvement (L-index), first individually and then concurrently. We implemented the APOPSO algorithm on a total population of 200 particles, with a maximum iteration run of 100.

Table 3-1: The test system's main parameters.

Description	**IEEE 30**	**IEEE 57**	**IEEE 118**
Buses, N_B	30	57	118
Generators, N_G	6	7	54
Transformers, N_T	4	15	9
Shunts, N_Q	9	3	14
Branches, N_E	41	80	186
Equality constraints	60	114	236
Inequality constraints	125	245	572
Control variables	19	27	77
Discrete variables	6	20	21
The base case for *P*loss, MW	5.66	27.8637	132.45
Base case for *VD*, p.u.	0.58217	1.23358	1.439337

3.4.1. IEEE 30 Bus Test System

The IEEE 30-bus test system has a total of six synchronous generators located at buses 1 (the slack bus), 2, 5, 8, 11, and 13, 41 transmission lines, four power transformers with off-nominal tap-settings at lines 6–9, 6–10, 4–12, and 28–27, and nine reactive power compensators at buses 10, 12, 15, 17, 20, 21, 23, 24, and 29, respectively. This test system has

a total active and reactive consumption of 2.834 and 1.262 per unit on a 100-MVA base. It has a total of 19 control variables that we considered in our study: six generator voltage inputs, four transformers tap-settings, and nine reactive power compensation devices. For this study to be precise, we constrained the level of the system's voltages to be strictly within limits of 0.95 and 1.10 p.u. The lower and upper limits of the transformer's tap settings are set to be between 0.9 and 1.1 p.u., whereas the reactive compensation devices should be ranged from 0 to 5 MVAR. Failure for a result to be within these limits will result in the use of the penalty factors we introduced in the multiobjective fitness function in Equation (3.21). The test system data was obtained from [117].

We measure the strength of our developed algorithm by initially investigating each targeted objective (loss minimization, Vd minimization, and VSI improvement) individually. Table 3.2 shows the results obtained for the hybrid APOPSO when applied on the IEEE 30 bus system. The table illustrates the results when the simulation performed via APO and PSO separately at first before their hybridization. The results show great robustness over their integration throughout 100 consecutive trials. The initial values were developed from previous literature conducted on the same test system, yet for different studies [120, 121, 122]. The optimal results obtained are then compared with previous findings reported in the literature in an attempt to illustrate the high consistency and power of the APOPSO algorithm. Table 3.3 presents the values for the three obtained objectives in comparison with other results reported by differential evolution algorithm (DE) [15], gravitational search algorithm (GSA) [19], particle swarm optimization with agent leader algorithm (ALCPSO) [13], and comprehensive learning particle swarm optimization (CLPSO) [123] in regard to the control variables of this study. The results show the superiority of the APOPSO algorithm over the reported results from these studies. For example, the power flow results in [13, 19] specify values that are not considered optimal at some buses in the system. For instance, reactive power outputs from

compensators at buses 15, 17, 20, 21, and 23 are either at or near the violation of their minimum limits, where they are too small to be operationally feasible, compared with the values obtained in DE, CLPSO, and APOPSO. The overall findings for each case study considered demonstrate APOPSO to be superior to the reported algorithms. The final values at 100, 80, and 50 trials, respectively, for a population of 200 objects are as follow: Ploss = 4.3982 MW; Vd = 1.0477; L-index = 0.1267. Table 3.4 shows the statistical analysis of our simulation, with the best, worst, mean, and standard deviations over 100 trials. Fig. 3.3 illustrates the Vd throughout these trials for the three test systems. The convergence performance of the PSO significantly improved with the hybridization, and Fig. 3.4 shows the algorithm's fast convergence characteristic towards the optimal results considering the loss minimization case on the IEEE 30 bus system, while Fig. 3.5 provides an insight into the statistical accuracy of the algorithm, presenting the Weibull distribution of the VSI values in 100 trials around the mean value.

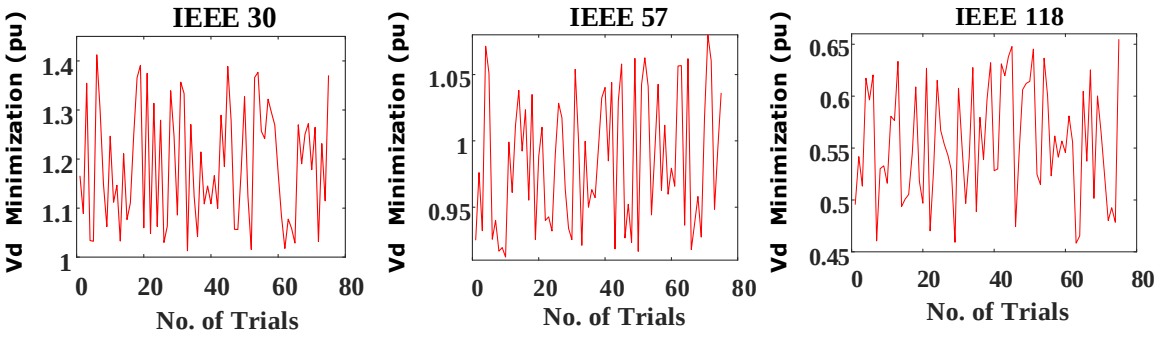

Figure 3-3 The obtained results of voltage deviation (Vd) for 80 trials.

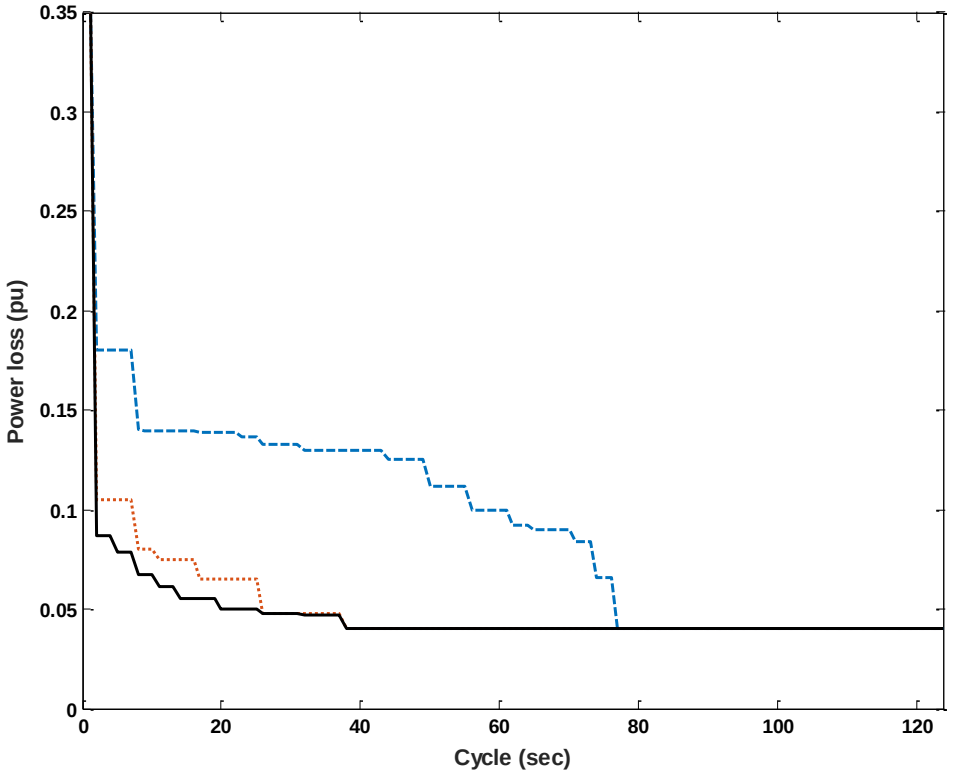

Figure 3-4 Convergence performance of the developed algorithm on the IEEE 30 test system.

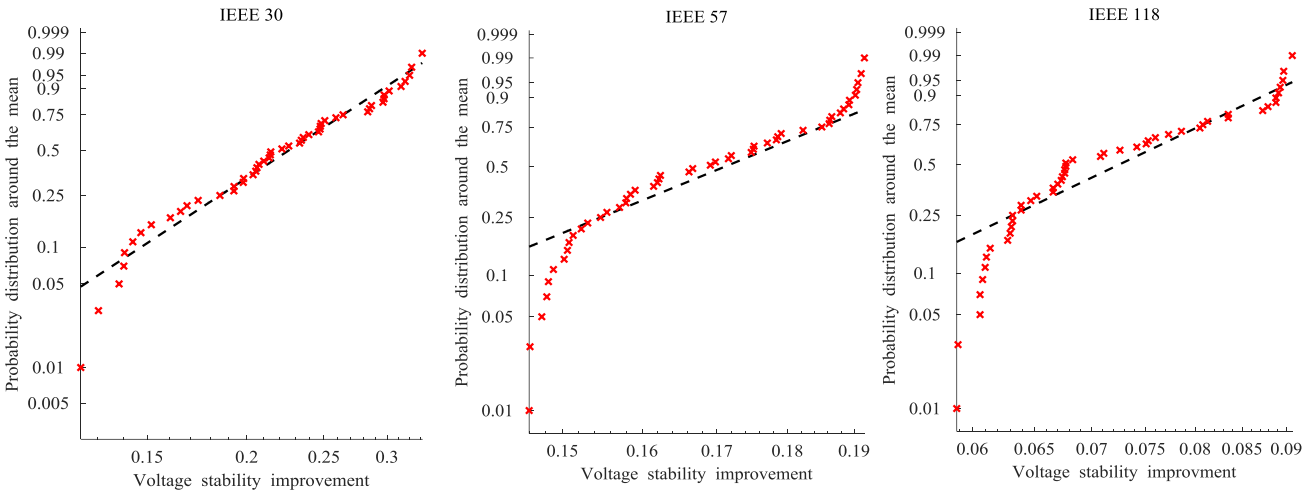

Figure 3-5 The Weibull distribution of the obtained voltage stability improvement (VSI) values around the mean in 50 trials.

Table 3-2: Results obtained for the developed algorithm on the IEEE 30 bus test system.

Variables	Initial Values	MW Loss Minimization			Vd Minimization			Voltage Stability Improvement		
		APO	PSO	APOPSO	APO	PSO	APOPSO	APO	PSO	APOPSO
*VG*1	1.04	1.1000	1.1000	**1.100**	1.0211	1.0299	**1.012**	1.0922	1.0679	**1.044**
*VG*2	1.05	1.1200	1.0844	**1.084**	1.0110	1.0390	**1.001**	1.0992	1.074	**1.061**
*VG*5	1.01	1.0710	1.0748	**1.056**	1.0180	1.0110	**1.014**	1.0988	1.068	**1.061**
*VG*8	1.01	1.0772	1.0768	**1.076**	0.9981	1.0522	**1.009**	1.0991	1.0799	**1.057**
*VG*11	1.05	1.1400	1.1310	**1.091**	1.0411	0.9854	**0.954**	1.0987	1.0699	**1.048**
*VG*13	1.05	1.1430	1.1100	**1.100**	0.9814	0.9910	**1.000**	1.098	1.091	**1.089**
*QC*10 (MVAr)	0	5.0000	3.5717	**5.000**	4.9652	1.9754	**4.102**	0.0019	0.0411	**0.040**
*QC*12 (MVAr)	0	5.0000	3.0984	**5.000**	0.0000	0.4245	**2.124**	0.0255	0.0422	**0.039**
*QC*15 (MVAr)	0	5.0000	3.2925	**4.879**	4.9681	2.2103	**4.512**	0.0004	0.0413	**0.038**
*QC*17 (MVAr)	0	5.0000	4.0166	**4.976**	4.9967	2.8845	**0.000**	0.0001	0.0462	**0.040**
*QC*20 (MVAr)	0	3.4130	3.0309	**3.821**	4.8456	4.0412	**5.000**	0	0.049	**0.037**
*QC*21 (MVAr)	0	5.0000	4.0339	**4.541**	4.8745	3.2412	**5.000**	0.0001	0.018	**0.009**
*QC*23 (MVAr)	0	5.0000	2.9874	**2.354**	4.9964	2.4120	**5.000**	0	0.0191	**0.019**
*QC*24 (MVAr)	0	5.0000	4.3100	**4.654**	4.9974	2.6612	**5.000**	0.007	0.04	**0.010**
*QC*29 (MVAr)	0	2.2233	2.7120	**2.175**	4.9781	2.8456	**4.120**	0	0.0014	**0.0011**
*T*11 (6–9)	1.080	1.0377	1.0320	**1.029**	1.0512	0.9721	**0.998**	0.9712	0.9285	**0.919**
*T*12 (6–10)	1.072	0.9200	0.9200	**0.911**	0.8912	0.8450	**0.822**	0.8999	0.9301	**0.924**
*T*15 (4–12)	1.039	0.9910	0.9827	**0.952**	0.9327	0.9144	**0.954**	0.9489	0.9478	**0.938**
*T*36 (28–27)	1.068	0.9541	0.9699	**0.958**	0.9612	0.9601	**0.958**	0.9488	0.9311	**0.924**
Ploss (MW)	5.8223	4.5388	4.5515	**4.398**	5.4890	5.6980	**5.698**	4.9011	5.4111	**4.478**
VD (p.u.)	1.1500	2.0521	1.9421	**1.047**	0.1001	0.1189	**0.087**	1.9781	1.8497	**1.857**
L-index (pu)	0.145	0.127	0.1277	**0.1267**	0.1482	0.1479	**0.1377**	0.1239	0.1234	**0.1227**

Table 3-3: Comparison with different metaheuristic algorithms reported in the literature for the IEEE 30 bus system

Variables	**MW Loss Minimization**					**Vd Minimization**					**Voltage Stability Improvement**					**MO APOPSO**
	DE	**GSA**	**ALCPSO**	**CLPSO**	**APOPSO**	**DE**	**GSA**	**ALCPSO**	**CLPSO**	**APOPSO**	**DE**	**GSA**	**TLBO**	**CLPSO**	**APOPSO**	
*VG*1	1.1	1.071	1.05	1.1	**1.100**	1.01	0.983	0.998	1.1	**1.011**	1.09	1.1	1.06	1.09	1.043	**1.020**
*VG*2	1.09	1.022	1.038	1.1	**1.084**	0.99	1.044	1.011	1.1	**1.001**	1.09	1.1	1.08	1.06	1.061	**1.033**
*VG*5	1.07	1.040	1.010	1.07	**1.056**	1.02	1.020	0.996	1.07	**1.014**	1.09	1.1	1.07	1.07	1.061	**1.000**
*VG*8	1.07	1.051	1.021	1.1	**1.076**	1.02	0.999	1.001	1.08	**1.009**	1.04	1.1	1.08	1.08	1.057	**1.004**
*VG*11	1.1	0.977	1.05	1.1	**1.091**	1.01	1.077	1.011	1.05	**0.954**	1.09	1.1	1.07	1.02	1.048	**1.032**
*VG*13	1.1	0.968	1.05	1.1	**1.100**	1.03	1.044	1.001	1.1	**1.000**	0.95	1.1	1.09	1.05	1.091	**1.028**
*QC*10 (MVAr)	5	1.653	0.009	4.92	**5.000**	4.94	0	0.009	0.72	**4.102**	0.69	5	0.03	3.58	0.040	**0.051**
*QC*12 (MVAr)	5	4.372261	0.0126	5	**5.000**	1.0885	0.473512	0.0073	1.6812	**2.124**	4.7163	5	0.0466	3.306	0.039	**0.002**
Q_C15 (MVAr)	5	0.119957	0.0209	5	**4.879**	4.9985	5	0.0088	2.6462	**4.512**	4.4931	5	0.0392	4.617	0.038	**0.044**
*QC*17 (MVAr)	5	2.087617	0.05	5	**4.976**	0.2393	0	0.0399	3.4105	**0.000**	4.51	5	0.0464	4.945	0.040	**0.009**
*QC*20 (MVAr)	4.41	0.357	0.003	5	**3.821**	4.99	5	0	1.98	**5.000**	4.48	5	0.0051	3.814	0.037	**0.048**
*QC*21 (MVAr)	5	0.2602	0.0293	5	**4.541**	4.90	0	0.0432	0.476	**5.000**	4.60	5	0.02	5	0.009	**0.041**
*QC*23 (MVAr)	2.8004	0	0.0226	5	**2.354**	4.9863	4.999834	0	3.5896	**5.000**	3.8806	5	0.0101	4.8723	0.019	**0.033**
*QC*24 (MVAr)	5	1.383953	0.05	5	**4.654**	4.9663	5	0.0269	2.9998	**5.000**	3.8806	5	0.0043	5	0.011	**0.050**
*QC*29 (MVAr)	2.5979	0.000317	0.0107	5	**2.175**	2.2325	5	0	1.1098	**4.120**	3.2541	5	0.0016	5	0.001	**0.015**
*T*11 (6–9)	1.04	1.0985	0.9521	0.915	**1.029**	1.02	0.9	1.0103	1.018	**0.998**	0.90	0.9	0.93	1.01	0.919	**1.042**
*T*12 (6–10)	0.9097	0.982481	1.0299	0.9	**0.911**	0.9038	1.1	1.0818	0.9738	**0.822**	0.9029	0.9	0.9318	0.9469	0.924	**0.909**
*T*15 (4–12)	0.98	1.095	0.972	0.9	**0.952**	1.01	1.051	1.019	1.02	**0.954**	0.90	0.9	0.95	0.99	0.938	**1.023**
*T*36 (28–27)	0.9689	1.059339	0.9657	0.9397	**0.958**	0.9635	0.961999	1.0151	0.9896	**0.958**	0.936	1.019538	0.9331	0.968	0.924	**0.958**
Ploss (MW)	4.555	4.51431	4.4793	4.5615	**4.398**	6.4755	6.911765	6.28	4.6969	**5.698**	7.0733	4.975298	5.4129	4.676	4.478	**4.842**
VD (p.u.)	1.9589	0.87522	0.8425	0.4773	**1.047**	0.0911	0.067633	0.0437	0.245	**0.087**	1.419	0.215793	1.8586	0.5171	1.8579	**1.009**
L-index (pu)	0.5513	0.14109	NA	NA	**0.1267**	84.352	0.134937	NA	0.1247	**0.1377**	0.1246	0.136844	0.1252	0.0866	0.1227	**0.1192**

Table 3-4: Statistical analysis of the APOPSO algorithm for three test system

Test System	Best	Worst	Mean	SD	No. of Trials
MW Loss Minimization					
IEEE 30	**4.398**	5.252	5.037379	0.1093	100
IEEE 57	**19.212**	21.131	20.1194	0.5488	100
IEEE 118	**128.591**	129.129	128.86098	0.1595	100
Vd Minimization					
IEEE 30	**1.009**	1.421	1.1875	0.1189	75
IEEE 57	**0.911**	1.081	0.9855	0.05	75
IEEE 118	0.455	0.659	0.5554	0.05452	75
VSI					
IEEE 30	**0.1192**	0.3372	0.2246	0.05725	50
IEEE 57	**0.1455**	0.1927	0.1686	0.01522	50
IEEE 118	0.0587	0.0918	0.072236	0.01015	50

The multiobjective values obtained for MW loss, voltage deviation and L-index are simultaneously shown in the rightmost column in Table 3.3, whereas Fig. 3.6 depicts the produced Pareto optimal values for the multiobjective fitness function on the IEEE 30 test system. In addition to its superiority compared in the reported literature, the results obtained from APOPSO show no violations at any dependent variables in the system. It should be mentioned that we considered the nondomination criteria in the sorting and crowding of the distances when it comes to solving the multiobjective equation. Specifically, fuzzification of each fitness function incorporated in Equation (3.21) and applied on particle *Z* can be carried according to:

$$\mu_i^Z = \begin{cases} 1 & f_i \le f_i^{min} \\ \dfrac{f_i^{max} - f_i}{f_i^{max} - f_i^{min}} & f_i^{min} \le f_i \le f_i^{max} \\ 0 & f_i \ge f_i^{max} \end{cases} \tag{3.44}$$

Where the maximum and minimum limits correspond to the objective function of the i^{th} objective function, respectively. The normalization of contribution from each fitness function on particle *Z* can be calculated as:

$$\mu^Z = \frac{\sum_{i=1}^{N} \mu_i^Z}{\sum_{K=1}^{R} \sum_{i=1}^{N} \mu_i^Z} \tag{3.45}$$

where R is the number of non-dominated obtained results, and N is the total number of fitness (objective) functions.

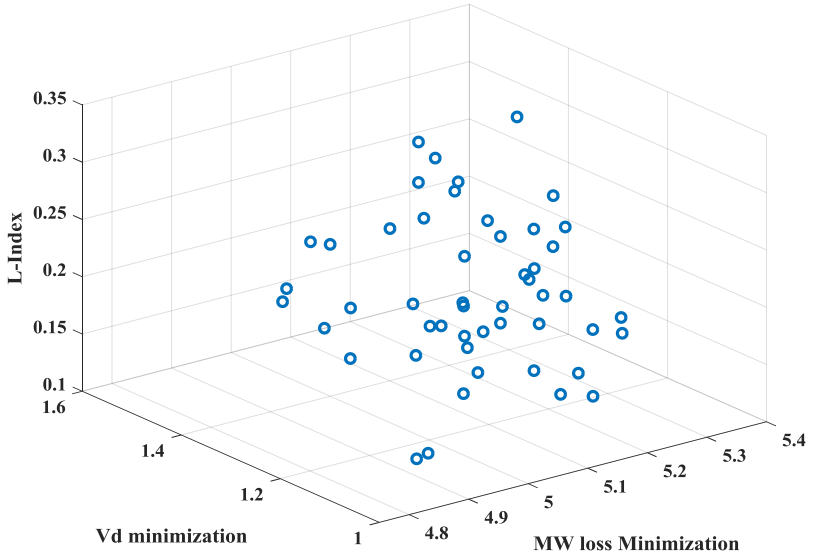

Figure 3-6 Pareto optimal front for the IEEE 30 test system.

3.4.2. IEEE 57 Bus Test System

The IEEE 57-bus system consists of seven synchronous generators located at buses 1, 2, 3, 6, 8, 9, and 12, 80 transmission lines, three reactive power compensators located at buses 18, 25, and 53, and 15 transformers with off-nominal tap ratio. Line data, bus data, variable limits, and the initial values of the control variables are given in [118, 119]. Twenty-five variables are set within the decision space to be investigated using the APOPSO algorithm, which are seven generator voltages, three reactive compensators, and 15 power transformers' tap-settings. Details about the tests system parameters are shown in Table 3.1. Table 3.5 presents the values obtained when applying the APOPSO algorithm on the IEEE 57 test system. It also shows the multiobjective results in the rightmost column when implementing the algorithm over the defined multi-objective function MOF function in Equation (3.21) to solve for the three cases with defined penalties for violation of the limits. It shows the

capacity of APOPSO to efficiently optimize nonlinear, constrained problems in complex systems.

As the results show, APOPSO demonstrates greater search capabilities in finer results obtained compared with GSA [19], multiobjective differential evolution algorithm (MODE) [124], and chaotic krill herd optimization (CKHA) [125]. Further comparisons show the dominance of APOPSO over other reported findings that are not presented for simplicity of presentation. Table 3.4 shows the statistical analysis of the obtained results for the IEEE 57 test system over 100, 75, and 50 trials for MW loss minimization, Vd minimization, and voltage stability improvement respectively. While Fig. 3.3 plots the Vd minimization values obtained over the trials, Fig. 3.7 presents the Pareto optimal obtained for the IEEE 57 test system. The eminence search capabilities of the APOPSO are perfectly illustrated in the Weibull distribution presented in Fig. 3.5, which shows the precision of the algorithm to determine the optimum values around the mean obtained over 50 trials.

Table 3-5: Analysis and comparison of results for the IEEE 57 test system

Variables	MW Loss Minimization				Vd Minimization				Voltage Stability Improvement				MO APOPSO
	GSA	MODE	CKHA	APOPSO	GSA	MODE	CKHA	APOPSO	GSA	MODE	CKHA	APOPSO	
*VG*1	1.1	1.04	1.06	**1.04**	1.1	1.04	1.023	**1.02**	1.06	1.04	1.0125	**1.02**	**0.998**
*VG*2	1.1	1.0101	1.059	**1.021**	1.1	1.0099	1.012	**1.009**	1.0553	1.0103	1.0111	**1.099**	**1.001**
VG3	1.08981	0.9849	1.048	**1.001**	1.07379	0.9851	1.003	**0.977**	1.0348	0.9847	1.0145	**0.981**	**0.979**
*VG*6	1.08422	0.9805	1.043	**0.980**	1.04227	0.9803	1.005	**0.976**	1.0246	0.98	1.0014	**0.992**	**0.879**
*VG*8	1.1	1.0054	1.06	**0.998**	1.05239	1.0051	1.018	**1.044**	1.0418	1.005	1.0014	**0.992**	**0.879**
*VG*9	1.08467	0.9803	1.0447	**0.989**	1.04551	0.9804	1.0427	**1.001**	1.0253	0.9805	1.0345	**0.996**	**0.997**
VG12	1.08006	1.0147	1.041	**1.02**	1.04682	1.0152	1.003	**1.012**	1.0232	1.015	1.0041	**1.009**	**1.001**
QC18 (MVAr)	0	0.0488	0.089	**0.098**	0.08	0	0.074	**0.02**	0.0898	0.0401	0.0519	**0.033**	**0.025**
*QC*25 (MVAr)	0.156	0.0012	0.045	**0.048**	0.108	0.0008	0.051	**0.097**	0.0588	0.059	0.0545	**0.052**	**0.045**
*QC*53 (MVAr)	0.15	0.0001	0.063	**0.110**	0.078	0.0583	0.058	**0.042**	0.063	0.0166	0.0456	**0.060**	**0.049**
T4–18	1.1	1.0987	0.918	**1.022**	1.01	0.9831	0.965	**0.998**	0.9348	0.9801	0.9647	**0.922**	**0.919**
T4–18	1.01	1.082	1.026	**1.009**	1.01	0.951	0.988	**0.944**	0.9939	0.9526	0.9818	**0.944**	**0.933**
T21–20	1.1	0.9221	0.9	**0.982**	1.03	0.9507	0.958	**0.959**	1.0017	0.9501	0.9415	**0.978**	**0.934**
T24–26	1.1	1.0171	0.902	**0.992**	0.98	1.0043	1.009	**0.980**	1.0058	1.0045	1.0047	**0.999**	**1.000**
T7–29	0.97	0.996	0.910	**0.995**	0.98	0.9769	1.011	**0.968**	0.9681	0.9777	1.0104	**0.980**	**0.979**
T34–32	1.1	1.0999	0.901	**0.996**	1.02	0.9139	0.9	**0.931**	0.9718	0.9138	0.9007	**0.899**	**0.921**
T11–41	1.1	1.075	0.9	**1.005**	1	0.9461	0.978	**0.922**	0.9008	0.9465	0.9747	**0.882**	**0.821**
T15–45	0.9	0.9541	0.9	**0.942**	1	0.9258	0.9	**0.911**	0.9604	0.9269	0.9111	**0.919**	**0.891**
T14–46	0.9	0.937	1.071	**0.922**	0.98	0.9957	0.971	**0.979**	0.9476	0.9962	0.9814	**0.939**	**0.919**
T10–51	0.98	1.016	0.995	**1.021**	1.02	1.0379	1.042	**1.001**	0.9571	1.0385	1.0314	**1.022**	**1.001**
T13–49	0.97	1.0998	0.981	**0.998**	1	0.9053	0.914	**0.882**	0.9195	0.9052	0.9145	**0.901**	**0.821**
T11–43	0.98	1.098	0.973	**1.000**	0.99	0.9229	0.922	**0.871**	0.9477	0.924	0.9014	**0.884**	**0.872**
T40–56	0.94	0.9799	0.900	**0.966**	1.01	0.9868	0.976	**0.966**	1.0017	0.9875	0.9415	**0.977**	**0.991**
T39–57	1.09	1.0246	1.014	**0.995**	0.99	1.0095	1.030	**0.951**	0.9621	1.0098	1.0141	**0.944**	**0.950**
T9–55	1.03	1.0371	1.009	**1.011**	1.02	0.9367	0.915	**0.911**	0.9628	0.9373	0.9045	**0.929**	**0.910**
Ploss (MW)	23.46	15.843	23.41	**14.992**	24.441	29.917	28.94	**23.989**	24.388	34.969	27.14	**24.011**	**19.212**
VD (p.u.)	1.09	3.6588	1.052	**0.988**	1.11	0.6634	0.660	**0.943**	0.21895	1.0947	0.6514	**0.9221**	**0.911**
L-index (pu)	NR	0.1625	0.412	**0.1597**	NR	2.7554	0.197	**0.1827**	NA	0.0977	0.1897	**0.1134**	**0.1455**

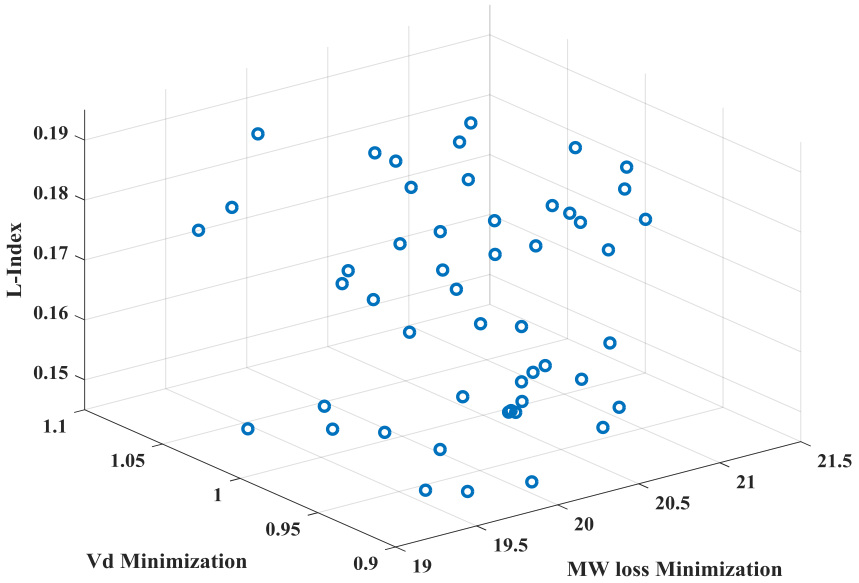

Figure 3-7 Pareto optimal front for the IEEE 57 test system.

3.4.3. IEEE 118 Bus Test System

For us to confirm the capacity performance and robustness of the developed APOPSO algorithm for solving the ORPD problem on a large scale, we applied it on the IEEE 118 test system. This system's line data and parameters were adopted from [119]. It has 54 synchronous generator-buses, 64 load-buses, 12 reactive power compensators, nine tap-setting power transformers, and 186 transmission lines. The bus voltages levels are

constrained to remain within the strict boundary of the per unit range [0.95, 1.1]. Details of the test system's parameters are shown in Table 3.1. The table presents the values of the simulation results on the IEEE 118 test system.

The results for the multiobjective function in Equation (3.21) after its fuzzification are presented in the rightmost column of the table, and its Pareto optimal is shown in Fig.3.8. The results present evidence of the strength and robustness of APOPSO in solving real-life, highly complex scenarios, as the produced outcomes show good optimization for the highly constrained, nonlinear, multiobjective fitness function in a large complex system like the IEEE 118. Table 3.4 presents the statistical analysis of the simulation process for each objective, while Table 3.6 shows the results obtained for each fitness function when simulated individually and simultaneously. No violations have been recorded in the dependent variables throughout the study. Fig. 3.9 presents an illustration of the range of values obtained over the 100 trials for the MW loss reduction objective for this test system. The results show superior consistency in getting the results within a close range over a large number of iterations.

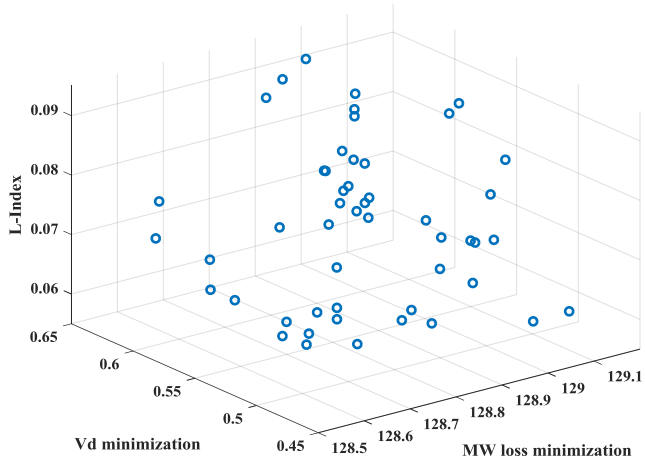

Figure 3-8 Pareto optimal front for the IEEE 118 test system.

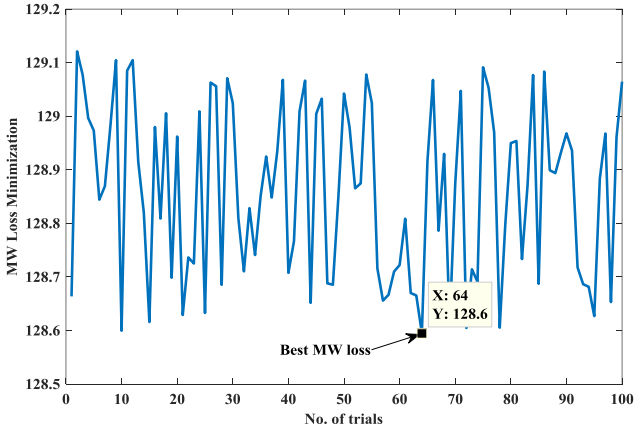

Figure 3-9 Megawatt (MW) loss minimization for the IEEE 118 test system over 100 trials.

Table 3-6: Results of the single and multiobjective functions of the algorithm on the IEEE 118 test

Variable	MW Loss Mini	Vd Mini	VSI	Multiobjective	Variable	MW Loss Mini	Vd Mini	VSI	Multiobjective
Vg1 (pu)	1.019	1.091	0.978	1.002	*Vg99 (pu)*	1.049	0.959	0.971	0.998
Vg4 (pu)	10.344	0.998	0.998	0.998	*Vg100 (pu)*	1.059	1.047	1.045	0.989
Vg6 (pu)	1.032	0.982	0.982	1.008	*Vg103 (pu)*	1.038	0.961	1.087	1.001
Vg8 (pu)	1.072	0.949	0.998	0.971	*Vg104 (pu)*	1.021	1.099	0.990	1.019
Vg10 (pu)	1.082	1.019	1.019	1.028	*Vg105 (pu)*	1.029	0.988	1.022	0.999
Vg12 (pu)	1.022	1.032	0.979	1.029	*Vg107 (pu)*	1.001	1.087	1.016	0.998
Vg15 (pu)	0.019	1.011	1.042	1.089	*Vg110 (pu)*	1.021	1.021	1.071	0.990
Vg18 (pu)	1.090	0.961	1.029	1.031	*Vg111 (pu)*	1.034	0.957	1.039	0.992
Vg19 (pu)	1.011	1.042	1.011	1.009	*Vg112 (pu)*	1.011	1.098	0.990	0.982
Vg24 (pu)	1.050	0.978	1.039	0.989	*Vg113 (pu)*	1.051	1.002	1.033	0.998
Vg25 (pu)	1.100	1.029	1.078	0.995	*Vg116 (pu)*	1.109	0.990	1.062	0.992
Vg26 (pu)	1.082	1.019	1.041	1.011	QC_5 *(pu)*	0.002	−0.323	−0.291	−0.298
Vg27 (pu)	1.042	1.011	1.032	0.981	QC_{34} *(pu)*	0.087	0.079	0.011	0.149
Vg31 (pu)	1.031	0.998	1.035	1.001	QC_{37} *(pu)*	0.019	−0.192	−0.163	−0.255
Vg32 (pu)	1.029	0.987	1.078	1.012	QC_{44} *(pu)*	0.098	0.099	0.091	0.104
Vg34 (pu)	1.029	0.989	1.077	1.012	QC_{45} *(pu)*	0.098	0.098	0.099	0.094
Vg36 (pu)	1.028	1.008	1.011	0.997	QC_{46} *(pu)*	0.019	0.052	0.043	0.092
Vg40 (pu)	1.021	1.009	1.043	1.019	QC_{48} *(pu)*	0.089	0.012	0.004	0.009
Vg42 (pu)	1.098	1.010	1.074	1.020	QC_{74} *(pu)*	0.123	0.029	0.119	0.098
Vg46 (pu)	1.043	1.058	1.099	1.035	QC_{79} *(pu)*	0.192	0.018	0.129	0.010
Vg49 (pu)	1.050	0.998	1.051	0.999	QC_{82} *(pu)*	0.182	0.198	0.345	0.192
Vg54 (pu)	1.021	1.033	1.098	1.029	QC_{83} *(pu)*	0.091	0.099	0.062	0.085
Vg55 (pu)	0.020	1.018	1.097	1.012	QC_{105} *(pu)*	0.190	0.087	0.104	0.011
Vg56 (pu)	1.021	1.041	0.961	0.982	QC_{107} *(pu)*	0.001	0.022	0.075	0.017
Vg59 (pu)	1.038	1.034	0.959	0.998	QC_{110} *(pu)*	0.041	0.056	0.045	0.045
Vg61 (pu)	1.042	1.019	0.970	1.002	*T8-5*	1.037	0.929	0.956	0.943
Vg62 (pu)	1.034	0.957	1.090	0.974	*T26-25*	1.089	0.998	1.098	1.087
Vg65 (pu)	1.087	0.968	1.021	1.092	*T30-17*	1.029	1.081	1.026	1.092
Vg66 (pu)	1.042	1.040	0.990	1.089	*T38-37*	1.031	1.009	0.989	0.981
Vg69 (pu)	1.054	0.949	0.987	1.072	*T63-59*	1.033	0.981	1.092	1.029
Vg70 (pu)	1.024	0.971	0.993	1.056	*T64-61*	1.088	1.014	0.921	0.944
Vg72 (pu)	1.055	0.998	1.076	1.044	*T65-66*	0.998	1.042	1.058	0.900
Vg73 (pu)	1.039	1.058	1.062	0.992	*T68-69*	0.956	1.098	0.919	1.001
Vg74 (pu)	1.043	1.035	1.076	0.998	*T81-80*	1.029	0.995	0.999	0.953
Vg76 (pu)	1.039	1.018	1.034	1.022					
Vg77 (pu)	1.055	1.016	1.009	1.001					
Vg80 (pu)	1.098	1.011	0.998	1.010					
Vg85 (pu)	1.100	1.010	1.019	1.015					
Vg87 (pu)	1.101	1.001	0.998	0.998					
Vg89 (pu)	1.098	1.008	1.075	1.018					
Vg90 (pu)	1.078	0.960	1.097	0.997					
Vg91 (pu)	1.088	1.098	0.976	0.998					
Vg92 (pu)	1.082	0.998	1.008	0.997					
Ploss (MW)	111.873	182.091	281.920	128.591					
VD (pu)	1.711	0.198	1.198	0.455					
L-index (pu)	0.09882	0.0721	0.0692	0.0587					

3.5 Conclusion

A new hybrid technique for solving the ORPD problem was developed in this chapter. The developed APOPSO algorithm was tested and verified on three IEEE test systems: the 30, 57, and 118 bus systems. The results demonstrated the excellent search capacity of the PSO and APO algorithms when they are integrated. This process creates a robust hybrid algorithm to solve the ORPD optimization problem. Furthermore, the consistency of the optimized results in large complex systems such as the IEEE 57 and 118 bus systems prove that the combined algorithm overcomes some of the difficulties the PSO traditionally faces. For instance, being trapped in local optima, which usually lead to slower convergence. Comparison with previously reported ORPD results based on different metaheuristic methodologies verified the obtained results of the APOPSO algorithm, which shows superiority in most of the obtained results for MW loss minimization, voltage deviations minimization, and voltage stability improvement. The results obtained were based on the solution of both single and multiobjective fitness functions. The results of the hybrid algorithm produced no violations of any of the constraints placed on the dependent variables. Overall, the APOPSO algorithm shows great potential for various types of studies. Future studies may include the incorporation of electric vehicles to improve the voltage profiles' test system during specific operation criteria of the ORPD problem. Another aspect to investigate is the integration of flywheel energy storage systems (FESS) in the ORPD problem when integrated into the grid [126].

Chapter 4 Hybrid Microgrid Energy Management and Control Based on a Metaheuristic-Driven Vector-Decoupled Algorithm Considering Intermittent Renewable Sources and Electric Vehicles Charging Lot

4.1 Introduction

In this chapter, an energy management and control strategy is developed to overcome the fluctuations of the voltage and frequency levels due to the presence of intermittent renewable energy sources and electric vehicle charging structure in hybrid microgrids. Furthermore, a hybridization algorithm of the Particle Swarm Optimization (PSO) and Applied Artificial Physics (APO) is utilized to tune the vector-decoupled control parameters of the interlinking converters to ameliorate the performance of the hybrid microgrid to achieve better resiliency and operation. Our developed strategy highlights guaranteed stability of operation in the DC part of the microgrid while efficiently coordinate with the AC part during severe operating conditions such as high pulsed demands and islanding operation. The developed algorithm is tested via a hardware-in-the-loop testbed at the Florida International University to for results verification. The results embolden the validity of our developed strategy and hybridized algorithm to establish secure and safe active and reactive power exchange between the two sides of the hybrid microgrid without invoking an operational violation.

This chapter is organized as follow; section 4.2 shows in detail the system description and corresponding illustration of the modelling and control of the bidirectional converter, section 4.3 presents the APOPSO algorithm deployed in our work to provide the converter with optimized control parameters, section 4.4 presents the experimental modelling and results of the developed control mechanism, with section 4.5 provides concluding remarks.

4.2 System's Description, Modeling and Control

Fig. 4.1 presents the system of study in this chapter which is implemented in hardware at the Energy Systems Research Laboratory group (ESRL) of the Florida International University (FIU). More information about the hardware testbed and its connections can be found in the previously published literature [127, 128, 129]. The hybrid microgrid at the testbed incorporates different harvested AC and DC sources that are integrated through interfaced power converters. Both sides are interlinked via a bidirectional converter, with the DC part contains PV systems, electric vehicles parking structure, and local and pulsed DC loads. On the other hand, the AC part of the microgrid is supplied with a synchronous generator as well as the typical load demands. During islanding operation, the microgrid is isolated and maintain its supply to local loads via both AC and DC sources. The microgrid is designed such that it can autonomously satisfy the energy demands without interruption under any circumstances. Two DC-to-DC boost converters are used in this work to link the DC components to the bidirectional power converter, as illustrated in Fig. 4.1. Table 4.1 presents the parameters of the interlinking converter used in this work.

Table 4-1: The Converter Parameters

Parameter	Value
DC BUS Voltage	380±20 V
Rating	10kW
$R_{s,}$	0.01 ohm
C_{out}	1200 µF
Rc_{out}	0.008 ohm
L	12.7 mH
C_{in}	1200 µF
R_{cin}	0.008 ohm

where $R_{s,}$ Rc_{out} and R_{cin} are the resistance of the voltage source located at the DC side, resistances of the output and input capacitor of the power converter, while C_{out} and C_{in} are the values of the output and input capacitors.

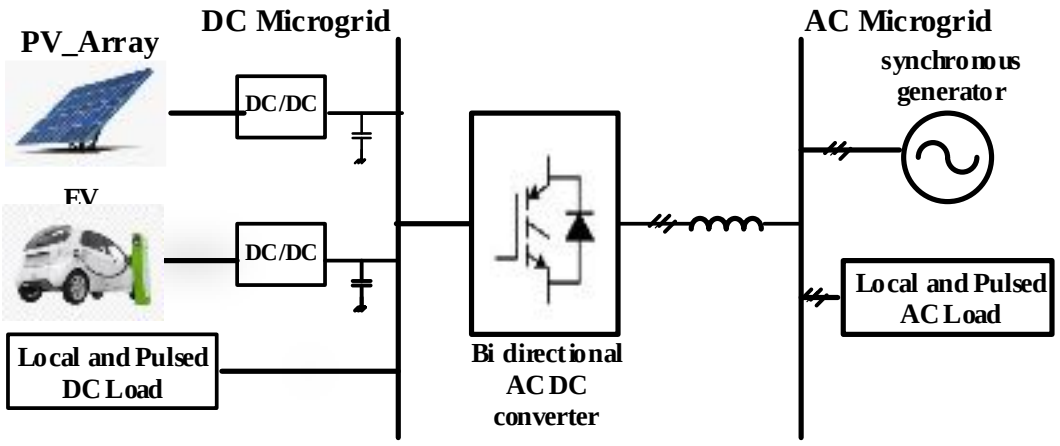

Figure 4-1 Schematic configuration of the hybrid microgrid in this work

4.2.1 PV System Model and Interface

The PV system is modeled with a PV emulator that has a maximum capacity of 6 kW and can imitate a real-time PV system with different characteristics and under various operational conditions such as during temperature and irradiance changes. The PV emulator is constructed to utilize real-time algorithms that represent the PV array's mathematical models to generate reference power output from a programmable DC supply. Specifically, the PV models are established in Simulink and resembled in real-time operation via dSPACE following a graphic user interface (GUI). Accordingly, the emulator is then tested with real-time execution of the PV model considering various dynamic operational and steady-state conditions. Fig. 4.2 presents the configuration of the laboratory PV emulator, which was first introduced by the authors in previous work [128]. Fig. 4.3 shows a schematic illustration of the PV system connectivity with the boost converters for accurate integration with the microgrid's DC side. It is worth mentioning that the type of PV module in this work is the SPR-305-WHT PV system manufactured commercially by SunPower and can generate 305

watts as an output power per module with an efficiency of 18.9%. The IV characteristic of the PV system could be represented by a single diode model as it provides accuracy and simplicity [130]. The current output of the PV arrays can be found by

$$I_{PV} = I_L - I_S \left[exp\left(\frac{q(V_{PV}+I_{PV}R_S}{K_B\, T\, A} - 1\right) - \frac{q(V_{PV}+I_{PV}R_S)}{R_{sh}}\right] \quad (4.1)$$

where I_{PV} is the output current of the PV array, V_{PV} is the voltage reference which is established based on the perturbation and observation (P&O) algorithm that takes into consideration the temperature and solar irradiation levels, I_L is the internal PV current, I_S is the diode's reverse saturation current, R_{sh} is the parallel leakage resistance, R_s is the series resistance, *A* represents the ideality factor of the solar cell, while *q* is the charge of the electron that is assumed to be 1.6×10-19 C, and *KB* is the Boltzmann constant which is 1.3806488×10−23 J/K. The DC-to-DC boost converter is used to step up the voltage level of the PV arrays to the voltage level of the microgrid's DC side when needed while ensure maximum power extraction based on the concept of maximum power point tracking (MPPT). Specifically, the P&O algorithm [131, 132] is utilized in this work. This algorithm mainly depends on perturbing the voltage level of the PV panels by small magnitude (ΔV) and accordingly observing the change of power level (ΔP) to optimize the tracking of maximum power transfer from the arrays to take into consideration potential temperature variability during the day.

Figure 4-2 The PV emulator setup in our hardware testbed

The main contribution from utilizing the (P&O) algorithm in our work is to aim for zero difference of power received from the PV arrays in two successive iterations, denoted ΔP. This is accomplished by measuring the level of power at each iteration based on the PV output current so that the power level at the k^{th} iteration is recorded, P_k, and $P_{(k+1)}$ for the following iteration. The DC-to-DC boost converter adjusts the power output of the PV system by either decreasing in the case of a negative ΔP or increasing it for the case of a positive ΔP. Once ΔP approaches zero, the PV system is said to be reaching its maximum power point (MPP). The process is updated iteratively throughout the operation hours to ensure maximum power production from the PV arrays. Fig. 4.4 illustrates the described iteration process, while fig. 4.5 shows the implementation of the control process for the DC-to-DC converter in our work.

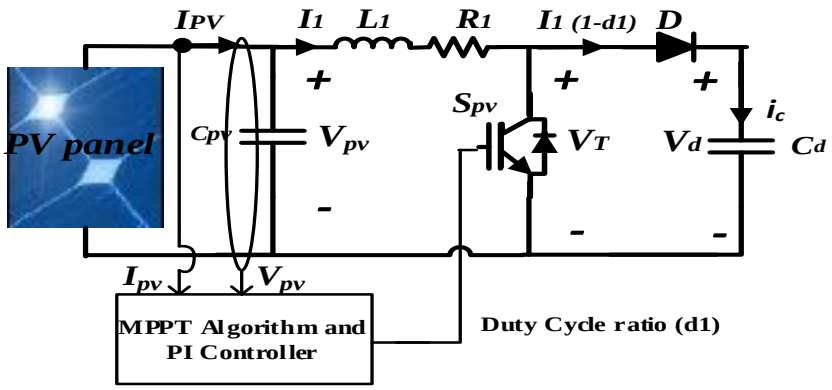

Figure 4-3 Schematic configuration of the PV system interface with the DC side of the hybrid microgrid.

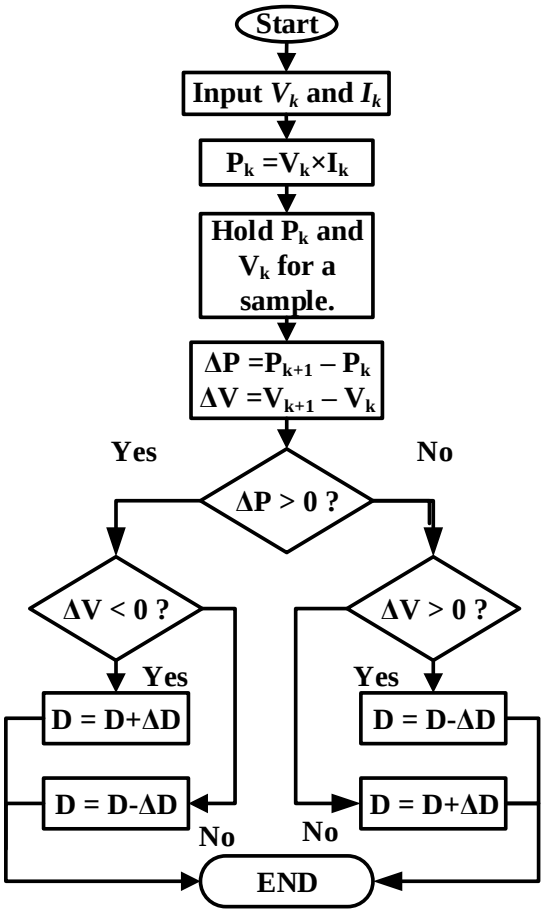

Figure 4-4 The P&O algorithm utilized in this work.

The control mechanism for the DC-to-DC boost converter is achieved based on the following formulas

$$V_{PV} - V_T = L_1 \frac{\partial L_1}{\partial t} + L_1 R_1 \tag{4.2}$$

$$I_{PV} - I_1 = C_{PV} \frac{\partial V_{PV}}{\partial t} \tag{4.3}$$

$$V_T = V_D(1 - D_1) \tag{4.4}$$

Where L_1 and R_1 are bidirectional converter inductance and resistance, I_1 is the current corresponding to the duty-cycle ratio D_1 of the switch S_{PV}. V_T is the voltage across the switch, while V_{pv} is the voltage reference across capacitance C_{PV} and is determined following the utilization of the P&O algorithm based on the temperature and solar irradiation levels of PV arrays, as mentioned earlier. It should be noted that the control process is based on the dual-loop control mechanism. The inner current loop assists in the improvisation of the dynamic response, while the outer voltage loop keep tracks with the reference voltage levels given zero steady-state error.

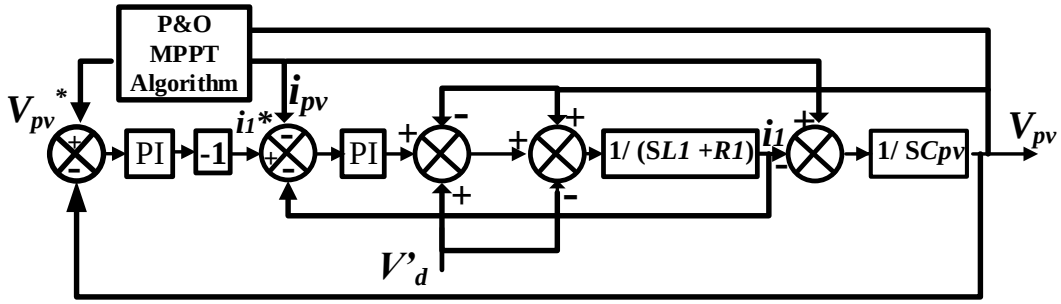

Figure 4-5 Block diagram for the boost converter control.

4.2.2 Electric Vehicle's Battery Converter Model and Control

The developed scheme for the electric vehicle charging converter is shown in fig. 4.6. The converter topology is a composed of a bidirectional DC-to-DC converter, with the EV is

connected to the low-voltage side of the converter. The high-voltage side of the converter is directly connected with the microgrid DC bus. The converter is composed of two switches, Sc and Sd, with each has its own operation mode and time. Specifically, switch Sc is on when the converter operates at the buck mode for charging activity during power transfer from the DC Bus to the EV's battery.

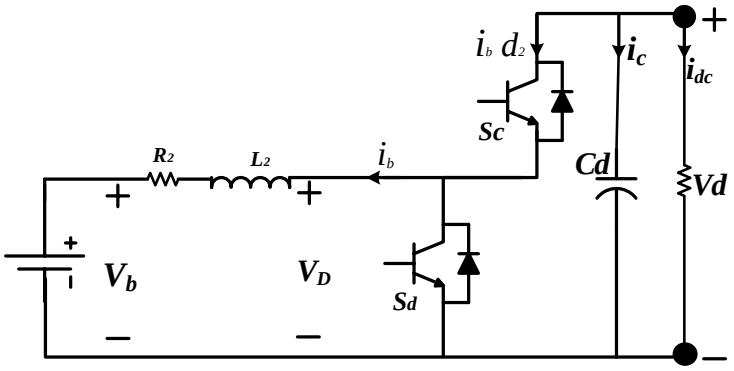

Figure 4-6 Configuration of the DC-to-DC converter interface with the EVs battery and the DC bus

The switch Sd is on when the converter operates at the boost mode during the discharging process of the EV during power transfer from the EV's battery back to the DC bus. The control mechanism for the EV's battery converter is shown in fig. 4.6, and is mathematically illustrated as follows:

$$V_D - V_b = L_2 \frac{\partial I_b}{\partial t} + R_2 I_b \tag{4.5}$$

$$V_D = V_D D_2 \tag{4.6}$$

$$I_1(1 - D_1) - i_{ac} - i_{dc} - I_b D_2 = C_D \frac{\partial V_D}{\partial t} \tag{4.7}$$

Where V_d and i_{dc} are the DC side's voltage and current, i_{ac} is the current corresponding to the AC side of the hybrid microgrid, $V_b \; and \; I_b$ is the EV battery's voltage and current, C_D is the bidirectional converter capacitance for boost mode, $L_2 \; and \; R_2$ are bidirectional converter inductance and resistance. It should be noted that the main task of the bidirectional DC-DC converter connected to the EVs charging structure is to regulate the DC bus voltage. To

achieve this purpose, a dual-loop control is utilized to assist in providing a stable DC link voltage. Specifically, the external voltage-controlled loop establishes a reference charging current as a signal for the internal current-controlled loop. The difference between the reference and measured bus voltage serves as an input signal to the PI controller. This difference is used to measure the reference charging current since the internal current-controlled loop compares this estimated current-signal with that one of the referenced current flowing inside the converter. The produced output of this loop control serves as an input signal for a second PI controller for further optimization of the inner controller.

The EVs battery current i_b is calculated based on equation (4.5), while the duty cycle is estimated by equations (4.6) and (4.7). The discharging current can be calculated as follow

$$I_b = I_1(1 - D_1) - i_{ac} - i_{dc} \tag{4.8}$$

If the voltage of the microgrid's DC bus is higher than the desired reference voltage signal, then the outer voltage control generates a negative reference current signal for the inner current-controlled loop. The generated signal current is used to adjust the correspondent duty cycle in order to influence the converter to operate in a buck mode only and suspend any discharging activity at the moment. On the other hand, if the voltage of the microgrid's DC bus is lower than the desired reference voltage signal, then the outer voltage control generates a positive reference current signal to regulate the current flow during the discharging process. As a result, an additional amount of energy is incurred and injected to the DC bus while improving the voltage profile at the moment. It is worth mentioning that the physical reference for the voltage source of the DC bus is 400 V.

4.2.3 Bidirectional DC-to-AC converter model and control

In hybrid microgrids, managing robust frequency and voltage levels is challenging, especially during forced islanding operation where the AC side loses its connection to the grid's main slack bus. Typically, a hybrid microgrid owns synchronous generators that can manage load variations and maintain energy supply, even during islanded operation. However, high demands connected to the hybrid microgrid may lead to severe consequences such as frequency deficiency and potential voltage collapse. As a result, the bidirectional DC-AC converter's main task is to enable strict frequency and voltage regulation considering severe operational scenarios [133]. We consider this controller type to ensure a smooth power exchange between the DC and AC sides of the microgrid. The mathematical representation of the DC-AC converter model cis illustrated as follows:

$$L_3 \frac{d}{dt}\begin{bmatrix} ia \\ ib \\ ic \end{bmatrix} + R_3 \begin{bmatrix} ia \\ ib \\ ic \end{bmatrix} = \begin{bmatrix} V_a \\ V_b \\ V_c \end{bmatrix} - \begin{bmatrix} e_a \\ e_b \\ e_c \end{bmatrix} + \begin{bmatrix} \Delta_a \\ \Delta_b \\ \Delta_c \end{bmatrix} \tag{4.9}$$

Considering D-Q coordinates, equation (4.9) could be rewritten as follow

$$L_3 \frac{d}{dt}\begin{bmatrix} i_d \\ i_q \end{bmatrix} = \begin{bmatrix} -R_3 & wL_3 \\ -wL_3 & -R_3 \end{bmatrix}\begin{bmatrix} i_d \\ i_q \end{bmatrix} + \begin{bmatrix} V_{cd} \\ V_{cq} \end{bmatrix} - \begin{bmatrix} V_{sd} \\ V_{sq} \end{bmatrix} \tag{4.10}$$

The control mechanism of the bidirectional DC-AC converter utilized in our work is shown in Fig. 4.7, where two-loop controllers, for both real and reactive power, are applied. The overall goal is to allow proper and intelligent control of both frequency and voltage levels at the hybrid microgrid. For frequency control, the difference between the measured frequency signals from that of the obtained reference frequency is established. The result is subtracted from the difference error between the measured and referenced DC voltage level, as described in part B of this section. The obtained value serves as an input signal to the PI

controller, which initiates the current reference value, Id. Likewise, another control loop is deployed to achieve voltage stability employing optimized reactive power flow in the hybrid microgrid. This is made in the same manner as frequency control, where the difference between the measured and referenced voltage levels is calculated to produce a signal that serves as input to another PI controller to generate the Iq reference current. In the next section, we present a metaheuristic methodology based on the hybridization of Particle Swarm Optimization (PSO) and Artificial Applied Physics (APO) to tune the vector-decoupled control parameters illustrated in fig. 4.7 optimally.

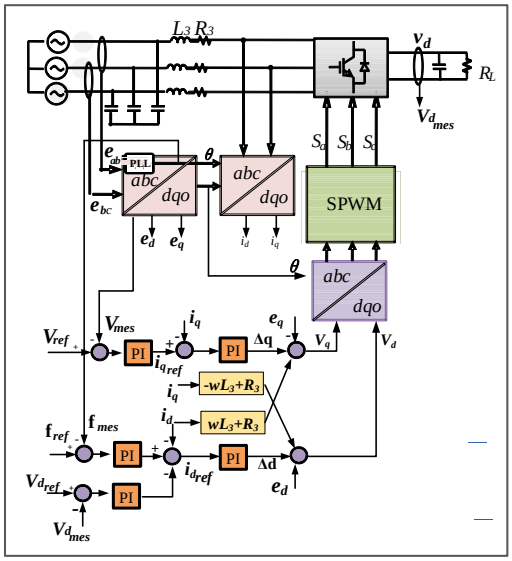

Figure 4-7 Schematic diagram of the bidirectional DC-AC converter

4.3 Control Parameters Design Using APOPSO

The central concept of applying our hybridization of PSO and APO is to integrate their individual strengths to establish an optimization algorithm that exhibits both the dominant global search abilities of the APO and efficient local exploration performance of the PSO while enhancing its convergence rate. In this chapter, the hybrid algorithm is utilized to optimize the vector-decoupled control parameters of the bidirectional converter to ensure efficient energy management driven by optimized variables while reducing the trial-error

method described in section 4.2. In a previous study, the authors developed an optimal reactive power dispatch study based on the hybrid APOPSO [134].

4.4.1 *Artificial Physics Optimization (APO)*

APO is a physics-based metaheuristic technique that is based on the idea of a gravitational metaphor that enables forces to produce attractiveness or repulsiveness movements on the articles that resemble the solutions of the optimization problem [23, 114, 134]. These movements represent the searching criteria for estimating the values of local and global optima. Furthermore, this is accomplished since the APO treats the examined parameters as physical objects that exhibit a mass with relative position and velocity. The mathematical description of the APO is as follows

$$m_i = \text{g}\,[\text{f}\,(x_i)] \tag{4.11}$$

When f(x) € [-∞ , ∞], then; arctan [-f(x_1)] € [$\frac{-x}{2}$, $\frac{x}{2}$], and $\tanh[-f(x_i)]$ € $[-I, I]$ with

$$\tanh(x_i) = \frac{e^x - e^{-x}}{e^x + e^{-x}} \tag{4.12}$$

where equations (4.11) and (4.12) is mapped into the interval (0,1) via basic transformation function. Therefore, the mass functions of the APO is described as follows

$$m_i = e^{\frac{g\,[\,f(x_{best})-f\,(x_i)\,]}{f\,(x_{worst})-f\,(x_{best})}} \tag{4.13}$$

where f (x_{best}) is the objective function corresponding to the position of the best-achieved value for the individual solution, which in this work resembles the best-obtained control parameter. On the other hand, f (x_{worst}) refers to the value of the worst particular solution reported during the searching process. Both represented as follow:

$$\text{Best= avg } \{\min f(x_i)\,,\ \ i \in S\} \tag{4.14}$$

$$\text{Worst= avg } \{\max f(x_i),\ i \in S\} \tag{4.15}$$

where S is a set that is composed of N population of controlling parameters. A velocity vector is produced once each particle's mass is identified, with the level of exerted force influencing the change in velocities in an iterative manner. The amount of exerted force on each particle i (solution) can be found as follows

$$F_{ij,k} = \begin{cases} sgn\left(r_{ij}\,,k\right) G\,.\left(r_{ij}\,,k\right)\,.\frac{m_i m_j}{r_{ij}\,,\ k^2}; & if\ f\ (x_j) < f(x_i) \\ sgn\left(r_{ji}\,,\ k\right).G\left(r_{ji}\,,k\right)\ .\ \frac{m_i m_j}{r_{ij}\ ,\ k^2}; & if\ f\ (x_j) \geq f(x_i) \end{cases} \tag{4.16}$$

and

$$r_{ij,k} = x_{j,k} - x_{i,k} \tag{4.17}$$

Where $F_{ij,k}$ is the k[th] force exerted on particle *i* via another particle *j* in their corresponding dimensions; $x_{i,k}$ and $x_{j,k}$ are the k[th] dimensional coordinates of the swarm particles *i* and *j*; $r_{ij,k}$ is the distance between the two measured coordinates. Sgn(r) represents the signum function, whereas G(r) depicts the gravitational factor that follows the changes on $r_{ij,k}$ iteratively, both represented mathematically as follows

$$\text{Sgn(r)=} \begin{cases} 1 & if \quad r \geq 0 \\ -1 & if \quad r < 0 \end{cases} \tag{4.18}$$

$$\text{G (r) =} \begin{cases} g|r|^h & if \quad r \leq 1 \\ g|r|^q & if \quad r > 1 \end{cases} \tag{4.19}$$

In a thorough manner, the total force applied on all particles (control parameters of study) can be modeled as:

$$F_{i,k} = \sum_{\substack{j=1 \\ i \neq j}}^{m} F_{ij\,,\;k} \quad \forall\, \mathrm{i} \neq best \tag{4.20}$$

One crucial aspect to consider when deploying the APO to solve an optimization problem is the understanding of its particles' motion paradigm in the solution space. Specifically, the measured force could be used to estimate the velocity of the moving particles and therefore find in an iterative fashion their respected positions in the solution space. Such motion paradigm is set in a two- or three-dimensional space and is modeled as follow:

$$V_{i\,,k}\,(\mathrm{z+1}) = w.\, V_{i,k}(\mathrm{t}) + \beta * {}^{F_{i,k}}\!/_{m_i} \tag{4.21}$$

$$x_{i,k}\,(\mathrm{t+1}) = X_{i,k}(\mathrm{t}) + V_{i,k}(\,\mathrm{t+1}) \tag{4.22}$$

$V_{i\,,k}$ and $x_{i,k}$ represent the k^{th} velocity and distance components corresponding to particle *i* during an iteration *t*, while β is a uniformly distributed random variable within the interval [0,1] and *w* is a user-defined inertia weight that is updated iteratively and usually assume a value between the interval 0.1 to 0.99. Furthermore, the inertia weight is a good indication of the level of performance of the APO algorithm, with higher values of *w* indicates greater velocity changes. It should be noted that at each iteration, each particle identifies the information of its nearby particles (solutions) which emphasizes the great search strategy of the APO. Once an iteration is performed. All the particles' relative positions are identified and consequently the objective fitness function adjusted to the newly obtained positions. A stopping criterion is enabled once a pre-determined number of iterations are reached without significant difference in the obtained best particle position.

4.4.2 *The Particle Swarm Optimization (PSO)*

Considered one of the most popular metaheuristic techniques, PSO is a bio-inspired, population-driven algorithm first presented by Kennedy in [22]. PSO advances based on evolutionary computations with a sample of preliminary randomized solutions at the first iteration, updated iteratively to establish local and global optima values. The obtained solutions are deemed particles that fly in the solution space with a determined velocity from preceding iterations. It should be noted that the obtained velocity and position values of each solution set are updated iteratively as follows:

$$V_{ij}(\mathrm{t}+1) = [\mathrm{W} * V_{ij}(\mathrm{t})] + [C_1 + r_1 + [Pbest_{ij} - X_{ij}(\mathrm{t})]] + [C_2 + r_1 + [\ gbest_{ij} - X_{ij}(\mathrm{t})]] \quad (4.23)$$

$$X_{ij}(\mathrm{t}+1) = X_{ij}(\mathrm{t}) + \mathrm{C}\ V_{ij}(\mathrm{t}+1) \quad (4.24)$$

Here, X_{ij}(t) and V_{ij} (t) are both vectors representations of velocity and position in the solution space for particle *i*, whereas *Pbest* and *gbest* stand for the best individual and global obtained solutions, respectively. The popularity of PSO as a well-established and referred metaheuristic algorithm is attributed to its efficient searching strategy along with prematurely convergence rates without the requisite of finding a local optimum in first place.

4.4.3 *The Hybridization of APO and PSO to Optimize the Vector-Decoupled Control Parameters*

The hybridization of APO and PSO is to establish in this chapter to take advantage of their individual strengths that lead to an overall improvement in the optimization process. Specifically, such integration utilizes the high efficiency of global search of the APO with the strong local exploratory search of the PSO while significantly enhancing its convergence

rate. In this chapter, the two algorithms are integrated following a low-level heterogeneous routine. As a consequence, the velocity and positions equations are modified as follows:

$$v_{i,k}(t+1) = W\,.\,v_{i,k}(t) + \beta_1 - r_1\,.\left[\frac{F_{i,k}(t)}{m_i}\right] + \beta_2\,.\,r_2\,.\left[g\ best\ -\ x_{i,k}(t)\right] \tag{4.25}$$

$$x_{i,k}(t+1) = x_{i,k}(t) + v_{i,k}(t+1) \tag{4.26}$$

This developed hybridization allows parallel search within a set of population which leads to avoidance of getting trapped in local optima. The control parameters to be optimized are K_{p_f}, K_{i_f}, K_{p_vdc}, K_{i_vac}, K_{p_m}, K_{i_vdc}, K_{i_m} and K_{p_vac}. Following the microgrid's dynamic simulation, the hybrid APOPSO algorithm evaluates the integral absolute values of both the frequency (Δf) and the RMS voltage (ΔV_{rms}) deviation levels corresponding to the AC part of the microgrid. In this chapter, two fitness functions are applied to the hybrid algorithm to properly estimate the self-tuning of the gains of the PI controller. The output of the fitness functions is used to control the power-sharing levels of the bidirectional converter, as follows

$$min\{F = e(t) = y(t) * -y(t)\} \tag{4.27}$$

$$\text{MO}F = Min\left\{\int_{t_0}^{t_f} x_f\,|\Delta f|dt + x_v \int_{t_0}^{t_f} |\Delta V_{rms}|dt\right\} \tag{4.28}$$

Where e(t) represents the level of the errors, y(t)* the desired value to be obtained and y(t) is the actual measured value per each iteration, while x_f and x_v represent penalty factors to enforce the voltage and frequency levels to be within the desired limits. Fig. 4.8 shows the flowchart of the developed hybrid algorithm to optimize our control parameters.

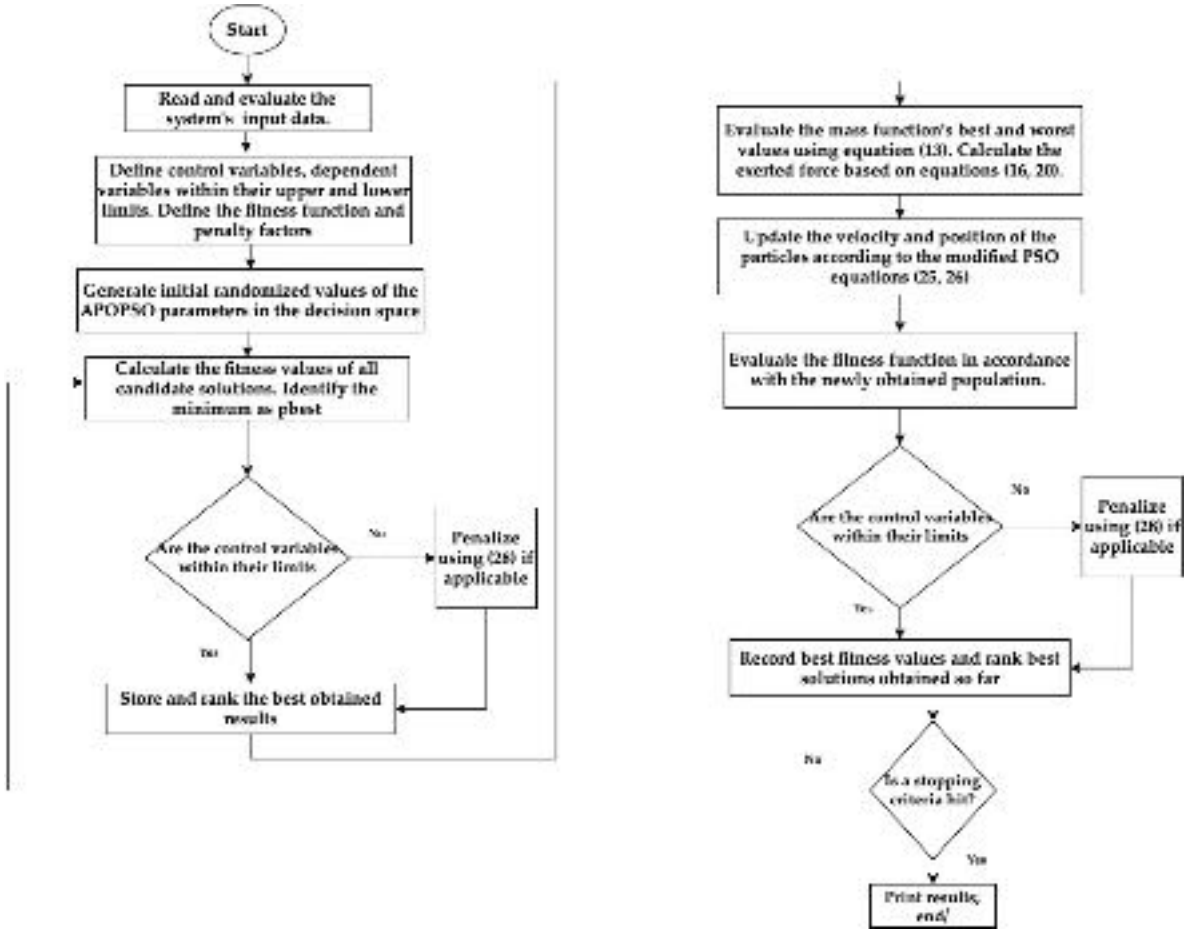

Figure 4-8 The developed hybrid APOPSO applied to the energy management and control of hybrid microgrids

The purpose of utilizing this search strategy is to ensure safe and optimal sharing of the power between the two sides of the hybrid microgrid in terms of providing the bidirectional controller with optimized vector-decoupled control parameters to achieve ideal converter's operation and ensure operation within system's limits which are defined in our study not to exceed $\pm 5\%$ of the frequency, and $\pm 8\%$ of the base voltage levels. The results of applying this hybrid algorithm is shown in Table 4.2 with the produced optimal parameters to ensure optimized damping performance. Fig. 4.9 presents the convergence performance of the developed algorithm while fig. 4.10 shows the results for best individual results per each of the eight variables in our study.

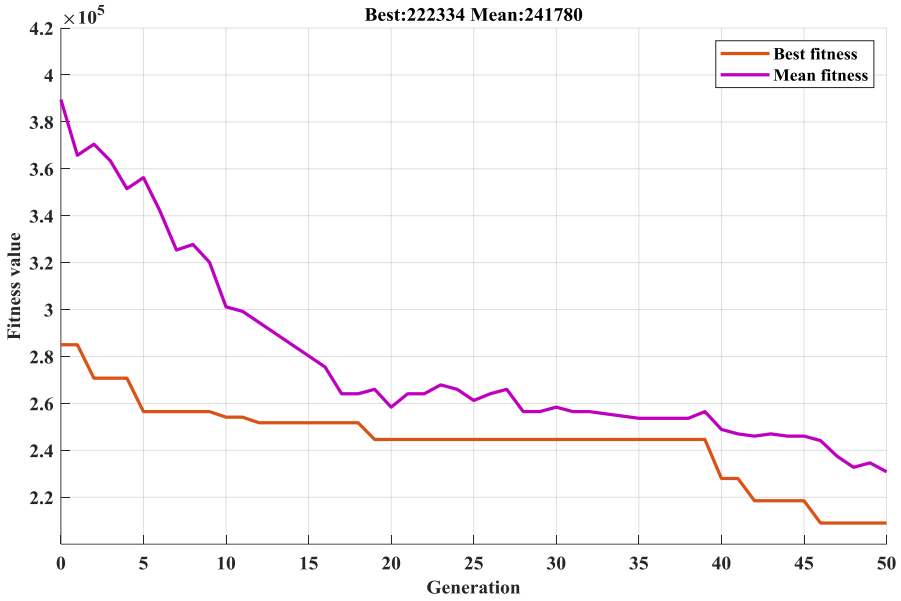

Figure 4-9 Convergence performance of the developed algorithm

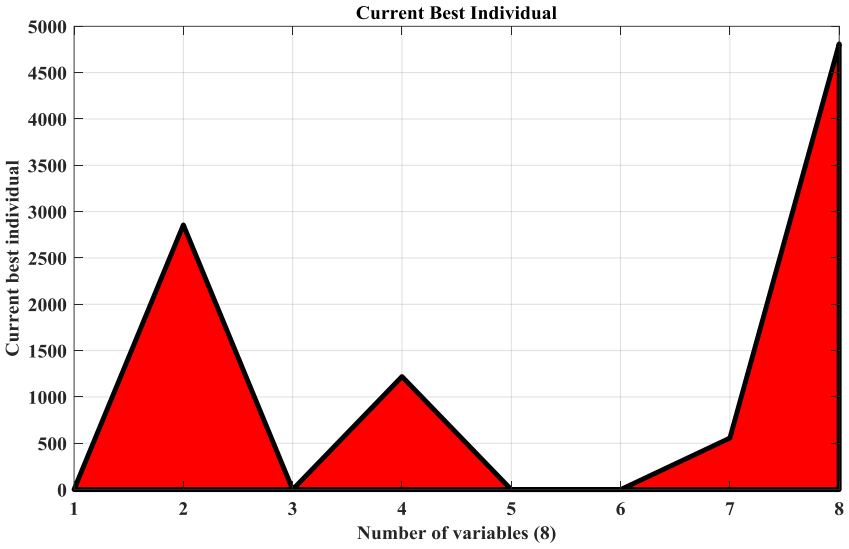

Figure 4-10 The optimization results of the developed hybrid algorithm.

Table 4-2: The optimal control parameters

Variable	Obtained Optimal Value
K_{p_f}	1.769
$K_{i\_f,}$	2856.447
$K_{p\_vdc,}$	0.604
$K_{i\_vdc,}$	1220.302
K_{p_vac}	0.025
K_{i_vac}	0.079
K_{p_m}	556.071
K_{i_m}	4810.291

The searching criteria stop if any of the following conditions have been reached; i) The hybrid algorithm reached the maximum allowed number of iterations, ii) Same solutions have been obtained for a predetermined number of iterations, or iii) Same set of solutions (by means of particles) are found in the same solution space.

4.4 Experimental Results

To verify our developed methodology, we demonstrate its concept via hardware-in-the-loop testbed at the Florida International University. A MATLAB/Simulink model is built and is shown in fig. 4.11. Specifically, it resembles the hybrid microgrid that consists of a synchronous generator and programmable AC loads connected at the AC side, with a PV emulator and a lithium-ion battery to resemble EVs activities at the DC side along with programmable DC loads. An interlinking bidirectional converter is utilized to connect the AC/DC sides of the microgrid. Fig. 4.12 shows the hardware components at our testbed lab to perform this study. We set the simulation time to be 4 seconds and applied the vector-decoupled with the optimization parameters obtained via the hybrid algorithm, as illustrated in this work. Fig. 13 through 15 shows the results, with the output of the PV system is dropping from 0.8 to 1.5 s as a result of a hypothetical cloud-dense during specific time of the day, as shown in fig. 4.13(a).

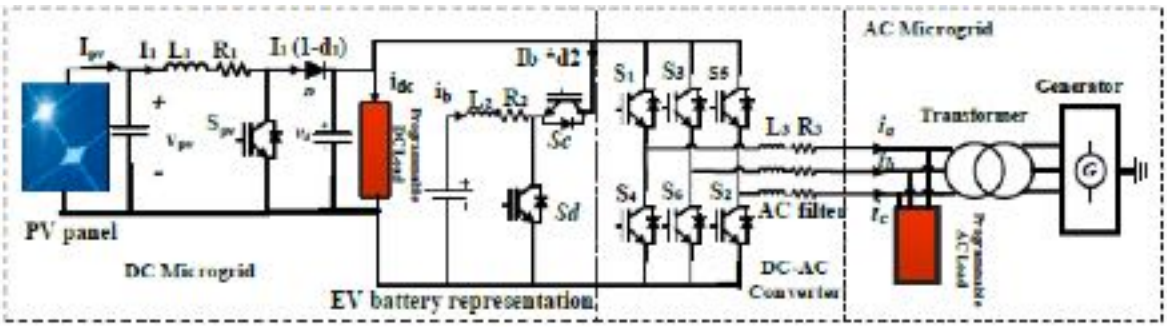

Figure 4-11 Schematic illustration of the hybrid microgrid connection at our testbed

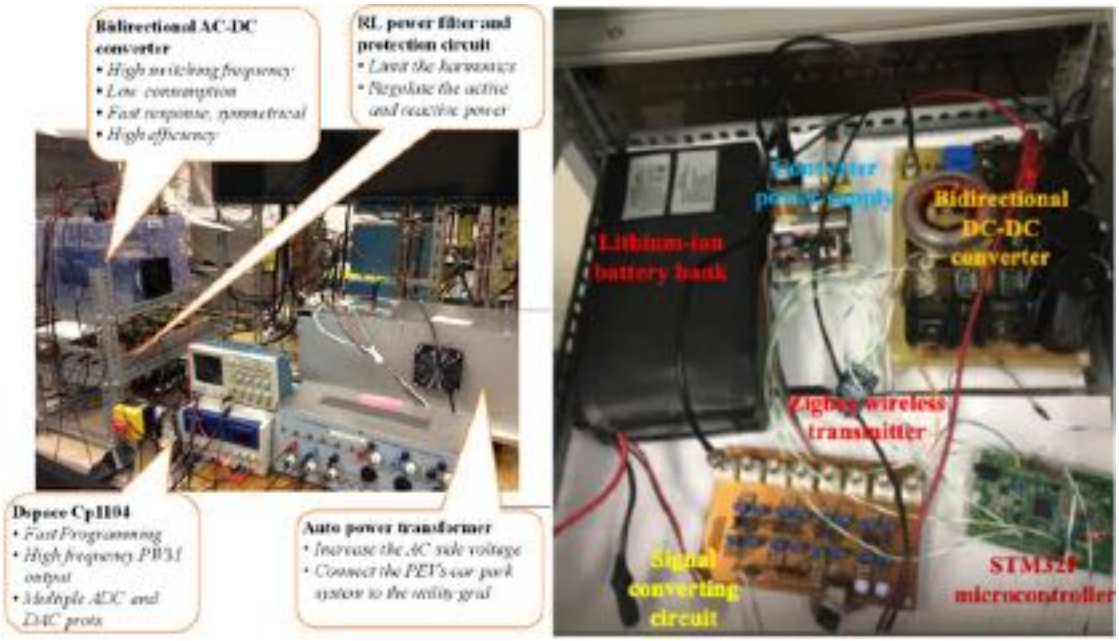

Figure 4-12 Hardware-in-the-loop equipment at our testbed

To be able to manage such deficiencies in PV generation, the microgrid operator allows more EVs discharging events via reduced monetary incentives to encourage the consumers to discharge during once such situation incur at any potential time of the day, as shown in fig. 4.13(b). In order to compensate for any potential lack of discharging due to the randomness of consumer participation, the AC generator increases its output to meet the remaining loads to keep the microgrid's operation in balance. This is demonstrated in fig. 4.15(a) and is achieved in rapid manner to keep the system's voltage and frequency levels unaffected. Fig. 4.13(c) and 4.15(c) present the load profiles, where considering the optimization of the vector-decoupled parameters, based on our hybrid algorithm, lead to more contribution from the AC generator side. It noted that assuming coordinated large-scale participation of EVs discharging the stress on the synchronous generator could be furtherly alleviated. Such incorporation of EVs in the balancing criterion could be then estimated, at the discretion of the microgrid's tertiary control, which eventually contribute to a smarter charging and discharging scheduling.

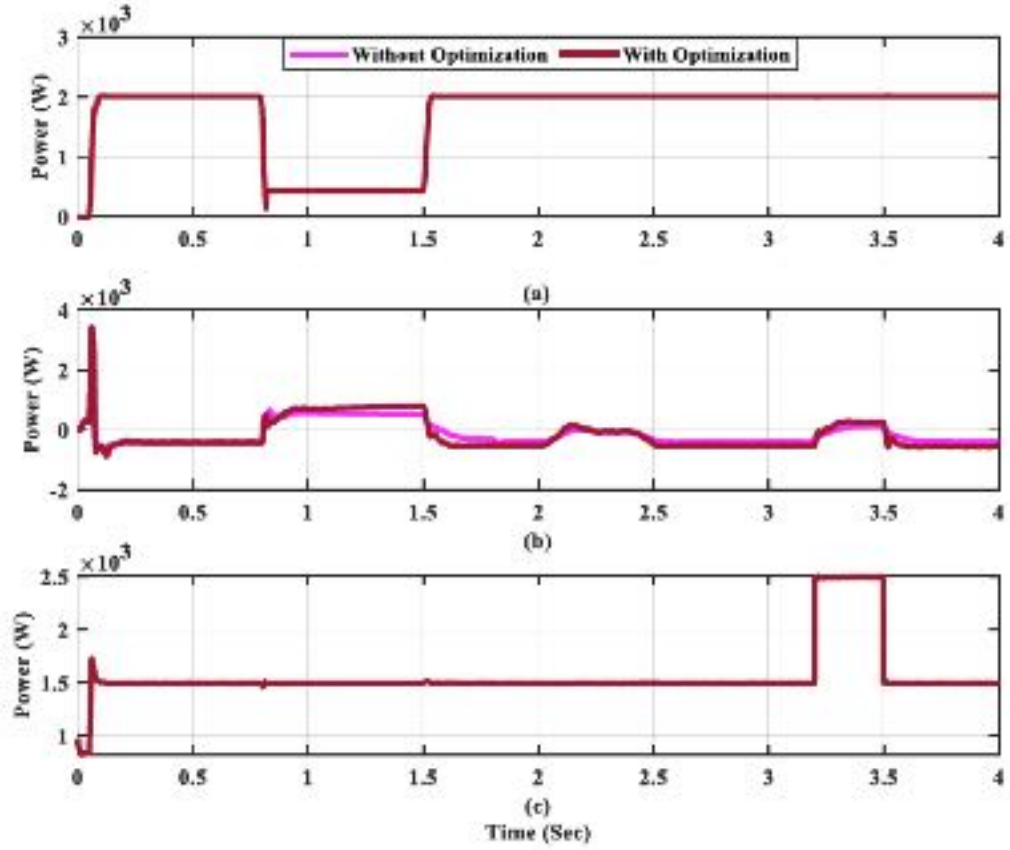

Figure 4-13 Results of the DC side: (a) Power generation from the PV system (b) EV's battery power (c) Load power.

As noted from fig. 4.14(a), 4.14(b) and 4.14 (c), the pulsed load of the DC side is energized for a total duration of 0.4 seconds between the timeslots 2 to 2.4 s, with another energized pulsed load between the timeslot 3.2 to 3.5 s. Following our developed mechanism, the controller performs the controlling procedure accordingly and mitigates the pulsed loads by balancing the power-sharing to a proper ratio to prevent any potential disturbances on the microgrid operation. Specifically, the controller force reversed power flow to the DC part of the hybrid microgrid if the DC loads are energized. Such a process is shown in fig. 4.15(b) in the case of negative power, which is an indication of power flow from the AC part of the grid to its DC side to compensate for the deficiency at the DC voltage level. As shown in Figure 14, our controlling mechanism achieves stable and secure microgrid operation by acceptable variations of the frequency and voltage levels. Although voltage variations are a bit high, we emphasize that they remain within a safe and acceptable level of operation. Fig.

4.15 (c) shows the DC side voltage level and is stable around the reference value of 400 V. As expected, variations of the generator output lead to fluctuations of frequency levels that exceed allowable and safe limits, which could trigger the operation of under- or over-frequency protection relays. However, these fluctuations are significantly reduced and managed following our developed control mechanism based on optimized parameters using APOPSO. This shows the robustness and effectiveness of our developed technique.

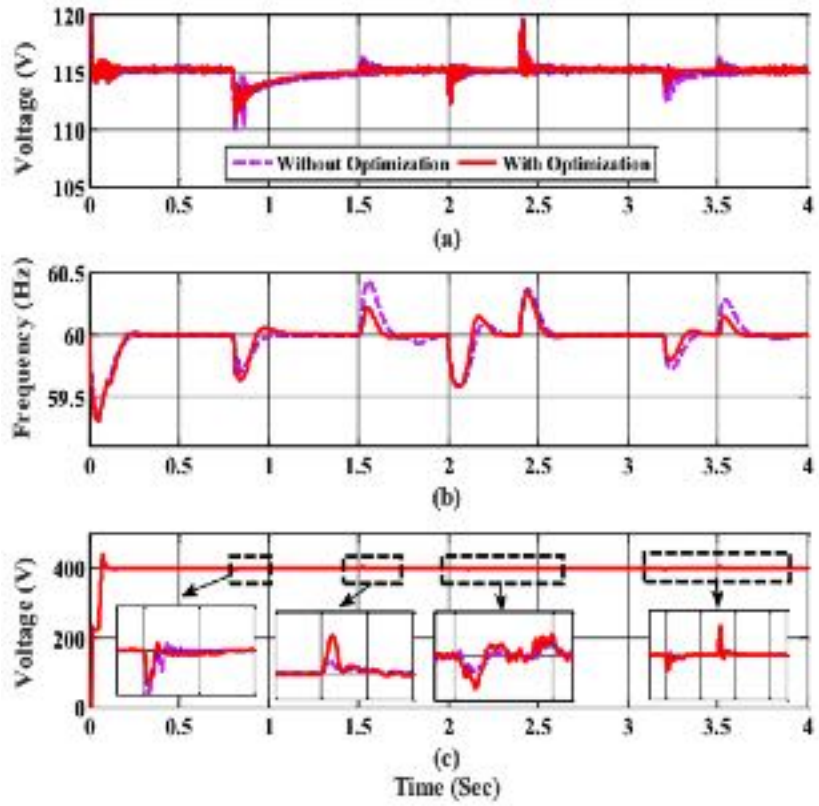

Figure 4-14: (a) AC voltage (RMS value) of phase a (b) AC side frequency level (c) DC voltage level.

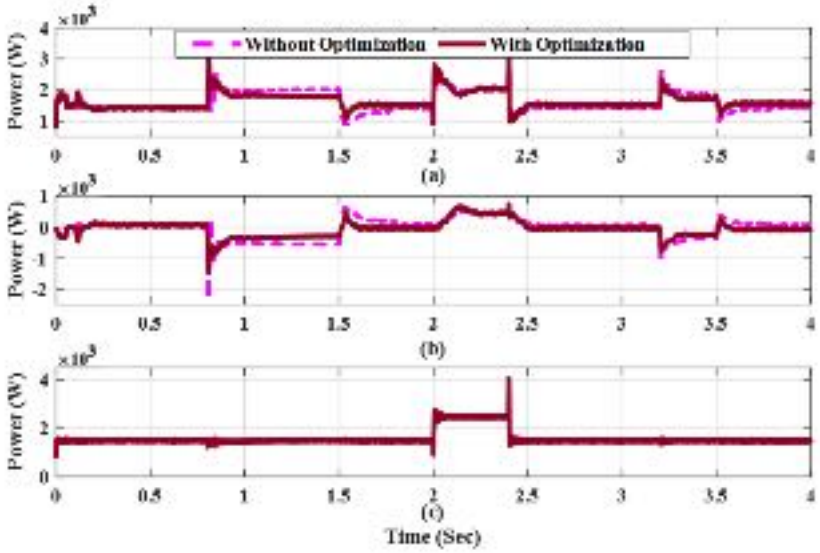

Figure 4-15: Results of the AC side of the hybrid microgrid: (a) AC generator output power (b) Inverter power at the point of common coupling (c) Load power

4.5 Conclusion

In this chapter, a metaheuristic-based vector-decoupled algorithm for hybrid microgrid energy control and management is developed. The algorithm aims to ensure safe and stable power-sharing between the DC and AC parts of the microgrid considering variable renewable energy sources, EV charging structure as well as severe operational condition such as in the case of forced islanding operation. The metaheuristic algorithm provides the interlinking converter with optimized parameters to manage the microgrid's operation under various load and resources conditions. A hardware-in-the-loop implementation verifies and validates the developed technique and offer stable and robust operation even during islanding situation. Furthermore, stable voltage and frequency levels are achieved and the power sharing between the two parts of the microgrid are accomplished. Specifically, we assumed a reduction at the power level of the DC side due to dense cloud in the time between 0.8s to 1.5s, as shown in fig. 4.13 (a). Accordingly, the controller requests more energy discharge from the EVs during this period to compensate for this deficiency, as illustrated in fig. 4.13 (b), while it allows for

power sharing from the synchronous generator located at the AC side as shown in fig. 4.15 (a) to assist the deficiency in the DC side. This is pivotal in the balancing of the operation especially in the case of insufficient participation of the EVs to discharge their energy during the scenario of reduced PV output. It is noted from the results that this has been achieved in rapid and robust manner without impacting the load levels. It should be noted that the parameter optimization of the developed hybrid algorithm allows more participation from the AC side. Since large variations in the generator output may lead to frequency fluctuations, optimization of the parameters is required in this work. This is achieved by optimizing those parameters using the developed APOPSO algorithm. As can be shown in fig. 4.14 (c), the optimized parameters reduced the fluctuations significantly in comparison with case of non-optimized parameters. Fluctuations in the non-optimization scenario may harm the operation of the hybrid microgrids and could trigger false operation of the over/under frequency protection relays. The success of the hybrid algorithm in reducing the fluctuations indicate its robustness and effectiveness in the hybrid microgrid energy management and control.

Future work is expected to incorporate algorithms that propose dynamic pricing structure to accurately reflect the real-time energy prices as result of control activities in hybrid microgrids. Soon, huge participation of EVs as well as privately owned small-scale PV systems are expected, and fair pricing structure will be required to encourage more participation from consumers sides. The authors of this work propose a new pricing scheme that allocate special pricing tariff on electric vehicles that charge considering stochastic microgrids operation and energy management [135]. Furthermore, the authors suggest that this area of research needs further investigation. Additionally, future work is also anticipated in regard with machine learning applications in smart control of power quality problems as a result of large adoption of EVs in hybrid microgrids. In such studies, smart control is integrated to enhance the voltage fluctuations and harmonics as result of stochastic large-scale integration of EVs activities on microgrids.

Chapter 5 Modeling the Impact of the Bidirectional Integration of Electric Vehicles on the Hourly Operation of the Power Distribution Grid

5.1 Introduction

Most of the utility distribution feeders are radial where power flows in one direction from the substation to the user. The introduction of storage devices like EVs may result in revolutionary changes to the distribution system. It could be used as voltage support, provide backup power in case of interruption, reduce losses, and defer the need for distribution system upgrades [136]. The way the distribution network is connected and operated to provide power to a load that changes every minute requires a time analysis to see the effect on the network especially with changing household load and Electric vehicle charging and discharging timing or in other word demand response. Demand Response (DR) is a term defined by the US Department of Energy (DOE) as "***changes in electric usage by end-use customers from their normal consumption patterns in response to changes in the price of electricity over time, or to incentive payments designed to induce lower electricity use at times of high wholesale market prices or when system reliability is jeopardized***". According to [137], DR is composed of incentive-based programs and price-based programs (time-of-use, critical peak pricing, dynamic pricing, and day head pricing). In addition to the popularity of the demand response programs which could trigger the interest to acquire the EVs, the environmental virtues of operating the EVs are grabbing the attention of the environmentally concerned customers, where the level of toxic gases released to the environment will be greatly reduced as the EVs' operation produce zero-emission, albeit this will also be depending on the energy grid mix and the efficiency of the charging and discharging process. These are just factors that help in driving up the interest on the EVs, where there are over 3.2 million EVs as of 2018 worldwide, accounting for almost 2% of the current car market. This number is projected to surpass 14% of the market by the year 2030 [138]. Such high growth

in the electrification of the transportation sector requires extensive research and evaluation to measure the capability of the current grid to withstand such increase. Therefore, we aim in this work is to provide dynamical modelling of various scenarios, considering real-life feeder and data information, to study the capability of the distribution feeder to welcome EVs charging and discharging over the hour without hitting the system voltage limits. The organization of this chapter includes a literature review on the past work related to the area of EVs integrations, model development of our own work and simulation, testing scenarios and results, and a conclusion of our findings.

5.2 Model Development

The main goal of this work is to measure the impact of V2G technology on a distribution system, which mainly consists of the following steps:

1- Data collection: the first step of the methodology is the collection of specific system and feeder information. For this study we will use IEEE34 bus test feeder.

2- Feeder modeling and validation: build computational models of representative feeders and verify that they match the actual loads, voltages, etc. using OpenDSS.

3- Determination of EV charging scenarios: to determines when, where and how much EV load is expected.

4- Feeder analysis and simulation methodology: to calculate power flows incorporating 24-hr load data and EV penetration levels using OpenDSS.

5- Results analysis and mitigation: the impacts on electric and financial variables are analyzed.

The following subsections presents more details about the process of building our model in the OpenDSS dynamical software.

5.2.1. The Open Distribution System Simulator (OpenDSS) Software

Open Distribution System Simulator (OpenDSS) is a comprehensive system simulation tool for electric utility distribution systems. It is implemented as stand-alone executable program or can be driven from a variety of existing software platforms the support a component object model (COM) interface. The executable version has a basic text-based user interface on the solution engine to assist users in developing scripts and viewing solutions. The program supports frequency domain analyses commonly performed for utility distribution systems planning and analysis. In addition, it supports many new types of analyses that are designed to meet future needs, many of which are being dictated by the deregulation of utilities worldwide and the initiation of the “smart grid” technologies. The software is available to download from the website of the Electric Power Research Institute [EPRI] website [139]

Many of the software features were intended to support distributed generation (DG) analysis needs. Other features support energy efficiency analysis of smart grid applications, power delivery, and also harmonics analysis. The OpenDSS is designed to be expandable so that it can be easily modified to meet future needs. The other way to use OpenDSS is through the COM interface, the user is able to design and execute custom solution modes and features from an external program and perform the functions of the simulator which include definition of the model data. Thus, the OpenDSS could be implemented entirely independently of any database or fixed text file circuit definition. For example, it can be driven entirely from a MS Office tool through the visual basic for application (VBA), as we will see in the analysis of this study or from any other 3rd party analysis program that support COM interface. Users commonly drive the OpenDSS with MATLAB program, Python, C+, R, and other languages. This provides powerful capabilities and excellent way to show the results graphs. An overview of the system simulation engine and interconnection with other programs are shown in fig. 5.1.

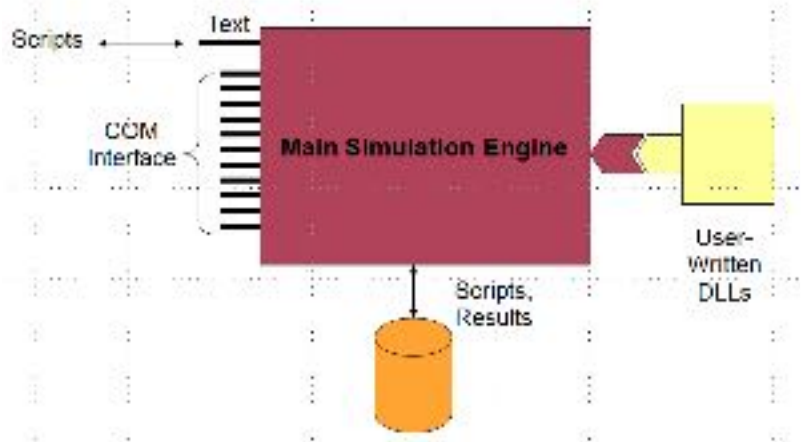

Figure 5-1 The OpenDSS model interface.

5.2.2. IEEE 34 bus Model Development using OpenDSS

The 34-bus test feeder model, shown in fig. 5.2, is modeled in this work using OpenDSS simulator. The system simulation results comparison between OpenDSS and another software named Electrical Distribution Design (EDD) and IEEE standard results are presented in table 5.1 [8]:

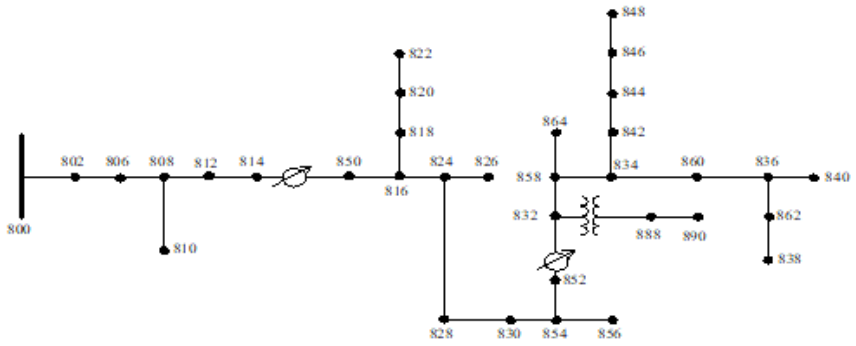

Figure 5-2. The IEEE34 Bus system Layout.

Table 5-1: IEEE34bus Model Steady State Data Comparison

	OpenDSS	**EDD**	**Standard**
Total Power MW	2.03247	2.04317	2.0428
Total Reactive Power Mvar	0.28252	0.29214	0.29025
Power Losses MW	0.270494	0.273	0.273049

Reactive Losses Mvar	0.0341963	0.03696	0.034999
Phase 1 Current A	51.507	54.15	51.58
Phase 2 Current A	44.202	46.81	44.57
Phase 3 Current A	40.593	42.98	40.93

It is worth mentioning that the EV are modeled as a dynamic kW load in the system in the OpenDss. The following equation better describe the amount of energy evaluated by the EV charging and discharging process as a dynamic load which was assumed in our modelling:

$$\mathrm{E}_{i,h} = (1 - \mathrm{d}_b)\mathrm{E}_{i,h-1} + \left(n_C \, \mathrm{P}_{i,h}{}^{C} - \frac{\mathrm{P}_{i,h}{}^{D}}{n_D} \right) \Delta t \qquad (5.1)$$

Where $\mathrm{E}_{i,h}$ is the amount of energy consumed as load by an EV i at an hour h, d_b as the EV's self-discharge rate,, n_C and n_D as both the charging and discharging efficiency which could be modeled in the software, $\mathrm{P}_{i,h}{}^{C}$ and $\mathrm{P}_{i,h}{}^{D}$ are the charging and discharging KW of EV i at time period h, respectively. While Δt is the time step, modeled in hours.

5.3 OpenDSS Model Testing Scenarios and Results

In order to test the system and study the effect of adding charging and discharging EVs to the system, we define the following cases:

Case 1: **Random EV Load Increase:** increase each load (spot or distributed) until bus or system limit (transformer loading, voltage, and line limit) is reached.

Case 2: **Distributed Incremental Increases:** Increase loads throughout the system in percentage proportion to the load at the bus (spot load only)

Case 3: Random EV load Charging and Discharging Increase: In addition to the charging at the spot bus, this case will have V2G loads at the spot bus to see the maximum kW that can be discharged to the system.

Case 4: Distributed 10% incremental increase of the charging and discharging loads: Increase charging and discharging loads throughout the system in percentage proportion to the load at the bus (spot load only).

In order to decide accurately the additional EVs that we can add to the system each hour, the following limitations are considered during different scenarios studied in this work:

- Transformer Loading Limit: current rating of 100% (normal), current rating of 125% (emergency).
- Voltage limit: minimum and maximum voltage levels are 0.92 pu to 1.08 pu respectively. The limit is calculated on 120 V base as 110-130 V.
- Line Loading Limit: 100% loading condition.

The above criteria are used in determining the level of incremental EVs that can be connected to the test systems. After analyzing different loading scenarios using OpenDSS, we found that the most sensitive parameter is the line voltages since the lines current in the range of 50A which represents around 25-30 % of the lines' capacity, whereas the most sensitive buses voltages are shown in table 5.2:

Table 5-2: Monitored Buses Voltages

Bus	Base kV	Phase 1 pu	Phase 2 pu	Phase 3 pu
814	24.9	0.94683	0.99543	0.98993
852	24.9	0.96451	0.96954	0.9644
890	4.16	0.92336	0.92513	0.91833

The buses above have the lowest voltage profile and as we test our system and add the electric vehicles to the network, these buses should be monitored closely to insure stable operation. In the original case without any additional load, we notice that bus 890 have low

voltage profile and need voltage support through shunt capacitors or voltage regulator. As we test the system for different scenarios, we will stop at the next low bus voltage level to see the amount of additional EVs that can be added to the system.

5.3.1. Load Profile of the Distribution Feeder

In this work we take into account that the load changes based on the daily time of use and this will affect the amount of EVs that can be added to the system at different time of the day. The way to test the model in OpenDSS is to increase the loads at the specified buses according to the cases. Once the system reach the maximum limit, the maximum amount of EVs Charging/ Discharging for each hour of the day can decided and the amount of EVs to be connected at that duration is calculated as well. As load change in fig. 5.3, the substation power output will vary as expected. The figure shows the substation single-phase power and the total three phase power.

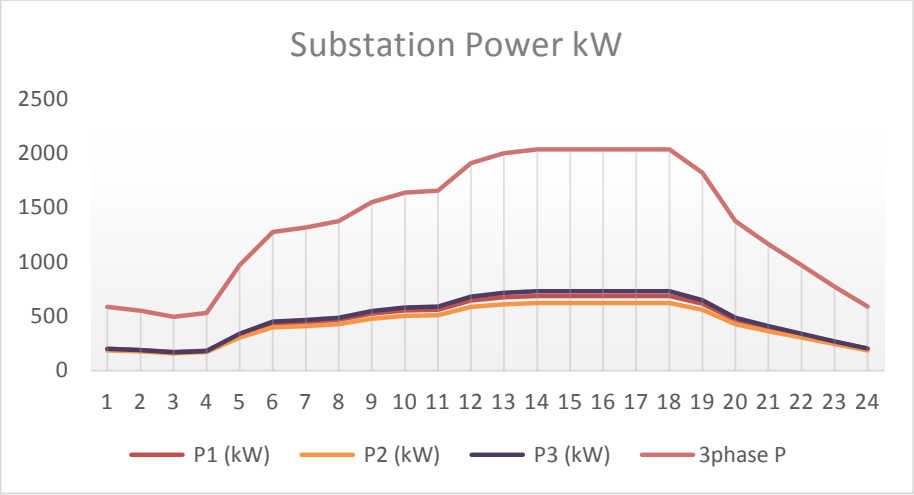

Figure 5-3. A daily power demand curve for a typical utility in California

We model the system using OpenDSS by utilizing the COM feature at the simulator to communicate with MS excel and Visual Basic Software to capture the data each hour and arrange it in a readable format and plot each transformer, line, bus and load data. Fig. 5.4

shows the way we introduce the demand load and EV charging/discharging demand and read the results.

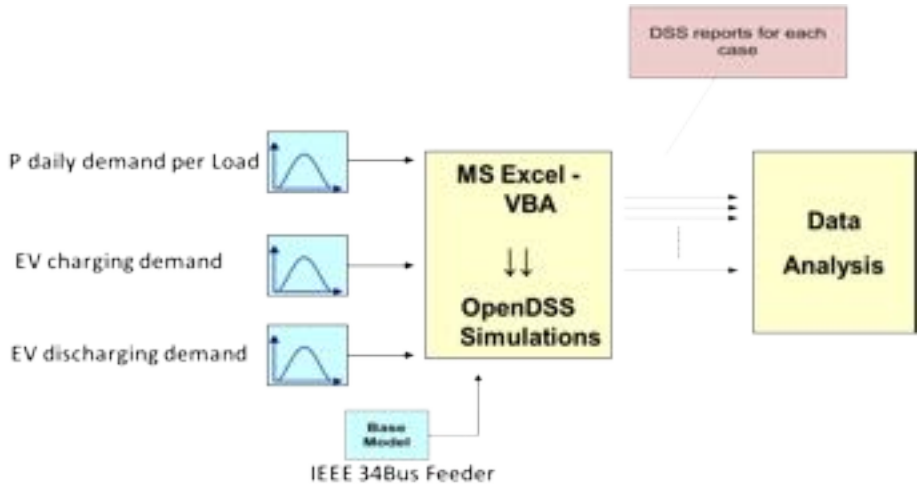

Figure 5-4. The simulation block diagram in OpenDSS

In addition to the amount of kW that can be added to the system, the cost of the additional charging and discharging kW can be calculated to see the effect of the time of use rate to the hourly charging and discharging loads. For a more realistic simulation of our work, we will use a time-of-use (ToU) rate for the Miami-Dade County in South Florida [140, 141], established by Florida's Public Service Commission to bill the EVs for their charging and discharging activities. We have made an assumption that the rate for discharging power to the grid is going to be the same rate. This assumption might not be accurate but for the purpose to complete the analysis until the final prices are issued by Southern California Edison (SCE). The price of the additional kW will be shown after each case daily power curve. The time-of-use rate used in this study is shown in table 5.3.

Table 5-3: Florida's Time of Use Rates.

Season, Date and Time	**Summer on peak**	**Summer off peak**	**Winter on peak**	**Winter off peak**
	June, 1 to October,1	June, 1 to October,1	October,1 to June, 1	October,1 to June, 1
	12:00 PM to 9:00 PM	all other time	12:00 PM to 9:00 PM	all other time
Total ($/kwh)	0.48964	0.17177	0.35203	0.1667

5.3.2. Model Testing Scenarios and Results Analysis

Fig. 5.5 shows sample of the network lines loading for nodes node 806 to node 808. The utilization is very low and the only option to measure the effect on the system is the voltage profile limit of the line not the loading limit.

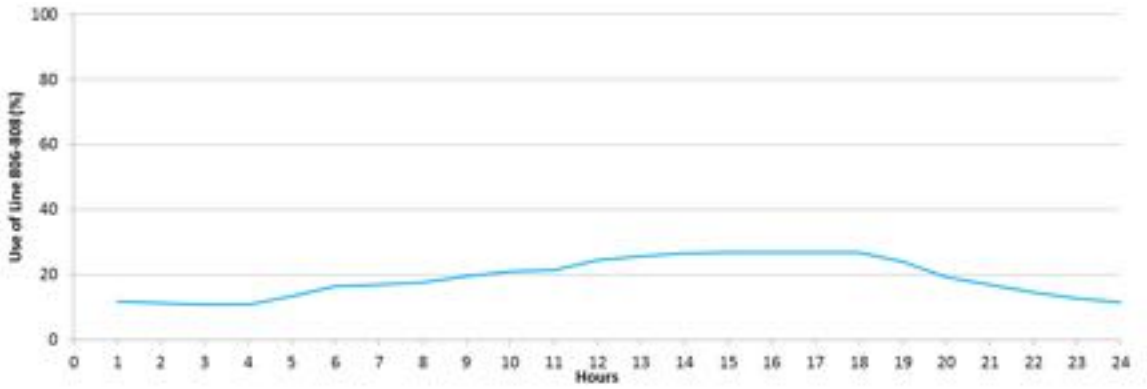

Figure 5-5. Buses 806-808 Line Loading Capacity.

Case 1: Random EV Load Increase: Increase each spot load until bus or system limit (transformer loading, voltage, and line limit) is reached:

For this case study, we worked on several buses on the system to analyze the effect of adding EVs as random load increase on the system. For convenience of our work, we show the results of work at spot bus 840. First, we start to increase the amount of additional EVs charging load to the bus until one of the three buses 890, 852 and 814 reach the lower limit. Table 5.4 below shows the amount we added to the bus and the per unit voltage at the three buses, while table 5.5 shows the overall results when model this scenario on several load buses. As results show, a maximum of 500 kW can be added to the bus without violation at buses 852 and 814. Also, one of the unique features of our study is that we were able to visualize the change of voltage level on each bus for each hour as can be seen in fig. 5.6 which presents the voltage profile of the load bus 890.

Table 5-4: Case 1 Maximum Additional kW on Bus 840 During Peak Hours

Bus	Base case	Additional 250 kW load on bus 840	Additional 500 kW load on bus 840
890	Below 0.92	Below 0.91	Below 0.90
852	No Violation	No Violation	0.92
814	No Violation	No Violation	0.92

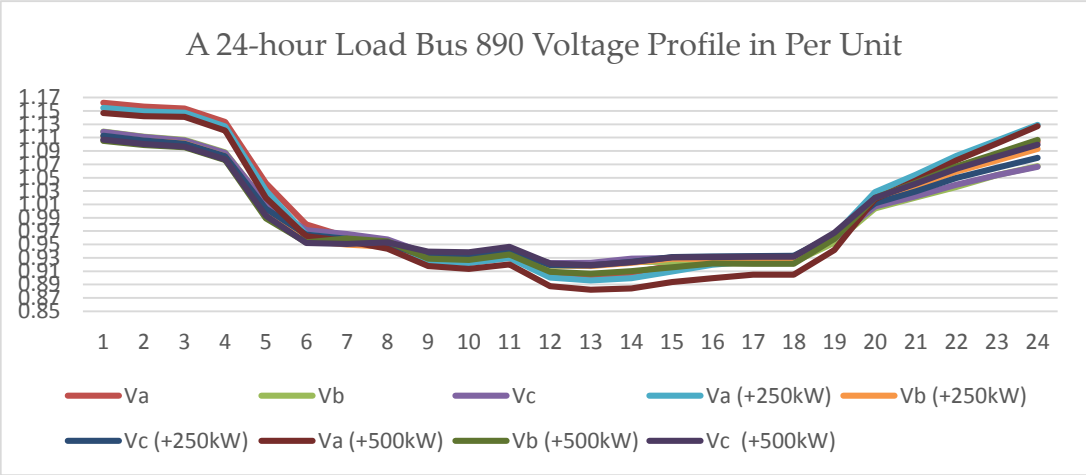

Figure 5-6. Case 1-1 Bus 890 Voltage (in PU) per Each Hour in the day

For instance, we assume that load bus 890 requires voltage support by adding shunt capacitor or voltage regulator if we consider the next bus to violate and hit system limit, the additional power would be 400 kW. As far as this study, we will not add any additional EV to bus 890 since the bus voltage will be very low (0.79). While other buses performs better as an ideal location for charging/discharging EVs, namely load bus 830, where the maximum power that can be added in period of peak hours (from hour 14 to hour 18) is 600 kW, which is equivalent to 75 EVs with level-2 charging and 300 EVs with level-1 charging. The plan now is to dispatch the EVs as the demand change. The system demand during the off-peak periods is low and the system can have additional charging EVs power added to the system. For each hour of the day, we will start to increase the EVs charging load to the buses until we reach the system limit. Fig. 5.7 shows the number of EVs charging into the distribution

grid, while fig. 5.8 shows the costs for adding them based on our use of SCE's time-of-use rates.

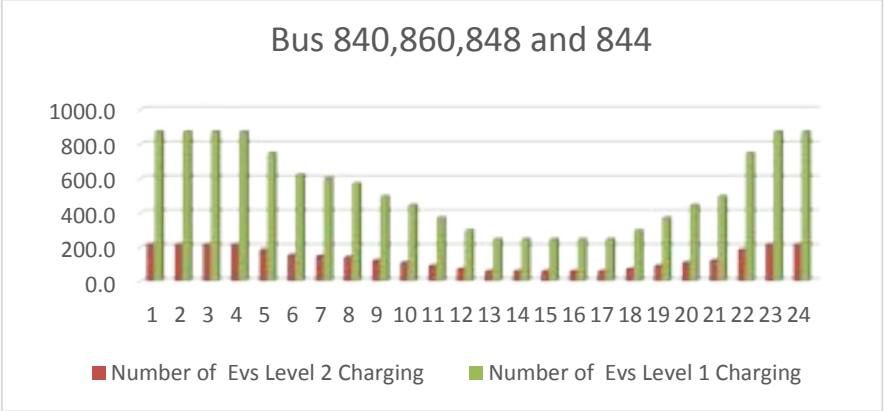

Figure 5-7. Case 1: Number of EVs on Bus 840,860,848 and 844.

Table 5-5: Summary of Case 1 buses Maximum Additional Load.

Spot Load Bus	Additional load	Bus 890 Voltage pu	Bus 852 Voltage pu	Bus 814 Voltage pu
Bus 840	Original Case	below 0.92	NO Violation	NO Violation
	250 kW	below 0.91	NO Violation	NO Violation
	500 kW	below 0.90	0.92	0.92
Bus 860	Original Case	below 0.92	NO Violation	NO Violation
	250 kW	below 0.90	NO Violation	NO Violation
	500 kW	below 0.89	0.92	0.92
Bus 848	Original Case	below 0.92	NO Violation	NO Violation
	250 kW	below 0.90	NO Violation	NO Violation
	500 kW	below 0.89	0.92	0.92
Bus 844	Original Case	below 0.92	NO Violation	NO Violation
	250 kW	below 0.90	NO Violation	NO Violation
	500 kW	below 0.89	0.92	0.92
Bus 890	Original Case	0.92	NO Violation	NO Violation
	10 kW	0.91	NO Violation	NO Violation
	250 kW	0.83	NO Violation	NO Violation
	400 kW	0.79	0.92	0.92
	500 kW	0.77	0.91	0.92
Bus 830	Original Case	0.92	NO Violation	NO Violation
	250 kW	0.91	NO Violation	NO Violation
	500 kW	0.9	NO Violation	NO Violation
	600 kW	0.89	0.92	0.92

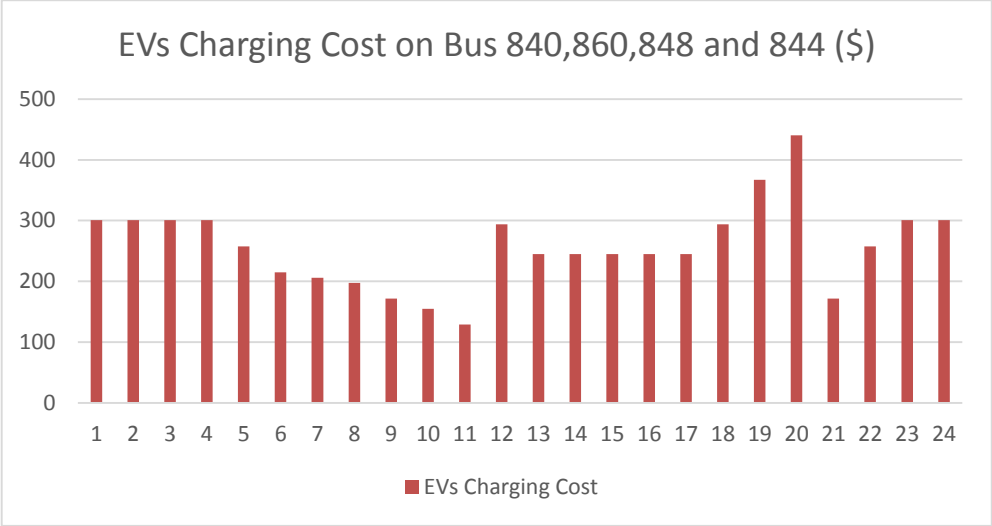

Figure 5-8. Case 1: Charging Cost on buses 840,860,848 and 844.

Case 2: Distributed Incremental Increases

For this case, we will start to increase the charging load at the spot buses all together at the same time 10% of the bus itself loads. The increment will be for all spot buses at the same time. For the peak hours, the maximum load that can be increased is as in the following table 5.6 until the system limit is reached:

Table 5-6: Case 2 Maximum Charging Load kW During Peak Hours.

Bus	10%	20%	30%	40%	50%
890	0.91	Below 0.91	Below 0.90	Below 0.89	Below 0.88
852	No Violation	No Violation	No Violation	No Violation	Below 0.92
814	No Violation	No Violation	No Violation	No Violation	Below 0.92

We can increase the spot loads 40% of their original load without any violation on buses 852 and 814. Using similar process to find the amount of additional load in the previous case, the additional changing load throughout the day was analyzed as well in this chapter. Fig. 5.9 shows spot buses 844 and 990 considering additional loads. After adding the different

amount of kW at different times of the day, the voltage level at the monitored buses 852 and 814 is almost constant above 0.92 as shown in fig.5.10.

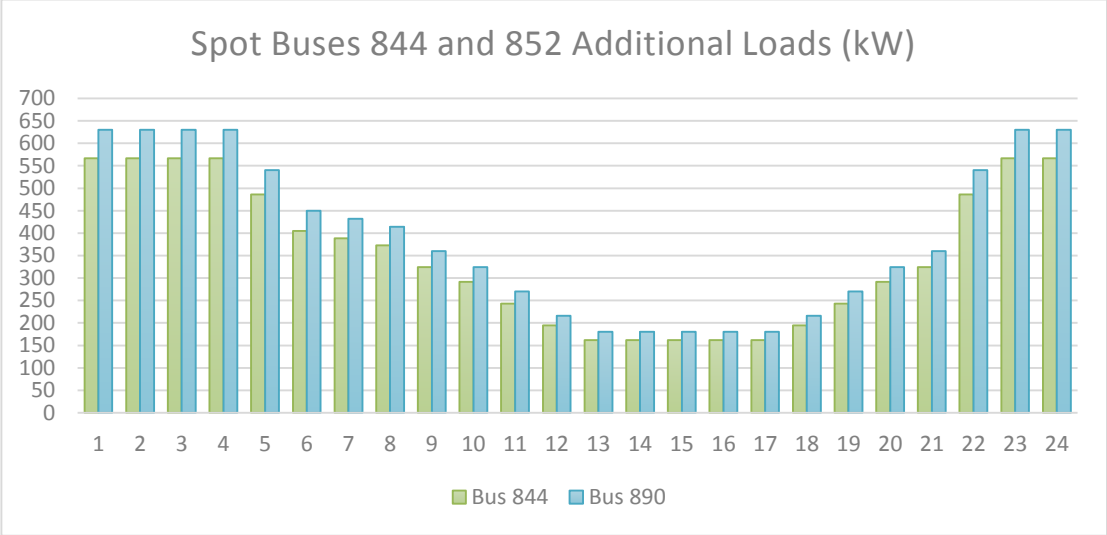

Figure 5-9. Case 2: Spot Buses 844 and 890 Additional Loads (kW).

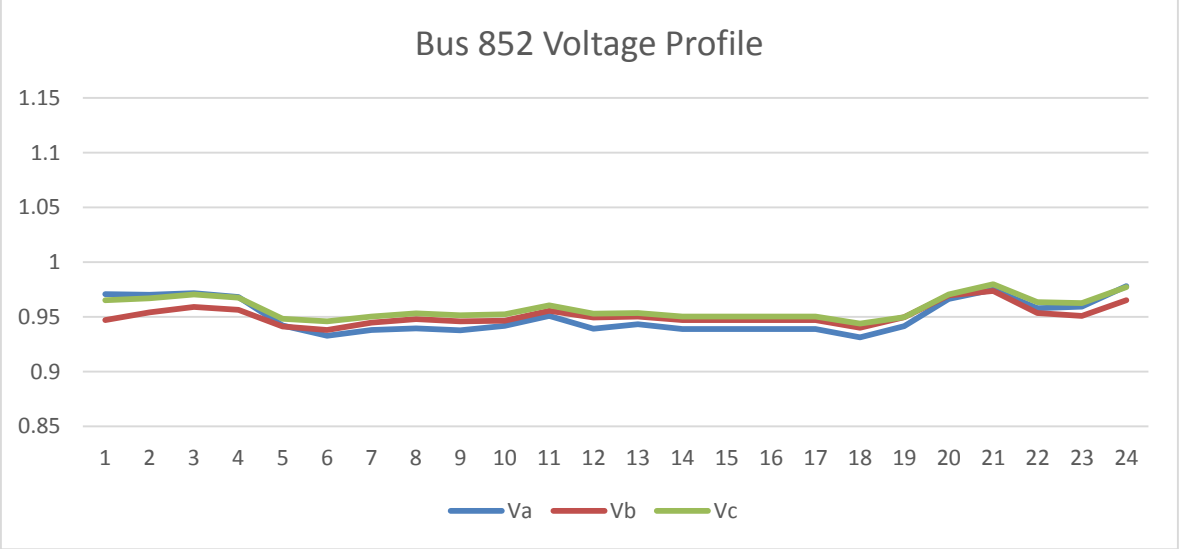

Figure 5-10. Case 2: Bus 852 Voltage Profile (in Pu) after adding the charging load.

Case 3: Random EV load Charging and Discharging Increase

In addition to the charging at the spot bus, this case will have discharging (V2G technology) loads at the spot bus to see the maximum kW that can be discharged to the system. Usually, the discharging will take place when the energy cost is high and during the peak hours. For our study, we consider the discharging process is going to be during the

peaking hours to support the system during high load in addition to the maximum charging loads at the spot buses. The results that we obtain should be considered as a good data that can be used for short-term operation planning to quantify the amount of the kW that can uphold the system during these hours. Table 5.7 shows the maximum charging and discharging during the peak hours before any violation to the buses' voltage level. It is worth mentioning that for the following cases the discharging of the EVs will take place while the maximum number of charging EVs is connected to the system at the same time. This will allow us to see the two bounders of charging loads and discharging loads without reaching the lowest and highest system voltage limits. As the demand change during the day the maximum additional charging and discharging load each hour for each spot bus is changed as well based on the grid's needs. Fig. 5.11 shows the additional charging/discharging and number of EVs connected to load bus 830 (provided as an example for the results obtained in this case). Such findings show that the idea of peak shifting could be valuably implemented with the kW discharging of the EVs during these hours, to be charged at other times in the day at predetermined agreements with the utilities.

Table 5-7: Case 3 Maximum Charging/Discharging Load kW During Peak Hours.

Spot Load Bus	EVs Charging kW	EVs Discharging kW	Violation
Bus 840	500	250	No Violation
	500	495	No Violation
	500	500	(Above 1.08pu) Violation on Buses 832,834,842,840,844,846,848,858,860,862 864
Bus 860	500	250	No Violation
	500	495	No Violation
	500	500	(Above 1.08pu) Violation on Buses 832,834,842,840,844,846,848,858,860,862 864
Bus 848	500	250	No Violation
	500	495	No Violation
	500	500	(Above 1.08pu) Violation on Buses 832,834,842,840,844,846,848,858,860,862 864
Bus 844	500	250	No Violation
	500	495	No Violation
	500	500	(Above 1.08pu) Violation on Buses 832,834,842,840,844,846,848,858,860,862 864
Bus 830	600	250	No Violation
	600	500	No Violation

	600	750	No Violation
	600	810	No Violation
	600	815	(Above 1.08pu) Violation on Buses 832,834,842,840,844,846,848,858,860,862 864

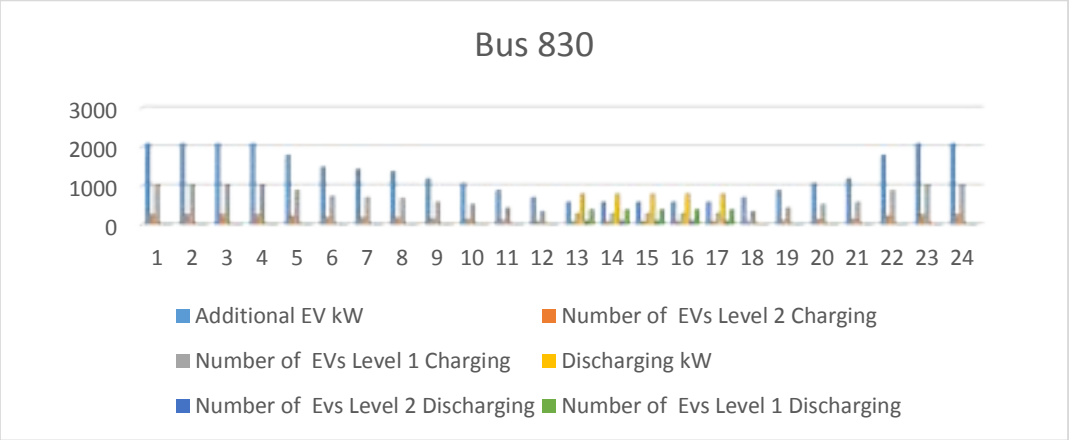

Figure 5-11: Case 3: Additional Charging/Discharging Load and number of EVs on Bus 830.

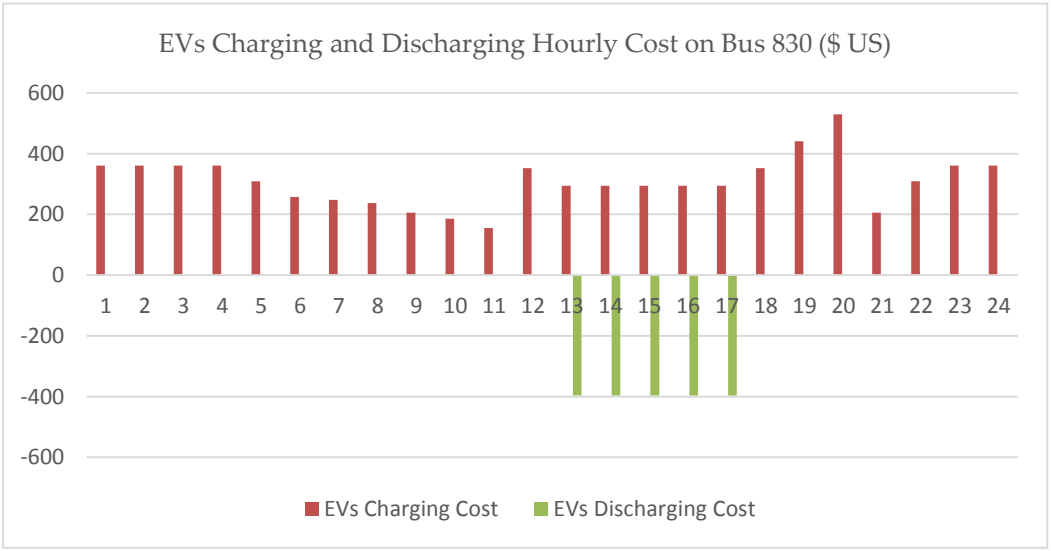

Figure 5-12. Case 3: EVs Charging and Discharging Cost on Bus 830.

Case 4: Distributed 10% Incremental Increase of the Charging and Discharging Loads

For this case, we increase EVs' charging and discharging kW throughout the system in percentage proportion to the load at the bus (spot load only). As we saw from case 3, the system will reach the maximum limit if we increase the charging load 40% of the bus total

load at certain locations. Table 5.8 shows the results of modeling the distribution feeder in this scenario. For EVs discharging loads, we will start to increase the discharging load at the spot bus until we reach the high limit (1.08 pu) of the voltage level. Such findings allow us to quantify the amount of EVs penetration that can be deployed (with previous agreements) into the system as controllable loads that provide local voltage support to help the operators in minimizing the congestion during peak hours, while enabling more EVs to charge during those hours without causing any voltage dips. Table 5.9 shows the maximum percentage amount increase in discharging load which is 80% of the spot buses loads. For the different hours of the day other than the peak hours, the charging and discharging loads are simulated in our work. Figures 5.13 and 5.14 shows the results for load buses 860 and 844.

Table 5-8: Case 4 Maximum Charging Load kW During Peak Hours.

Bus	10%	20%	30%	40%	50%
890	0.91	Below 0.91	Below 0.90	Below 0.89	Below 0.88
852	No Violation	No Violation	No Violation	No Violation	Below 0.92
814	No Violation	No Violation	No Violation	No Violation	Below 0.92

Table 5-9: Case 4 Maximum Charging/Discharging Load kW During Peak Hours.

Distributed increase on Spot Buses	EVs Charging Violation	EVs Discharging Violation
10% Charging and 10% Discharging	No Violation	No Violation
20% Charging and 20% Discharging	No Violation	No Violation
30% Charging and 30% Discharging	No Violation	No Violation
40% Charging and 40% Discharging	No Violation	No Violation
50% Charging and 50% Discharging	Violation on bus 814	No Violation
40% Charging and 60% Discharging	No Violation	No Violation
40% Charging and 70% Discharging	No Violation	No Violation
40% Charging and 80% Discharging	No Violation	No Violation
40% Charging and 90% Discharging	No Violation	(Above 1.08pu) Violation on Buses 832,834,842,840,844,846,848,858,860,862 864

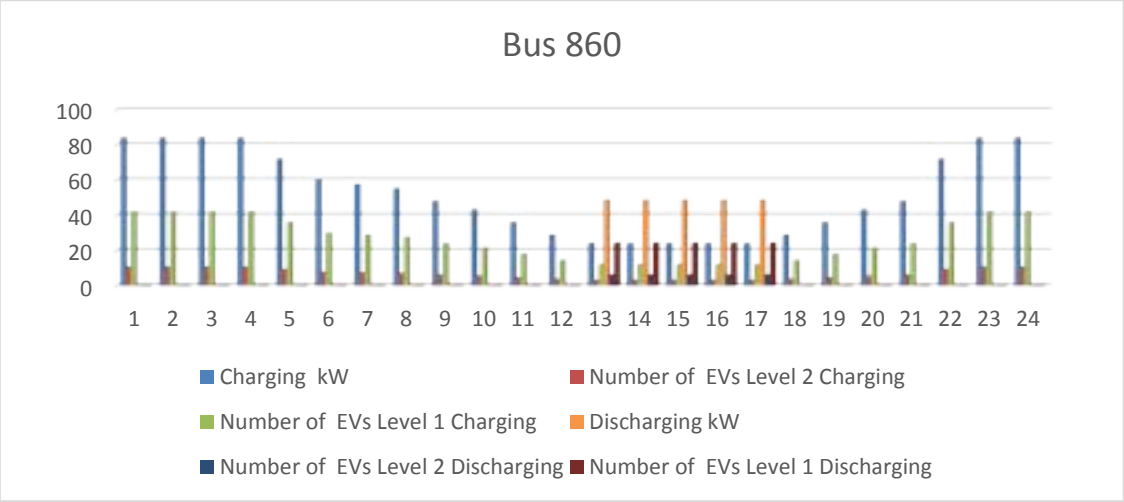

Figure 5-13. Case 4: Additional Charging/Discharging Load and Number of EVs on Bus 860.

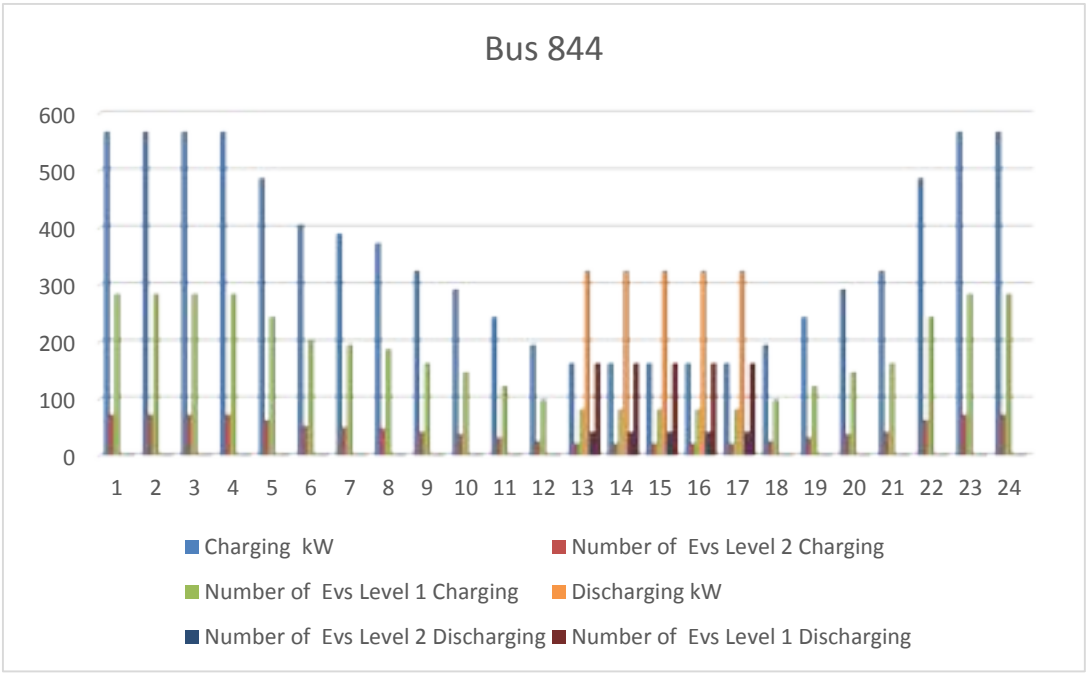

Figure 5-14: Case 4: Additional Charging/Discharging Load and Number of EVs on Bus 844.

Table 5-10: Summary of the different Cases Charging and Discharging Costs.

	Total charging Energy (kWh)	**Total discharging Energy (kWh)**	**Net Energy (kWh)**	**Total charging cost ($ US)**	**Total discharging cost ($ US)**	**Net cost ($ US)**
Case 1 buses 840,860,848,844	26,100	0	26,100	6,183.8	0	6,183.8
Case 1 bus 830	31,320	0	31,320	7,420.56	0	7,420.56
Case 2	26,100	0	26,100	6,183.8	0	6,183.8
Case 3	21,861.36	0	21,861.36	5,179.63	0	5,179.63
Case 4 buses 840,860,848,844	26,100	2,295	23,805	6,183.8	-1,123.724	5,060.07
Case 4 bus 830	31,320	4,050	27,270	7,420.56	-1,983	5,437.56
Case 4	21,861.36	4,198.5	17,662.86	5,179.63	-2,055.806	3,123.82

5.4 Conclusions

This chapter presents a study to model the impact of the Electric Vehicle integration on the hourly performance and operation of the distribution grid. The system's sensitive parameter to identify violation in our scenarios was the voltage limit not to exceed or degrade from the 8% limit of the bus voltage level. In our study, we modeled the IEEE 34 test system considering all of its parameters such as transmission line parameters, voltage, line loading capacities and frequency, transformers connections, as well as considered a real-life 24 hour load data to present results that simulate a real-life outcomes. We took into consideration the financial variables to model the pricing of the EVs charging throughout the day based on defined TOU rates for each season of the year. The results show the expected number of EVs that could be connected to charged, or discharge as in cases 3 and 4, in each node of that test system, along with the projected costs to do so. The results show the locations in the system that in need voltage support throughout the charging process in each hour of the day, as well as pointing to the most ideal locations to potentially host a charging station to serve the test feeder, as our study quantifies the approximate number of the EVs that could be served on an hourly basis without causing any violation during the normal daily operation. Table 5.10 below summarize the different cases total charging and discharging energy of the day and summarize the total cost for charging and discharging for each case. We can conclude that the additional load on bus 830 for case 1 and case 4 seems to be the best place to have the highest possible energy and eventually the highest number of Electric Vehicles.

Chapter 6 Real-Time Metadata-Driven Routing Optimization for Electric Vehicle Energy Consumption Minimization Using Deep Reinforcement Learning and Markov Chain Model

6.1 Introduction

Rapidly improving EV technologies promise to overcome many concerns related to the EV's battery capacities and energy management. The latter include extending the driving range of the vehicle and reducing the need for charging away from the customer's home. Unlike traditional methodologies, reinforcement learning (RL) is an artificial intelligence technique that has been widely used in solving many scientific problems in recent years [59, 60]. The concept of Q-learning was first introduced in [61], and a Deep Q-learning Network (DQN) is an extension to it [62]. Applications of RL has been widely employed to perform studies related to EVs such as in proposing efficient smart charging algorithm [63], as well as energy management and control strategies for hybrid and pure electric vehicles [64, 65]. In addition to the battery's energy management, RL techniques and methodologies have covered a wide range of topics related to power and energy engineering, such as electricity market trading in smart grids [66], energy production scheduling [67], and multi-agent distributed energy management of a microgrid [68]. RL has been extensively investigated in the automotive industry in recent years. The authors of [64] employed RL to measure an adaptive optimal energy control strategy based on different driving schedules. They tested the learning ability of HEVs and verified via simulation the impact on fuel efficiency. They made comparisons of their developed strategy with results obtained previously utilizing Stochastic Dynamic Programming (SDP). Similarly, based on the Q-learning algorithm, the authors of [69] studied a predictive energy management framework for a parallel hybrid electric vehicle (HEV). Their results show significant reductions in both fuel consumption and computational time. Additionally, the authors in [70] tested the capabilities of deep

reinforcement learning to train autonomous, self-driving automobiles that are aware of other elements in their surroundings, such as pedestrians, other vehicles, etc. The probabilistic nature of driving patterns of EVs is modeled in many recent works of literature as a Markov decision process (MDP). In [71], researchers tested the behavioral response of the stochastic charging of an EV station using MDP methodology. In [72] MDP was utilized to model the impact of stochastic driving, parking, and charging patterns of EV loads on the local distribution grid. Range anxiety is one of the major obstacles in the EVs market. In addition to the automotive industry, RL has been a widely used technique in many fields of research in recent years, such as in robotic control [73, 74], computer systems applications [75, 76], image processing [77, 78], agent-learning systems [79], traffic improvement and coordination systems [80, 81], as well as wirelesses and communication networks [82, 83, 84].

This chapter develops an RL-based energy consumption minimization strategy to achieve an EV routing optimization considering real-life driving environment. This RL study is based on evaluating Q-values through the Double Deep Q-Network (DDQN) algorithm to train the EV as an agent that aims to choose actions corresponding to best obtained Q-values. This eventually leads to extending the vehicle's driving range. Modeling energy consumption on the road has been achieved based on Markov Chain Modeling (MCM) to estimate the energy requirements of traveling paths in accordance to input parameters and learning strategy. The learning experience is supported with real-time data retrieved from Google's API platform that serves as the source for input information, feeding the agent with real-time status of roads. The remainder of this chapter is organized as follows: section 2 illustrates the main concept of the RL and MCM applied in this work with the DDQN algorithm; section 3 presents the structure of our framework of modeling energy management for the EVs routing problem; the metadata utilization based on Google's API; and the application of the RL by calculating the reward arrangement in the RL algorithm; and section 4 presents the results

obtained based on experimentation and validation of the developed methodology on two geographically distinct routes; section 5 concludes the work with final remarks.

6.2 Reinforcement Learning

6.4.1 Deep Q-Learning Network (DQN)

RL is based on the concept of an agent, an environment, an inferred policy, Π, trajectory, a value *V*, set of actions a_i, set of states s_i, computed Q-values and established rewards *R*. An agent is an entity or unit that performs an action, with the action being any possible move that the agent can make within a given environment. The environment only provides a list of some possible actions that are self-explanatory, from which the agent can choose a specific action depending on its current state. Depending on the action chosen by the agent, a reward, either positive or negative, is initiated by the learning algorithm and the agent receives a discounted factor to decrease the effect of the current reward on the agent's choice. This discounted factor is denoted as γ, and the closer it gets to unity, the more influence the next reward will have on the current state, and vice versa. Furthermore, the reward could be seen as feedback that indicates the possibility of failure or success of the action in relation to the overall driving experience of the agent. The reward can be either immediate or delayed, depending on the agent's available choices for a specific action. Additionally, a set of Q-values is generated based on the number of actions considered at each state. The state-action relationship is considered a generalized policy iteration and is better described by the following equation that integrates both the future and current reward of a given action:

$$Q_{i+1}(s,a) = r_i(s,a) + \gamma \sum_{\dot{s} \in S} P_i(s'|s,a)\, Q_i(\dot{s},\dot{a}) \tag{6.1}$$

Where *A* is the complete set of possible actions $a_i \in A$; $s_i \in S$ is the complete set of possible states the agent may experience, with $Q_i(s,a)$ as the Q-value based on them; $r_i(s,a)$

is the reward function corresponding to a_i and s_i; *P(s'| s, a)* is the probability of state transition between two states, given an action; *s', a'* are the updated next state and next action, respectively. In an environment, i.e., roads in a given region to navigate toward a destination, the agent can find itself in an instant real situation, known as the state. The agent, presumed to be an EV in our study, has the authority to move from its current state to the next state by inferring a strategy that achieves maximal rewards/minimal energy consumption, known as the travel policy Π.

This policy determines the next action to be taken by the agent, based on the artificial learning provided by the RL algorithm. The information accumulated from the learning process influences a long-term reward value *(v)* of the current travel policy and is denoted as $v_\pi(s)$.

The Q-value is used to show the long-term benefit of the current state. The concept of Q-values was first introduced by Watkins in reference [61] as an extension of Asynchronous Dynamic Programming (ADP). Q-values give the agent powerful learning capabilities via successive evaluations of each action the agent aims to perform. Specifically, the agent and the environment interact dynamically, based on discrete time steps, and, at each step, the agent receives feedback regarding the current state of the environment. With each additional step the agent takes, the next reward $r_{i+1} \in R$ is achieved.

This reward influences the learning process to establish the new state, s', with a particular probability for the transformation between states corresponding to each performed action. This mapping constitutes the policy of the agent's learning process and the sequence of actions and states for achieving any reward is known as a trajectory. Fig. 6.1 provides a clear illustration of the concept of RL performed in this work.

For exploration and exploitation, the agent uses the action-value method via the greedy policy to achieve the optimum result by choosing the highest-value actions at each state. The following value function grades the states and measures the relative strength of the actions based on the weights of the associated Q-values:

$$v_\pi(s) = \sum_{a' \in A} \pi(a|s)\, Q_\pi(s, a) \tag{6.2}$$

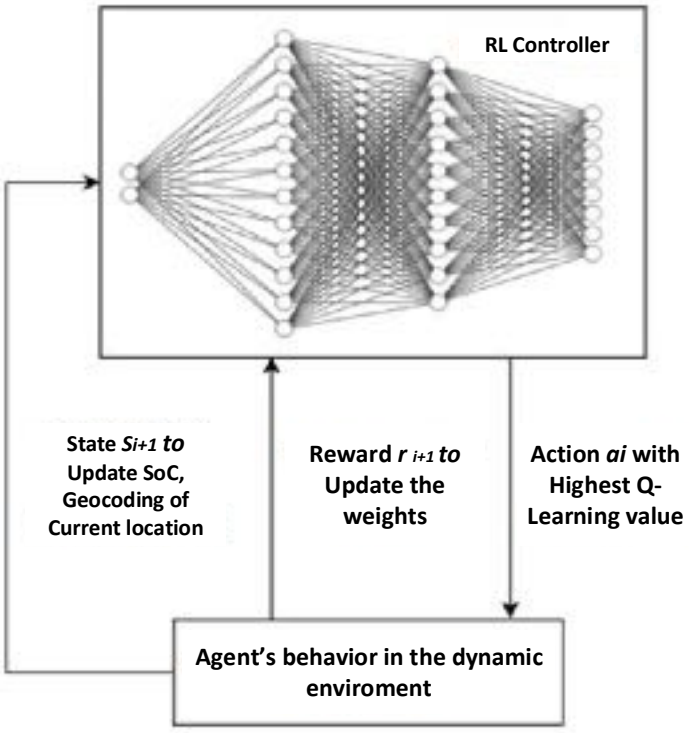

Figure 6-1. Illustration of the learning process in RL

In a continuous-state environment, we may end up having a very large number of states. This leads to the fact that the Q-function may not fully converge, even when we can estimate the condition under which it should converge. In such cases, we need to perform approximations to allow generalization for the states the agent has not yet visited. The deep Q-learning network (DQN) estimates for us the Q-values of these states and continues to improve them until optimal solution is found, which happen when the estimation of these

states converges. To properly train the Q-function estimator, a common loss function is used as follows:

$$L_i(\theta_i) = 0.5[g_i - Q_i(s, a; \theta_i)]^2 \tag{6.3}$$

Where $L_i$is the loss value to be estimated at the ith iteration, θ_i is the parameter of the Q-function at the ith iteration, and g_i is the target value at the ith iteration which could be found as follows:

$$g_i(s, a) = r_i(s, a) + \gamma \sum_{\grave{s} \in S} P_i(s'|s, a)\, Q_i(\grave{s}, \grave{a}; \theta_{i-1}) \tag{6.4}$$

To ensure more stability while decreasing the loss function, we deploy a target network $\overline{Q}_i(s, a)$ that has the same neural network architecture of the regular Q-value network $Q_i(s, a)$, but with different parameters. When the DQN algorithm updates the Q-values, this target network is updated as well. Then, the updated target network is used to calculate the target value as follows:

$$g_i(s, a) = r(s, a) + \gamma \sum_{\grave{s} \in S} P(s'|s, a)\, \overline{Q}_i(\grave{s}, \grave{a}; \theta_{i-1}) \tag{6.5}$$

The drawback of only using the DQN method is the problem of the overestimation of the Q-values. Typically, DQN estimates the Q-value as follows

$$Q_{i+1}(s, a) = r_i(s, a) + \gamma\, max Q_i(s', a) \tag{6.6}$$

Sometimes, taking the highest Q-value to represent the best action at the beginning of the training process could be misleading, since we have less information about the states. This could even complicate the learning process of the agent especially when non-optimal actions falsely give higher Q-values than those provided by the optimal-actions. To solve the

overestimation problem, the DDQN algorithm was developed by the authors of references [59, 60]. Utilizing the DDQN, we first use the DQN to find the best action for the agent corresponding to the highest Q-value. Then, we use a target network to estimate the target Q-value of the agent taking that action for the next state. Accordingly, equation (6) can be rewritten as follows:

$$Q_{i+1}(s,a) = r_i(s,a) + \gamma Q_i(s', argmaxQ_i(s',a)) \tag{6.7}$$

Where $argmaxQ_i(s',a)$ is the DDQN target network which is used to assess the Q-value of taking an action, a, at a state s'. This adds robustness and stability to the learning process and eliminate any potentials for overestimation of the Q-values

6.4.2 **Double Deep Q-Learning Network (DDQN)**

As we mentioned earlier, the role of the DDQN in this work is to produce a set of actions to be taken by the EV in Google API's environment and arrange the obtained Q-values in descending order from highest to lowest for the EV to adopt the action with the highest value. While Van Hasselt [60] thoroughly explained the DDQN algorithm, the performance of the algorithm was investigated and tested in [142] on the Atari 2600 games console, achieving performance close to a human level. Specifically, they built a massively distributed architecture that lays the foundation for other applications to utilize the DDQN algorithm, based on four major aspects: actors that influence new behavior; artificial learners, stored consistently, that are trained based on a previous learning experience; a neural network to model a value function in accordance with a behavioral policy; and, eventually, a set of continually stored experiences to direct the next step of learners.

Here, we mainly relied on the DDQN algorithm to model and represent the EV drive's learning experience to achieve optimal energy consumption by routing the vehicle toward an alternative path that reduces the vehicle's energy utilization. Metadata for the region of study

in this experiment was acquired from Google's API platform, as explained in section 3 of this work.

6.4.3 **Operation Modes**

The main mission of the neural network in this work is to allow mapping from R_n to R_m, correspondingly from the state, s, to updated $Q(s,.)$.The input is a two-dimensional vector that represents coordinates of the geocoded location of the agent, while the output is an eight-dimensional vector that contains the generated Q-values representing the possible actions, i.e., the directions in front of our agent (North, South, West, East, Northeast, Northwest, Southeast, and Southwest). We carefully integrated the hidden layers between the input and output to avoid any data trapping. Network depth represents the capacity of our framework, and proper modeling of the problem is required, as establishing extra or fewer neurons than needed in the hidden layers could lead to significant issues of either over-fitting or under-fitting. Moreover, misrepresentation of the neurons' numbers results in trapping the training data in extreme simulation times that are impractical [143, 144, 145].

In this energy consumption minimization framework, the input layer represents the metadata information retrieved from Google's API platform, by means of geocoding that comprises the longitude and latitude of the starting location for each segment of the road during the trip. It is followed by two connected hidden layers, with the first hidden layer of 12 neurons connected to the second hidden layer of 10 neurons. Lastly, the output represents an eight-dimensional layer of eight actions, which are the directions that are offered for the EVs to choose from. In this experiment, we set the drop-out rate to 0.30, and the learning rate to 0.1 for every step. It worth noting that the drop-out rate is a regularization factor that is used to reduce overfitting and improve generalization in deep learning process. On the other hand, learning rate is a factor that controls the speed of the learning process in the neural network model. Fig. 6.2 shows the integrated neural network for our framework. It should be

noted that the Q-learning algorithm converges, given that two conditions are met. The first condition is that the reward levels are bounded, meaning that there exists a positive scalar *k*, such that the absolute value of $r(s, a)$ is always less than *k*, while the second condition is that the agent strictly explores all the action-state pairs produced in the learning experience. We emphasize that both conditions were met while conducting our experiment.

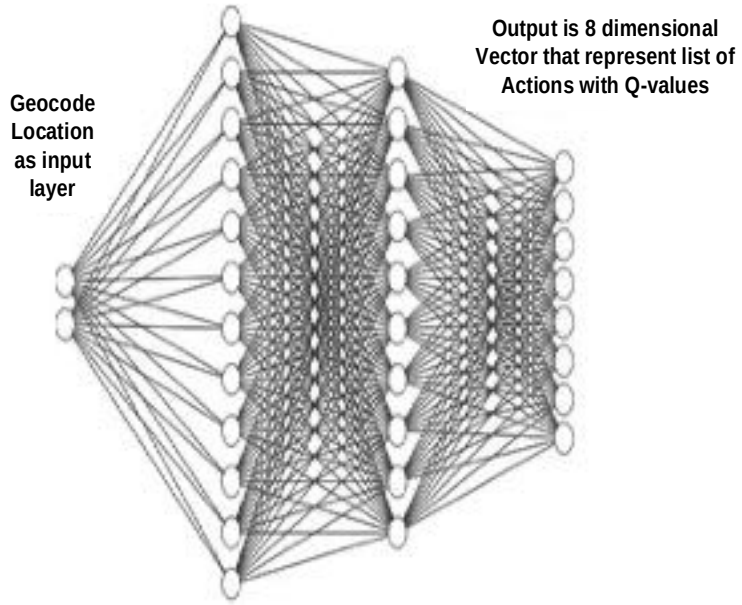

Figure 6-2. Integrated NN for our developed framework

6.4.4 **Markov Chain Modeling of Traffic Dynamics**

MCM is a popular method for generating traffic models, which we utilize in this work to model EV driving patterns and their corresponding energy consumption. The microscopic behavior of the MCM allows us to model the journey and driving possibilities of the EV realistically. The performance of the MCM was initially evaluated in [146] for capturing and modeling a dynamically complex system. It is also suitable for use with large datasets containing millions of data, and hence, it is useful for urban network traffic modeling as it can handle a large number of roads. MCM is based on a stochastically discrete process with finite states. In a homogenous MCM, these states change probabilistically at each time step. The probabilities of transition between these states largely depend on the state of the previous time step.

Modeling roads and vehicle travel is dynamic and is difficult to estimate properly. Consequently, the best way to handle these difficulties in the analysis of complex dynamic systems is to perturb them to produce the Markov model for the agent's travel and energy consumption requirements that we can integrate with our RL energy minimization framework. As required for any dynamic system, we need to set a reference point to quantify the contribution from all involved points in the boundary of study. Such a reference point is set up to establish the probability of transition between any two states. We define the region of study *(G, T)* to be a mapping from *T: G*, where *G* is a non-empty subset belonging to the space *T* and is partitioned into mutually exclusive and collectively exhaustive connected sets $\{S_1, S_2, \ldots, S_T\}$, where T is the total number of states. Each set is labeled with a specific state i of the Markov chain.

To put it succinctly, the Markov chain modeling process starts when the agent moves from state s_i to state s_j, in what is known as a step. Such a move can be continued successively, with P_{ij} describing the probability of moving between any two states. The collection of these probabilities forms the transition probabilities, which in return, establish a matrix of associated transitional probabilities, known as the transition matrix T_M needed to model the EV's drive.

The drive starts at a particular, pre-defined location (the agent starting position), which establishes the initial probability distribution for the MCM process. It should be noted that the process could be a standstill in a specific state, which, in this case, will have a probability of P_{ii}. Generally speaking, when we have r states in an experiment, then the ijth element of the transition matrix after n steps can be found using

$$p_{ij} = \sum_{k=1}^{r} p_{ik} p_{kj} \tag{6.8}$$

After calculating p and p_n, we normalize p_n so that the sum of all probabilities equals 1, as follows:

$$P_{n,ij} = \frac{m(A_{n,i} \cap T^{-1} A_{n,j})}{m(A_{n,i})} \tag{6.9}$$

$$\sum_{i=1}^{n} P_{n,i} = 1 \tag{6.10}$$

It should be highlighted that the transition matrix T_M must have no negative entries since the sum of probabilities will be added to one, with the probabilities of transitions forming its diagonal entries. However, we show in the next section how we deal with negative entries that are injected due to the regenerative braking property of the EV. Also, in this work, a set of graphs is used to model the EV's geocode history for each drive and is retrieved from Google's API as described in part 1 of the next section. We assume in our modeling that all transition matrices produced are primitive and irreducible. The Mean First Passage Time (MFPT), an average factor that assess timescale for a stochastic event to first occur, estimates the possible paths between vertexes in each episode in the road randomly [147]. Modeling the road of interest can be achieved using Markov chain with vertexes representing specific geocodes that resemble intersections on roads. Vertexes i and j are connected by an oriented graph G if there is a road segment between them such that $G = <G_i, G_j>$ is represented by the weights p_{ij} if $p_{ij} > 0$. We define the weight W_{ij} as the average energy consumed during the drive between vertexes i and j, as we will discuss in part 2 of section 3 of this work.

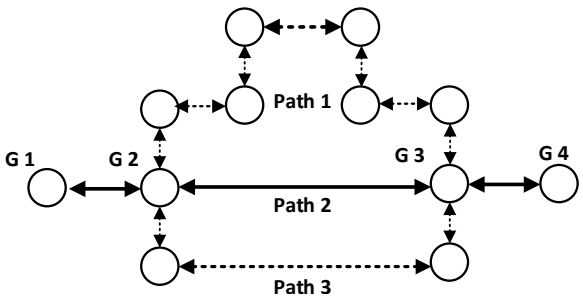

Figure 6-3. Example of graph representation considering MCM

Segments connect the vertexes whenever there is a drivable path. Fig. 6.3 provides an illustrative example of graph modeling, considering MCM. Vertexes $G_1, \dots, G_4$ represent road points in a region where an EV is driving. The segment G_1G_2 is the connecting road between geocodes represented as $G_1$and G_2, which represent the geocodes found in what would be the least energy-consuming path, based on the learning experience. It is worth mentioning that the main concept in MCM is its description of the actual transition from one node to another as a step unit of time. In this work, we modify this concept to represent the energy consumption information between these nodes instead, in the form of a unit step of energy consumed. We considered in our model the extension of the work in [148, 149].

6.3 RL for Energy Management of the EVs

RL provides a promising learning environment for different EV studies. As mentioned earlier, RL focuses on the cumulative return instead of immediate reward. Likewise, the EV's energy management focuses on minimizing the energy consumption of the entire driving cycle. As an agent, the EV's energy management relies on information on its current vehicle power demand, battery level, and driving conditions, including speed, road condition, etc. Similarly, RL ensures that the agent only needs the current state knowledge and resultant reward; it does not have to acquire prior knowledge of the whole system state. Our RL experiment is based on the DDQN utilized in the TensorFlow open library. In this experiment, the EV serves as our agent navigating in an environment (Google's Map platform). The set of actions to be made is to choose the best direction in the driving cycle, in accordance with the energy consumption minimization requirement in the battery model that is set up for eight choices, as described previously.

The main concept of learning is that the EV, as an agent, randomly starts the drive, providing geocodes of its current location as an input layer to the neural network. The two inner layers have Rectifier Linear Unit (ReLU) serving as an activation function, with the set of actions

gradually reduced as a result of feedback from the DDQN algorithm, which consists of arranging decisions (actions) based on their respective Q-values, provided in the output layer of the network.

The amount of energy consumed due to changes of state during the EV's drive is modeled, based on the MCM, as a step unit of energy. Similar changes were made in other studies, where the authors in [150], for example, utilized the step unit as a unit of pollution in their modeling rather than a unit of time. The GridSearch tool was used for hyperparameter tunning in this work. This defines a boundary for each hyperparameter, which values will be tested. Our discounting factor and learning rate were set to be 0.85 and 0.1, respectively, in this experiment. Losses along the drive train are assumed to be 15%, and only 50% of the energy can be retained during deceleration [151]. The effect of the regenerative braking has been carefully considered in this study, as described in part 5 of this section.

6.4.1 **Interaction with Google's API**

The Google Maps Geocoding API is a service provided by Google to transform any physical location into geographical coordinates on a map. We utilize the geocoding API to get the navigation geocodes needed in the experiment, from the starting through the destination positions. We used both the starting and destination geocodes to construct a rectangular boundary on the grid map so that the system allows the EV to navigate only within its boundaries. The grid map may not always be a rectangle, given spherical geometry and any restriction imposed on the length of the stride, with the stride being the distance of a step (segment) the vehicle drives toward its final destination.

In our study, the EV is set to move in one of eight possible directions. Therefore, the Direction API iteratively provides eight possible navigation instructions to the agent at each state. The Elevation API provides the height of each position by using the navigation API instruction list geocodes. We highlight that, in the case of an unreachable position on the map

(e.g., a lake on the road), then the Direction API will return 'FALSE', whereas in cases of a reachable position, the route is evaluated by making sure the agent will only navigate within the boundary of the grid map utilized. Google's Roads API provides the agent with real-time metadata concerning the road to be navigated, such as imposed speed limits, number of traffic signals and stop signs, traffic congestion, etc. Such information is important to determine the optimal energy consumption route for our agent throughout the learning process. We also highlight that raw traffic data were estimated in this experiment based on the returned "duration in traffic" results for each trip provided in Google's Duration, as access to instantaneous traffic data is restricted and hard to obtain.

6.4.2 **Energy Consumption in the Markov Chain Traffic Model**

As mentioned in section 2, modeling the road of the region of interest can be achieved using an oriented graph, where each vertex represents a specific geocoded location, with edges (G_i, G_j) as the path between each pair of vertexes. We define the weights $w(G_i, G_j)$ which correspond to the average energy consumption of the agent's battery on the i^{th} state during the traveling path. These weights can be estimated as follows

$$W_i(P) = \sum_{i=1}^{k} \frac{w_{(v_{i-1},v_i)} - \beta_{(v_{i-1},v_i)}}{w_{(v_{i-1},v_i)}} \tag{6.11}$$

Where i = 1... n, and β can be chosen as the step size in the interval between zero and weights w_i. To properly integrate these weights into our problem, we transform the transitional matrix T_M into another MCM matrix, Q_M, as follows:

$$Q_M = (I_M - D)T_M + D \tag{6.12}$$

Where D = diag (w_1,.. ,w_n), which is a diagonal matrix that has weights w_i= 1, ..., n, is the number of vertexes in the grid map, with I as the identity matrix of the same dimensions of the transition matrix T_M. Since the step unit in MCM is modeled as a step unit of energy,

rather than a step unit of time, the energy consumption is calculated according to the driving style of the agent. In this work, three phases of driving are assumed: cruising, acceleration, and deceleration phases. The sum of energy used is calculated as the integral of the EV dynamics considering the three forces, F_{acc}, F_{rol}, F_{ad}, together with F_{slope}. In this calculation, F_{acc}, is the accelerating force; F_{rol} is the force for overcoming rolling resistance; F_{ad} is the aerodynamic drag force; and F_{slope} is the hill-climbing force. These dynamics are calculated as:

$$W_1 = \int_0^{x_1} \left(ma_1 + \mu_{ro1} mg + \frac{1}{2} \rho A C_{\mathrm{d}}\, v^2 + mg \sin(\emptyset) \right) dx \tag{6.13}$$

$$W_2 = \int_{x_1}^{x_2} \left(\mu_{ro1} mg + \frac{1}{2} \rho A C_{\mathrm{d}}\, v^2 + mg \sin(\emptyset) \right) dx \tag{6.14}$$

$$W_3 = \int_{x_2}^{x_3} \left(ma_2 + \mu_{ro1} mg + \frac{1}{2} \rho A C_{\mathrm{d}}\, v^2 + mg \sin(\emptyset) \right) dx \tag{6.15}$$

Where α is the EVs acceleration factor; A is the area in front of the vehicle; m is the vehicle mass at speed V; μ_{ro1}, ρ, C_d and g are constants and φ is the incline of the traveled path. Table 6.1 presents the parameters of the EV modeled in our experiment, where $x_1$is the traveled distance of the cruising phase; x_2 is the traveled distance at which the deceleration process starts; while x_3 corresponds to the total length of the travel path. Such information provides accuracy for our modeling, as geophysical metadata and relative limitations are reflected in the equations accordingly

Table 6-1: Parameters of the assumed EV

Parameter	**Value**
Gravity (g)	9.81 m/s^2
Air density (P)	1.2 kg/m^3
Rolling resistance (μ_{ro1})	0.01
Drag coef. (Cd)	0.35
Area in front of the EV (A)	1.6

Acceleration constant (a_1)	3.5 m/s^2
Deceleration constant (a_2)	-3.5 m/s^2
Mass (m)	1,961 kg

6.4.3 **Value-Iteration Network**

During our simulation, we successfully overcame the issues related to continuous control and visual constraints by depending on the approximation model of the Value Iteration Network (VIN) planning algorithm illustrated in [152]. Specifically, the author of [152] introduced the VI module as a neural network (NN) layer that could encode and enable a differentiable planning computation. As highlighted in reference [153], each iteration of the VIN module can be assumed to pass the previous of both the value and reward functions through both a CNN layer and a max-pooling layer. Considering such an analogy, each channel in the CNN layer will correspond to a Q-function to estimate a specific action. Similarly, the convolution kernel weights will correspond to weights belong to the discounted transitional probabilities. We utilize this concept to develop a VIN structure with backpropagation, to improve the learning process and reduce errors in the obtained travel policy. As described in fig. 6.4, the input represents an image of the coordinates at the current state of the drive. The output produced, based on the attention and observation logic, influences the travel policy to ensure robust outcomes. From the input, both the P_{ij}, state-transition function, and *fr*, which is a convolutional neural network (CNN) layer that transforms the input grid image into another, belong to the reward, with pixels considered reward values. The results from the MCM directly influence the value-function described in equation (2). Fig. 6.5 explains further the mechanism of the VI module in our training process. Specifically, at each iteration, the module treats the input of the probabilities of transitions and reward values from the actions into the CNN layer to influence the value of V.

As we illustrated, each channel in the CNN layer represents a Q-value corresponding to the list of actions produced for the EV. Moreover, the CNN layer provides weights based on the discounting factor and then starts the process of the next iteration. This layer arranges the actions in accordance with their Q-values, where *V* then provides feedback signals on successive iterations of Z to reach a finalized reward information corresponding to the current state of the journey. Once iterations conclude, the final policy values are produced.

6.4.4 **Battery Model**

The battery model incorporated in our simulation is adapted from [154]. Originally, they utilized the battery model in [155], but incorporating an update to include the transient response effect after long driving schedules to report an accurate SoC throughout the different driving cycles. Studies [153, 156, 157] present fast time factors of lithium batteries during driving cycles and are incorporated into the calculation of the state of charge by [157] for more accurate representations of battery condition during driving patterns. The SoC, battery's voltage, as well as power losses, can be evaluated using the following mathematical formulation:

$$V_{terminal} = V_{oc}(SOC, T) - i_{bat}(t) \times R_{int}(SOC, T) + i_{bat}(t) \times R_{transient}(\mathfrak{T}_{sec}, \mathfrak{T}_{min}, \mathfrak{T}_{hour}) \tag{6.16}$$

where $\mathfrak{T}_{sec}$, $\mathfrak{T}_{min}$, $\mathfrak{T}_{hour}$ are multiple time-constant factors of the battery consumption behavior with time, with the temperature, number of cycles, and, together with discharge rate, have been adapted from [157]. $V_{terminal}$, V_{oc}, are battery's terminal and open circuit voltage level; R_{int}, $R_{transient}$ are the internal and trainset resistance of the battery; $C_{battery}$ and $I_{battery}$ are the battery's capacity and corresponding current and is modeled as a current source [158]. It is found as follows:

$$I_{SoC} = -I_{bat}(t)/C_{battery} \tag{6.17}$$

$$V_{SoC} = V_{terminal}/C_{battery} \tag{6.18}$$

Parameters used in our simulation study is adopted from table 1 of reference [157]. We highlight that the degradation level of the battery itself is not incorporated in our experiment.

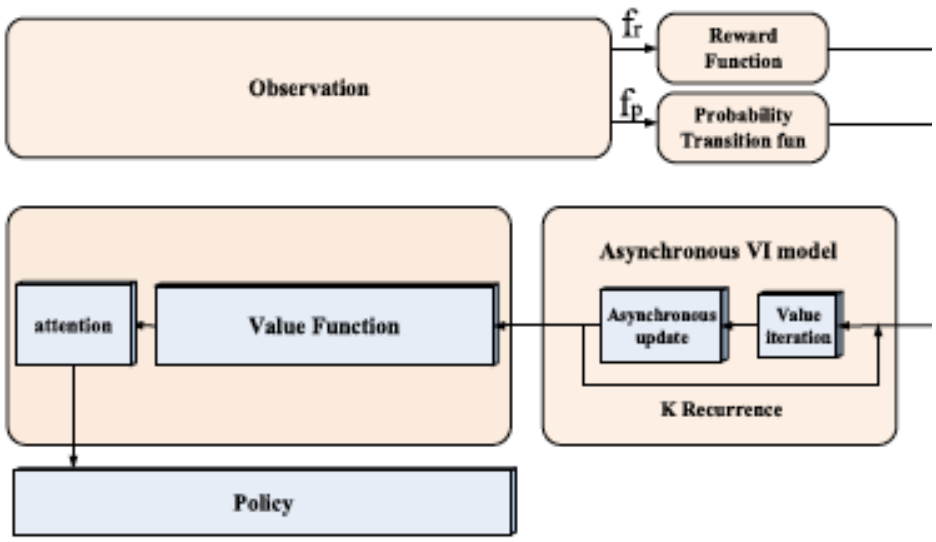

Figure 6-4. Representation of the VIN structure of our framework

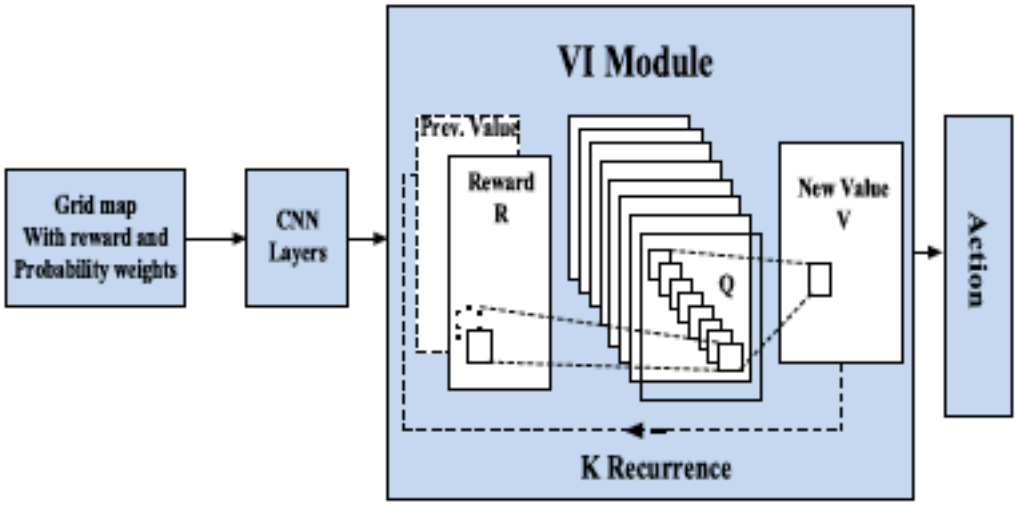

Figure 6-5. Iterations feedback for the value function

Table 6-2: Total number of episodes and steps per route

	No. of Episodes	No. of Failed episodes	Steps	Unreachable positions
First Route	140	20	5715	1711
Second Route	143	18	7226	1501

6.4.5 **Dealing with Negative Values from Regenerative Braking**

Practically speaking, the diagonal entries in the transition matrix should be only positive values, which will not be the case considering the impact of the regenerative braking in the EV during the trip as a result of the influence of the weights, which may either lead to zero entry on the diagonal or produce eigenvectors that are highly complex to solve. This leads us to strictly require the energy summation on any road segment to never produce a zero-entry in the diagonal. This can be achieved by introducing a medial matrix that has absolute values of the unit step of energy in the traveled path. Accordingly, all the weights are rearranged as follows:

$$|W| = diag(|w_1|, \dots\dots, |w_n|) \tag{6.19}$$

$$D = I - \propto |W|^{-1} \tag{6.20}$$

Where α indicates the sign of a change of energy transferred from the vehicle to the network and is strictly limited within the range $0 < \alpha <$ minimum w_i.

6.4.6 **Application of Reinforcement Learning**

The reward is defined as the relative factor to prioritize the levels of energy consumption minimization from the current position to the next in one step for the EV. It should be noted that the design of any reward signal is mainly heuristic, aiming to accelerate the learning process through providing feedback signals to indicate if desired objectives have been reached. We decided to simplify the reward feedback in the algorithm, rather than establishing a complex reward function, as this usually will not advance the learning process but will result in trapping the agent in local optima. The cornerstone of RL is to allow the agent to navigate through different alternatives based on the reward feedback signal received.

The agent starts with an initial state and follows the learning process to achieve the goal of optimal energy consumption (+1 reward) while establishing knowledge at the same time on how to escape the other set of states (-1 reward) that are presented in its environment.

Table 6-3: Experimental information and results

Routes	Starting Geocodes	Destination Geocodes	Energy consumed by framework	Energy consumed by Google's main route	Energy from Regenerative Braking	Simulation time
FIU college of Engineering & Computing – Doral's EV's Charging Station	25.768506, -80.366891	25.809732, -80.331379	1.9388 Kwh at 25 minutes	2.0548 Kwh at 19 minutes	Negligible	3709 s
J. Paul Getty Museum – Ventura's EV Charging Station	34.077823,-118.475863	34.158980, -118.499940	2.1066 kwh at 31 minutes	2.3548 kwh at 22 minutes	0.211 kwh	2,881 s

So the reward is multiplied by either 1 or -1 as follows

$$R_x \quad \begin{Bmatrix} 1 & if\ the\ position\ is\ reachable \\ -1 & if\ the\ position\ is\ unreachable \end{Bmatrix} \tag{6.21}$$

The discounted sum of rewards is defined using the optimal value of a state(s) and calculated as follows:

$$V^*(s) = \max_{\pi} E\left(\sum_{t=t_0}^{t=t_\rho} \gamma^t r_t\right) \tag{6.22}$$

Because of uniqueness, its value can be reformulated as

$$V^*(s) = \max_{a}\left(r_i(s,a) + \gamma \sum_{\acute{s}\in S} P_{s'|s,a} V^*(\acute{s})\right) \tag{6.23}$$

We calculate the optimal control policy as follows:

$$\pi^*(s) = arg\max_a \left(r_i(s,a) + \gamma \sum_{\grave{s} \in S} P_{i_{s'}|s,a} V^*(\grave{S}) \right) \quad (6.24)$$

The updated Q-learning algorithm is expressed as

$$\overline{Q}_{i+1}(s,a) \leftarrow Q_i(s,a) + \gamma[r_i(s,a) + maxQ_i(s',a')Q_i(s',a')] \quad (6.25)$$

The Q-value is obtained using equation (1), while optimal Q-values are calculated as follows

$$\overline{Q}_{i+1}(s,a) = r_i(s,a) + \gamma \sum_{\grave{s} \in S} P_{s'|s,a} \max_{\grave{a}} \overline{Q}_i(\grave{s},\grave{a})] \quad (6.26)$$

Then, the DDQN target network estimates the Q-value of the action, as follows

$$Q_{i+1}(s,a) = r_i(s,a) + \gamma \sum_{\grave{s} \in S} P_i(s'|s,a)\, \overline{Q}_i(s', argmaxQ_i(s',a)) \quad (6.27)$$

It is important to remember that we have assumed the discounting factor to be 0.85.

6.4 Results and Discussion

Consistent with the energy minimization requirement, the EV optimal routing problem is achieved based on the learning experience. Translating this problem within the context of Q-values, our agent follows the learning process to find a travel policy that maximizes the reward of its decisions as a mean of minimizing energy consumption throughout the trip. Through the MCM process, we represented the dynamics of the traveling path as a Markov chain, influenced by p_n that are updated throughout the drive to reflect energy consumed at each path between two vertexes. Our experiment protocol is established based on DDQN. The EV is evaluated over 140 episodes of the drive it was trained on, where each episode represents a complete set of steps, states and rewards derived from the agent-environment interaction. The agent was allowed to navigate until the end of each segment of the road or

was terminated if violates any restrictions placed on episodes. Such restrictions may be domain-specific, like violating several allowed steps per episode, having already achieved the objective of driving that segment optimally, or simply returning FALSE due to an un-derivable path option (e.g., flooding or a permanently closed road, among others).

As the agent is a purely electric vehicle, the only source available to its drive is the energy stored in its battery. Therefore, our objective in training the agent is to find the optimal path that requires least energy consumption to get the agent to its final destination, by extending the driving range of the vehicle as much as possible. However, we emphasize that some routes may actually result in more drive time for the EV's owner. Therefore, the duration of the drive is neglected in our study, assuming that the EV driver's main concern is to reach the charging location with the most optimal energy. Two routes have been selected to test the accuracy and strength of our developed energy consumption minimization framework. The first route starts at the College of Engineering and Computing of the Florida International University (FIU), Miami, Florida and the destination is set as an electric vehicle charging station located nearly six miles away, in Doral, Florida. The second route was chosen in a location that exhibits different geographic characteristics, to add more credibility to the testing of the developed strategy. It starts at the famous J. Paul Getty Museum, located at a hilltop site in the Santa Monica Mountains in West Los Angeles, California. The destination is set as a charging station located 5.8 miles away in Ventura, California. The geocodes of the starting and ending locations of each route are given in table 6.2, whereas Table 6.3 shows the total number of episodes and steps obtained during the simulation of both routes. The type of car used in both experiments is assumed to be a Tesla V, and its parameters are shown in Table 6.1 in part 2 of section 3. We assume 200 meters as a length of stride to evaluate the energy needed to travel between any two vertexes in the grid map, with no more than 80 steps within an episode; otherwise, it will be considered an unreachable position and thus labeled

as a failed step. The battery degradation level has been ignored in this study, as the focus of this study is on finding optimal routing to minimize the energy requirements of the EV. Specific features of the dynamic environment, such as time, location and route, could be different from one experiment to another. It should be noted that the performed date and time for these trips were April 25th at 4:30 PM for each location. It is also of interest to highlight that the energy for internal utilization (e.g., using the air conditioner in the car during the trip) has been ignored in this experiment.

The simulation was carried out in an extended Python environment, with TensorFlow, NumPy, and Pandas library requirements, at the FIU energy systems research laboratories. The input data for this simulation were the current geocodes for each vehicle, which provided the physical context around the vehicle and correspondent data related to the road (e.g., elevation, height, traffic flow, and allowed speed, among other factors). These data were imported into the simulation directly from Google's Map platform, where a combination of APIs and Software Development Kits (SDKs) allow retrieval of information from Google's map systems. Also, we highlight that traffic information and data were not easily obtained, as we had to query the Google's Directions API every time during the simulation to estimate the traveling time for each route considering real-time traffic conditions. The simulation takes into consideration the energy consumption for each state during the vehicle traveling, and then produced the results for the best optimal route that saves energy the most during the developed trip. Then, the results are compared with those obtained when strictly imposing Google's suggested route on the vehicle. Fig. 6.6 and Fig. 6.7 show the consumed energy throughout the trip, based on our framework versus Google's suggested routes for the trips taken in Miami, FL, and Los Angeles, CA, respectively. The results show that, in both simulation scenarios, the EV can reach its intended destination with lower energy than the main route developed by Google Maps, by 5.89% and 11.82%. The reason for such

differences in the reported results is due to the significant temporal and spatial differences at each location, which influence the level of energy consumption.

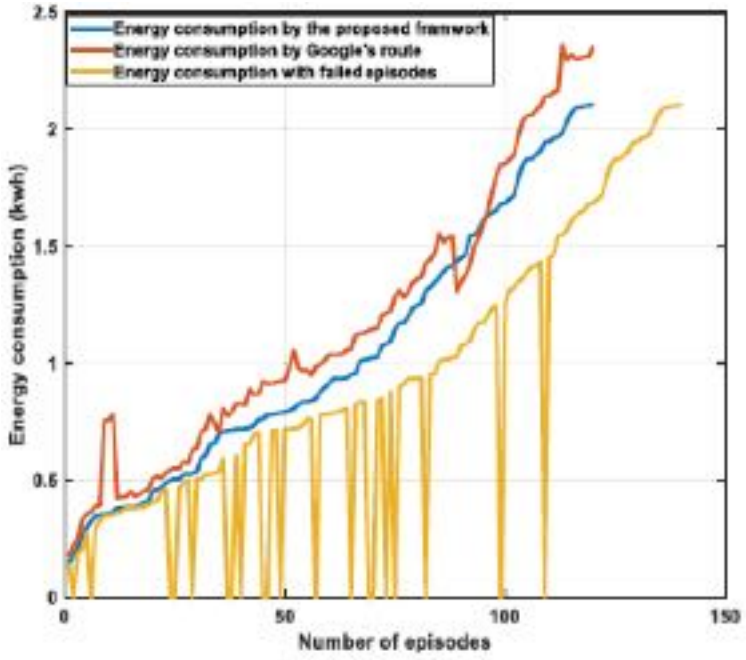

Figure 6-6. Energy consumption of the first route by the developed framework vs. Google's suggested route.

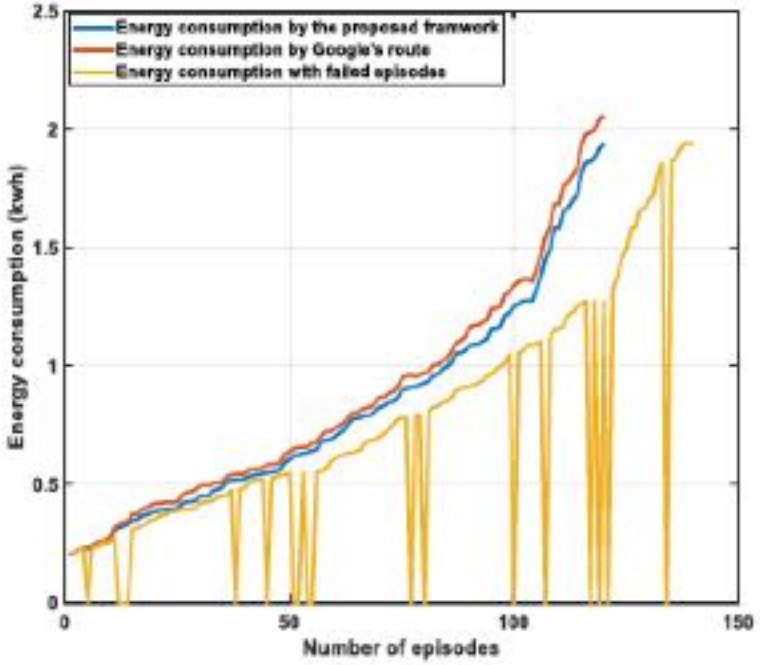

Figure 6-7. Energy consumption for the second route by the developed framework vs. Google's suggested route.

The results of both trips are presented in Table 6.3. It is noted that no detectable amount of energy was produced as a result of the regenerative braking mechanism, as the value recorded in the first route was trivial, while we can mark 0.211 kWh regenerated energy in the second route experiment. This amount of reproduced energy is attributed to driving downhill to reach Ventura from the hilltop location of the Getty Museum. We emphasize that more energy might have been consumed if the route had been in the opposite direction, such that if the drive was toward the museum instead of away from it. Based on 140 episodes of simulation, fig. 6.8 and fig. 6.9 present the level of reward returns as feedback that influenced the drive of the agent in the two routes. The reward value is influenced by the number of steps received by the learning experiment, returning negative values whenever there is a failed episode. Furthermore, the returned reward presented in fig. 6.8 and fig. 6.9 provides insight into the level of benefits of each action taken by the EV at each state throughout the trip; it shows the accumulated sum achieved for each step of the travel policy, based on the discounted rate set earlier, γ, at each time-step t.

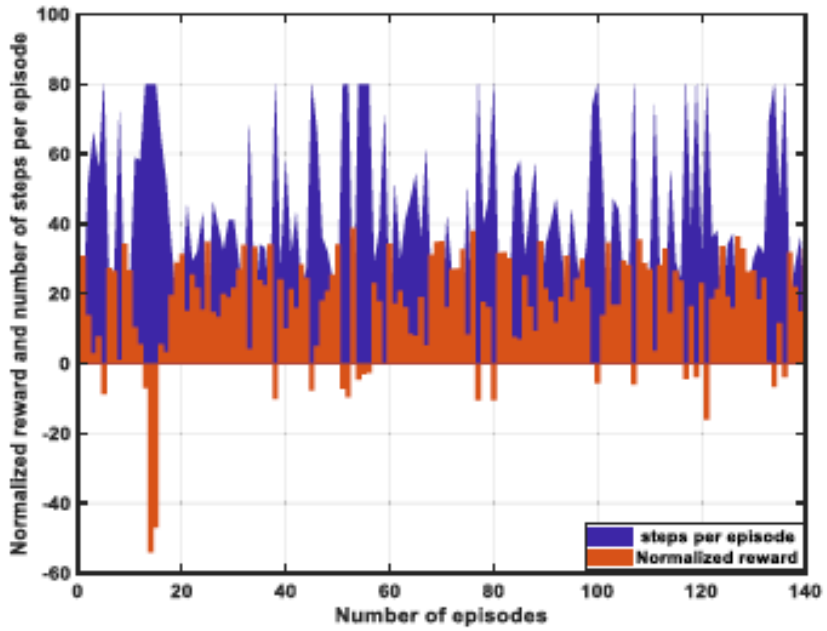

Figure 6-8. Reward details per number of steps in the first route Framework vs. Google's suggested route.

We highlight that the produced rewards of the experiment show low variation, which is an indication of the robustness of our developed framework in executing actions within the timeframe of the experiment. However, we believe that the limitation of the number of episodes per experiment, due to the highly constrained access to Google's API platform, has greatly restricted our ability to perceive variant rewards. It is of note that, as the training process advanced, the random behavior decreased significantly, as shown in fig. 6.10.

This has an immediate influence on the obtained reward, as the trend of the returned rewards indicates more positive outcomes and less negative values that represent failed steps. It is also noteworthy that the agent starts the navigation on a limited random action basis, but the impact of the learning process reduces this randomness effectively, as fig.6.10 shows for the first route. Throughout the journey, it is observed that the level of SoC improves with the improving certainty of actions taken as a result of improvement in energy consumption retained in the battery.

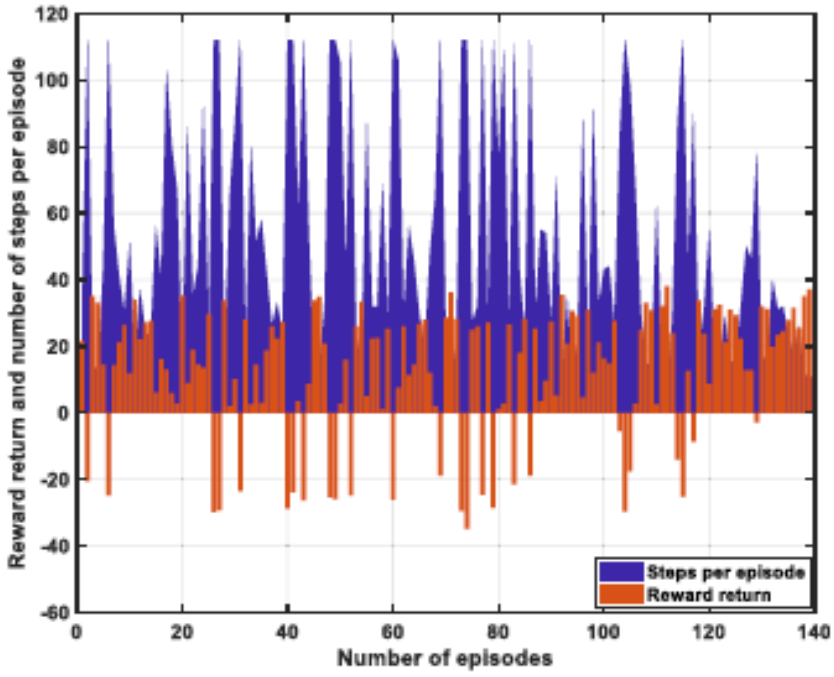

Figure 6-9. Reward returns per number of steps in the second route.

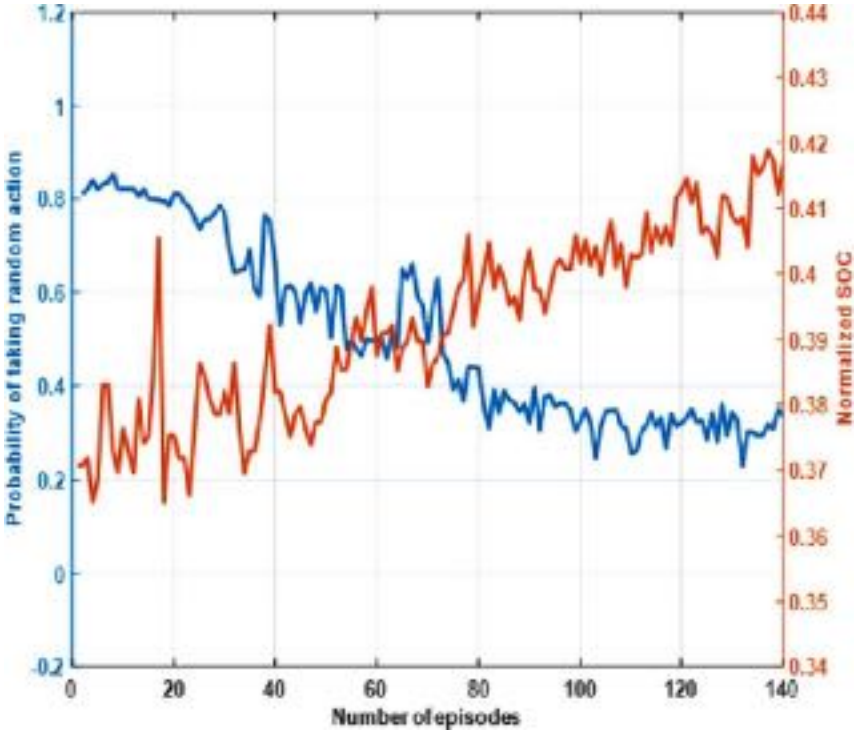

Figure 6-10. SoC vs. probability of taking random actions

6.5 Conclusion

An energy minimization framework was developed in this work, based on reinforcement learning, to optimize the energy consumption of EVs. The main concept of reaching optimal decisions for the EV movement is achieved based in on the deep reinforcement learning. The DDQN was utilized in order to overcome any potential overestimation of Q-values produced from the target network. A carefully integrated but appropriate neural network was designed to provide feedback to the agent as a means of optimizing the travel policy. For the EV's traffic dynamics, we utilized the MCM concept to model each part of the roads in a sequenced manner, based on successive portioning. To verify the developed framework in this work, two experiments were conducted considering two routes of similar length, but at locations that exhibit different geographic characteristics. Both experiments were set at a specific time and date, assuming limited SoC of the EV's battery. The results of the simulations show that the energy consumption based on the

developed framework is considerably lower than when following the main routes developed by Google Maps, for each journey. Additionally, we considered the journey of the EV to be at continuous states, and the transitional probabilities are updated throughout as the agent considers real-time data absorbed into the framework from the Google Maps Platform. It is worth mentioning that a greater number of occurrences would be desirable to produce more accurate results. However, this would have resulted in an extremely long simulation time, possibly extending to days, in addition to which restrictions from Google's API platform occasionally interrupt the simulations.

Chapter 7 Dynamic Real-Time Pricing Structure for Electric Vehicles Charging Considering Optimal Microgrids Energy Management System

7.1 Introduction

Large-scale integration of Electric Vehicles (EVs) is one of the key solutions to meet primary environmental goals, such as reducing greenhouse gases through offering low- or free-emissions alternative transportation to the conventional vehicles [159]. However, this will undoubtedly lead to add extra burden on the electrical infrastructure. In addition to the high-level uncertainty involving the charging activities, the presence of small-scale stochastic renewable energy sources adds complexity to the energy management process and the establishment of fair pricing at the grid level [160, 161, 162]. Such uncertainty leads to either overestimation or underestimation of the real energy prices, as non-EVs owners may have to bear extra financial burdens, although they may be participating effectively in demand-side programs [163, 164].

To the best of our knowledge, no research work has considered a pricing structure that allocates the responsibility of any additional charges that may arise due to EVs charging during peak demand to the EVs owners. This work proposes a dynamic, real-time energy pricing structure adopted with an optimal energy management system to offer a balanced and fair energy consumption and billing. The concept of fairness meant in this work is to allocate the financial responsibility of charging EVs during peak demand hours to their owners only. This scheme is fairer than increasing the energy prices for all consumers, of whom many of them may be participating effectively in demand-side programs that aim to reduce bills via efficient energy consumption during peak hours. Moreover, the developed pricing structure considers various stochastic dynamics of the microgrid operation, such as forecasting day-ahead solar energy generation, projecting EVs connectivity, and mobility models based on Markov Model. It also estimates the microgrids' daily energy consumptions based on

adaptive Artificial Neural Network (ANN), with real-time changes of energy prices based on historical data. The developed multi-agent framework allows every microgrid to broadcast fair energy prices to all of its consumers, including EVs owners who would like to charge their vehicles when the microgrid is congested. The developed pricing structure is managed in a distributed, hierarchal multi-agent framework. Specifically, a central agent assumes full authority in estimating the fair pricing values for a number of microgrids agents per their timely corresponding energy production and consumption. It is worth mentioning that dynamic real-time energy prices are usually determined in accordance with biddings within the wholesale market participants. In this work, incorporating bidding scenarios is out of scope. The utilized retail energy prices data are acquired from the yearly average prices of the Florida Public Service Commission, the agency that is responsible for establishing energy prices rates and regulations for utilities in Florida [140, 141].

The rest of the chapter is organized as follow: Section 7.2 presents the system architecture of the hierarchal multi-agent environment; Section 7.3 presents the stochastic dynamic models of Markov chain-based solar PV forecast model, stochastic EVs connectivity and mobility model, and the adaptive ANN load forecasting model; Section 7.4 presents the developed dynamic, real-time pricing structure for multi-agent hierarchal microgrids operation; Section 7.5 presents stochastic energy management optimization problem; Section 7.6 provides numerical results and analysis on the developed framework; Section 7.7 concludes the work with a final remark.

7.2 System Architecture

Let us consider a microgrid m that belongs to a set of microgrids M such that $m \in \{1,2,\dots,M\}$. Each microgrid is represented with an agent connected to a central agent, as shown in fig. 7.1. The set of microgrids under the same central agent are assumed to be connected electrically. Each microgrid has EVs charging stations, on-site variable-scaled PV

systems, and regular loads to serve, and can receive energy from the main grid only when needed. The microgrids operate in an equal duration time-slotted fashion, with each timeslot is composed of ten timesteps Δt. We propose that the energy price of each timestep is composed of two pricing categories; *retail energy price* that follows time-of-use (ToU) rates and *congested energy price* that is imposed solely on EVs charging events during the times when the microgrid operation reaches a congested level. Furthermore, the retail energy part of the pricing structure is valued by the supervisor operator at the top of the chain for each central agent. On the other hand, we propose that the central agent is responsible for the estimation of the congested part of the energy price for each timeslot and broadcast it to each microgrid based on its supply and demand curve at the timeslot of interest. The total energy generation and demands for each microgrid is modeled as the average power produced $P^{t,m}$ and demand consumed $D^{t,m}$ at each timeslot t and is variable throughout the day such that $t \in T\ \{t_0 - \Delta t, t_0, t_0 + \Delta t, \ldots, T\}$, where $E^{t,m} = P^{t,m}.\Delta t$. Fig. 7.2 illustrates the timely interaction between various components within the developed environment.

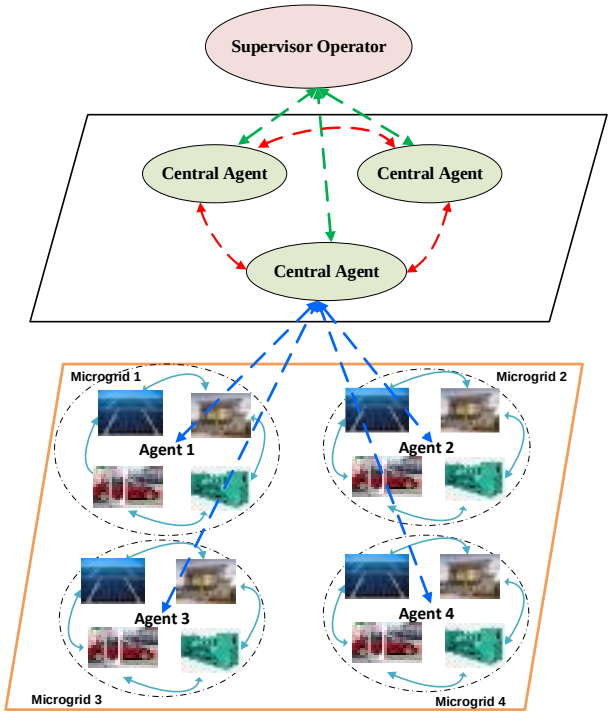

Figure 7-1. The developed hierarchal multi-agent environment

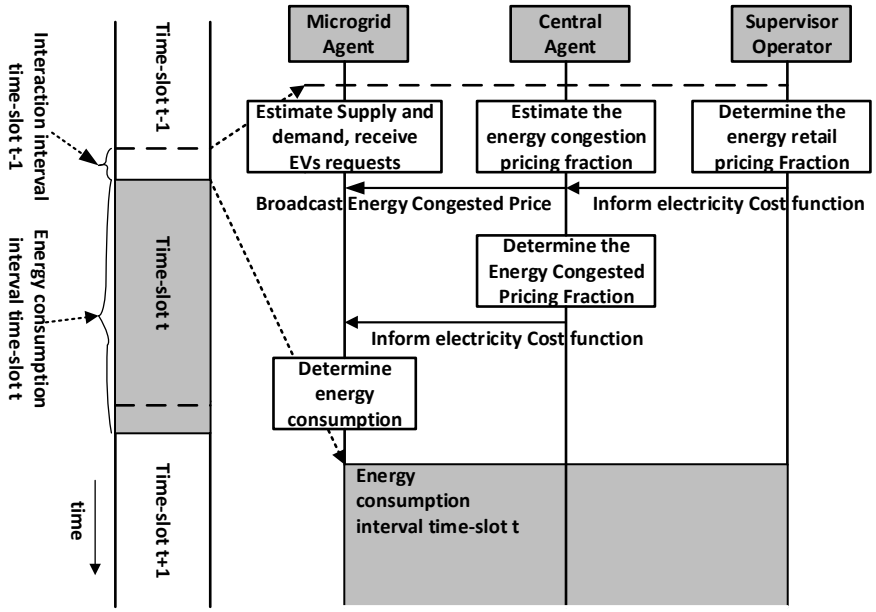

Figure 7-2. Timeline of information exchange in the developed structure.

7.3 Stochastic Model Development

7.4.1 *PV Markov Chain Model*

To achieve our purpose in this chapter, we develop a statistical solar power forecast for parts of the region of South Florida based on a discrete-time Markov chain model. The outcomes of the Markov model are scaled to fit the size of our study of three microgrids and serve as an input to the formulated energy optimization problem discussed in section 7.5 of this chapter. The solar generation level is estimated as a random process, with ρ^t as the transition probability of the forecasted power levels, as follows:

$$P_{ij}^{t} = \wp r[G^{t+1} = G_j \text{ I } G^{\mathrm{t}} = G_i, t] \tag{7.1}$$

Where $\wp r$ is the transitional probability of moving from state i to state j between any two consecutive timesteps Δt within a timeslot t, as shown in fig. 7.3. We define a finite set G that is composed of variables (i.e. G_j and G_i) that resemble the projected solar energy generation for microgrid m, such that $G = \{G_1, G_2, \ldots, G_N\}$, where N is the total number of states, and the variables of this set are arranged in ascending order from the lowest obtained

values in the time horizon to the highest obtained values. To properly procure the transitional probability of the solar power generation based on the available historical data, we count the number of transitions between each two power levels and divide it over the total number of transitions for each timeslot. Specifically, the transition probability ρ_{ij}^{t} between states i and j at timeslot t can be found by the following formula:

$$P_{ij}^{t} = \frac{n_{ij}^{t}}{\sum_{j} n_{ij}^{t}} \text{ s.t. } \sum_{j}^{N} P_{ij}^{t} = 1 \ \forall i, j \tag{7.2}$$

Where n is the number of transitions between every two states observed over the string of historical solar data accounted for timeslot t. After measuring all the transitional probabilities for a timeslot, a transition matrix, sized NxN is established, with each column corresponding to timesteps while rows corresponding to accumulated states transitions and eventually summed up to 1. The transitions between states stop when the data revels zero solar power generation, and the output will be denoted zero for that state. The transition matrix of the estimated solar power generation could be constructed as follows:

$$T_m = \begin{bmatrix} P_{11} & \cdots & P_{1N} \\ \vdots & \ddots & \vdots \\ P_{N1} & \cdots & P_{NN} \end{bmatrix} \tag{7.3}$$

The produced transition matrix is utilized to produce the stationary distribution vector of the discrete-time Markov chain such that $\pi_G^t = \pi_G^t \,.\, T_m^*$, with $\sum \pi_G^t = 1\,,\ s.t.\ \pi_G^t \in [0,1]$. The variable π_G^t is a stationary distribution of a Markov chain and is defined as the probability distribution that remains unvaried in the Markov process as time proceeds forward. In other words, π_G^t is invariant to the transition matrix T_m^*, since it is represented as a row vector whose entries are probabilities that summed up to 1. As a result, the projected solar power generation at each of the timeslot can be found by the multiplication of π_G^t by the transposed vector of the solar power states values G^t, as follows:

$$\overline{P}_{G,total}^{t} = \pi_{G}^{t}.\, G^{t} \tag{7.4}$$

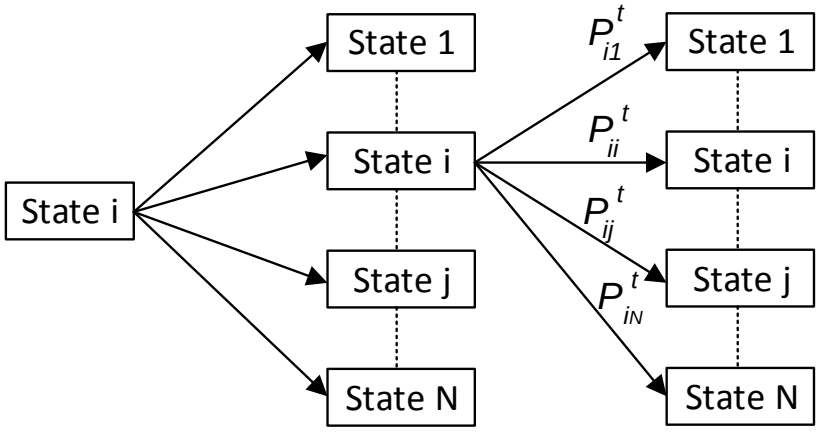

Figure 7-3. Illustration of the construction process for *Tm*

7.4.2 *EV Mobility and Connectivity Model*

Numerous studies have investigated EVs charging strategy and predictive mobility models based on the Markov chain. Some of these studies include a statistical approach developed for assessing the impacts of EVs presence on a defined electricity network service boundary [165]; utilizing geospatial data to estimate spatial loads of EVs on the electrical grid and their relative impact on power quality [166]; and developing a coordinated charging strategy to achieve global optimal energy utilization [167].

We assume that an EV i operates within the boundaries of microgrid m. We utilize a Markov chain model to estimate the EVs connectivity time to the microgrids and corresponding energy levels based on obtained historical traveling data for South Florida [168]. As per our study's scope, we categorize EV i to be either connected to the microgrid for charging purposes (C_t^m=1) with $q(t)$ as its corresponding transitional probability, or not connected (C_t^m=0) with $p(t)$ as corresponding transitional probability. We estimate the

interaction of the EVs with the microgrid, and its available energy, as random processes for each timeslot t by discrete Markov chain as follows:

$$P_{ij,t} = \wp r[C_{t+1} = j \text{ I } C_t = i, t] \ \forall i, j \in \{0,1\}^2 \tag{7.5}$$

Such that

$$P_{1-0,t} = \wp r[C_{t+1} = 0 \text{ I } C_t = 1, t] = p(t) \tag{7.6}$$

$$P_{0-1,t} = \wp r[C_{t+1} = 1 \text{ I } C_t = 0, t] = q(t) \tag{7.7}$$

$$P_{1-1,t} = \wp r[C_{t+1} = 1 \text{ I } C_t = 1, t] = 1 - p(t) \tag{7.8}$$

$$P_{0-0,t} = \wp r[C_{t+1} = 0 \text{ I } C_t = 0, t] = 1 - q(t) \tag{7.9}$$

To properly evaluate the randomness of the EVs charging requests and corresponding level of energy, we estimated the driving patterns of 2,000 vehicles assumed to be EVs [168, 169]. Those vehicles' trips are assumed to be for regular daily work with a roundtrip that starts at 6.30 Am and ends by returning home at 6 Pm, with an average roundtrip distance of 15.8 km [168]. Therefore, we neglect any trips for pleasure or those carried out during the weekends for the simplicity of the study. The temporal distribution of the EVs' connectivity to the microgrids due to their traveling times is shown in fig. 7.4. As per the results, the EVs' plug-out time for the morning trips is centered between the hours 6.45-9 Am with a mean value 7.55 Am and a standard deviation of 0.51 hours. On the other hand, the EVs' plug-in time after the evening drive reaches its peaks in the hours 4.30-6.45 Pm with a mean value of 5.50 Pm and a standard deviation of 0.59 hours.

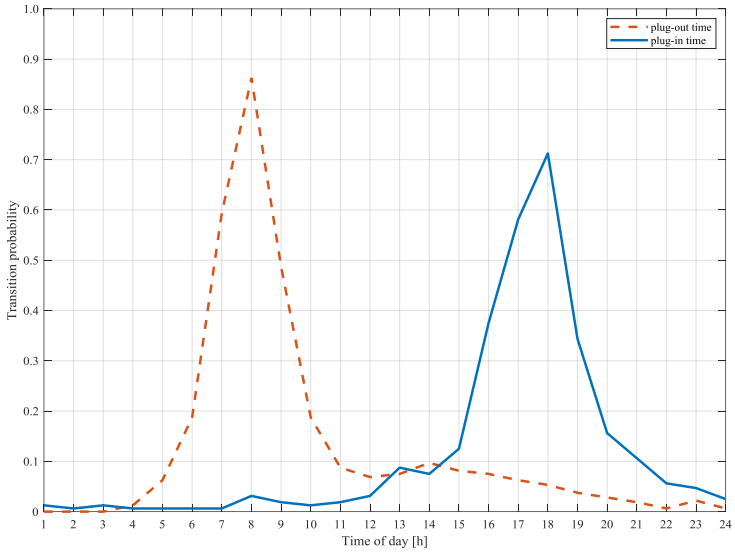

Figure 7-4. Temporal distribution of EVs connection times

We present a strong assumption that all of the EVs start charging process once they conclude their daily trips. In fact, several factors influence the amount of energy of the EV at the beginning of the connection time such as driving distance between every two charging processes, temperature levels in their surroundings [42], type of chargers [170, 171], types of generation and energy prices [172], to name few. For the simplicity of our model, we assume the state of the charge (SoC) during the time of the connection to be between 30% to 80%. We estimate the SoC of an EV i as follows

$$SoC^{t+1,i} = \begin{cases} SoC^{t,i} + P_{EV}^{t,i}\eta\Delta t & if\ charging \\ SoC^{t,i} & else \end{cases} \tag{7.10}$$

Where $P_{EV}^{t,i}$ is the power charging requirement at timeslot t and charging efficiency η. The SoC is a function of the distance d^i of the trip it had taken before timeslot t at an efficiency η_d^i, velocity $v^{t,i}$ and consumption level $\ell^{t-1,i}$, as follows

$$SoC^{t,i} = SoC^{t-1,i} - \ell^{t-1,i}(v^{t,i}, \frac{d^i}{\eta_d^i}) \tag{7.11}$$

During the time of connection, the amount of energy of an EV i at each timeslot is estimated as follows:

$$E_{EV}^{t+1,i} = \begin{cases} E_{EV}^{t,i} + P_{EV}^{t,i}.\Delta t & if\ connected \\ E_{EV}^{t,i} & else \end{cases} \quad (7.12)$$

Upon receiving a request to connect the EV to its infrastructure at time t, the microgrid is going to dispatch the price for the EVs owner, as follows

$$E_{Cost}^{t+1,i} = \begin{cases} E_{cost}^{t,i} + X_p^t P_{cost}^{t,i}.\Delta t & if\ connected \\ E_{cost}^{t,i} & else \end{cases} \quad (7.13)$$

Where X_p^t is a factor that represents the instantaneous charging price issued by the central agent to charge the EVs at microgrid m and is determined for each timeslot based on the congestion level of m. It is composed of two pricing structures E_r and E_c, as we describe in section 7.6 of this work.

7.4.3 *Adaptive ANN Load Forecast Model*

We utilize real peak load data for Miami Dade County in South Florida for the years of 2017 through 2019 to forecast the load demand of 2020 of three hypothetical microgrids located in the same region [140, 173]. To properly overcome the uncertainty level in such a process, we use adaptive Artificial Neural Network (ANN) as a tool to perform the forecasting study. Hourly load curves, which represent electricity utilization during a period of one day, are highly dependent on seasonal changes and on other special days like weekends and holidays. Hence, it is more convenient to categorize data based on these factors and build

a unique artificial neural network for each category. Fig. 7.5 shows the categorization of 2017 peak load data into five categorizes: summer weekends and weekdays, winter weekends and weekdays, and finally holidays (e.g. Independence day, labor day weekends). Fig. 7.6 shows the cumulative peak load of the years 2017, 2018, 2019, which we use as training (2017, 2018) and testing (2019) data for our ANN forecasting model. We use graphical-correlation analysis to ensure proper ANN forecasting process. The selected input variables should acquire specific characteristics; they have to be highly correlated to the output as their level of variation carrys information about output. The developed technique here is to select input variables based on a hybrid graphical/statistical technique. Firstly, we use the graphical representation of the output to predict the peak load. We intuitively suggest some input variables that will have a significant impact on the output, as follows:

- X_1: Peak load of the day before the day to be predicted
- X_2: Peak load of two days before the day to be predicted
- X_3: Peak load of three days before the day to be predicted
- X_4: Peak load of four days before the day to be predicted
- X_5: Average of the peak load of three days before the day to be predicted
- X_6: Average of the peak load of four days before the day to be predicted
- X_7: Difference of the peak load between the day before and three days before the day to be predicted
- X_8: Weekday type, i.e. Mon., Tue., ……, etc.

Then, we utilize statistical inference to estimate the correlation index *r* as follow

$$r = \frac{\sum_m [(T - T_{avg}) x (U - U_{avg})]}{\sum_m (T - T_{avg})^2 x \sum_m (U - U_{avg})^2} \tag{7.14}$$

Where T and U are any two vectors that have the same length, T_{avg} and U_{avg} are their corresponding average values. If the correlation index is high, then we ought to keep it; otherwise, it will be excluded. We then calculate the cross-correlation index between each pair of the remaining variables, and we will exclude any variables with a low correlation to the output. A sample of the correlation analysis is shown in Table 7.1. The correlation index is an index that ranges from -1 to +1. It indicates how much any two vectors are linearly representative to each other, e.g., two vectors that have +1 correlation index are perfect representative for each other.

Table 7-1: Sample results of the graphical-correlation analysis

Correlation Index	Correlation Level
$r_{X8,y}$	-0.1410
$r_{X1,y}$	0.8945
$r_{X2,y}$	0.8133
$r_{X1,X2}$	0.8918

As shown in Table 7.1, the correlation index between the input variable, X_8, and the output is - 0.1410, which is very small. This indicates that using X_8 as an input will mostly lead to insufficient forecasting results and may further lead to more complications and processing time for the ANN model. We also note that the correlation index between X_1 and X_2 with respect to the output is high; 0.8945 and 0.8133, respectively. This means that they both can be used as inputs, yet once we measure their intra-cross correlation, we find them highly correlated. Therefore, we exclude X_2 as it shows less correlation to the output. Based on our analysis, the best input variables after finishing the correlation analysis are found to be X_1, X_5 and X_7. As there might be significant changes in their ranges, we normalize the inputs and output data to avoid any saturation, of the ANN model, as follows

$$T_n = \frac{T}{T_{max}} \tag{7.15}$$

The developed ANN model's topology consists of one input layer with three neurons representing the optimal three inputs, two hidden layers with four neurons in each one, and one output layer with one neuron corresponding to the output results. We used the Levenberg-Marquardt training algorithm [174, 175] with a 0.01 learning rate. The ANN is trained using the data of years 2017, 2018 as training data, while 2019 data is used as testing data to ensure our forecasting model's adequacy before deploying it to forecast data of the year 2020. The ANN model adapts to every new set of data; it predicts the data of a particular day, and when we get the actual data of that day, we adapt the network with the new data so that it get furtherly trained, which improves the quality of the ANN model. This is achieved in MATLAB by coding a statement for training the same network in a loop such that it predicts the next day then takes the actual data of that day for training the network for very few iterations, which is three epochs in this case. Fig. 7.7 presents forecasted results for 120 days of peak load demands in parts of Miami, assumed to be the location of three microgrids in our simulation in this work.

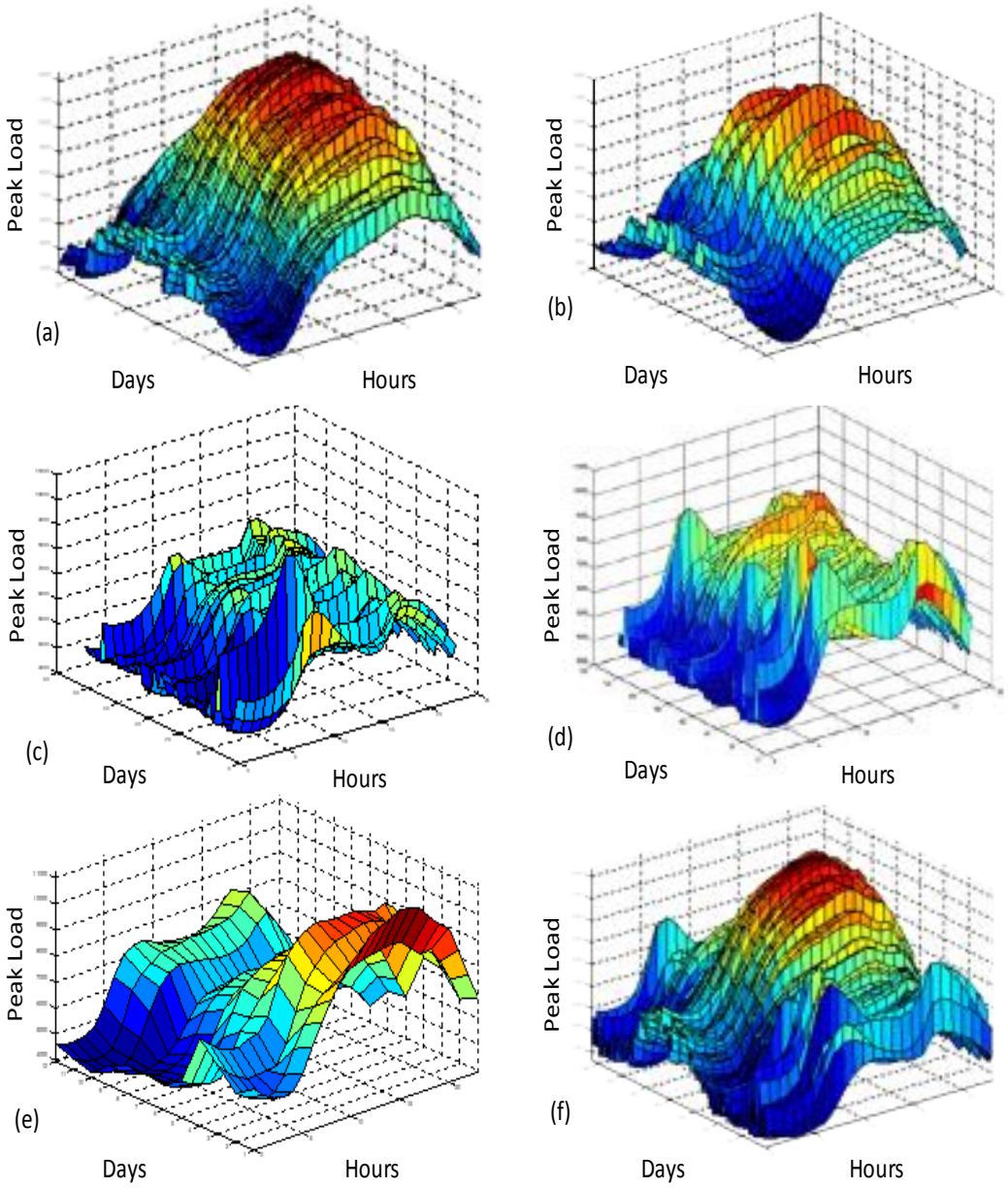

Figure 7-5: Data categorization for 2017 peak load of parts of Miami-Dade County: (a) Summer weekdays, (b) Summer weekends, (c) Winter weekdays data, (d) Winter weekends data, (e) Holidays, (f) 2017 aggregated peak load data.

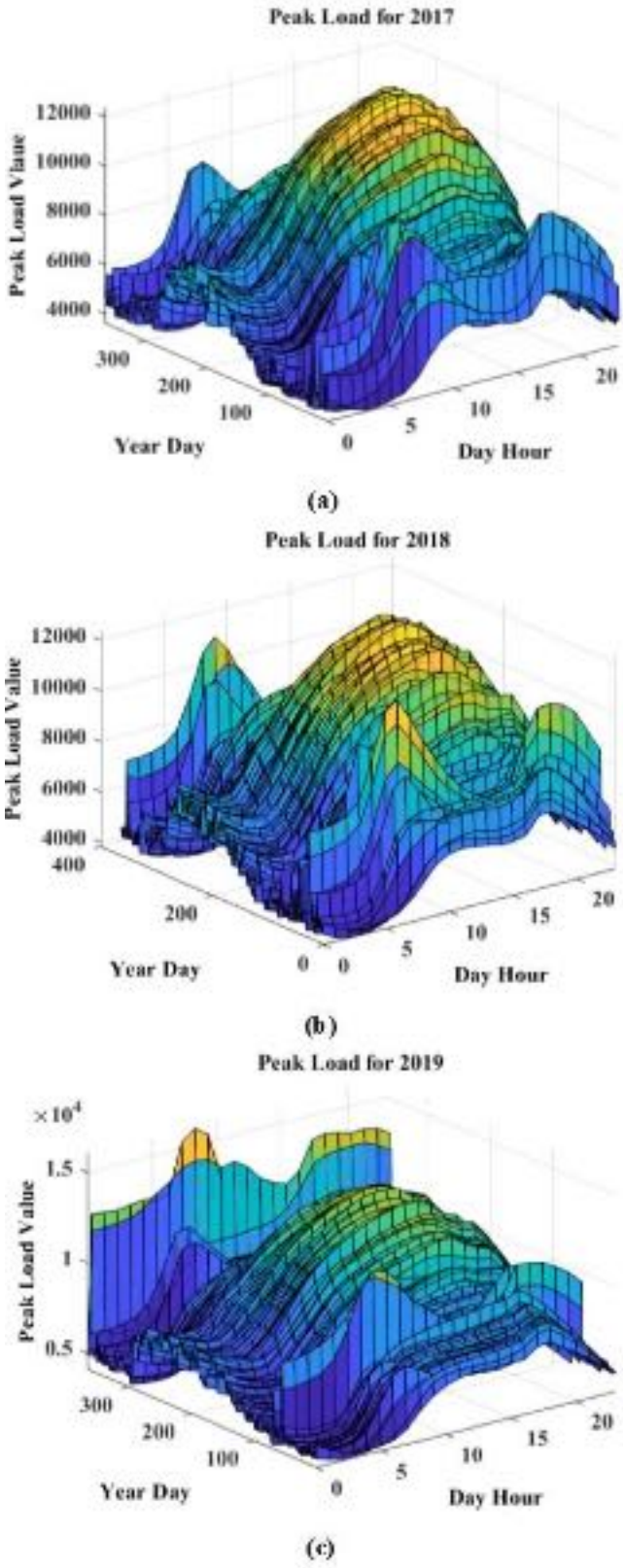

Figure 7-6: Training and testing input data for the ANN model.

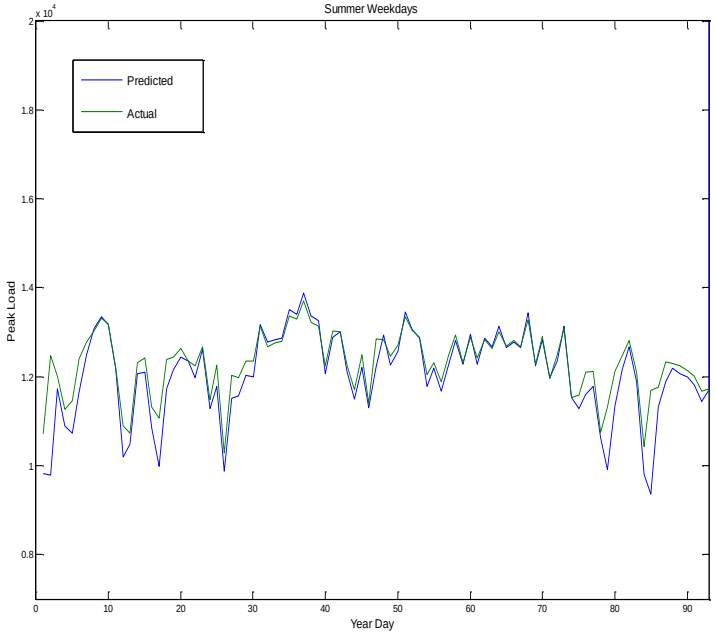

Figure 7-7. 120-days load peak demand forecast results

7.4 Dynamic Real-Time Pricing Structure

The operation of the microgrid is highly constrained with the main objective to meet all demands at the most reasonable price. Therefore, the supply level of the microgrid must be either equal or greater than the total demand D_t

$$S_t \geqslant D_t \tag{7.16}$$

During peak loads, microgrid increases its energy prices to maintain its demand and relieve its extra load for reliability purposes. Consequently, this may sometimes lead to unfair charges to their consumers who are obligated to participate in such a pricing scheme, although they may participate effectively in demand response programs to help in alleviating the grid's congestion. As a result, we categorize the supply level in two parts; supply for regular demand S_r, and supply for congested demand S_c of which we focus our attention to the load of EVs during timeslots that experience higher demands, such that

$$S_t = S_r + S_c \tag{7.17}$$

The demands on each microgrid throughout the time horizon can be represented in vector form, $D = \{D_1^m, D_2^m, \ldots, D_T^m\}$. We assume that every microgrid will has two categories of energy prices; E_r as the regular energy price for energy consumption which follows the retail prices set by the supervisor operator and changes for every timeslot to reflect the ToU rates, including high peak demands price, and E_c as the congested energy price to bill the EVs vehicle owners who decide to charge their vehicles during timeslot where their corresponding microgrid is overloaded. The central agent establishes the latter in accordance with the type and level of generation and demands at each microgrid for every timeslot. We can represent both of the energy pricing factors in vector form as follows:

$$E_r = \{E_r^1, E_r^2, \ldots, E_r^T\} \tag{7.18}$$

$$E_c = \{E_c^1, E_c^2, \ldots, E_c^T\} \tag{7.19}$$

To ensure proper pricing scheme that reflects the real-time dynamics of the microgrid operations, we define a fixed-based rate E_{fixed}^t, that follows ToU rates, to manipulate the real-time retail prices in accordance with the level of demands at each microgrid, as follows:

$$E_r^t = E_{fixed}^t + arc\tan\left(e^{\lambda^t} - c\right) \tag{7.20}$$

Where c is a pre-defined variable set by the supervisor operator, λ^t is a variable that resembles the per timeslot difference between the supply and demand levels, as follows:

$$\lambda^t = (D_c^t + D_r^t) - S_t \tag{7.21}$$

It should be noted from equation (7.20) that e^{λ^t} plays a central role in establishing a curve-oriented pricing scheme that follows changes on the demands on a timely basis and

influence the pricing fractions. Specifically, a decrease of the level of supply will result in the increase of the retail energy price E_r^t at either a fixed or increase in load demands (both EVs and non-EVs). On the contrary, the retail energy prices will witness a reduction in the case of increase supply at either fixed or decrease in load demands. Equation (7.20) represents how the supply-demand curve influence the consumers' energy consumption. Usually, customers tend to consume more energy when the retail price is low, and vice versa when the retail prices are high. The congested price could be assessed based on the following quadratic function:

$$E_c^t = E_r^t + [\alpha(D_c^t)^2 + \beta D_c^t + \gamma] \tag{7.22}$$

Where α, β and γ are predetermined coefficients that could be manipulated based on the discretion of the central agent. As someone may note from equation (7.22), the energy congested price can always be either greater than the retail energy price, giving that at least one of the predefined constants are above zero; or equal to the retail energy price when those coefficients are set to zero. The latter is true only when the grid is at normal operation with no grid's congestion. Therefore, we update equation (7.13) to reflect the charging cost for an EV i at microgrid m, as following:

$$E_{Cost}^i(m) = \begin{cases} E_{cost}^{t,i} + E_r^t P_{cost}^{t,i}.\Delta t & for\ regular\ pricing \\ E_{cost}^{t,i} & else \\ E_{cost}^{t,i} + E_c^t P_{cost}^{t,i}.\Delta t & for\ congested\ pricing \end{cases} \tag{7.23}$$

It should be noted that the grid is set to be congested when a microgrid asks its relative central agent for energy supply from the grid, P_{grid}, at a specific timeslot to be able to provide service to its consumers. We apply the developed dynamic charging model in accordance with results obtained via the optimal energy management optimization, discussed in the next section.

7.5 Optimal Energy Optimization Problem Formulation

The energy optimization problem is solved at the central agent level with a goal for proper optimal EVs charging schedule by the mean of reducing the charging cost at the microgrid while maintaining an optimal energy management process. This is achieved in light of strictly enforced constraints. The energy optimization problem considers the projected day-ahead solar power generation, highly stochastic EVs connection times and estimated level of energy, and forecasted load demand for every timeslot at each of the three microgrids that are assumed to be located in South Florida. The finite-time optimization function is formulated as follows:

$$Min \sum_{t=1}^{T} E_r^t \Delta t \, (C_t P_{EV,t} + \overline{P}_{d,t} - \overline{P}_{PV,t} + P_{grid,t}) \tag{7.24}$$

The state variable in the optimization problem is the amount of energy at each EV at the time of connection, while the decision variable is $\overline{P}_{EV,t}$. We assume that both the energy and rated power of the EV is strictly constrained as follows

$$P_{EV_{min}} \leqslant P_{EV}^t \leqslant P_{EV_{max}} \tag{7.25}$$

$$E_{EV_{min}} \leqslant E_{EV}^t \leqslant E_{EV_{max}} \tag{7.26}$$

For every EV i connected at each timeslot t, the SoC is between the minimum allowed charging level b_{min}^i of the full battery capacity

$$b_{min}^i SoC_{max}^{t,i} \leqslant SoC^t \leqslant SoC_{max}^{t,i} \tag{7.27}$$

The amount of power from the upstream grid is restricted:

$$-P_{grid_{max}} \leqslant P_{grid,t} \tag{7.28}$$

$$P_{grid_{max}} \geqslant 0 \tag{7.29}$$

Table 7-2: Simulation model parameters

Parameter Description	**Value**
Microgrid area	4 mi x 3 mi
Number of microgrids	3
Total number of EVs	2,000
Minimum energy level & SoC	15 kWh, 30%
Maximum energy level & SoC	50 kWh, 80%
Average retail price over 24 hr	10.75 cents/kWh
Charging eff ratio η	0.85
Timeslot, duration per each	96 T, 900 seconds

7.6 Results and Discussions

In this work, we data from the Florida Department of Transportation [168], historical solar radiation database [141, 176, 177], and load demand forecast [140, 173] for parts of South Florida. Table 2 lists the parameters we used in the simulation process. All the simulations are performed on a PC with an i7 Intel Core, 3 GHz, 16 GB RAM of internal memory with a 2018-b MATLAB version at the Energy Systems Research Laboratories of the Florida International University. We solved the optimization problem using a modified MATLAB optimization toolbox [178], with the execution period for the solar power projection of 24-hour ahead. The day's cycle in the simulation is estimated for every 15 minutes (T= 96 timeslots, each slot is 900 seconds). Fig.7.8 shows the projected solar power generation compared with the measured data of solar power profiles for parts of South Florida based on the Markov model for a randomly selected day with a window size of 320 days. The historical database's solar energy values may not match precisely the corresponding values of the

projected solar energy generation set, G. Therefore, we utilized a linear interpolation algorithm to estimate the solar set's values, which appears within the proximity range to the real database values. Fig. 7.9 shows the simulation results when we scale the results into three microgrids in parts of Miami Dade County. For E_r^t, we derived its price based on the average ToU energy rates established by [23, 24]. We assumed that each microgrid estimates its supply and demand for every 90 seconds interval as a defined timestep, where each timeslot is composed of 10 timesteps. The corresponding changes in the real-time energy prices for the microgrids are presented in fig 7.10. The upper curve shows the retail energy prices during peak timeslot without large-scale EVs charging, while the lower curve resembles the total energy prices that include the congested energy price as a result of large-scale EVs charging. It is clearly shown that without the implementation of the developed pricing mechanism, the total energy price surpasses high levels up to 14.8 ¢$/kwh$ for all customers during times of demands peak. We estimated the changes in the prices for each of the three microgrids from equations (7.20) through (7.23). We assume that the central agent is responsible for establishing the values of the pre-determined coefficients, which we set in the simulation as $\alpha = 0.01, \beta = \gamma = 0.0001$. Fig. 7.11 illustrates the price difference between the two curves presented in fig. 7.10, which coincides with the time of high peak demands D_c^t when there are requests to charge EVs per the model presented in section 7.3 of this chapter. We can see that the price difference is always positive and follow the changes in the supply-demand curve for each microgrid solely. We propose that this price difference should be billed to the EVs owners who charge their vehicles during the timeslots of peak demands.

To validate the effectiveness of our developed pricing structure, we compare the results obtained in our simulation after applying the developed pricing with previously published pricing policies to reduce energy billing at peak times. Specifically, the results of Usage-based dynamic pricing (UDP) [179], Quadratic-based cost function (QCF) [180], and

Distributed Demand Response (DDR) [91] are drawn in comparison with our developed pricing policy, as shown in fig. 7.12. The pricing structure, coupled with the stochastic energy management formulation, yield lower real-time retail energy pricing rates during congested grid operation. We note that our fair pricing structure is reached through reasonable rates and that only EVs owners who charge their vehicles during timeslots when their microgrid is severely overloaded will incur the extra burden. To us, such a pricing scheme is fairer than distributing the rate on all consumers who may be collaborating with the utility to reduce the demands in specific hours to balance their energy bills. The stochastic energy management framework has helped reduce the cost of system operation via accurate incorporation of PV energy into the supply curves of the microgrids.

7.7 Conclusion

This work proposes a dynamic, real-time pricing structure to equitably distribute and reflect energy prices when the microgrids are congested. The pricing mechanism operates in a hierarchal multi-agent framework with an optimal energy management system to reduce real-time retail energy prices. The inputs to this stochastic energy optimization problem include solar energy generation, EVs connectivity, corresponding energy availability, and load demand forecast models, all performed based on historical data that belong to parts of South Florida based on discrete-time Markov chain and adaptive ANN models, respectively. Through simulations, we presented the case that our developed pricing mechanism performs better than some of the previously published centralized approaches. We believe this is achieved by allotting the congested price scheme for EVs owners to assume responsibility for charging during congested timeslots, while the microgrid operates on an optimized energy management scheme to reduce overall cost. In other words, consumers will not have to bear responsibility for any potential increase in demands due to large-scale EVs charging requests during congested energy conditions.

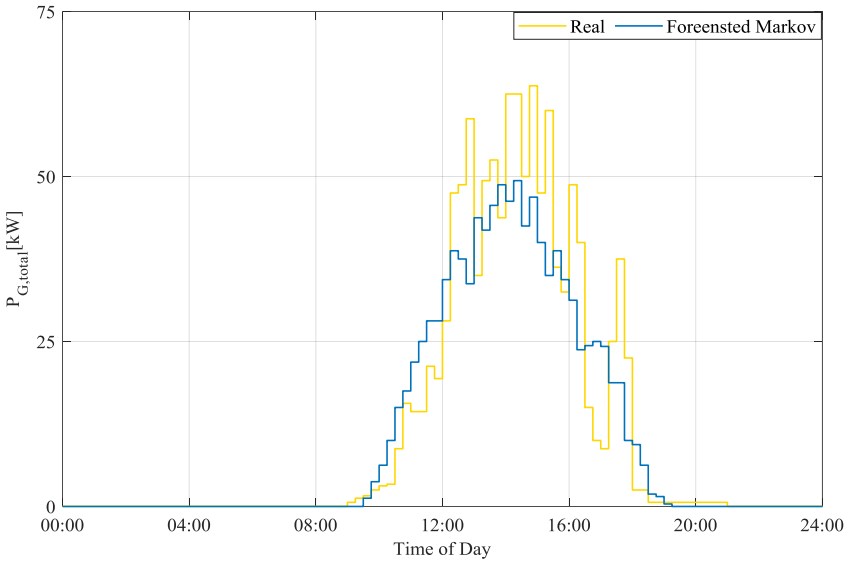

Figure 7-8. Real vs Markov chain-based forecasted solar power

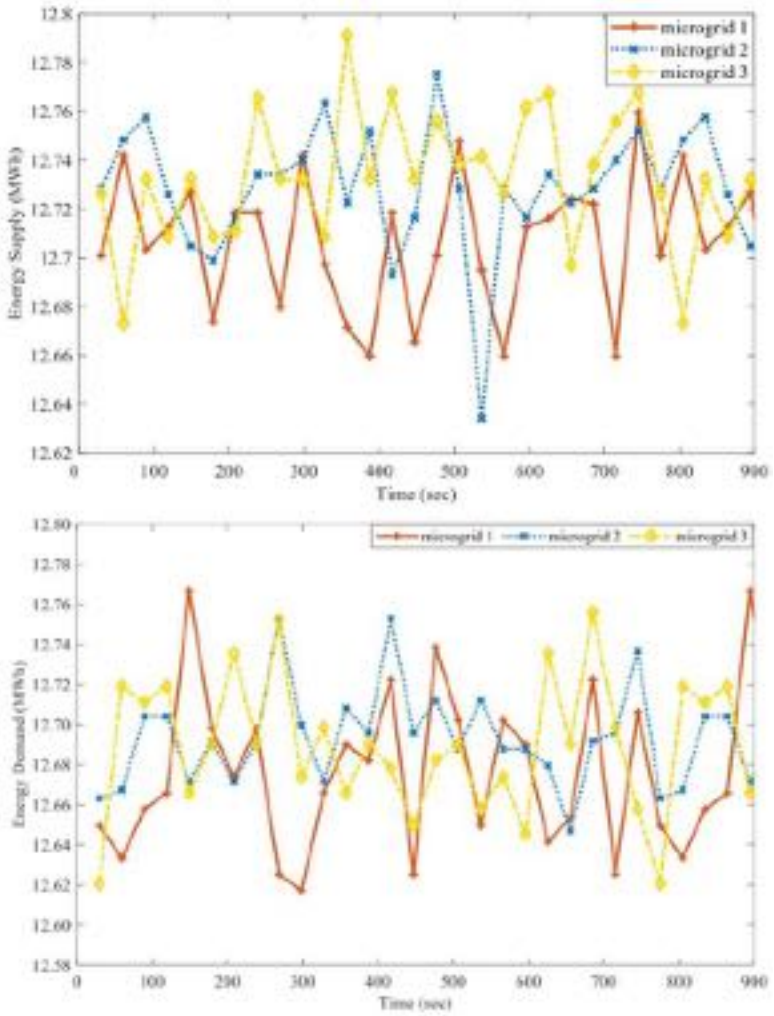

Figure 7-9: Supply (upper) and demand (lower) for three microgrids in Miami-Dade County, South Florida

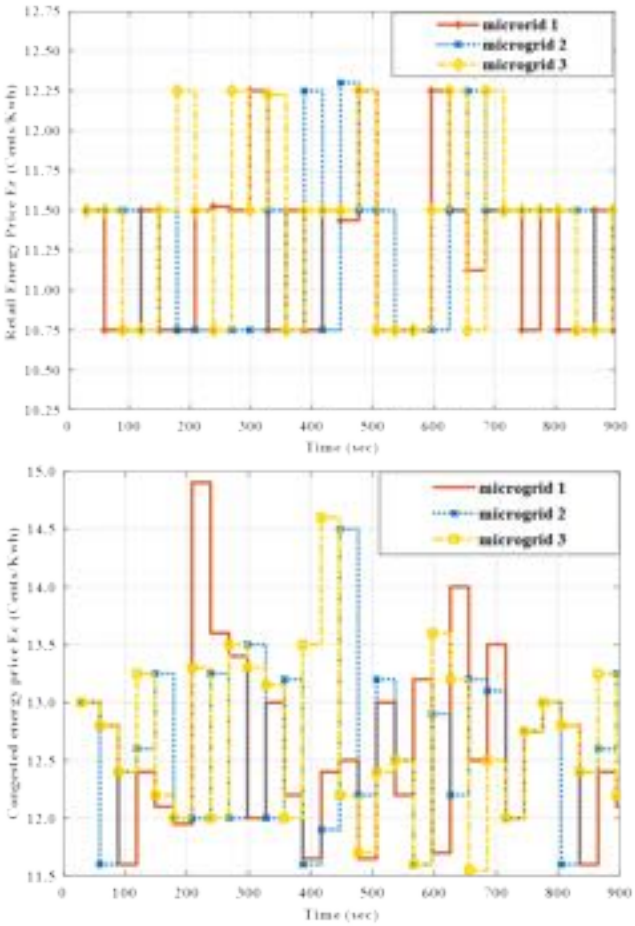

Figure 7-10. Results for retail pricing (upper) and congested pricing (lower)

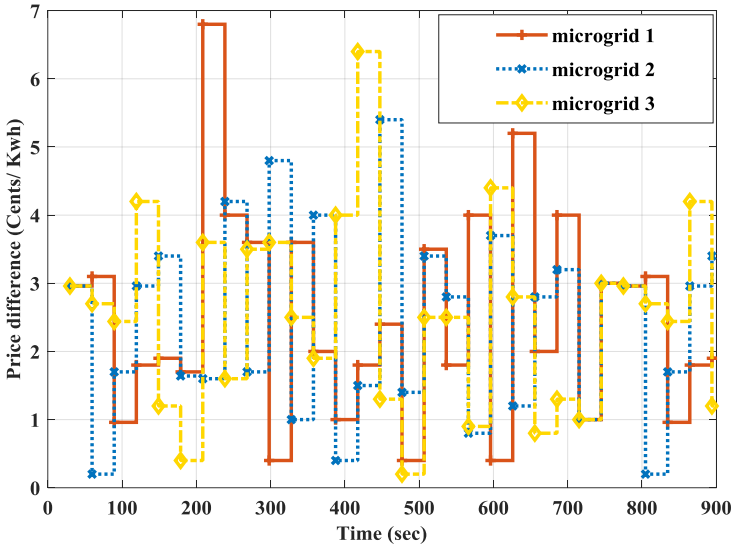

Fig. 7.11. Price difference between the two pricing fractions per each time step

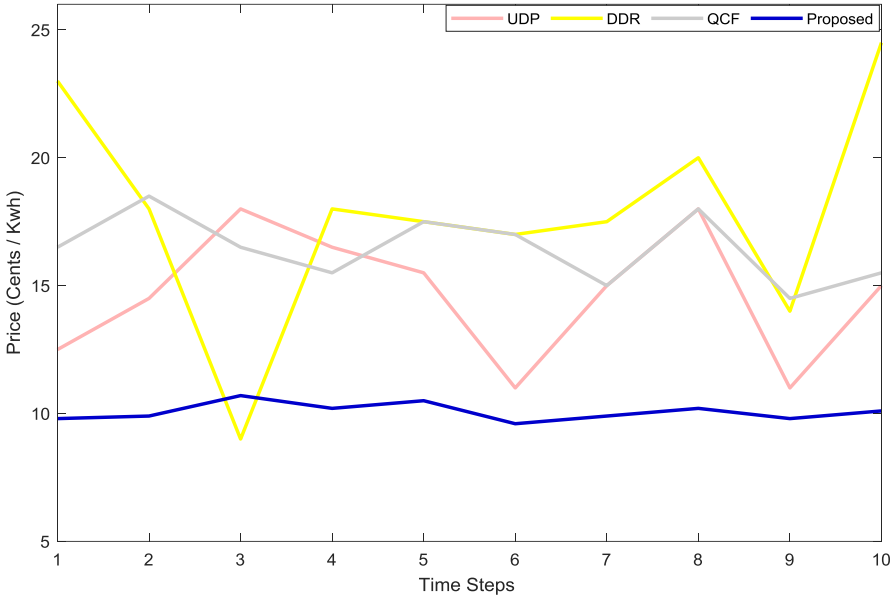

Figure 7-11: Comparison of the results of developed pricing structure versus previously published work

Chapter 8 A Two-Stage Optimization Strategy for Solving the Voltage-Var Problem Considering High Penetration of Plug-in Electric Vehicles to Unbalanced Distribution Networks

8.1 Introduction

Plug-in Electric vehicles (PEVs) offer a great opportunity for mankind to reduce greenhouse gas by offering low- or free-emissions alternative transportation to conventional vehicles. Moreover, power utilities can exploit the large-scale integration of PEVs to allow real-time management and control in the power distribution networks (PDNs) and microgrids via providing voltage, frequency, and load support. However, amidst the many merits of the PEVs, its increased penetration on a yearly basis may adversely influence the power grid's overall control and operation. Specifically, The proliferation of PEVs with uncoordinated charging and discharging may lead to significant damages to the grid's apparatus and introduce operational difficulties to overcome its charging demands, especially those during peak hours. Therefore, a necessity for proper coordination and control of the power grid is the meticulous incorporation of the PEVs scheduling in a way to make it contribute efficiently to the grid's operation; their exponential growth could also be seen as a golden opportunity to get rid of operational deficiencies and extend the lifespan of voltage and reactive power support devices. This is true, giving the detrimental impacts of renewable energy sources' intermittency on the operation of conventional voltage and reactive power compensation devices such as the on-line tap changing transformer (OLTC) and shunt capacitor banks (CBs). Additionally, uncoordinated large-scale penetration of PEVs could significantly stress these devices and, therefore, contribute to unnecessarily extensive tap operations [93]. As a result, accounting for PEVs into the voltage-var optimization (VVO) of the PDNs should be recognized as a priority.

Regularly, the VVO problem deploys OLTC and voltage regulators (VRs) to regulate the voltage level across the PDNs, while considering CBs and other reactive power compensation devices (RPCs) such as dispersed energy sources (i.e. photovoltaic systems (PVs) inverter) for VAR support. Ideally, the problem of VVO has been investigated within the context of centralized control schemes, requiring massive communication infrastructure to promptly deal with thousands of equipment. In [94], the authors utilized a genetic algorithm (GA) to solve multiobjective voltage regulation control to reduce the system's losses and voltage fluctuations. Nevertheless, voltage control from generation resources was not incorporated into their formulation. Conversely, the authors of [95] developed an optimal voltage-var control scheme with the incorporation of large-scale distributed generators (DGs) to ensure adequate voltage regulation on the distribution level. However, their control scheme neglected the impact of OLTC and the prospect of active power curtailment (APC) on the voltage regulation problem. Besides, reference [96] presented an optimal voltage-var coordination scheme that considers day-ahead PV active and reactive power production to reduce OLTC tap operation, yet without including the effect of APC in the utilization of PV voltage support schemes. Moreover, one potential concern is that their day-ahead forecasting methodology could be adversely influenced by common margin errors usually inherited in the traditional forecasting techniques. Additionally, PEVs were not accounted for in their VVO control scheme. In fact, literature that reports the utilization of PEVs in the VVO problem is still limited. Reference [97] has indeed considered PEVs in the distribution network's voltage regulation process, yet only in a centralized manner. It is clear that only a limited amount of literature has considered solving the VVO problem on a decentralized scale, with few considering the integration of PEVs. Therefore, more research should be performed to fill the gap in this area. Generally, solving for the VVO within the context of a decentralized framework requires some sort of decomposition methodologies to divide the distribution system into several subgroups. Furthermore, the accuracy of the decomposition

technique plays a pivotal role in the realistic modeling of the information exchange among the divided subgroups of the network topology. Reference [98] presented a valuable study on the tradeoff of implementing various algorithms on the convergence speed for solving problems related to clustering-based decentralized optimization. The study indicates that strategies of low-coupling degrees may lead to an insignificant impact of one cluster over its neighboring subgroups. This emphasizes the potentiality of obtaining results that inaccurately represent a solution for highly complex and dynamical systems like the PDNs. Therefore, careful consideration must be advocated while designing decomposition methodologies that model efficiently the steady-state operation of the electrical systems. Recent literature has investigated various clustering methodologies applied to the power grids. References [99, 100] developed decomposing the large-scale power grids into subgroups based on spectral clustering. Specifically, reference [99] developed operationally constrained spectral clustering to identify intentional controlled partitioning of wide areas of the power network to defend against cascading failures. The developed methodology allows system operators to constrain, without disconnection, branches against minimal power flow disruptions. The developed islanding technique was tested to reduce power grids that have the size of the United Kingdom's power network. Similarly, reference [100] defined the internal connectivity of the system's nodes via an undirected edge-weighted graph based on spectral clustering and developed solving the VVO problem with respect to the quality factor of each obtained partition, yet with no account for PEVs' integration. Other methodologies aimed for solving the VVO problem in a decentralized manner without incorporating the decomposition of the PDNs into subgroups. Reference [101] developed agent-based for reactive power compensation via DGs to regulate the voltage levels in a distributed manner with lower communication capabilities. However, no consideration of the active role of OLTC and VRs has been identified which does not provide the technical option for voltage regulation if reactive power outputs of the incorporated DGs are reached. On the other hand, reference

[102] developed a voltage regulation scheme to account for parallel distribution networks with a strong assumption that VVO is performed considering only the OLTC device. While such assumption may yield valid results, it is a not recommended practice as it will increase operational stress on the OLTC and potentially forfeit its economical lifespan. Additionally, the solution might be infeasible giving that voltage boundaries of larger distribution systems may exceed the capability of the OLTC to solve the problem efficiently.

Generally speaking, an extensive amount of research is needed to assess the capability of solving the VVO problem, considering the coordination of stochastic integration of the PEVs (incorporating economic compensation for PEVs' energy demand curtailment) as well as the careful implementation of active power curtailment (APC) on the unbalanced operation of the PDNs. Moreover, utilizing detailed and organized intelligent optimization techniques that consider electrical-coupling degrees to accurately reflect the updated operational status of the PDNs are still lacking more studies for proper investigation. In this work, a two-stage optimization strategy is developed to reach an optimal solution for the VVO that satisfies economic gain while meeting various operational constraints. That is to say, this work recognizes the interaction of various elements that influence the optimal decision of the VVO problem such as stochastic integration of PEVs to meet all of its demands economically, utilization of the APC and RPC capability of the PV inverters in an efficient way, as well as consideration to relax the nonlinearity of CBs, VRs, and OLTCs devices to extend their lifespan.

The rest of the chapter is organized as follows: Section 8.2 presents the two-stage optimization strategy to tackle the VVO problem in a decomposed PDN; section 8.3 presents the partitioning process of the PDNs into smaller subgroups via the developed CBDPSO algorithm; section 8.4 presents MILP formulation to solve the VVO economically; section

8.5 presents case scenarios and discusses obtained results of applying the developed optimization strategy on the decomposed PDN; section 8.6 concludes with final remarks.

8.2 The Two-Stage Optimization Problem Formulation

In this work, the first stage in the developed optimization strategy aims to decompose the PDN into several partitions per its operational status in an optimal manner. Such decomposition is achieved considering the voltage level sensitivity values with respect to the amount of active and reactive power flow in the system, respectively. The intention of reaching optimal partitioning lays in the desire to solve the VVO problem for carefully identified "smaller networks" in a decentralized framework, rather than performing it for a whole unified distribution network. The mathematical model behind this decomposition is based on the concept of the community-detection algorithm, first developed in [109], and later expanded in [110]. Measured by what is known as the modularity index, the virtue of the community-based algorithm lays in its robustness and strength in performing cross-check on the quality of the nodal partitioning of a complex network. In this work, we utilize this index to implement partitioning of the PDNs via the estimation of the electrical-coupling degree among any connected nodes in the systems. This degree of coupling realizes the instantaneous change of voltage levels across the system due to active and reactive power activities, whether caused by charging and discharging events or by non-EVs load demands. To ensure reaching optimal partitioning results, this work develops an intelligent optimization technique based on the particle swarm optimization (PSO) that aims to produce optimal partitioning, taking into consideration the modularity index function as its fitness function. The developed intelligent technique is identified as the community-based-detection particle swarm optimization (CBDPSO) algorithm, which is described in detail in part B of the next section of this work. Once an optimal partition has been developed for the PDN, the first stage optimization ends to allow calculation for the VVO problem considering each

partition's voltage capabilities and operational needs, which is presented as the second stage of our developed work. The second stage optimization strategy in this work proposes MILP to solve the objective function that aims to minimize the operation costs of the PDN in the context of the VVO problem. This is achieved at the beginning of each timeslot at this stage based on the steady-state operational status of the PDN devices (i.e. active power production and demand status, CBs and OLTC status …etc) as well as on the updated PEVs scheduling based on stochastic arrival, departure and requested energy. The optimal charging and discharging scheduling of the PEVs is estimated for each timeslot based on modified model inspired by the study presented in references [181, 182]. Furthermore, the updated scheduling of the PEVs considers the unbalanced nature of the three phase PDN. Each group of PEVs are going to be scheduled based on the unbalanced load flow per each phase to avoid any potential voltage violation on the grid. To reduce computational complexities, decision variables for timeslot $t-1$ are relaxed, enabling the integrality of the decision variables for timeslot t based on the updated PEVs arrival, departure, current and requested SoC. Eventually, a coordination plan that satisfies the operational constraints of each partition is dispatched with required level of energy from the grid, energy from the PV system, control action of RPC devices (i.e. number of modules to be connected from CBs, OLTC tap position), and energy demand curtailment of PEVs, if any. The decomposition of the PDN into several autonomous partitions will significantly reduce the computational requirements and complexities by performing the optimization problem on a smaller scale, rather than for a whole unified network. Consideration such as of fixing the control variables of the previous timeslots or decomposing the network into small fractions will not impact the 24-hour operation of the PDN.

It is worth mentioning that the first stage optimization process is performed in a time-ahead fashion that is set based on the discretion of the system operator. On the other hand, the

second stage optimization is performed considering real-time platform to account for steady-state operation of the PDN. Fig.8.1 presents an illustration of the timely combination of the two stages. It is assumed that for a timeslot in the first stage optimization that ranges from T_o to T_1, smaller timeslots t_c to t_f represent the timely limits to perform the second stage optimization. The size of the timeslots of the second optimization stage is assumed to be 96 timeslots in every 24-hour horizon, with each timeslot equal to 15 minutes in duration.

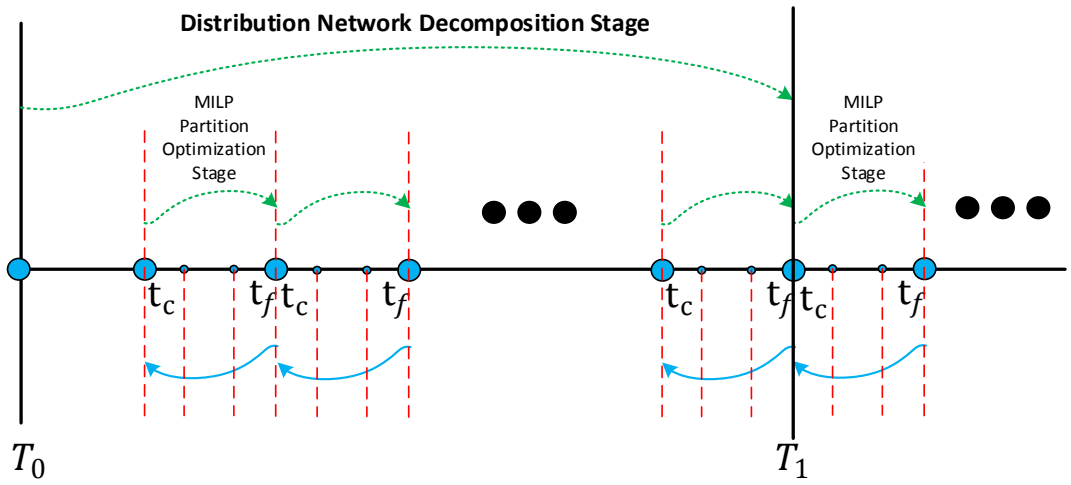

Figure 8-1. Illustration of the timely interaction of the two-stage optimization strategy

8.3 The Distribution System Decomposition Based on Community-Based Detection Algorithm

8.4.1 *Community-Based Partition Detection Index*

As mentioned in the previous section, the decomposition of the PDN into smaller partitions is based on the concept of community-based detection algorithm presented in [109, 110]. The idea is to establish a categorization process that considers the degree of electrical coupling among the nodes and assesses if they are qualified to form a community of their

own with other nearby nodes, or to join an already established community made by other neighboring nodes. The virtue of such modeling methodology lies in the ability to decompose the distribution feeder and identify the weakest nodes on the system, due to both the charging/discharging activities as well as the other non-PEVs load consumption. For two nodes $i\ and\ j$, the modularity index, M, can be expressed as

$$M = \frac{1}{2w}\sum_{i}\sum_{j}\ (A_{ij}^{t} - \frac{\ell_i \ell_j}{2w}).\ \delta(i,j) \tag{8.1}$$

where A_{ij}^{t} is matrix with entries that represent the correspondent weighted values of either voltage-active power or voltage-reactive power sensitivity values at timeslot t, respectively. Furthermore, A_{ij}^{t} is established for any two connected nodes at the feeder and is described as follows:

$$A_{ij}^{t} = 1 - \frac{ED_{ij}^{t}}{\underset{u,v\in N}{max}\ ED_{uv}^{t}} \tag{8.2}$$

With

$$\delta(i,j)\ = \begin{cases} 1, & if\ there\ is\ a\ link\ the\ nodes \\ 0, & otherwise \end{cases} \tag{8.3}$$

Where ED_{ij}^{t} refers to electrical distance between nodes $i\ and\ j$ at a timeslot t, a coupling degree measure that estimates the electrical connection strength between any two nodes; ℓ_i and ℓ_j represents the aggregated weighted values of all nodes connected to nodes $i\ and\ j$; $\delta(i,j)$ represents a connection factor that is labeled zero if there is no connection between nodes $i\ and\ j$, and assumed unity otherwise; and w is the cumulative edge weight of all nodes. The incremental changes in the values of active power (ΔP), reactive power ($\Delta\theta$), voltage (ΔV) and phase angle ($\Delta\delta$) at the distribution feeder during time slot t could be represented as follows:

$$\begin{bmatrix}\Delta\delta\\ \Delta V\end{bmatrix} = \begin{bmatrix}S_{\delta P} & S_{\delta\theta}\\ S_{VP} & S_{VQ}\end{bmatrix}\begin{bmatrix}\Delta P\\ \Delta\theta\end{bmatrix} \tag{8.4}$$

the entries of the matrix in (4) are filled with values that represent the sensitivity values of phase angel in regard with active power level ($S_{\delta P}$), sensitivity value of the phase angle in regard with reactive power level ($S_{\delta Q}$), sensitivity value of the voltage in regard with active power level (S_{VP}), and sensitivity value of the voltage in regard with reactive power level (S_{VQ}), respectively. In this work, the decomposition of the PDN into well-defined partitions is achieved in a time-ahead fashion based on the instantaneous values of S_{VP} and S_{VQ}. We define the electrical distance between any two nodes by the voltage sensitivity levels at node i with respect to the changes of active power, $ED_{VP}^{ij,t}$, and reactive power, $ED_{VQ}^{ij,t}$, at the neighboring nodes j, as follows:

$$ED_{VP}^{ij,t} = S_{VP}^{ii,t} + S_{VP}^{jj,t} - (S_{VP}^{ij,t} + S_{VP}^{ji,t}) \tag{8.5}$$

$$ED_{VQ}^{ij,t} = S_{VQ}^{ii,t} + S_{VQ}^{jj,t} - (S_{VQ}^{ij,t} + S_{VQ}^{ji,t}) \tag{8.6}$$

Where $S_{VP}^{ij,t}$ and $S_{VQ}^{ij,t}$ represents the sensitivity levels of voltage magnitude at node i as a result of active power activities (i.e. PEVs activities, PVs generation or curtailment …etc), and reactive power activities (i.e. capacitor bank support) at nodes j. It is worth mentioning that the closer the electrical distance between any two nodes, the more mutual sensitivity values they will share. Since $ED_{VP}^{ij,t}$ is proportionally related to $ED_{VQ}^{ij,t}$, the weighted electrical distance at a given timeslot could be formulated as follows:

$$ED_{ij}^{t} = \psi\mathcal{S}_{R}^{VP} + (1-\psi)\mathcal{S}_{R}^{VQ} \tag{8.7}$$

To properly decompose the distribution feeder, an improved index that is estimated based on the local voltage and reactive power levels is utilized to ensure optimal partitioning. It is worth mentioning that the higher the index assessed by equation (8.1), the more accurate the partitioning is with respect to the sensitivity values. Therefore, for any timeslot t, the voltage capability levels within a partitioning subgroup R is assessed according to an average sensitivity values for both active power, $\mathcal{S}_R^{VP}$, and reactive power, $\mathcal{S}_R^{VQ}$, as follows:

$$\mathcal{S}_R^{VQ} = avg\,[\sum_{i,j\in R} ED_{VQ}^{ij,t}] \tag{8.8}$$

$$\mathcal{S}_R^{VP} = avg\,[\sum_{i,j\in R} ED_{VP}^{ij,t}] \tag{8.9}$$

For instance, the higher value for $\mathcal{S}_R^{VQ}$at a timeslot t, the more sensitive the voltage level at partition subgroup R for any reactive power support, and vice versa. Accordingly, the voltage capability of partition R, denoted Γ_R, could be updated based on the status-quo of the active power curtailment (APC) and reactive power support to solve the intra-partition voltage level problems as follows:

$$\Gamma_R = min\{R_{VQ}^t + R_{VP}^t, 1\} \tag{8.10}$$

Where R_{VQ}^t refers to the voltage regulation-freedom degree with respect to RPC devices at node j , defined as follows:

$$R_{VQ}^t = \begin{cases} 1 \;\; if \;\; \Delta V_i \leqslant \sum_{j\in R} S_{VQ}^{ij,t} * RPC_j^t \\ \dfrac{S_{VQ}^{ij,t} * RPC_j^t}{\Delta V_i} \;\; ,, otherwise \end{cases} \tag{8.11}$$

While R_{VP}^{t} refers to the voltage regulation-freedom degree with respect to active power curtailment (APC), defined as follows:

$$R_{VP}^{t} = \begin{cases} 1 \;\; if \; \Delta V_i \leqslant \sum_{j \in R} S_{VP}^{ij,t} * APC_j^t \\ \dfrac{S_{VP}^{ij,t} * APC_j^t}{\Delta V_i} \qquad\qquad\qquad\qquad , otherwise \end{cases} \tag{8.12}$$

In equations (8.11) and (8.12), ΔV_i represents the gradual voltage change for node i, and is filled with zero when there is no change of the voltage level from the previous timeslot; APC_j^t and RPC_j^t represent the maximum allowed active power curtailment and reactive power compensation at node j during timeslot t with respect to voltage magnitude at node i. The estimation of the optimality of the decomposition is mainly achieved based on the quantification of the electrical coupling levels. Such estimation is achieved by the modularity index value that is influenced by the average sensitivity values presented in eqs (8) and (9) as well as the voltage regulation degrees (10)~(12). Once the distribution feeder is divided into *N* partitions, then the improved index could be estimated as follows:

$$M_{improved} = M - \frac{1}{N} \sum_{R=1}^{N} (\Gamma_R + S_R^{VQ} + S_R^{VP}) \tag{8.13}$$

8.4.2 *Community-Based Detection Particle Swarm Optimization (CBDPSO) Algorithm*

This section utilizes PSO as a searching strategy to reach the optimal partitioning of the PDN with respect with the highest obtained modularity index value. The search for an optimal decomposition of a network can be consider as an optimization problem [183], and therefore PSO, a powerful nature-inspired stochastic optimization technique, is seen by the

authors as an ideal methodology to be applied to acquire the optimal decomposition of the PDN based on the voltage sensitivity values as discussed in part A of this section.

The main concept of the PSO is to treat a group of objects as particles that fly only within a searching space. Each of the particles of interest acquires a vector representation for its relative position and velocity. The position vector produces a candidate solution to the applied problem, while the velocity vector indicates the tolerance of the position vector for potential changes. The process is repeated iteratively to update the velocity vector and current position of the solution particles with respect to other neighboring particles, until a local and global optimum is achieved. To place this searching mechanism within the context of the PDN's partitioning process, the PSO utilizes information that represent the distribution network topology. Thus, the searching strategy updates the particle's position and velocity with respect to the network linkage information. Denoting the population size as *Pop*; the velocity, $\mathcal{V}E_i$, and position, $\mathcal{X}E_i$, of a particle ith could be established as follows:

$$\mathcal{V}E_i(t+1) = \mathcal{V}E_i(t) + c_1 r_1\big(Pbest - \mathcal{X}E_i(t)\big) + c_2 r_2\big(Gbest - \mathcal{X}E_i(t)\big) \tag{8.14}$$

$$\mathcal{X}E_i(t+1) = \mathcal{X}E_i(t) + \mathcal{V}E_i(t+1) \tag{8.15}$$

where $i = [1,2,\ldots,Pop]$; r_1 and r_2 represent random numbers that belong between [0.1]; c_1 and c_2 represent user-specified cognitive and social learning coefficients, while *Pbest* and *Gbest* represent the ith particle best local and global positions such that:

$$Pbest_i = [Pbest_i^1, Pbest_i^2, \ldots, Pbest_i^D] \tag{8.16}$$

$$Gbest_i = [Gbest_i^1, Gbest_i^2, \ldots, Gbest_i^D] \tag{8.17}$$

$$\mathcal{V}E_i = [\mathcal{V}E_i^1, \mathcal{V}E_i^2, \ldots, \mathcal{V}E_i^D] \tag{8.18}$$

$$\mathcal{X}E_i = [\mathcal{X}E_i^1, \mathcal{X}E_i^2, \ldots, \mathcal{X}E_i^D] \tag{8.19}$$

The evaluation criterion of the developed algorithm follows the fitness function presented in equations (8.1) and (8.13) which evaluates, as discussed in the previous section, the optimality of the partitioning process. Fig. 8.2 provides an illustration of the application of the developed CBDPSO to establish an optimal decomposition for a given network topology. Specifically, the position vector, $\mathcal{X}E_i$, is redefined to represent the actual partitioning of the network where $\mathcal{X}E_i$ represents the i[th] particle position permutation $\mathcal{X}E_i = [\mathcal{X}E_i^1, \mathcal{X}E_i^2, \ldots \mathcal{X}E_i^j, \ldots, \mathcal{X}E_i^N]$ s.t. $\mathcal{X}E_i^j$ is an integer that holds the partition's information such that if $\mathcal{X}E_i^j = \mathcal{X}E_i^l$, then nodes j and l will be categorized within the same subcommunity, given that both $\mathcal{X}E_i^j$, $\mathcal{X}E_i^l \in [1, N]$. It is worth mentioning that the diminution of the fitness function equals the number of nodes in the to-be-decomposed network. Fig. 8.3 provides an illustration of the CBDPSO's searching strategy for updating the network topology into optimal partitions.

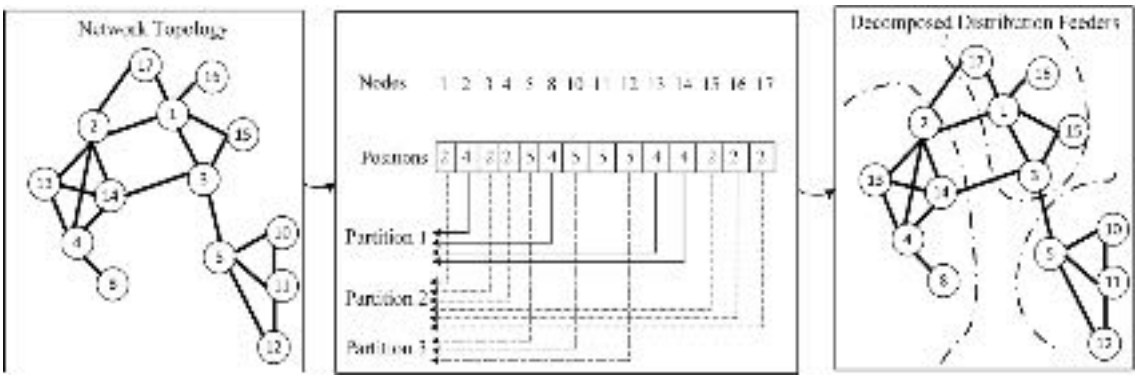

Figure 8-2. The partitioning ideology of the CBDPSO

That's to say, the i[th] particle velocity permutation is arranged in a vector representation, $\mathcal{V}E_i = [\mathcal{V}E_i^1, \mathcal{V}E_i^2, \ldots \mathcal{V}E_i^j, \ldots, \mathcal{V}E_i^N]$, where $\mathcal{V}E_i^j$ is an integer s.t. $\mathcal{V}E_i^j \in [0,1]$.

For the case of $\mathcal{V}E_i^j = 1$, then the relative entry element at the position vector, $\mathcal{X}E_i^j$, is ought to change; otherwise, for any other value of $\mathcal{V}E_i^j$, it will remain in the same position. Following the same manner at each iteration, the *Pbest* vector are initialized similar to the position vector, while the *Gbest* vector is set to be the best obtained position vector for the solution space. Accordingly, the mathematical operators will be redefined as following:

$$\mathcal{V}E_i(t+1) = \omega\mathcal{V}E_i(t) \oplus (c_1 r_1(Pbest \ominus \mathcal{X}E_i(t)) + (c_2 r_2(Gbest \ominus \mathcal{X}E_i(t))) \tag{8.20}$$

$$\mathcal{X}E_i(t+1) = \mathcal{X}E_i(t) \otimes \mathcal{V}E_i(t+1) \tag{8.21}$$

where ω is a user-specified inertia assumed to be 0.75 while c_1 and c_2 are assumed to be 1.497, respectively. Since a particle in the solution space adjusts its information based on knowledge provided from its nearby particles, the learning process is seen as a comparative one between two consecutive position. Specifically, any two generated position permutations, $\mathcal{P}_1 = [\mathcal{P}_1^1, \mathcal{P}_1^2, \dots, \mathcal{P}_1^N]$, and $\mathcal{P}_2 = [\mathcal{P}_2^1, \mathcal{P}_2^2, \dots, \mathcal{P}_2^N]$ will lead to velocity vector as following:

$$\mathcal{P}_1 \ominus \mathcal{P}_2 = \mathcal{V}E = [\mathcal{V}E_1, \mathcal{V}E_2, \dots, \mathcal{V}E_N] \tag{8.22}$$

where the operator $\ominus$ indicates the difference between compared network topology indicated by the positions such that:

$$\begin{cases} \mathcal{V}E_i = 1, & for\ \mathcal{P}_2^i \neq \mathcal{P}_2^i \\ \mathcal{V}E_i = 0, & for\ \mathcal{P}_2^i = \mathcal{P}_2^i \end{cases} \tag{8.23}$$

Additionally, the operator $\oplus$ ensures the velocity will be binary coded which eventually eases the reordering of the position vectors. That is to say, when two velocity

vectors are added, an updated velocity vector such that $\mathcal{V}E_1 + \mathcal{V}E_2 = \mathcal{V}E_3 = [\mathcal{V}E_3^1, \mathcal{V}E_3^2, \ldots, \mathcal{V}E_3^N]$, where

$$\begin{cases} \mathcal{V}E_3^i = 1, & if\ \mathcal{V}E_1^i + \mathcal{V}E_2^i \geq 1 \\ \mathcal{V}E_3^i = 0, & if\ \mathcal{V}E_1^i + \mathcal{V}E_2^i < 1 \end{cases} \tag{8.24}$$

Once a new velocity vector is obtained, the i[th] particle updates its position following the use of the operator $\otimes$ as shown in equation (8.25). The goodness of the operator $\otimes$ will be reflecting in its ability to place the particle within its most ideal partition that shares with it the same sensitivity values described in the previous section. For a modified position permutation $\mathcal{P}_{pre} = [\mathcal{P}_{pre}^1, \mathcal{P}_{pre}^2, \ldots, \mathcal{P}_{pre}^N]$, and a velocity $\mathcal{V}E = [\mathcal{V}E_1, \mathcal{V}E_1, \ldots, \mathcal{V}E_N]$ of the previous iteration, the new position permutation is achieved by utilizing the operator $\otimes$ such that $\mathcal{P}_{pre} \otimes \ \mathcal{V}E = \mathcal{P}_{updated} = [\mathcal{P}_{updated}^1, \mathcal{P}_{updated}^2, \ldots, \mathcal{P}_{updated}^N]$, s.t.:

$$\begin{cases} \mathcal{P}_{updated}^i = \mathcal{P}_{pre}^i, & if\ VE_i = 0 \\ \mathcal{P}_{updated}^i = \tan^{-1}\left(M_{improved}(\mathcal{P}_{pre}^i, j | j \in K_i\right), & if VE_i = 1 \end{cases} \tag{8.25}$$

where K_i resembles the neighboring nodes to node i s.t. $K_i = [K_1, K_2, \ldots, K_N]$, while $M_{improved}$ is calculated from equation (8.13). The flowchart of the partitioning process based on the concept of CBDPSO is illustrated in fig. 8.4.

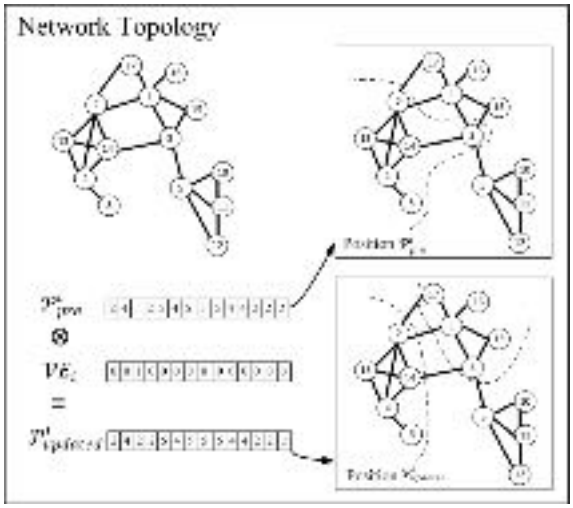

Figure 8-3. An illustration of the CBDPSO algorithm for updating the network topology using operator

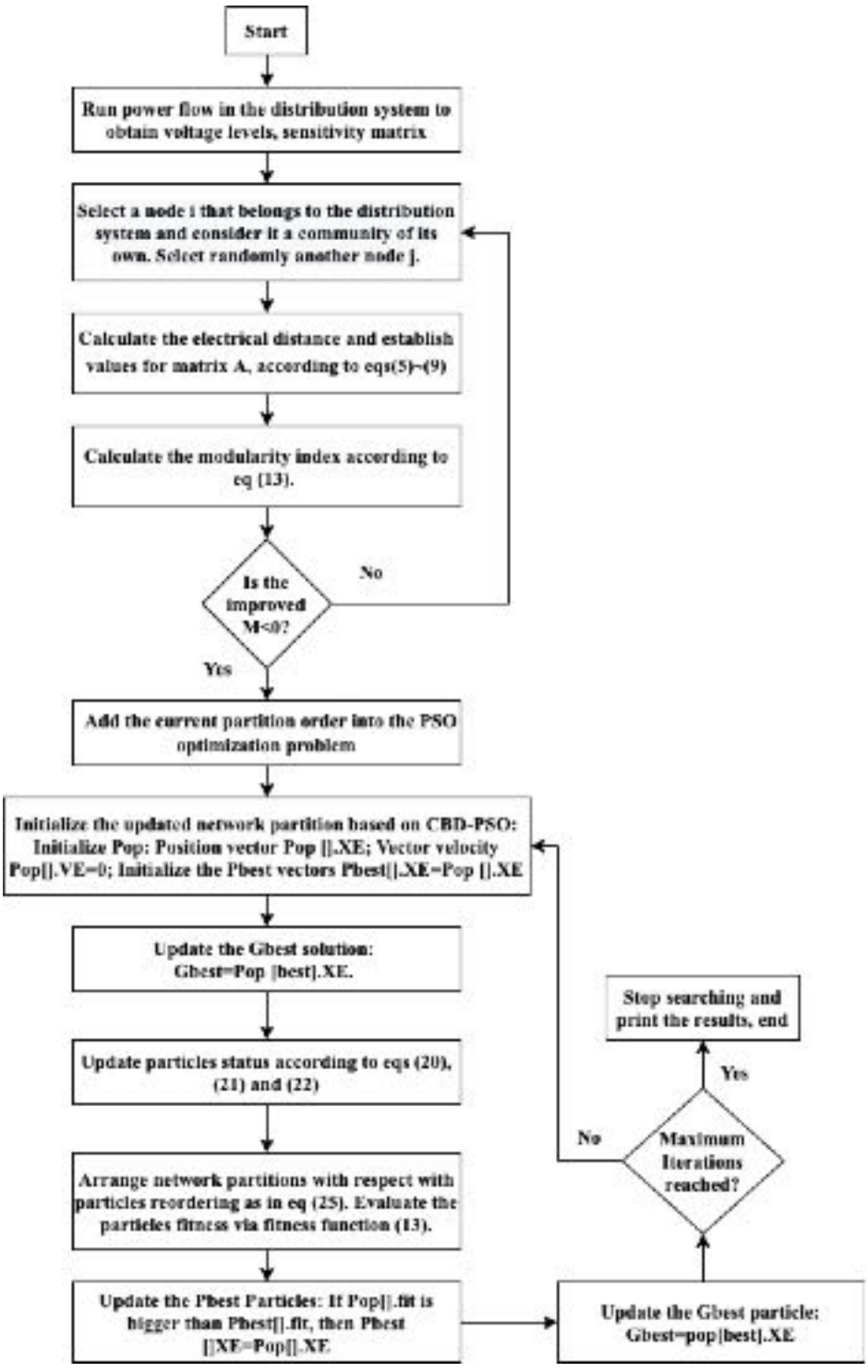

Figure 8-4. Flowchart of the decomposition of PDN based on CBDPSO

8.4 MILP Problem Formulation

8.4.1 *Mixed-Integer Non-Linear Programming Model*

MINLP is considered a well-established and widely used powerful tool to model vast types of general optimization problems; an advantage of the reformulation of MINLP into MILP lays in the capability it possesses to solve the latter class problems while avoiding the computational burden. An additional virtue is the ability to use the widely available commercial programs for solving MILP problems while guaranteeing the existence of a unique solution. Throughout the way, an emphasis on the equality and inequality constraints associated with voltage and reactive power support must be carefully considered. Such emphasis is pivotal to satisfy the requirement of the developed VVO methodology. The solution to the objective function is achieved based on optimal values for the energy provided by the upstream grid, the energy provided by the PV systems, the amount of reactive power support per the CB modules, and OLTC, and the charging and discharging schedule for PEVs.

1) ***The objective function***: the optimization formula, to achieve economical operation in the context of VVO problem while considering stochastic bidirectional penetration of PEVs, is formulated as follows:

$$OF = Min\ (J_1 + J_2 + J_3 + J_4) \tag{8.26}$$

The first variable, J_1, aims to minimize the energy cost from the upstream network as follows:

$$J_1 = \sum_{t=1}^{24} \sum_{\rho=a}^{c} \sum_{i=1}^{N} \sum_{j=1}^{N} [\mathcal{S}_t^G \,.\, \Delta t \,.\, [Re(V_{p,t}, I_{p,t}) + imj(V_{p,t}, I_{p,t})] \tag{8.27}$$

Where $\mathcal{S}_t^G$ represents the energy costs, $V_{p,t}\ and\ I_{p,t}$ represent the per-phase voltage and current per timeslot t. To coordinate the PEVs charging and discharging activities with the timely stead-state operation of the grid, this work proposes an objective function that aims to minimize the cost of energy discharged to the grid from a set of PEVs. Additionally, this work aims to minimize the energy demand curtailment of PEVs during congestion period to avoid increasing energy prices. These two objectives are formulated as follows:

$$J_2 = \sum_{t=1}^{24} \sum_{\rho=a}^{c} \sum_{v=1}^{Nv} [\Delta t\ .\ [(\mathcal{S}_{v,p,t}^{disch}.PEV_{v,p,t}^{disch}) - (\mathcal{S}_{v,p,t}^{ch}.PEV_{v,p,t}^{ch})] \tag{8.28}$$

$$J_3 = \sum_{t=1}^{24} \sum_{v=1}^{Nv} [\ \Delta t\ [\mathcal{S}_{curt}^{PEV}.PEV_v^{curt}]] \tag{8.29}$$

where $\mathcal{S}_{v,p,t}^{disch}$ and $\mathcal{S}_{curt}^{PEV}$ represent the costs for PEV's energy discharge and PEV's energy demand curtailment for a vehicle *v*, respectively. Finally, this work aims to reduce the cost associated with active power curtailment from the PV system during time when the PV inverters are used to maintain certain voltage limits, as follows:

$$J_4 = \sum_{t=1}^{24} \sum_{i=1}^{N} \sum_{j=1}^{N} [\ \Delta t\ [\mathcal{S}_{i,t}^{PV.cur}\ .\ PV_{i,t}^{cur}]] \tag{8.30}$$

where $\mathcal{S}_{i,t}^{PV.cur}$represent the cost for APC of the PV systems, $PV_{i,t}^{cur}$, at timeslot *t* for node *i*.

2) ***The Kirchhoff Laws constraints****:* an important aspect of ensuring an accurate representation of the problem formulated in this work is to model constraints that govern the physical law of operation for unbalanced power distribution networks. The voltage-current relationship of KCL possesses natural nonlinearity for their description of the timely-changing quantities of power and voltage levels on the grid. Equations (8.31)-(8.40) provides mathematical modelling for these relationships as follows:

$$re\,(I_{m,p,t}^{load}) + \sum_{v\in Nv}(re\;(I_{v,t}^{EV}\,.\gamma(v,m,p)) - re\,(I_{i,p,t}^{G}) - [re(\sum_{i\in C_R} I_{i,t}^{CB} + \sum_{lm\in U} I_{lm,p,t} - \sum_{mn\in U} I_{mn,p,t})] + [imj\,\frac{V_{m,p,t}}{2}(\sum_{lm\in U} B_{lm,p} + \sum_{mn\in U} B_{mn,p})] = 0 \quad (8.31)$$

$$imj\,(I_{m,p,t}^{load}) + \sum_{v\in Nv}(imj\,I_{v,t}^{EV}\,.\gamma(v,m,p) - I_{i,p,t}^{imj} - [imj(\sum_{i\in C_R} I_{i,t}^{CB} + \sum_{lm\in U} I_{lm,p,t} - \sum_{mn\in U} I_{mn,p,t})] + [re\,\frac{V_{m,p,t}}{2}(\sum_{lm\in U} B_{lm,p} + \sum_{mn\in U} B_{mn,p})] = 0 \quad (8.32)$$

where equations (8.31) and (8.32) present the amount of current at phase P for node i at timeslot t in branch U within a defined partition. γ represnts a binary number that indicates the status of connection of a PEV v that belongs to a set of PEVs associated with node i at the timeslot of interest. The current-voltage equations represent the timely consumption of active and reactive power at the branch of interest. Equations (8.33) and (8.34) represent the branch's per phase voltage level, while equations (8.35) and (8.36) represent mathematical modeling of KCL summation for each circuit *lm* within a partition, as follows:

$$re\,(I_{i,p,t}^{load}) = \frac{[(P_{i,p,t}^{load}\,.re\,V_{i,p,t}) + (Q_{i,p,t}^{load}\,.imj\,V_{i,p,t})}{re\,V_{i,p,t}^{2} + imj\,V_{i,p,t}^{2}} \quad (8.33)$$

$$imj\,(I_{i,p,t}^{load}) = \frac{[(P_{i,p,t}^{load}\,.imj\,V_{i,p,t}) - (Q_{i,p,t}^{load}\,.re\,V_{i,p,t})}{re\,V_{i,p,t}^{2} + imj\,V_{i,p,t}^{2}} \quad (8.34)$$

$$re(V_{l,p,t} - V_{m,p,t}) - \sum_{p,h\in P}[(R_{lm,p,h}\,.re\,(I_{lm,h,t}) - (X_{lm,p,h}\,.imj\,(I_{lm,h,t}))] = 0 \quad (8.35)$$

$$imj\left(V_{l,p,t} - V_{m,p,t}\right) - \sum_{p,h\in P} \left[\left(X_{lm,p,h} \,.re\, \left(I_{lm,h,t}\right) \; - \; \left(R_{lm,p,h} \,.imj\, \left(I_{lm,h,t}\right)\right)\right] = 0 \tag{8.36}$$

Equations (8.37) and (8.38) represents exponential mathematical modeling of the load voltage level from active and reactive power aspect, while equations (8.39) and (8.40) define the allowable limitation of both voltage and current at each circuit, as follows:

$$P_{i,p,t}^{load} = P_{i,p,t}^{nominal}\left[\frac{\sqrt{re\; V_{i,p,t} \; + \; imj\; V_{i,p,t}}}{V_{nominal}}\right]^{\alpha} \tag{8.37}$$

$$Q_{i,p,t}^{load} = Q_{i,p,t}^{nominal}\left[\frac{\sqrt{re\; V_{i,p,t} \; + \; imj\; V_{i,p,t}}}{V_{nominal}}\right]^{\beta} \tag{8.38}$$

$$V_{min}^2 \leq re\; V_{i,p,t}^2 + imj\; V_{i,p,t}^2 \leq V_{max}^2 \tag{8.39}$$

$$0 \leq re\; I_{lm,p,t}^2 + imj\; I_{lm,p,t}^2 \leq I_{max,lm}^2 \tag{8.40}$$

3) ***The OLTC Constraints****:* equations (8.41)-(8.49) represent the mathematical formulation for the constraints on voltage output at tap position r of the OLTC, as follows:

$$re\left(V_{l,p,t}\right) - \varepsilon_{r,tp}\; re\left(V_{m,p,t}\right) - R_{lm}\; re\left(I_{lm,p,t}\right) + \; X_{lm}\; imj\left(I_{lm,p,t}\right) + \Delta u_{lm,tp}^{re} = 0 \tag{8.41}$$

$$imj\;\left(V_{l,p,t}\right) - \varepsilon_{r,tp}\; imj(V_{m,p,t}) - X_{lm}\; re(I_{lm,p,t}) \; - \; R_{lm}\; imj(I_{lm,p,t}) + \Delta u_{lm,tp}^{imj} = 0 \tag{8.42}$$

$$\pm\left(\Delta u_{lm,tp}^{re}\right) + LGN\; b_{lm,tp} \leqslant LGN \tag{8.43}$$

$$\pm(\Delta u_{lm,tp}^{imj}) + LGN\; b_{lm,tp} \leqslant LGN \tag{8.44}$$

$$-I_{lm}^{min} b_{lm,tp} \leqslant re\; I_{lm,tp} \leqslant I_{lm}^{max} b_{lm,tp} \tag{8.45}$$

$$-I_{lm}^{min} b_{lm,tp} \leqslant imj\; I_{lm,tp} \leqslant I_{lm}^{max} b_{lm,tp} \tag{8.46}$$

$$\sum_{tp=1}^{Ntpt} b_{lm,tp} = 100\% \tag{8.47}$$

$$re\ [I_{lm,h,t} - \sum_{tp=1}^{Np} I_{lm,h,t,tp}] = 0 \tag{8.48}$$

$$imj\ [I_{lm,h,t} - \sum_{tp=1}^{Np} I_{lm,h,t,tp}] = 0 \tag{8.49}$$

Where $re(I_{lm,p,t})$ and $imj(I_{lm,p,t})$ represent the phase currents at the primary side of the OLTC for tap position r with corresponding tap rations, ε_r. To ensure the tap position, tp, is on r, we define a binary variable $b_{lm,tp}$ that equal to 1 when *tp* is on, and zero for any other positions. Additionally, two auxiliary variables $\Delta u_{lm,tp}^{imj}$ and $\Delta u_{lm,tp}^{re}$ are furtherly introduced to incorporate OLTC's terminals voltage differences. For the case of $b_{lm,tp} = 0$, $re(I_{lm,p,t})$ and $imj(I_{lm,p,t})$ are going to be zero to limit any excessive operations of the OLTC over a specific period to ensure safety of the equipment. I_{lm}^{min} and I_{lm}^{max} represent the feasible current values of the OLTC, while LGN is an adequate large number that applies linear relaxation following the concept the big-M method. Equations (8.48) and (8.49) describe the real and imaginary for the regulated current and voltage output of the OLTC. The modeling of the VRs strictly follows the mathematical formulation of the OLTC.

4) ***The CBs Constraints****:* the mathematical representation of the OLTC constraints, the real and imaginary current output of the CB are represented by equations (8.50) and (8.51), as follows:

$$\frac{re\ I_{i,t,sp}^{CB}}{B_{i,t,sp}} + imj\ V_{i,t} + \Delta u_{i,sp}^{CB,re} = 0 \tag{8.50}$$

$$\frac{imj\ I_{i,t,sp}^{CB}}{B_{i,t,sp}} - re\ V_{i,t} + \Delta u_{i,sp}^{CB,imj} = 0 \tag{8.51}$$

$$\pm(\Delta u_{i,sp}^{CB,re}) + LGN\ b_{i,sp}^{CB} \leqslant LGN \tag{8.52}$$

$$\pm(\Delta u_{i,sp}^{CB,imj}) + LGN\ b_{i,sp}^{CB} \leqslant LGN \tag{8.53}$$

$$-re\ I_{CB,i,t}^{min} b_{i,sp}^{CB} \leqslant re\ I_{i,t,sp}^{CB} \leqslant re\ I_{CB,i,t}^{max} b_{i,sp}^{CB} \tag{8.54}$$

$$-imj\ I_{CB,i,t}^{min} b_{i,sp}^{CB} \leqslant im\ I_{i,t,sp}^{CB} \leqslant imj\ I_{CB,i,t}^{max} b_{i,sp}^{CB} \tag{8.55}$$

$$\sum_{sp=1}^{Nsp} b_{i,sp}^{CB} = 1 \tag{8.56}$$

$$re\ [I_{i,t}^{CB} - \sum_{sp=1}^{Nsp} I_{i,t,sp}^{CB}] = 0 \tag{8.57}$$

$$imj\ [I_{i,t}^{CB} - \sum_{sp=1}^{Nsp} I_{i,t,sp}^{CB}] = 0 \tag{8.58}$$

The shunt CBs are assumed to be either connected or disconnected in accordance with the steady-state operation of each partition, with sp represents the switching positions s.t. $sp \in Nsp$, and $B_{i,t,sp}$ is its corresponding susceptance of the CB. Analogous to the OLTC tap position representation, a binary variable $b_{i,sp}^{CB}$ is defined in equations (8.51)~(8.55) to represent the connection of the CBs, where it equals 1 once a particular position is set and zero otherwise. Equations (8.54) and (8.55) constraint the limit of the real and imaginary CBs currents, $I_{CB,i,t}^{min}$and $I_{CB,i,t}^{max}$. Additionally, two auxiliary variables, $\Delta u_{i,sp}^{CB,imj}$and $\Delta u_{i,sp}^{CB,re}$, are defined to be zeros if $b_{i,sp}^{CB} = 1$, or otherwise regulated by an adequate large number. Equation

(8.56) assumes one switching position to be selected at a timeslot, otherwise the CB modules are considered disconnected, to ensure limited switching actions.

5) ***The PV Inverter Constraints****:* the APC of the PV inverter is constrained as shown in equation (8.59), while the active and reactive power injection of the PV inverter are established in accordance with equations (8.60) and (8.61).

$$0 \leqslant PV_{i,t}^{Cur} \leqslant PV_{i,t}^{available} \tag{8.59}$$

$$(PV_{i,t}^{reactive})^2 \leqslant (PV_{i,t}^{capacity})^2 - (PV_{i,t}^{available} - PV_{i,t}^{Cur})^2 \tag{8.60}$$

$$\left|PV_{i,t}^{reactive}\right| \leqslant \left[\left(PV_{i,t}^{available} - PV_{i,t}^{Cur}\right) tan\,(Cos^{-1}PF)\right] \tag{8.61}$$

7) ***The PEVs Constraints****:* equation (8.62) constrains the charging and discharging process of a PEV v connected at a phase p at node i to not occur simultaneously at timeslot t, as follows:

$$\mathbb{X}ch_{i,p,t}^{v} + \mathbb{Y}disch_{i,p,t}^{v} \leqslant 1 \tag{8.62}$$

where $\mathbb{X}ch$ and $\mathbb{Y}disch$ are binary variables associated with the PEV charge and discharge at a certain timeslot s.t. $\mathbb{X}ch, \mathbb{Y}.disch \in [0,1]$. Equations (8.63)~(8.67) present the active and reactive power requirements of the PEV connection to the grid, as follows:

$$Q_{i,p,t}^{EV} \leqslant \sqrt{(PEV_{i,p,t}^{capacity})^2 - (PEV_{i,p,t}^{grid})^2} \tag{8.63}$$

$$0 \leqslant PEV_{i,p,t}^{grid_{nominal}} \leqslant PEV_{i,p,t}^{grid\_max} \tag{8.64}$$

$$Q_{i,p,t}^{EV,min} \leqslant Q_{i,p,t}^{EV} \leqslant Q_{i,p,t}^{EV,max} \tag{8.65}$$

$$-\varsigma_{i,p,t}^{grid}\, PEV_{i,p,t}^{grid} \leqslant Q_{i,p,t}^{EV} \leqslant \varsigma_{i,p,t}^{grid}\, PEV_{i,p,t}^{grid} \tag{8.66}$$

$$PEV_{i,p,t}^{grid} = PEV_{i,p,t}^{grid\_nominal} . \sum_{v=1}^{Nv} [(re\ V_{v,i,p,t} . re\ I_{v,i,p,t}^{PEV}) + (imj\ V_{v,i,p,t} . imj\ I_{v,i,p,t}^{PEV})] \quad (8.67)$$

$$PEV_{i,p,t}^{grid} = \mathbb{X}ch_{i,p,t}^{v} . [\sum_{v=1}^{Nv} PEV_{v,i,p,t}^{ch} . \eta_{ch}] - \mathbb{Y}disch_{i,p,t}^{v} . [\sum_{v=1}^{Nv} PEV_{v,i,p,t}^{disch} . \eta_{disch}] \quad (8.68)$$

$$\overline{E}_{v,i,p,t}^{EV} = E_{v,i,p,t}^{EV} - E_{v,i,p,t}^{EV\_Cur} \quad (8.69)$$

Equation (8.63) set the limits for the reactive power of a PEV based on its own power requirement as well as the node's KVA rating. On the other hand, equation (8.64) set the real power constraints for a group of PEVs connected during each timeslot. This leads to the influence on the amount of reactive power PEVs could support the grid during at any phase and nodes during any timeslot which are highlighted in the constraints shown in equations (8.65) and (8.66). Specifically, this work defines a fixed variable $\varsigma_{i,p,t}^{grid}$ for each PEV's charger converter, set in the simulation to be 0.25, with capability to modulate the power factor up to 0.95 of inductive or capacitive capabilities [181, 182]. Equation (8.67) and (8.68) represent the PEVs charging and discharge power per phase p at node i during timeslot t, while equation (8.69) measures the level of energy curtailment the grid is forced to implement at each timeslot as a result of grid's operational status. Fig. 8.5 presents the capability curve of a PEV's bidirectional charger, which shows the operational zones of when the PEVs can supply the grid with either active or reactive power and in which mode.

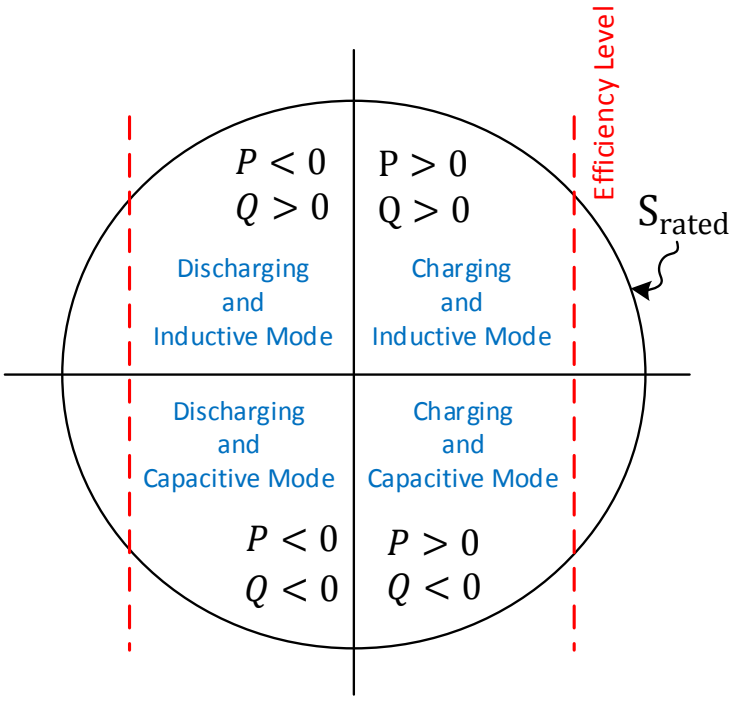

Figure 8-5. The PEV's bidirectional converter capability curve.

8.4.2 *Mixed-Integer Linear Programming Model Formulation:*

The incorporation of discrete decision variables into the problem formulated in the previous section is extremely non-trivial due to its non-convexity and non-linearity nature. Therefore, in order to reduce complexities and to solve the formulated problem efficiently using the available commercial programs, we must apply linearization to the non-linear expressions in equations (8.31)~(8.69). This is true since the current available MINLP programs do not acquire enough maturity as compared to MILP programs. Several research works have investigated linearization of coefficients related to the operation of the distribution system. Large part of this subsection of the work is considerably influenced by the work of references [184, 185].

1. ***Linearization of the Load Flow Non-linear Constraints****:* it is worth to highlight that equations (8.33), (8.34), (8.37) and (8.38) are non-linear in nature, and therefore they must be linearized to be solved using the developed MILP formulation. Equations (8.70) and (8.71) present the linearized form of the above-mentioned expressions, while equation (8.72) and (8.73) present first-order approximation of the newly linearized expressions. This work defines points of operation, $(re\ V^{*}_{i,p,t}, imj\ V^{*}_{i,p,t})$ for the first-order approximation to be operating around. Both e^{*} and f^{*} are nonlinear functions that represent the real and imaginary parts of the voltage.

$$w(re\ V_{i,p,t} + imj\ V_{i,p,t}) = P^{nominal}_{i,p,t} . \frac{re\ V_{i,p,t}}{V^{\alpha_{i,p}}_{nominal}} . [re\ V^{2}_{i,p,t} + imj\ V^{2}_{i,p,t}]^{\frac{\alpha_{i,p}}{2}-1} \tag{8.70}$$

$$\begin{aligned} z(re\ V_{i,p,t} + imj\ V_{i,p,t}) \\ = P^{nominal}_{i,p,t} . \frac{imj\ V_{i,p,t}}{V^{\alpha_{i,p}}_{nominal}} . [re\ V^{2}_{i,p,t} + imj\ V^{2}_{i,p,t}]^{\frac{\alpha_{i,p}}{2}-1} \\ - Q^{nominal}_{i,p,t} . \frac{re\ V_{i,p,t}}{V^{\beta_{i,p}}_{nominal}} . [re\ V^{2}_{i,p,t} + imj\ V^{2}_{i,p,t}]^{\frac{\beta_{i,p}}{2}-1} \end{aligned} \tag{8.71}$$

$$re\ (I^{load}_{i,p,t}) = w^{*} + (re\ V_{i,p,t} - re\ V^{*}_{i,p,t}) \frac{\partial e}{\partial re\ V}\Big|^{*} + (imj\ V_{i,p,t} - imj\ V^{*}_{i,p,t}) \frac{\partial e}{\partial imj\ V}\Big|^{*} \tag{8.72}$$

$$\begin{aligned} imj\ (I^{load}_{i,p,t}) = z^{*} + (re\ V_{i,p,t} - re\ V^{*}_{i,p,t}) \frac{\partial f}{\partial re\ V}\Big|^{*} + (imj\ V_{i,p,t} \\ - imj\ V^{*}_{i,p,t}) \frac{\partial f}{\partial imj\ V}\Big|^{*} \end{aligned} \tag{8.73}$$

2. ***Linearization of the OLTC Constraints****:* it should be mentioned that part of the linearization process of the OLTC constraints in this work is inspired by the model of reference [186, 187]. Equations (8.74) and (8.75) can be linearized in the same way presented in the KCL load flow linearization process explained in the previous subsection of this part. We incorporate with these equations an integer variable,

$U_{lm,p,t}$, that resemble the actual selection of the tap-position of the OLTC located in the circuit lm at a given timeslot.

$$\left[re\left(V_{l,p,t}\right) - U_{lm,p,t}\, re\left(V_{m,p,t}\right) - R_{lm}\, re\left(I_{lm,p,t}\right) + X_{lm}\, imj\left(I_{lm,p,t}\right)\right].\mu_{lm} = 0 \tag{8.74}$$

$$\left[imj\left(V_{l,p,t}\right) - U_{lm,p,t}\ imj\left(V_{m,p,t}\right) - X_{lm}\, re\left(I_{lm,p,t}\right) - R_{lm}\, imj\left(I_{lm,p,t}\right)\right].\mu_{lm} = 0 \tag{8.75}$$

$$\mu_{lm} = \mu_{lm}^{min} + U_{lm,p,t}\,.\Delta\mu_{lm} \tag{8.76}$$

$$\Delta\mu_{lm} = \frac{\mu_{lm}^{max} - \mu_{lm}^{min}}{k_{lm}} \tag{8.77}$$

Equations (8.76) and (8.77) represent the non-convex mathematical expression that describe the work of the OLTC, with $\mu_{lm}^{max}$and μ_{lm}^{min}resemble the maximum and minimum turn rations of the OLTC, while k_{lm}represents its total allowed steps. To linearize it, a binary variable $\delta_{lm,tp}$is introduced and equation (8.76) could be rewritten as follows:

$$\mu_{lm} = \mu_{lm}^{min} + \Delta\mu_{lm}.\sum_{tp=0}^{Ntp} 2^{tp}.\delta_{lm,tp} \tag{8.78}$$

s.t.

$$\sum_{tp=0}^{Ntp} 2^{tp}.\delta_{lm,tp} \leqslant k_{lm} \tag{8.79}$$

With Ntp represent the total length that represent the binary expression of k_{lm}. Multiplying both sides of (8.78) by V_{OLTC}, the following formulation is obtained:

$$V_{OLTC}\,.\mu_{lm}^{min} + \Delta\mu_{lm}.\sum_{tp=0}^{Ntp} 2^{tp}.\delta_{lm,tp}V_{OLTC} = V_{OLTC}\,.\mu_{lm} \tag{8.80}$$

The variables $\delta_{lm,tp}V_{OLTC}$ could be furtherly replaced by a large number to allow transformation of the non-convexity into MILP context as follows:

$$0 \leqslant V_{OLTC}\left(1-\delta_{lm,tp}\right) \leqslant \left(1-\delta_{lm,tp}\right).LNG \tag{8.81}$$

$$0 \leqslant V_{OLTC}.\delta_{lm,tp} \leqslant \delta_{lm,tp}.LNG \tag{8.82}$$

3. ***Linearization of the CB and PEVs Constraints****: t*he linearization process of the CB as well as PEVs follows the same linearization process explained in the KCL load flow part of this subsection in defining points of operation ($re\ V^{*}_{i,p,t}$, $imj\ V^{*}_{i,p,t}$). In this context, equations (8.50) and (8.51) could be rewritten as follows:

$$\frac{re\ I^{CB}_{i,t,sp}}{B_{i,t,sp}} + imj\ V^{*}_{i,t} + \Delta u^{CB,re}_{i,sp} = 0 \tag{8.83}$$

$$\frac{imj\ I^{CB}_{i,t,sp}}{B_{i,t,sp}} - re\ V^{*}_{i,t} + \Delta u^{CB,imj}_{i,sp} = 0 \tag{8.84}$$

while equation (8.67) could be rewritten as follows:

$$PEV^{grid}_{i,p,t} = PEV^{grid_{nominal}}_{i,p,t}.\sum_{v=1}^{Nv}\left[\left(re\ V^{*}_{v,i,p,t}\ .re\ I^{PEV}_{v,i,p,t}\right) + \left(imj\ V^{*}_{v,i,p,t}\ .imj\ I^{PEV}_{v,i,p,t}\right)\right. \tag{8.85}$$

4. ***Linearization of the PV Inverter Constraints***: this work realizes the PV inverter's capability to perform reactive power-voltage control following the real-time steady-state operation of each partition of the distribution network [188]. Fig. 8.6 shows the concept of linearized reactive power-voltage control via six illustrative points [a1, a2, a3, a4, a5 and a6]. The PV inverter goes in capacitive mode (reactive power injection to the grid) for the positive value of reactive power on the curve. In contrast, it goes in absorption mode when the reactive power values are negative. The latter is performed when the steady-state operation requires a reduction in the increased value of the per unit voltage. This is primarily achieved to maintain the voltage not to violate acceptable limit to achieve economical operation, as this work investigates in the results section. The allowed voltage limits must reside between

[0.95-1.05]. The PV inverter operational zones are indicated in points [a1, a2, a5, and a6], whereas it provides nor absorbs reactive power support in operational points a3-a4, which is when the voltage limit of each partition is within permissible levels. The reactive power of the PV inverter is achieved using equation (8.60). Auxiliary continuous variable ϑ_k (s.t. $k \in \{1\sim6\}$), and integer variable σ_k (s.t.$k \in \{1\sim5\}$), are utilized in this work. Hence, the reactive power-voltage control of the PV inverter could be reformulated as follows:

$$V_{i,t}^{PV} = \sum_{k=1}^{6} \vartheta_k . V_{k,t} \tag{8.86}$$

$$PV_{i,t}^{reactive} = \sum_{k=1}^{6} \sigma_k . V_{k,t} \tag{8.87}$$

$$\vartheta_1 \leqslant \sigma_1 \tag{8.88}$$

$$\vartheta_6 \leqslant \sigma_5 \tag{8.89}$$

$$\vartheta_k \leqslant \sigma_k + \sigma_{k-1}, \forall k = 2,3,4,5 \tag{8.90}$$

$$\sigma_k \in \{0\sim1\}, \vartheta_k \geqslant 0 \tag{8.91}$$

$$\sum_{k=1}^{6} \vartheta_k = 1 \tag{8.92}$$

$$\sum_{k=1}^{5} \sigma_k = 1 \tag{8.93}$$

$$PV_{i,t}^{reactive} = g(V_{i,t}^{PV}) \tag{8.94}$$

where equation (8.94) presents the piece-wise linear function of the reactive power output of the PV inverter. Therefore, voltage-reactive power control mode could be utilized by the PV inverter located at each partition to stabilize the voltage limit within a certain limit.

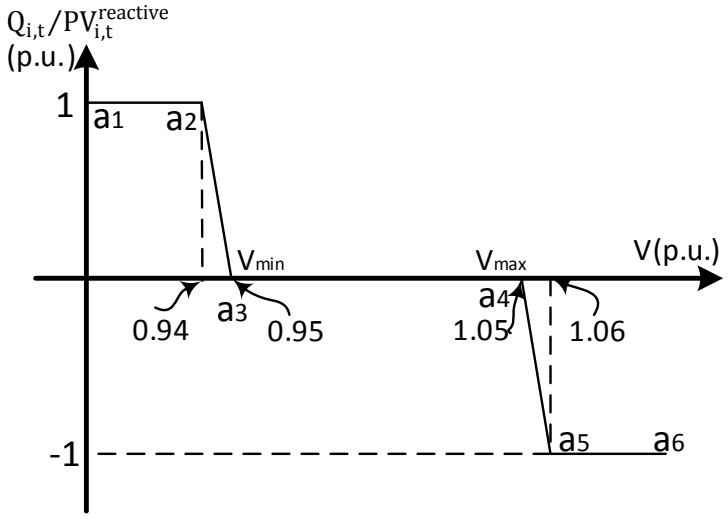

Figure 8-6. The voltage-var control for the PV inverter

8.5 Results and Discussion

To verify the efficiency of the developed strategy, this work utilizes the modified IEEE 123 bus distribution system to perform simulation for different case scenarios. The simulation is performed using MATLAB 2019b on a 64-bit, i-7 laptop with 16 G.B. RAM. The optimization model was programmed in the YALMIP platform [189] and was solved by the CPLEX optimizer [190]. The developed two-stage optimization strategy to optimally solve the VVO problem considering PEVs activities on the power distribution network (PDN) is constructed to incorporate conventional variables that describe the grid's steady-state operation (i.e. active and reactive power injection/absorption, voltage and current flow). The IEEE 123 bus system data has been obtained from [191], with modifications that resemble the integration of 500 PEVs assumed to be Tesla model 3 with 75 kWh battery capacity and up to 11.5 kW of charging power. The arrival and departure times as well as the charging model of the PEVs in this work have been adopted based on the study from references [181, 182]. Furthermore, the test feeder incorporates shunt capacitor banks, PV systems, and OLTC transformer and VRs to achieve the developed coordination scheme. The location and capacity of the installed equipment is shown in table 8.1. The values of the α and β

parameters, that are used to model different load types in the voltage equation model, are utilized from [191, 192].

The two-stage optimization strategy is modelled in a time-horizon fashion; the first stage, which aims to decompose the PDN based on the developed CBDPSO, is assumed to operate in a time-ahead platform, while the second stage assumes to operate in real-time platform with equally distributed 96 timeslots with 15 minutes duration per each timeslot. After partitioning the PDN at the first stage based on the sensitivity values of voltage levels with respect to active and reactive power levels on the system, the dynamic operation of each partitioned cluster follows the formulated MILP to dictate the operational status of the RPC devices as well as the APC levels for the PV inverters considering the PEVs charging and discharging schedule. It is worth mentioning that a PEV may request to connect or departs during any timeslot, but such a decision would only influence the following timeslot's operational status. The demand variations and subsequent energy prices of the PDN have been assumed for a typical Fall season's day in the region of Miami-Dade County, Florida, as shown in fig. 8.7 [141, 173].

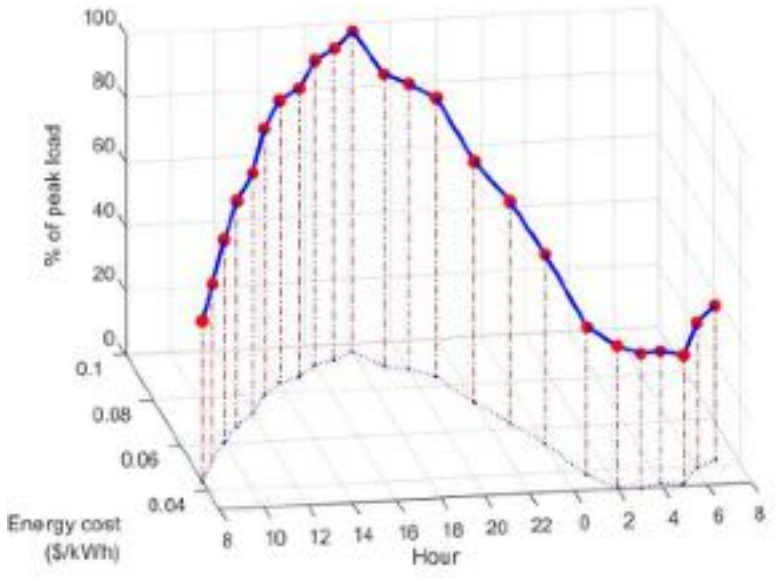

Figure 8-7. Energy demand and prices for a typical South Florida PDN

Table 8-1: Location and capacity of the equipment on the test feeder

Type	Taps	Capacity	Location		
			Partition 1	**Partition 2**	**Partition 3**
EVs Stations	-	-	3, 34, 57, 64	30, 24, 19, 46	97, 106, 111, 84, 91
PV Systems	-	850 kVA	55, 14, 16	40, 22, 28	108, 87, 74, 100
OLTC/VAR	20	0.005 pu	150 (OLTC)	25 (VR)	67 (VR)
CBs	10	25 kVar	17, 56, 66, 58	29, 32, 45	107, 70, 113, 94

The energy cost of the PV generation is set to be 0.10$/kWh, with capacity of 850 kVA. Additionally, this work assumes that the PDN operator assumes full ownership of the PV systems installed at premises. Therefore, the PV energy curtailment cost has been set in the simulation to be equal to the negative of its generation cost. This could be changed if someone desires to estimate true value of the curtailed PV energy to assess alternative economical options. In addition, since there is no universal pricing model that reflect the true cost for vehicle-to-grid (V2G) services, this work assumes a discharging price that equals to the energy costs of the timeslot multiplied by a factor of 100 (i.e. the PEV energy discharge costs for a timeslot at 13.00 would be priced at 7.93$/kWh). Since the energy demand curtailment of a PEV may significantly leads to customer dissatisfaction, a conservative pricing for PEVs energy demand curtailment is set to be $25/kWh in our simulation. A charging and discharging efficiency of 91% have been assumed in this work [42]. The permissible voltage operation levels are set to be within [0.95, 1.05], with the per unit voltage of the main bus is set at 1.02. The primary side of the OLTC devices is assumed to be at unity power factor, and the parameters of the RPC devices are illustrated in table 8.1. The goal of the second optimization stage is to reduce the voltage level fluctuations with an economical combination of RPC, APC of the PV inverters, and PEVs charging and discharging. This indirectly aims to relax the operation of OLTC (as in eqs (74) and (75)) and CBs (as in eqs (83) and (84)) to ensure their minimal participation in the reactive power-voltage coordination scheme, as the PEV and PV voltage support are prioritized as first line of defense. Finally, the simulation

time has been limited to 1000 seconds. If the time elapses at any timeslot without recognizing an optimal result, then the best integer's value is recorded as the best solution.

To verify the feasibility of the developed CBDPSO partitioning methodology, a simulation that consider the IEEE 123 distribution system parameters was carried out in MATLAB. Fig. 8.8 shows the overall decomposition of the feeder into optimal clusters to reduce the voltage variability during peak hours. The modularity index reaches its highest value when there the modified 123 distribution system is divided into three partitions with a measured modularity index value of 0.41, instead of the originally established 123 nodes with an index of 0.12, as the results show in fig. 8.9. The optimized decomposition of the system takes into consideration the preliminary steady-states operation of the feeder including PV system generation and PEVs load demands but before applying any of the developed reactive power-voltage coordination scheme that is to be incorporated into the second stage of our developed work.

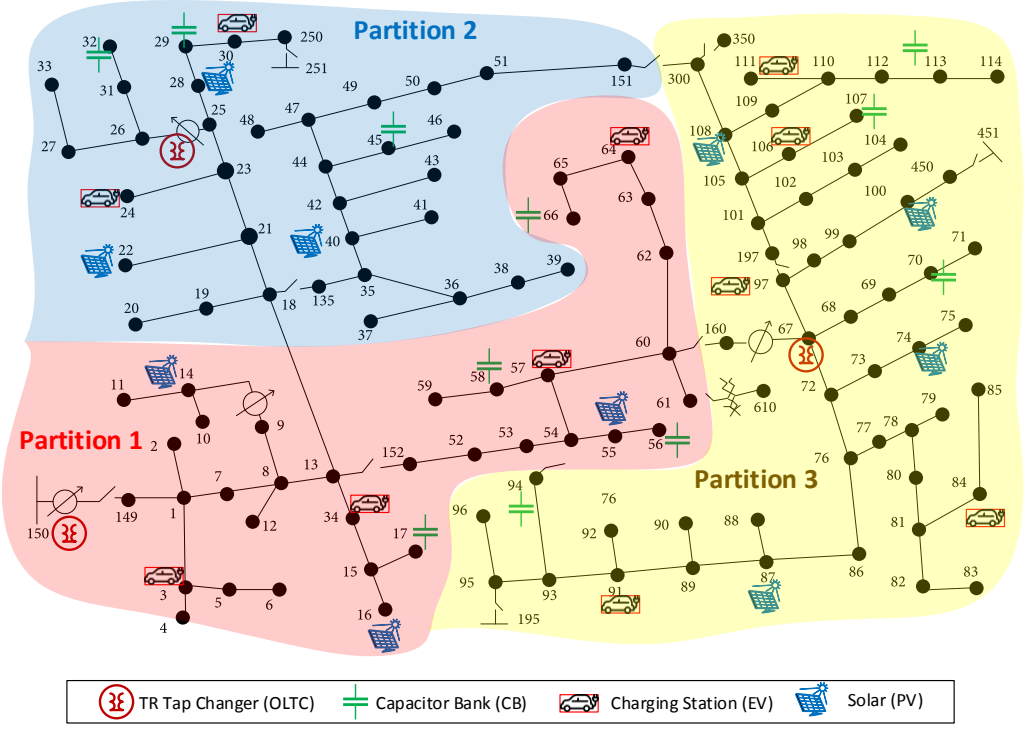

Figure 8-8. Results of the optimal network decomposition of three partitions

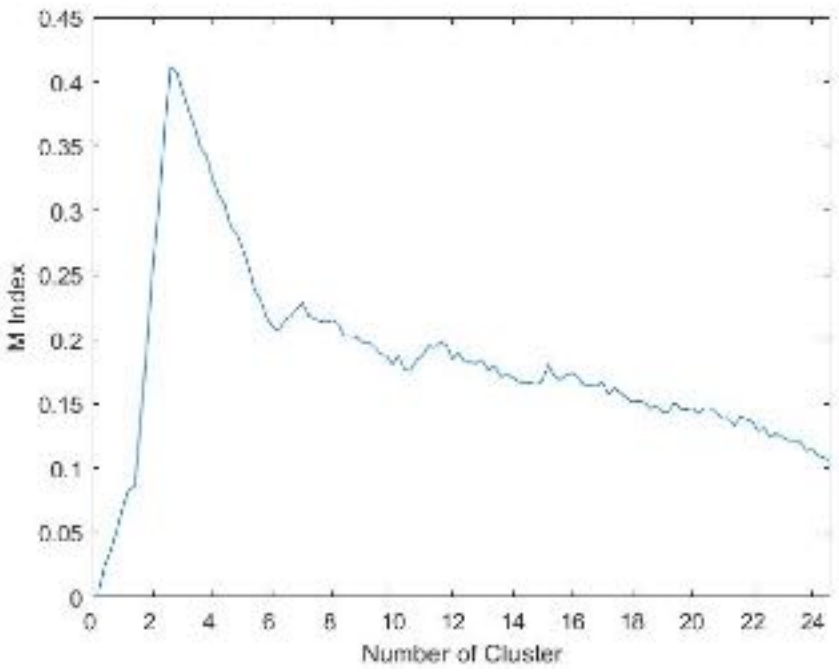

Figure 8-9. The modularity index results based on the CBDPSO

Four case scenarios have been modeled in this work, as follow:

1) Case A: No changes
2) Case B: EVs discharge; offline RPC control
3) Case C: No EVs discharge + APC curtailment; online RPC control
4) Case D: EVs discharge + APC curtailment; online RPC control.

Among the four case scenarios, only C and D were considered deploying the RPC devices according to the developed coordination scheme to implement the VVO coordination via OLTC, CBs, reactive power support from the PVs and PEVs. It is worth to mention that case scenarios A and B retain regular reactive power and voltage support that arise from normal operation of the PDN. A PEV energy demand curtailment occurs when a partition fails to meet the PEVs connection requests at reasonable charging rates due to high demands. Similarly, APC occurs when steady-state operations require extensive reactive power support from the PV inverters. In this work, no APC is achieved in the first two case scenarios. Additionally, it is worth to mention that the developed coordination consider greater PEVs

demands for case scenarios B and D during later times of the day to compensate for the PEVs discharge during timeslots of peak demands. Table 8.2 provides results corresponding to the implementation of the test scenarios. With no PEVs discharging events, case scenario A recorded the highest costs incurred on the distribution feeder's partitions. To maintain energy supply without increasing prices significantly on consumers, large-scale PEVs energy demand curtailment has been recorded during peak hours. As a result of inconvenience associated with PEVs owners rescheduled for other timeslots, the highest PEVs energy curtailment costs are recognized in the first case scenario. On the other hand, case B incorporates the stochastic model of a certain limit of PEVs discharge within each partition, without activating the RPC scheme. As expected, the results show a sound reduction of the amount of PEV's energy demand curtailment. The total cost has been reduced since each partitioned area is responsible for compensating the PEVs that participated in the discharging process, based on per kWh rate that is substantially lower than the penalty cost associated for curtailing the energy from PEVs. On the other hand, PEVs owners who engage in discharging processes during timeslots of congestion demands would receive economic compensations for their participation that make it profitable for both parties; the system's operator and the PEVs' owners. As shown from the results, the third partition would be benefited the most in this case scenario, since their PVs generation outmatched their respective PEVs demands, and therefore had significantly lower to almost non-PEVs energy curtailment. For the following case scenarios C and D, the VVO coordination scheme have been considered. For case C, no PEVs discharge has been allocated. However, it is noted that the total production

costs of energy at the grid level has increased slightly to compensate for the PVs active energy curtailment during peak hours.

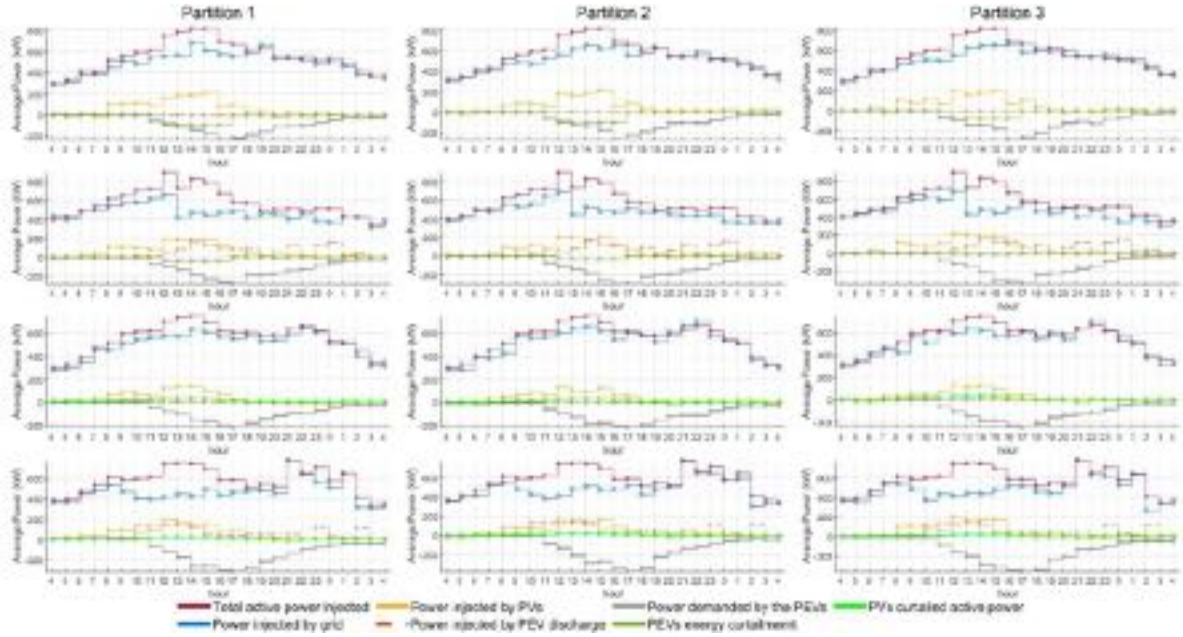

Figure 8-10. Real power injection to the decomposed PDN for: 1) case A, 2) case B, 3) case C, 4) case D.

Surely, it is not desirable to curtail active power from the PV systems, as someone may argue that this is uncalled economic waste. However, incorporating APC at minimized levels could be greatly exploited to relax the OLTC and CB operations while keeping the voltage level within permissible limits. This contributed to a slight increase in the grid's generation cost. However, this controlling scheme has resulted in the riddance of PEVs energy demand curtailment costs, which significantly improve the total operational costs of the grid as shown in table 8.2, and all PEVs demands were met successfully without incorporating significant cost on the PDN. Lastly, case scenario D represent the best financial and operational outcomes. It allows for PEVs owners participation to discharge their energy during congested timeslots, while the VVO coordination scheme is in effect. This will result in lowering the PVs energy curtailment by 17.8% than in case C, reducing the PEVs energy demand curtailment to zero in the three partitioned clusters throughout the peak demands hours, while producing the best financial gain to the grid with the lowest total energy costs incurred. Therefore, the results of case scenario D show the effectiveness of the developed coordination

scheme of this work. Fig 8.10. of this work presents the active power demand of each partition of the modified distribution feeder for the four cases. By convention, the power demand of the PEVs have been considered as negative load. It is worth to mention that the amount of energy requested from the upstream grid during timeslots of peak demands have been reduced in case D as a result of the coordination scheme. This contributes to lowering the energy cost from the grid as shown in table 8.2.

The voltage profile of the modified distribution system considering the four case scenarios is illustrated in fig.8.11. It is noted that the voltage levels for cases C and D are kept lower than nominal voltage levels for most of timeslots of the day as a result of the simultaneous enabling of both RPC and APC in these cases. This is justified from economical point of view, as the operational outcomes outlined in table 8.2 show significant economical savings for the steady-state operation. In addition, this leads to relaxed CBs and OLTCs operations which leads to significant extension to its lifespan. It is worth to mention that the VVO scheme could have improved the voltage level a bit higher in both case scenarios C and D, but the incorporation of APC contributes to reducing any voltage rise or fluctuations. Upon finishing the coordination scheme per each partition in case D, the total APC of the PV inverters is found to be 0.3019 MW, while the total RPC is achieved at 0.7811 Mvar, with the minimum per unit voltage for the system is improved from 0.9291 for case scenario A to 0.9612 for case scenario D at timeslots of 15.00. Primarily, the concept of making each partition solving the optimization problem within its own boundary and considering its own resources have yield better outcomes in resolving voltage violations issues. Fig. 8.12 presents the convergence speed for partition 3 as an example. It can be seen from fig. 8.12 that the per unit voltage as well as the RPC and APC levels are continually adjusted in the first few iterations while swiftly converges.

Table 8-2: Summary of the results for the applied case scenarios

Case	Energy from Grid	PV Energy Cost	Total Energy Cost	PEVs Energy Curtailment Cost			OF Cost
				Partition 1	Partition 2	Partition 3	
A	$3,259.87	$494.17	$3,754.04	$2,375.09	$2,551.64	$1,850.11	$10,530.88
B	$3,011.56	$399.29	$3,410.85	$1,175.82	$975.01	$278.63	$5,840.31
C	$3,407.11	$289.84	$3,696.95	0	0	0	$3,696.95
D	$2,697.09	$253.85	$2,950.94	0	0	0	$2,950.94

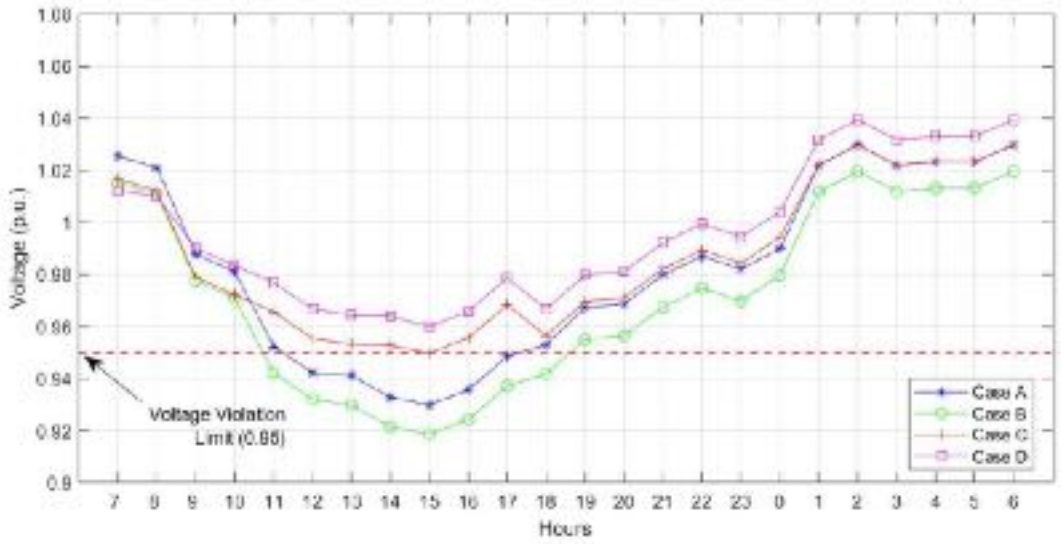

Figure 8-11. The voltage profile for the whole PDN for all case scenarios.

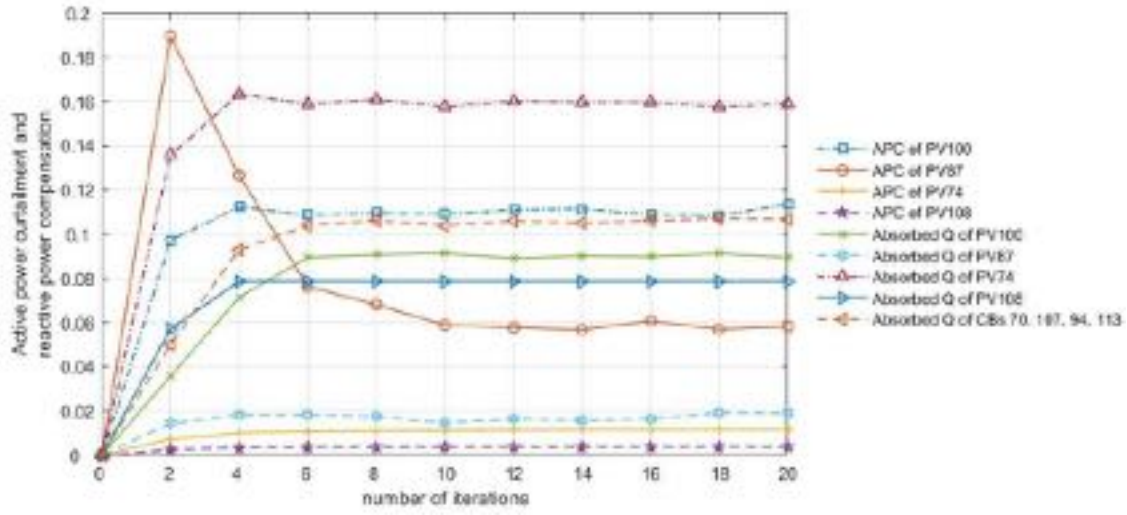

Figure 8-12. Iteration performance for curtailed active power and reactive power absorption for partition 3.

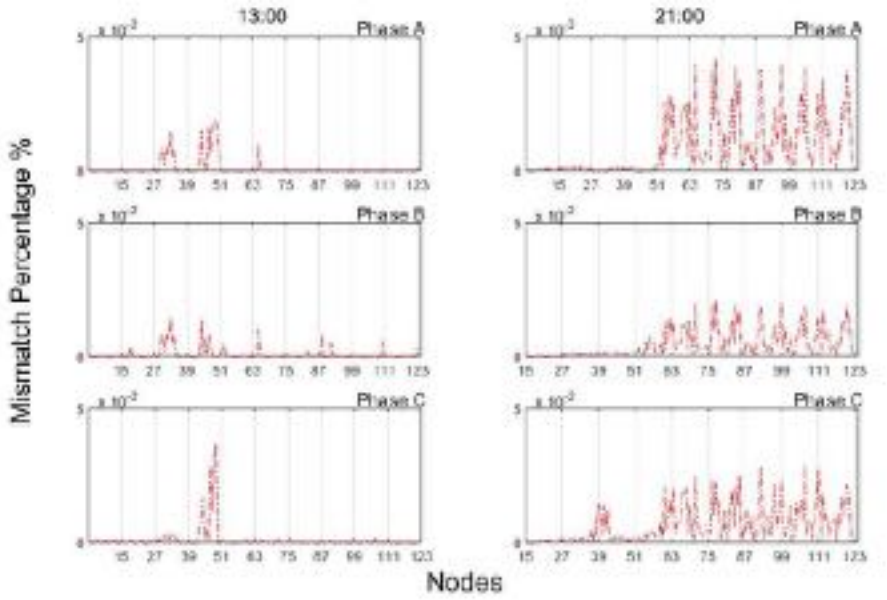

Figure 8-13. Mismatch error for the results of the case scenario A vs standard optimal power flow for the PDN considering the hours 13:00 and 21:00.

To ensure accuracy and robustness of the modified MINLP formulation, comparison against OPF for voltage levels is attained for the whole feeder during timeslots that coincides with peak load demands as well as PEVs demands is illustrated in fig.8.13. As the results shows, a mismatch percentage of 3.59% and 2.87% have been recorded for hours of operation at 13.00 and 21.00, respectively. Both resemble percentage of errors to be less than 5%, and thus indicate a reliable representation of the PDN steady-state simulation. It is worth to mention that the recorded time to find the solution and perform the developed calculations for three partitions ranged between 2.1~2.9 seconds per iteration. For each set of results, the maximum number of iterations was 125 iterations and 355.6 seconds to reach the border residual of less than 0.001.

8.6 Conclusion

Two-stage optimization strategy that aims to achieve optimal and economic power distribution network (PDN) operation within the context of the voltage-reactive power optimization (VVO) problem has been developed. The optimization formulation consisted of a first, time-ahead, optimization process that aims to decompose the PDN into optimal

partitions per the voltage sensitivity values for active and reactive power consumption/injection on the system. An intelligent searching strategy named the community-based-detection particle swarm optimization (CBDPSO) has been developed to ensure reaching an optimal partitioning. Considering the operation of the PDN during peak demands hours, the grid was optimally partitioned into three clusters, which set the stage for the second optimization process to be performed based on a modified MILP. The MILP solves to obtain feasible, economic results while satisfying the operational needs and constraints of the unbalanced three-phase PDN, within the context of the VVO. The goal is to allow a faster and accurate calculation of the VVO problem in a distributed manner. The developed two-stage strategy was tested on the modified IEEE 123 bus system. The obtained results indicate reaching optimal economic gains while maintaining the system's voltage regulation within permissible limits. Furthermore, the solution indicates lower active power curtailment of the PV system and zero energy demand curtailment for the PEVs, which means each partition in the PDN was able to meet its demand even during peak hours, including for the PEVs connection requests. For the PEVs arrival, departure and SoC levels, the work adopted models from previous, well-established stochastic studies that were verified in experimental hardware [181, 182]. Real-time energy prices and load variations have been adopted from real-life distribution feeder data located in Miami-Dade County, Florida, the United States of America, indicating accurate financial modelling in our simulation. Future studies should investigate monetary policies and financial models that regulate the PEVs charging and discharging schedule in a way that contribute to an optimal solution to the VVO problem.

Chapter 9 A Tri-Level Hierarchical Energy Management with Large-Scale Penetration of Electric Vehicles

9.1 Introduction

Major restructuring is in progress for industries that contribute significantly to the GHG emissions. Plug-in Electric Vehicles (PEVs) will play a central role in the significant restructuring of the sources of GHG emissions, the electric power industry and transportation sector. Large-scale penetration of PEVs is considered a major challenge, as the stochastic nature of the PEVs owners are hard to follow which make the process of predicting and ultimately controlling large-scale integration of PEVs a very challenging process. Moreover, uncoordinated EVs charging will lead to significantly overloaded power system networks, which introduces a great burden on the power system operation such as increase voltage fluctuations, overload power transformers and transmission lines, and amplify power system quality problems, to name few. To properly govern such complex process, energy management and control considering PEVs integration has been one of the most important topics in the electrical engineering literature in the recent decade. This chapter aims to provide a unique contribution to this field of study, by proposing tri-level hierarchical coordinated energy management framework, considering large-scale integration of PEVs to the power grid. It is worth mentioning that applied linearization and developed constraints have been achieved to solve the proposed mathematical formula but was removed from this chapter due to page limitations and to preserve the authors' rights to publish them in details as a novel work in their future publication in [201].

Several studies have studied the impact of the large adoption of PEVs without effective uncontrolled charging mechanism [103, 104, 105]. In this dissertation work, we aimed to test the impact of the uncoordinated large-scale adoption of PEVs on the hourly operation of the power distribution grid. Specifically, we provided in chapter five of this

dissertation dynamic modeling of the hourly impact of PEVs integration on the IEEE 34 bus system using the OpenDSS dynamic software of the Electric Power Research Institute (EPRI), considering different PEVs types and energy needs integrated throughout the whole day. Different testing scenarios were conducted and they are presented in detail in chapter five and in [103]. Our study in chapter five concludes that uncoordinated large-scale integration of the PEVs will definitely violate the system's voltage limits and lead to overloading condition and increased energy prices on all consumers connected to the distribution feeder. The authors of reference [104] provide extensive study on the impact of the integration of one million PEVs to the VACAR sub-region of the Southeast Electric Reliability Council (SERC). To achieve the purpose of testing the impact of modeling PEVs load of this size, the authors utilized the Oak Ridge Competitive Electrical Dispatch model to simulate the hourly dispatch of the power sources to meet this large loads. Furthermore, they consider various charging and discharging scenarios with different PEVs sizes, energy requirement and time of connectivity, and reach a conclusion that a typical-size residential power distribution feeder will not be able to withstand charging of PEVs for long hours without causing severe overloading and possibly outage. Reference [105] presents one of the earliest research literature that studies the impact of uncoordinated PEVs integration on the grid. Moreover, the author investigated the integration of 7.5 million PEVs and studied the impact of its integration on the technical, economical and operational aspect of the power grid. They reached a conclusion that unless PEVs load are managed to delay large-scale charging of PEVs from peak hours to off-peak hours, substantial increase of the energy prices is almost certain in several areas of the US interconnected network. Furthermore, reference [105] is one of the first studies that emphasize the needs for energy management and coordination of PEVs that consider postponing PEVs charging demands to times where both energy prices and demand are lower. Additionally, reference [106] concludes that simple charging strategies yield peak demands in several time slots of the day, which require major

investment to upgrade the system's overall generation and transmission capacities. Therefore, there is no doubt that proper energy management and control is needed to deal with the uncertainty of large-scale integration of PEVs. Several methodologies have been developed in the recent years to deal with the challenging task of accounting of PEVs load into the already-congested power grid. Reference [107] presents a two-step framework to coordinate the PEVs charging following a price-based coordination based on linear programming. The authors of reference [108] propose a methodology that account for the design of grid interfaced PEV charging systems incorporating stochastic renewable energy sources and storage units on the electrical infrastructure. Specifically, the authors utilize a linear programming-based framework to optimally choose designs that reduce the overall system's lifecycle cost.

This chapter is arranged as following: section 9.2 provides illustration on the relative information to the developed tri-level hierarchy. Section 9.3 provides the problem formulation for the tri-level energy management optimization. Section 9.4 presents case studies and results. Section 9.5 concludes this chapter with final remarks.

9.2 The Developed Tri-level Hierarchical Energy Management Methodology

9.2.1 The inverse-Demand Curve

As in any other market, consumers in the energy market are expected to naturally react to price variability, which influence on their decisions to obtain the desired services at certain times. This behavior could be effectively characterized by the inverse-demand curve (IDC), which model the price of energy given the overall generation (supply) levels and demand (loads) of an electrical system. Furthermore, the inverse-demand curve could capture the willingness of the consumers to pay additional price to utilize the electricity during specific time frame. This is called as willingness to pay (WTP) factor which indicates the

marginal benefit the consumers would acquire if they proceed to utilize the additional energy service. In accordance with the infamous microeconomic rules, such marginal benefits is estimated based on the requested benefits' size to the overall available quantity of the product, which is the energy service during a specific time period in our study. Rationally speaking, the consumers can expand their marginal benefits by utilize the electrical energy until they reach a level where their marginal benefits equal the energy market price, where at certain points it would be economically unviable and not cost-effective option to continue utilizing the energy. This raises from the fact that basic microeconomics state which is there must be an incremental increase of the cost of a product once it has limited supply. Such incremental cost is also called as the marginal cost, which is a reflection of other factors involved in the market condition, which is in our case, factors that include the level of generation, supply of fuel, violation of operational constraints, among others. These variables influence the marginal cost, especially on the short-term that characterize the daily and/or weekly operation of the power grid.

On one hand, PEVs owners are considered regular consumers of the electrical energy that is needed to charge their vehicles daily. With that being said, there are different energy utilization patterns that are attributed to individual PEV owner. Such patterns are characterized by several factors that are solely defined by only the PEV owner such as the driving patters, personal habits (travel, outdoor activities that require transportation), work condition, vehicle type, etc. Therefore, each PEV would require certain level of energy consumption in a decentralized manner. On the other hand, the power production companies is almost heterogeneous in regard with the energy's cost structure. Specifically, each generation unit that belong to an electrical utility has its own technical and operational status that define the price signal of its energy output. Usually, these generation units run under certain circumstances that lead to increase to its price signal. Circumstances of this nature include scarcity of its generation limits, environmental policies that could limit its production

levels to meet goals of lowering toxic released gases during the generation process, and regulations that requires the utility's operator to run certain types of generators to meet the renewable energy portfolio (RPS) goals, among other factors that contribute effectively in determining the level of supply of a power utility. Therefore, accurate broadcasting of the electrical energy prices must reflect the timely condition of both the supplier (the power utility or system operator) and consumer (PEVs owners in this case). Having said that, there is scarcity in literature to model this important relationship that is well-captured by the demand-inverse curve. Furthermore, the demand-inverse curve is seen by this dissertation as the most effective modeling strategy that better describe the minute-to-minute update of the electric network operation, which result in accurate and reliable energy price signals that could be utilized effectively when determined accurately to manage the energy demand considering large-scale integration of the PEVs. Therefore, the concept of the tri-level hierarchical control framework developed in this chapter is mainly built on the concept of establishing the energy price signals in accordance with the level of supply availability determined by the demand-inverse curve. Finally, this dissertation takes into consideration the operational and technical aspects of both the supplier and consumer when establishing the demand-inverse curve that represent the operation of the developed test system, such as level of congestion on the system, transmission lines constraints, overloading capacities of the lines and power transformers …etc. Fig. 9.1 shows an illustration of determining the price in an inverse-demand curve, based on the marginal cost established by the relation of the available quantity of a product (generation in the energy market) and consumers' demand.

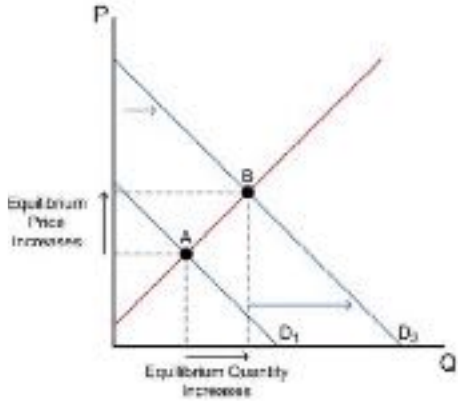

Figure 9-1. Illustration on the concept of the inverse-demand function in microeconomics

9.2.2 *Hybrid Centralized-Decentralized PEVs Charging Coordination*

One of the major benefits of the developed framework scheme is the feature hierarchal coordination process has in integrating the control aspect of both decentralized and centralized management paradigms. Specifically, hierarchal coordination utilizes the best of outcomes of both scheduling mechanisms, based on predetermined duties allocated to different parameters that are integrated in the decision process, such as aggregators at the station level, microgrid agents, and the system operator that oversee the whole energy grid's generation and operation capabilities. In previous literature, hierarchal coordination was developed following either price-based or schedule-based coordination. Decentralized charging mechanisms are mainly built on the price-based concept. However, very limited research in decentralized coordination have considered any form of dynamic charging, with the great majority of this literature focusing on the time-of-use rates, without actually giving considerations to the dynamic nature of the supply-demand of the power utilities that reflect the timely changes of the energy prices. On the other hand, schedule-based coordination is something well-established with the centralized coordination's concept, as there exists a centralized operator or agent that takes decisions, usually in the best of its interest only, based

on the abundant available information in front of it an entity that takes part in running the electrical grid.

In this work, utilization of features from both coordination schemes is a key component to achieve successful incorporation of the developed tri-level hierarchical control coordination strategy. Specifically, information about the PEVs is collected in decentralized manner from the EVs owners (such as the arrival and requested departure times, desired level of energy, … etc). The collected information is processed through an aggregator that is located at the station level. The aggregator collects the energy and power requirements of all connected and request-to-connect PEVs, send it to its attached microgrid for further processing. Then, the microgrid runs the lower-level energy optimization problem in a centralized manner based on inputs from its connected aggregator downstream, and from the system operator upstream. The coordination between the system operator and its attached microgrid are solved based on the upper-level energy optimization problem, formulated following the Stackelberg leader and follower model, and based on mixed-integer quadratic programming (MIQP) formulation that takes into consideration the carbon emissions cap and trade policies as well as the RPS requirement from the local authority. Next subsection presents the relationship between the system operator (as a leader) and microgrid (as follower) that is utilized in the developed energy management hierarchy in this chapter. It should be noted that the supply and demand requirements in all of the three levels of coordination are represented by the inverse-demand curves, as discussed in the previous subsection, and will be furtherly illustrated in the following sections.

9.2.3 *The Stackelberg Model for PEVs Charging Coordination*

The concept of the Stackelberg model is based on multi-period dynamic games, where two players decide their strategic moves in a sequential manner rather than simultaneously. Typically, the leader in the Stackelberg model starts with the first move based on knowledge

and anticipation of its follower reaction. Once the leader's move intact, the follower then provides its strategic decision in the sequential period with respect with the leader's first move. Such process could be modeled in bi-level optimization problem considering the sequential trends in issuing decisions, that could be in our work nothing but the strategic moves about the grid's operation considering large-scale PEVs integration. Specifically, the system operator will act in this scenario as leader that solve its own revenue-maximization optimization model based on the knowledge of the operation of its attached microgrids, which as followers, provide its strategic decisions based on the information from its lower-level optimization problem with the PEVs station aggregators. More detail on the scheme of the developed hierarchy of this chapter and the modeling of the upper-level optimization problem is given in the following section.

9.3 Mathematical Formulation of the Developed Tri-Level Hierarchical Energy Management Strategy

9.3.1 Mathematical formulation of the lower-level (Hybrid Centralized-Decentralized PEVs Charging Coordination)

Suppose that there are a large group of EVs that are looking to charge over a multi-period timeslot $\Im = \{0, \ldots, T-1\}$. The SoC of an EV n that would like to connect to an aggregator j under microgrid i is presented as:

$$SoC_{ijn}(t+1) = SoC_{ijn}(t) + \frac{h_n^{ev}}{B_{ijn}}.D_{ijn}^{EV} \tag{9.1}$$

Where η_n^{EV} represents the charging efficiency of EV n such that $\eta_{ijn}^{EV} \in [0.1]$, B_{ijn} represents the EV battery's energy capacity, and D_{ijn}^{EV} as the charging power demanded by the n^{th} EV at an aggregator j under a microgrid i, and is denoted by kW needs of the vehicle such that:

$$D_{ijn}^{EV} = [D_{ijn}^{EV}(t); t \hat{I} \acute{A}] \tag{9.2}$$

$$\sum_{t \in \Im} D_{ijn}^{EV}(t) = \sum_{n \in N_{ijn}^{t}} \frac{B_{ijn}}{\eta_{ijn}^{EV}} . [SoC_{ijn}^{dept\_mx} - SoC_{ijn}^{a}] \tag{9.3}$$

Where SoC_{ijn}^{a} and $SoC_{ijn}^{dept\_mx}$ represent the arrival and maximum possible SoC of an EV n. It should be noted that B_{ijn} highly dependent on several extrinsic factors such as the driving distance, driving speed, EVs' type, road condition and traffic jam. Moreover, the charging power is admissible to a charging station with an aggregator j if:

$$D_{ijn,t}^{EV} = \begin{cases} \in [-\zeta_{ijn}^{-}, \zeta_{ijn}^{+}], t \in \Im \\ = 0, \quad otherwise \end{cases} \tag{9.4}$$

Where $\zeta_{ijn}^{-}, \zeta_{ijn}^{+}$ are factors that resembles the uniform rate of charging and discharging power over time. It should be noted that for an EV to receive service, both (mark the last two equations) need to be satisfied. Additionally, the charging needs of an EV must be fully satisfied as follows:

$$\eta_{ijn}^{EV} . \sum_{k=0}^{T_{ijn}-1} D_{ijn}^{EV}(t+k) . \Delta + SoC_{ijn}(t) . B_{ijn} = SoC_{ijn}^{dept} . B_{ijn} \tag{9.5}$$

Additionally, the capacity of the power distribution transformer that aggregator j needs to be within safe limit, such that the accumlated charging demands of EVs do does not cause transformer overloading as follow:

$$\sum_{n \in N_{ijn}^{t}} \sum_{t \in \Im} D_{ijn}^{EV}(t+k) \leq M_{ij}.\sigma_{ij}(t+k) \tag{9.6}$$

$$[SoC_{ijn}^{dept} - J_n].B_{ijn} \leq h_n^{ev}.\sum_{k=0}^{T_{ijn}(t)-1} D_{ijn}^{EV}(t+k).\mathrm{D} + SoC_{ijn}^{a}.B_{ijn} \leq SoC_{ijn}^{dept}.B_{ijn} \tag{9.7}$$

Many studies in literature have considered coordinating EVs charging over multi-time period. Studies such as in [193] has considered blocking the service requests from EVs during peak demands to avoid causing congestion. While this might be a technically valid solution, it is against the basic concept of electricity market of which provides are legally obligated to provide services to consumers at all time, except when there is an outage. Furthermore, it is assuming that service providers must plan their operation in a way that make EVs charging request permissible at any time during the day. However, a service provider cannot guarantee the best price to the EVs owner based on the status of the grid's, as the pricing is highly dependable on the operational status of the provider (supply availability, lines and apparatus overloading, etc.) as well as the demand level.

Let us consider a microgrid i that is connected to a system of microgrids, all are operating under a unified system operator. Each microgrid i has G generation units s.t. ($g \in G_i$), with each g has generation capacity ($\mathcal{X}_i^g$) as well as associated marginal costs (C_i^g). The centralized objective function to be solved at the microgrid i level during timeslot t is formulated as follow:

$$J = J_1 + J_2 + J_3 + J_4 \tag{9.8}$$

The first objective function, J_1, accounts for the integration of the area beneath the inverse-demand curve for the base demand (non-EVs load) on microgrid i, denoted D_i^{Base}, given the instantaneous marginal cost C_i', as follows:

$$J_1 = [C_i'(t+k).D_i^{Base}(t+k) - \frac{C_i'(t+k)}{2\Gamma_i(t+k)}[D_i^{Base}(t+k)^2 - \sum_{J\in J_i}\sum_{g\in G_i} x_i(t+k)^2].\Delta \quad (9.9)$$

Where Γ_i is the cumulative capacity of microgrid i in MW, represented in the x-axis of the inverse-demand curve. The importance of this function is to model the energy price with respect to the change of demand of non-EVs loads on the microgrid. The second objective function, J_2, accounts for the integration of EVs load demand at the timeslot of interest beneath the inverse-demand curve, given microgrid i's operational cost directed as a result of aggregator j EVs scheduling, as follow:

$$J_2 = [b_{ij}'(t+k).D_{ijn}^{EV}(t+k) - \frac{b_{ij}'(t+k)}{2\Gamma_i(t+k)}[\sum_{n\in N_{ijn}^t} D_{ijn}^{EV}(t+k)^2].\Delta \quad (9.10)$$

The importance of this function is to accurately represent the change of demand in microgrid i's attached aggregators as a result of demand increase, and its subsequent increase in the production that the microgrid is expected to generate or buy to meet this specific extra demand. The third objective function, J_3, accounts for the adds-on prices as a result of capacity scarcity exchange between interconnected microgrids i and m. Someone can look at this price as the compensation for the capacity remuneration for being available to another market participant.

$$J_3 = [Y_{mi}^{g}(t)[x_{mi}^{g}(t) - \mathcal{X}_{mi}^{g}(t)].\Delta \tag{9.11}$$

The fourth objective function, J_4, estmates the discharging requirements of the PEVs which opt to provide their energy toward their assigned microgrids during the times when the grid faces higher demand, as following:

$$J_4 = \sum V_{ijn}(D_{ijn}^{EV\_Disch}(t+k)).\mathrm{D} \tag{9.12}$$

The fifth objective function, J_5, is the utility function associated with an PEV n, connected to an aggregator j under microgrids i, as follows:

$$J_5 = \sum_{n \in N_{ijn}} U_{ijn}(D_{ijn}^{EV}) \tag{9.13}$$

Where

$$U_n(D_n^{EV}) = \mathcal{U}(\| D_n^{EV} \|_1) - \sum_{t \in \Im} V_n(D_n^{EV}(t)) \tag{9.14}$$

$$V_n(t+k) = C_{ijn}^{extra}(t+k).D_{ijn}^{EV}(t+k)] + \zeta_{ijn}(t+k)D_{ijn}^{EV,disch}(t+k) \tag{9.15}$$

$$\mathcal{U}(\| D_n^{EV} \|_1) = -\varphi(\| D_n^{EV} \|_1 - B_{ijn})^2 \tag{9.16}$$

The battery degradation cost is found by the following expression [194, 195]:

$$\zeta_{ijn}(t) = \alpha_{ijn}^{1}(D_{ijn}^{EV}(t))^2 + \alpha_{ijn}^{2}(D_{ijn}^{EV}(t)) + \alpha_{ijn}^{3} \tag{9.17}$$

$$L(D_{ijn}^{EV}, \lambda) = J + \sum_{J \in J_i} \sum_{n \in N_{ijn}^{t}} \lambda_{ijn}.[B_{ijn} - \sum_{t \in \Im} D_{ijn}^{EV}] \tag{9.18}$$

This equation provides the LaGrangian multiplier methodology to

$$B_{ijn} = z_{ijn}[SoC_{ijn}^{dept\_mx} - SoC_{ijn}^{a}] \tag{9.19}$$

$$B_{ijn} = \xi_{ijn}.[SoC_{ijn}^{dept\_mx} - SoC_{ijn}^{a}] \tag{9.20}$$

$$\lambda_{ijn} = C_{ij}^{\prime,*}(D_{ijn}^{Base\_*}) + b_{ij}^{\prime,*}(D_{ijn}^{EV\_*}) - \zeta_{ijn}^{\prime}(D_{ijn}^{EV,disch\_*}) \tag{9.21}$$

$$\lambda_{ijn} \geq C_{ij}^{\prime,*}(D_{ijn}^{Base\_*}) + b_{ij}^{\prime,*}(D_{ijn}^{EV\_*}) - \zeta_{ijn}^{\prime}(D_{ijn}^{EV,disch\_*}) \tag{9.22}$$

$$\begin{cases} \text{eq}(9.21), \text{if } D_{ijn}^{EV\_*} > 0 \\ \text{eq}(9.22), \text{if } D_{ijn}^{EV\_*} = 0 \end{cases} \tag{9.23}$$

For a group of EVs n such that $n \in N_{ijn}^{t}$, the energy cost to meet the charging requirements for the n^{th} EV under an aggregator j is formulated as following:

$$J(D_{ijn}^{EV}, Pr(t)) = \sum_{t \in \mathfrak{T}} -\zeta_{ijn}(t).D_{ijn}^{EV,disch}(t) + Pr(t).D_{ijn}^{EV}(t) \tag{9.24}$$

Where $Pr(t)$ indicates the instantaneous charging price per each connected vehicle, and is broadcasted by microgrid i as follow:

$$Pr(t) = C_{ij}^{*}(t) + b_{ijn}^{*}(t) \tag{9.25}$$

Let us denote $D_{ijn}^{EV\_*}$ as the updated charging requirement for n^{th} EV, then the j^{th} aggregator that oversee the charging scheduling aims to minimize the per vehicle charging cost such that:

$$D_{ijn}^{EV\_*}(Pr(t)) = \underset{D_{ijn}^{EV} \in \mathcal{D}^{EV}}{argmin} \left[D_{ijn}^{EV}, Pr(t)\right] \tag{9.26}$$

Such that

$$C_{ij}^{*}(t) = \sum_{J \in J_i} D_{ij}^{B}(t) \,.\, [C_{ij}'(t)] + \omega_{ij}(t) \tag{9.27}$$

$$b_{ijn}^{*}(t) = \sum_{J \in J_i} \sum_{n \in N_{ijn}^{t}} D_{ijn}^{EV\_*}(t) \,.\, [b_{ijn}'(t)] + \kappa_{ij}(t) \tag{9.28}$$

Both $\omega_{ij}(t)$ and $\kappa_{ij}(t)$ represent a wheeling charge that resembles the cost of exchanging energy during time slot t with interconnected microgrids $\in I$, and with nearby stations. It should be noted that the first part of the summation in equation represent the system. The charging requirements for a collection of PEVs are updated in decentralized manner. Such requirements depend mainly on the arrival and requested (departure) SoC, parking duration and grid's operational status that dictate the energy prices based on the inverse-demand curve that resemble the grid's instantaneous supply and demand. Specifically, the aggregator receives requests to charge the vehicles for the next timeslot. Each aggregator then sends the charging scheduling that includes the currently connected EVs and the newly introduced requests to its upstream microgrid. The associated microgird then collects the updated scheduling of all aggregators beneath its authority and run its own centralized optimization problem (as discussed in the following subsection) based on other inputs that includes other load on its grid (non-EVs demand), power production from its own generation unit as well as from the system operator upstream, power exchange (receive or deliver) among its nearby microgrids, transformer and lines overloading conditions, among others. After updating its own inverse-demand curve, each microgrid that broadcast a unique price signal for each of its attached aggregators.

As mentioned earlier, the price signal that is sent specifically to an individual EV is composed of the power production price that is jointly determined by the upper layer (system operator) as well as the middle layer (microgrid), and the marginal operation price that is determined for each aggregator by its assigned microgrid.

$$C_{ij}^{(0)}(t) = [C_{ij}^{*}(t);\ t \in \Im] \tag{9.29}$$

$$b_{ijn}^{(0)}(t) = [b_{ijn}^{*}(t);\ t \in \Im] \tag{9.30}$$

An iterative, offline, decentralized pricing mechanism is implemented in this work prior for the charging timeslot to identify the best pricing signal for each vehicle. Mainly, this mechanism takes into consideration the best charging requirement decision taken by each EV's owner, which is assumed to be influenced with respect to the updated pricing signal. The decentralized mechanism works as follows:

- An initial power production and marginal operation prices (based on equations 9.29 and 9.30)
- Set

$$Pr^{(0)}(t) = [C_{ij}^{(0)}(t) + b_{ijn}^{(0)}(t);\ t \in \Im] \tag{9.31}$$

- Set $h = 0$, $\epsilon = \epsilon_0$, such that $\epsilon_0 > 0$
- For $\epsilon_0 > 0$,
  - Execute the charging requirement decision $D_{ijn}^{EV\_(h+1)}$ with respect to $Pr^{(h)}(t)$, at an aggregator level as follow:

$$D_{ijn}^{EV\_(h+1)}(Pr^{(h)}(t)) = \underset{D_{ijn}^{EV} \in \mathcal{D}^{EV}}{argmin} \sum_{t \in \Im} [\zeta_{ijn}.(D_{ijn}^{EV,disch}(t) + b_{ijn}(t).D_{ijn}^{EV\_*}(t)] \tag{9.32}$$

- Each aggregator sends the charging requirement decisions of $D_{ijn}^{EV\_(h+1)}$ to its attached microgrid.
- Each microgrid report its total demand (EVs and non-EVs), generation level as well as its committed power exchange with the system operator. Based on the signal from the system operator, the microgrid updates its power production price (that includes any energy purchases from upstream grid) as follows:

$$C_{ij}^{(h+1)}(t) = \sum_{J \in J_i} D_{ij}^{B\_*(h+1)}(t).[C'_{ij}] + \omega_{ij}(t) \tag{9.33}$$

- Each microgrid updates the pricing signal with respect to its own instantaneous inverse-demand curve and operational status as follow:

$$b_{ijn}^{(h+1)}(t) = \sum_{j \in J_i} \sum_{n \in N_{ijn}^{t}} D_{ijn}^{EV\_*(h+1)}(t).[b'_{ijn}] + \kappa_{ij}(t) \tag{9.34}$$

- The microgrid broadcasts the charging prices per each vehicle, based on the EV scheduling at aggregator j, as follow:

$$Pr^{(h+1)}(t) = C_{ij}^{(h+1)}(t) + b_{ijn}^{(h+1)}(t) \tag{9.35}$$

- Update ϵ, as follow:

$$\epsilon = \sum_{j \in J_i} \| Pr^{(h+1)} - Pr^{(h)} \| \tag{9.36}$$

- Update $h = h + 1$, if needed,

9.3.2 Mathematical Formulation of the Upper-Level Based on Stackelberg Model

Considering an oligopolistic energy market with a system operator that oversee collection of microgrids, each microgrid has its own generation units and has the capability of exchanging power (selling or receiving) with other interconnected microgrids. Let us assume that each microgrid has G generation units such that $g \in G$, with their marginal cost production at microgrid i is represented as C_i^g in $\$/_{MWh}$ with generation capacity x_i^g in MWh. The objective function is formulated as follow:

$$\mathrm{F} = \sum_{\mathrm{f}=1}^{10} \mathrm{f} \tag{9.37}$$

The following quadratic program (QP) optimization problem is formulated to solve for the Nash-Cournot equilibrium as a mixed-integer quadratic programming (MIQP) problem, as follow:

$$F_1 = \sum_{i \in I} \sum_{t \in \mathcal{J}} [C_i(t+l).D_i(t+l) - \frac{C_i(t+l)}{2\Gamma_i\,(t+l)}.[D_i(t+l)^2 + \sum_{i \in I} \sum_{g \in G} x_i(t + l)^2].\Delta - \sum_{i,g \in G_{i,t}} C_i^g(t+l).x_i^g(t+l).\Delta \tag{9.38}$$

The objective function F_1 intends to maximize the social-welfare of the consumers. At a timeslot t, the first part of the objective function sums the integral of the area covered under the demand-inverse curve, which is subtracted by the second part which represent the energy generation costs at microgrid i level. Γ_i represents the cumulative capacity in MW in the inverse-demand curve, D_i represents the total demand at microgrid i that include, at this level of the optimization problem, both the EVs and non-EVs loads.

$$F_2 = \sum_{i,g\in G_{i,t}} Y_i^g(t+l).[x_i^g(t+l) - \mathfrak{X}_i^g].\Delta \tag{9.39}$$

Objective equation (9.38) represents the net summations of capacity scarcity exchange on microgrid i during a timeslot t:

$$F_3 = \sum_{s,t} \lambda_s^+(t+l).[\sum_i \mathbb{Y}_{s,i}.\mathcal{L}_i(t+l) - \mathbb{Z}_s].\Delta \tag{9.40}$$

$$F_4 = \sum_{s,t} \lambda_s^-(t+l).[-\sum_i \mathbb{Y}_{s,i}.\mathcal{L}_i(t+l) - \mathbb{Z}_s].\Delta \tag{9.41}$$

Here, $\mathbb{Y}_{s,i}$ in equations (9.40 and 9.41) is a matrix representation of the reciprocal of the grid's reactance between microgrids $i\ and\ j$. It is worth mentioning that in case of a power transfer between the microgrids, then the column that represent the supplier microgrid is filled with zero entries to represent the node as a sink bus. Furthermore, matrix $\mathbb{Y}_{s,i}$is multiplied by either a positive or negative sign in a way that define the direction of the power flow in the interconnected energy network. On the other hand, $\mathcal{L}_i$ is a variable that represents the net energy mass-balance of receiving and delivering power at the microgrid during a timeslot t. Its multiplication of matrix $\mathbb{Y}_{s,i}$ indicates the upper and lower limits on the transmission line between microgrids $i\ and\ j$. Finally, $\mathbb{Z}_s$ represents the MW capacity limit of the transmission line between any two microgrids in the system.

$$F_5 = \sum_{i\in I}\sum_{t\in\mathcal{J}} C_i(t+l).[\mathcal{L}_i(t+l) - \sum_{l,g\in G_{l,t}} x_{li}^g(t+l) + D_i(t+l)].\Delta \tag{9.42}$$

$$F_6 = \sum_{t\in\mathcal{J}} \varphi_i(t+l).[-\sum_{i\in I} \mathcal{L}_i(t+l)].\Delta \tag{9.43}$$

The objective equations (9.42 and 9.43) quantify the total marginal price of each microgrid as a result of energy transmission charges between different microgrids. Specifically, the microgrid's locational marginal price, C_i, is composed of both the system price, φ_i, because of generating or purchasing/selling power, and wheeling charge, $\omega_i(t)$, that represents the charges accumulated for utilizing the network to transfer power when the grid is congested. Such charges could be found using the following formula:

$$\omega_i(t) = C_i(t) - \varphi_i(t) \tag{9.44}$$

Objective function (9.45) is formulated to regulate the carbon emission in the system, as follows:

$$F_7 = p^{co} \left[\sum_{l,i,g \in G_{l,i,t}} G_{li}^{co} . x_{li}^{g} . \Delta - \bar{G} \right] \tag{9.45}$$

Where p^{co} represents the CO_2 permit price that each microgrid must pay with respect with the level of emissions from its generating units. G_{li}^{co}represents the rate of CO_2 emission from microgrid i during timeslot t, and $\bar{G}$ is the emission's cap level, established by the system's operator with respect with the operational status of the interconnected system.

Transfer of MW between microgrids $i \; and \; m$ I affect directly the linear inverse-demand curve at both microgrids. Therefore, the elasticity price as a result of changes in both microgrids' x-axis level is described as follows:

$$F_8 = \sum_{m,i,g \in G_{m,i,t}} \mathcal{E}_{mig}(t+l) . (-x_{mi}^{g}(t+l)) . \Delta \tag{9.46}$$

Where

$$\varepsilon_{mi} = \frac{\frac{\pm \Gamma'}{\Gamma}}{\frac{\pm C'}{C}} \tag{9.47}$$

$$F_9 = p_{REP}[\sum_{i \in I} \sum_{q \in Q_i} x_i^q(t).\Delta - \Omega[\sum_{i \in I} \sum_{g \in G_i} x_i^g(t).\Delta]] \tag{9.48}$$

The objective function given in equation (9.48) represents the renewable energy portfolio (RPS) requirement per each microgrid at the interconnected system. Furthermore, an RPS level of the total generation sources is assumed to be mandated by the local authority so that a specific percentage, Ω, of the total generation must be incorporated from generators q that belongs to a set of renewable energy sources Q_i. p_{REP} represents the monetary obligations per each microgrid, with its signs as indication whether the microgrid is selling (positive) or receiving (negative) energy from renewable energy sources from a nearby microgrid. The emission cost is neglected in the case of RPS certification trading since renewable sources does not emit any CO_2 in the generation process.

Finally, availability of energy to provide to the nearby station (include it only in the lower level between the aggregator and microgrid), is represented as the capacity level each microgrid has after the implementation of the optimization problem in the previous timeslot, as follows:

$$F_{10} = \sum_{i \in I} \sum_{t \in \mathcal{J}} \mathcal{A}_i(t + 2l).\Delta \tag{9.49}$$

The upper level that represents the system's operator at the first layer could be modeled in a similar manner as following:

$$\sum_{i \in I} \sum_{g \in G_l} [C_i(t + l) - C_{li}^g(t + l) - p^{co} G_{li}^{co} -] \, x_{li}^g(t + l).\Delta \tag{9.50}$$

$$\mathcal{R} = \mathcal{R}_1 - [\mathcal{R}_2 + \mathcal{R}_3 + \mathcal{R}_4 + \mathcal{R}_5 + \mathcal{R}_6] \tag{9.51}$$

$$\mathcal{R}_1 = \sum_{i,t} [C_i'(t+l).D_i(t+l) - \frac{C_i'(t+l)}{\Gamma_i(t+l)}(D_i(t+l)^2)].\Delta \tag{9.52}$$

$$\mathcal{R}_2 = \sum_{m,i,g\in G_{mi,t}} [\frac{C_i'(t+l)}{\Gamma_i(t+l)}. \sum_{(g\prime,g)\in G_{mi}} x_{mi}^{g\prime}(t+l).x_{mi}^{g}(t+l)].\Delta \tag{9.53}$$

$$\mathcal{R}_3 = \sum_{m,i,g\in G_{mi,t}} C_{li}^{g}(t+l).x_{li}^{g}(t+l).\Delta \tag{9.54}$$

$$\mathcal{R}_4 = \sum_{s,t} [\lambda_s^+(t+l) + \lambda_s^-(t+l)].\mathbb{Z}_s.\Delta - p^{co}\bar{G} \tag{9.55}$$

$$\mathcal{R}_5 = \sum_{m,i,g\in G_{mi,t}} \Upsilon_{mi}^{g}(t+l).\mathfrak{X}_{mi}^{g}.\Delta \tag{9.56}$$

$$\mathcal{R}_6 = p_{REP}[\sum_{q\in Q_l} x_{li}^{q}(t).\Delta - \Omega[\sum_{g\in G_l} x_{li}^{g}(t).\Delta]] \tag{9.57}$$

The system operator projects revenue from selling energy to the downstream level of microgrids minus the operational costs that is imposed on it by its local or state governing agency. Such operational costs include the costs of the CO_2 permits and RPS permits imposed by state or local regulators. To obtain optimal solution to the microgrid's layer, variables of the system operator's layer need to be fixed. This to allow representation of the optimal primal and dual solutions at the microgrid level as functions of $x_{li}^{g}(t+l)$. The objective function given in (9.50) is now a convex mixed-integer quadratic programming function, with linear equalities and inequalities constraints. It could be solved using commercial optimization toolbox such as CPLEX [190] and Gurobi [199, 200]

9.4 Case Studies

In order to test the effectiveness of the developed tri-level hierarchal control of energy management considering large-scale integration of EVs, case studies were carried out on the modified IEEE 123 bus system. The case studies considered the optimal decomposition of this test system into three partitions, as discussed in the previous chapter of this dissertation. In this chapter, we assume that each partition is run by a microgrid. Thus, we assume that the system operator is dealing with three microgrid, each microgrid has four charging stations within its jurisdiction. The results of the case studies are presented and discussed in this section.

9.4.1 Case system description

Figure 9.2 of this chapter presents an illustration of the modified IEEE 123 bus system, with the incorporation of three microgrids. The system information are given in tables 9.1. The resistive and inductance parameters of the lines are set to be 0.05 and 0.11 per unit, while the system's base MVA is 100 [191]. The system includes ten PV system units at different capacities, five gas-fired micro turbines with 250 kW in capacity, and five diesel-fired micro turbine at 250 kW. The marginal costs as well as the emission costs of the generation units have been adopted from [196], and are labeled in table 9.2. The total load on the system is 3.8 MW. As stated earlier, when a microgrid reaches its maximum generation capability, it can purchase power from either the upstream grid, which run by the system operator, or from its neighboring microgrid, based on information supplied by the system operator.

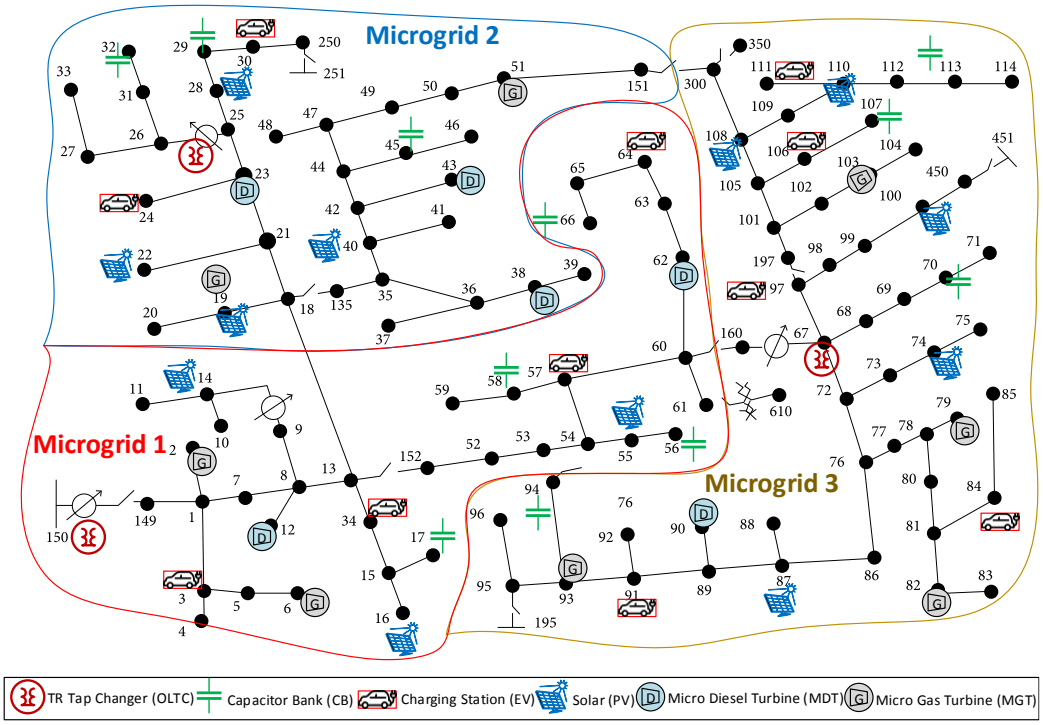

Figure 9-2. The modified IEEE 123 test system with the energy grid information

Table 9-1: Characteristic of the generation units in the system

Unit	No of Gen Units	Capacity	Marginal Cost	Capacity Factor	CO_2 emission rate
MGT	5	250 kW	0.199	0.72	0.2 kg. Cos /KWh
MDT	5	250 kW	0.125	0.72	0.28
PV	10	75 kW (4) 100 kW (4) 125 kW (3)	0	0.28	0

9.4.2 *Simulation Results*

The results of the developed tri-level structure show that the developed system is able to coordinate in an effective and efficient manner the energy management of electric grid, taking into consideration large-scale integration of the EVs. The arrival and departure of the EVs into the charging station is beyond the scope of this work; therefore, we adopt them based on the well-established studies in [181, 182]. As mentioned earlier, the system operator acts a leader in the Stackelberg hierarchy, while the microgrid operators act as followers. The emission cap is set in this work at 2500 kt. The solutions were obtained based on solving the

MIQP function illustrated in this chapter. To show effectiveness of the developed hierarchy, we make comparisons with the obtained results versus normalized results of previously-published energy management framework.

Tables 9.1 through 9.3 show the effectiveness of the developed framework in this chapter. The system operator acts as a leader that exert power in the level of generation, energy and permits prices. As noted, the production output is less than the Cournot-based framework [198], since the latter surpass the generation levels to increase their revenue margins. Nevertheless, the results show that the operational revenue under our developed methodology is the highest one which indicates an optimal combination among the generation resources and power exchange to reduce the CO2 emissions costs. Furthermore, it is noted that the developed hierarchy successfully minimizes the price of CO2 permits since the operator allows exchange of energy to reduce dependence on the diesel-fired generation units that emits higher level of CO2. As results in figs. 9.2 and 9.3 show, MG1 and MG2, which integrate four diesel units on their premises, buy energy from MG3, request energy discharge from PEVs consumers, and request energy support from the upstream network to support certain amount of energy rather than generating them from their diesel-fired generation units. As result of the decentralized charging algorithm, the energy prices successfully influence the PEVs owners to postpone their charging. It is worth to mention that the developed hierarchy, driven by the need to meet certain RPS percentage per microgird, allows more energy exchange. Certainly and as result of the cap and trade implementation, it would more cost efficient for MG1 to buy energy from MG3 than to produce it from its own diesel-fired micro tubines.

Table 9-2: Results comparisons between the developed tri-level framework vs previsouly reported literature in perfect competition (PC) and Cournot methdologies

	PC [197]	Cournot [198]	Ours
Generation Output (MWh)			

System operator	84.21	87.25	85.45
MG1	19.52	17.43	17.92
MG2	16.35	15.40	16.12
MG3	20.83	20.95	21.95
Total	140.91	141.03	141.44
CO_2 emissions [kt]	2500	2500	2500
Permit price [$/kt]	1500	890	100

As shown in tables 9.2 and 9.3, the developed hierarchy successfully led to reduced energy pricing throughout the day. It is worth to mention that prices vary per each microgrid as a result of the variety of generation levels of its distributed generators. It is noted from the presented results in table that as result of the energy exchange that both MG1 and MG2 perform during peak demand hours, their peak energy prices are slightly higher than those at MG3. This is contributed mainly to the wheeling charges illustrated in equation in this dissertation. The wheeling charges has no effect in the off-peak period since the level of congestion on the lines is significantly lower than during peak demands hours. Additionally, it is worth to mention that if the modified test system has higher congestion capacity, then the wheeling charges would have been significantly diminished during peak demand hours, and thus the energy prices during these time periods. Also, it is widely evident that the cournot model would yield higher energy prices since this type of energy market would lead to lower energy generation output and exchanges to drive the energy prices upward and obtain higher profits accordingly. This contributes to the developed model surpassing the Cournot model in terms of social-welfare to average consumers. Figures 9.3 and 9.4 shows the optimal energy prices obtained considering the developed hierarchy. Furthermore, it shows the effectiveness in shifting the PEVs loads into off-peak demands following the implementation of the developed energy management strategy. The two figures show great improvements in the system operation, where there is no system overloading conditions as shown in figures 9.4 and 9.5, compared with pre-implementation of our developed work.

Table 9-3: Peak and off-peak energy prices for the benchmark simulations

	PC		Co		Ours	
	Peak	Off-peak	Peak	Off-peak	Peak	Off-peak
Energy price ($/KWh)						
System operator	0.214	0.152	0.191	0.142	0.165	0.091
MG1	0.192	0.154	0.180	0.155	0.160	0.105
MG2	0.201	0.145	0.178	0.147	0.171	0.110
MG3	0.188	0.134	0.169	0.125	0.147	0.082

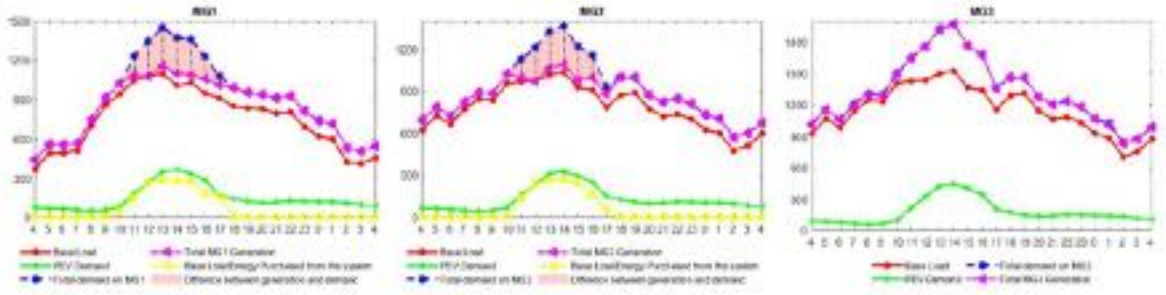

Figure 9-3. The system's daily operation before the implementation of the developed framework

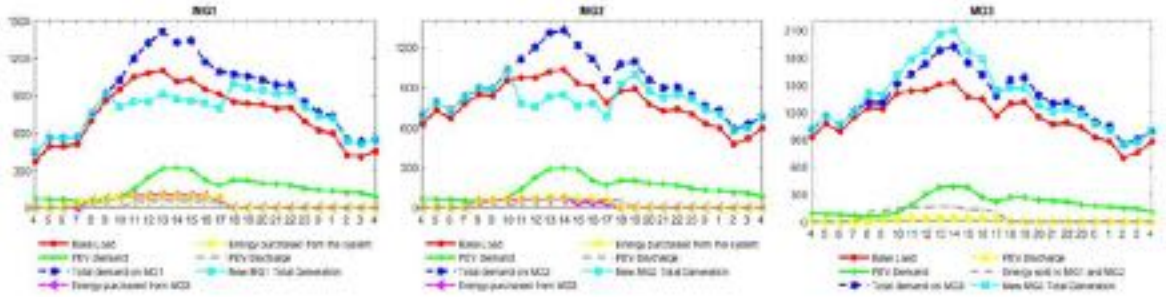

Figure 9-4. The system's daily operation after the implementation of the developed framework

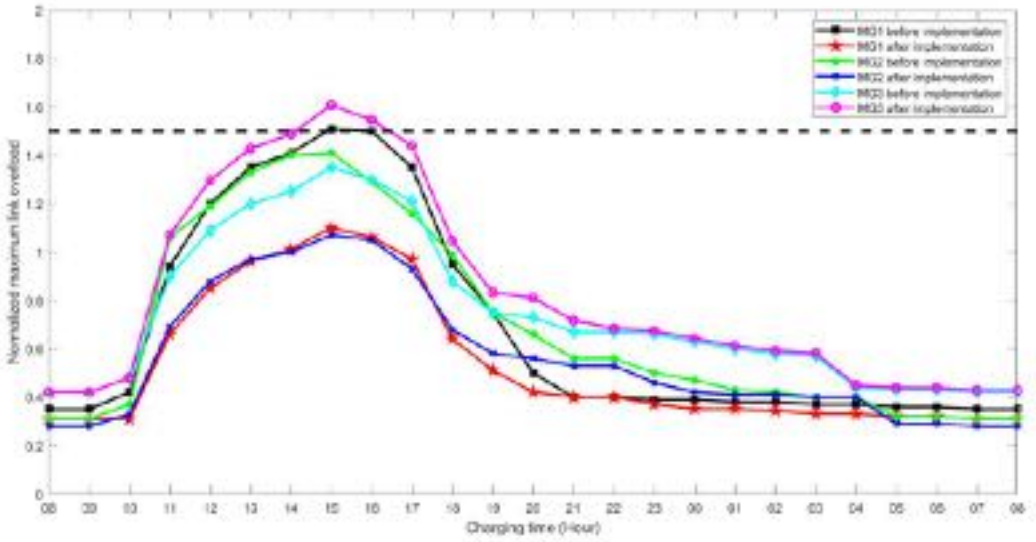

Figure 9-5. System overloading condition with and without the implementation of the developed framework

In addition, results show the impact of the updated aggregated charging needs of the EVs owners as result of implementing the developed framework. Figure 9.6 provides illustration on the charging loads after the implementation of the control strategy. Furthermore, the optimal energy management that incorporates accurate energy price signals based on the network condition considering the inelasticity of the base demand. Additionally, figure 9.7 shows the impact of the developed strategy on both energy and power requests on a station's aggregator under MG2. Specifically, each aggregator has upper and lower limit dictated by its attached microgrid. During the peak hours, and by implementing the discharging price offer illustrated in equation (9.12), the aggregator's limit move up in values, as positive values in figure indicates energy supply to MG2 during the peak demand hours windows. Finally, fig 9.6 shows the impact of the implemented strategy on the overloading capacity of the system. Specifically, pre-implementation shows that both power transformers at MG1 and MG2 violates their capacity limitations. Accordingly, incorporating the TRs capacity into the pricing scheme have forced good amount of PEVs to change their vehicles charging which successfully led to flattening the charging curve, as shown as well in fig. 9.4 of this chapter.

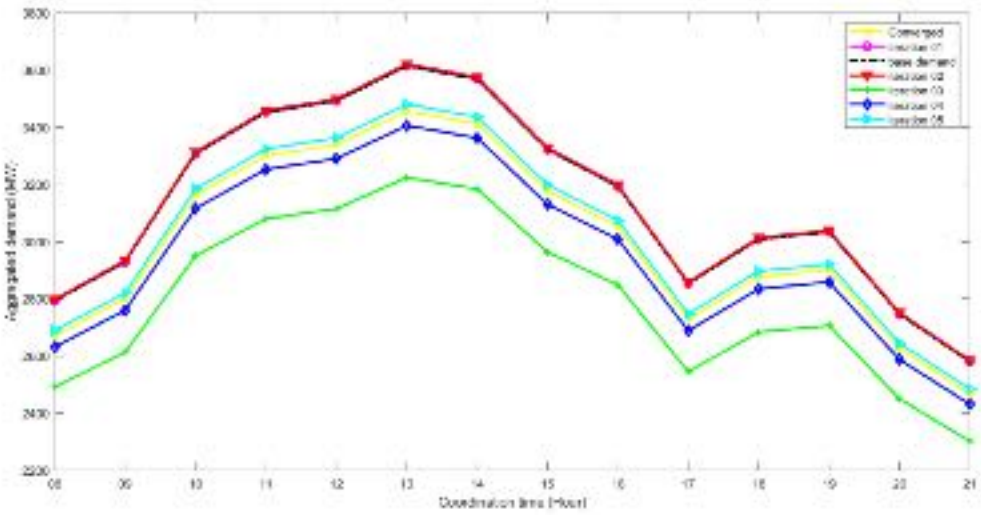

Figure 9-6. Convergence of the hybrid centralized and decentralized strategy on the lower-level of the developed framework

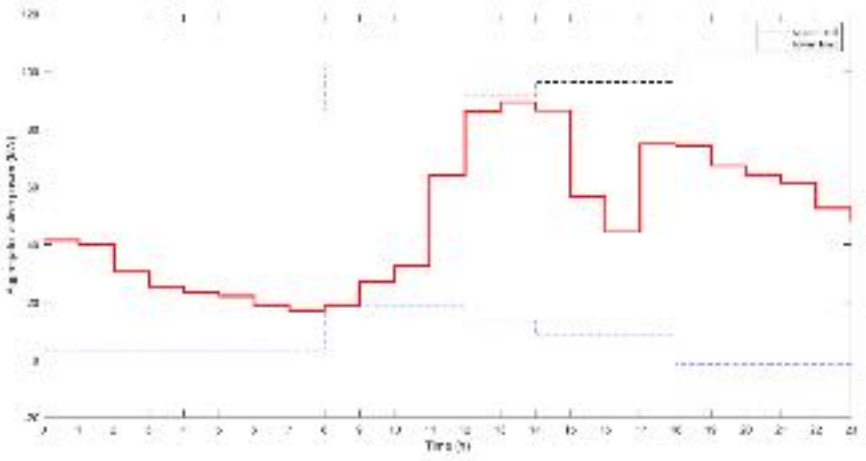

Figure 9-7. Aggregator's (A) of microgrid#1 upper and lower limits

9.5 Conclusion

In this chapter, we developed a tri-level, hierarchical energy management coordination mechanism that aims to optimally manage the electric network considering large-scale integration of the PEVs. The main concept that this framework is based on establishing energy price signals via following the timely updates of the inverse-demand curve. This chapter realizes that the utilization of the inverse-demand function is the best strategy to produce accurate and supply-influenced energy prices, since price estimation based on the concept of this curve account for any slight modification in the quantity of supply (system's

energy generation) and demand of products (consumers' utilization of energy). That is to say, the tri-level energy optimization problem took into account various operational and policy constraints that are imposed on the real-life operation of the system. Such constraints including line and transformer overloading, renewable energy portfolio (RPS) requirement, carbon emission requirement, and PEVs charging and discharging limitations due to the system's condition. The formulation of the developed framework was achieved by MIQP representation, and KKT approximation was performed to ensure accurate implementation of the electrical energy system's constraints, where there is a need to account for its non-linearity nature. The IEEE 123 bus system was used to test the developed tri-level framework. Furthermore, we assumed three microgrid entities that are directly connected to the system operator at its upper-level, and charging stations run by aggregators at its lower-level. The reason behind such dissection lies in the results obtained in chapter eight, where optimal decomposition of the system into partitions based on their voltage, active and reactive power limits have been performed. Finally, results have showed that successful implementation of the developed framework led to influencing the charging behavior of hundreds of the PEVs owners to delay their charging requirements as a result of the dynamic energy price signals that are issued based on the system's timely operation. Additionally, the results show the optimal exchange of energy between different microgrids to support their overall operation and reduce their overall cost incurred from their generation units.

Chapter 10 Conclusion and Recommendation for Future Work

10.1 Conclusion of the Dissertation

Electric Vehicles (EVs) are considered one of humanity's greatest hopes to combat the climate change crises considering their great potentials to reduce GHG emissions from two main emissions contributors: the power industry and transportation. For the former, EVs are expected to play a central role in constructing smarter and cleaner power grids, offering the resiliency and flexibility to support the grid's operation in a meaningful and reliable way. For the latter, zero-emissions EVs, fueled by electricity generated by renewables and low-emissions fuels, are seen as the future of transportation, next to electric buses, trains, and trolleys. However, to help expedite the adoption of thousands of EVs on the roads and win average consumers' trust over conventional vehicles, lots of effort is still needed to make EVs a vital option for regular and middle-class consumers. Specifically, optimal solutions are needed to overcome the technical and operational barriers that face the electrical network due to the introduction of significant numbers of loads from EVs; a substantial amount of them are expected to be during peak demand hours. In this dissertation, we propose different solutions related to the optimization and control of large-scale Electric vehicle integration to the power distribution grids.

There is a great need to understand the mathematics that better model the EVs' activities on the power networks. For this purpose, we presented a mathematical framework in chapter two of this dissertation that includes linearization of the non-linearities of the voltage and power levels variations due to EVs' integration. The theories behind this mathematical formulation lie in the concept of linear algebra, matrix analysis, and nodal superposition. This mathematical framework was utilized to model the dynamics of the hourly EVs' charging and discharging activities on the distribution grid presented in chapter five of this dissertation. Additionally. Chapter two of this dissertation lays the foundation for

utilizing the concept of modularity index algorithm to decompose the distribution grid into optimal partitions. The overall aim is to define the network into partitions based on their voltage sensitivity values with respect to the active and reactive power levels variations. This will allow better exploration of optimal strategies for EVs smart scheduling, which is discussed in detail in chapter eight of this dissertation with the proposal of a smart algorithm that we call community-based detection particle swarm optimization (CBDPSO). Specifically, the developed CBDPSO algorithm is used as the first part of a two-stage optimization strategy to optimally manage the reactive power and voltage levels in unbalanced distribution networks, considering the high-penetration of EVs. To sum up the introduction of the modularity index concept on the power distribution system's decomposition, a case study considering the IEEE 34 bus system with real-life data was performed. The overall results show that the test system could be optimally decomposed into six zones based on their voltage sensitivity levels during peak demand hours. This makes it easier for the system operator to manage and oversee the impact of large-scale integration of EVs and the system's need for voltage and reactive power support.

The importance of metaheuristic techniques has been increasing rapidly in recent years due to its powerful capabilities in solving a wide range of power system optimization problems efficiently. While it is hard to find the best solution to many of those optimization problems, metaheuristic algorithms guarantee optimal or near-optimal solutions in reasonable time and more manageable computational burdens. Therefore, parts of this dissertation were dedicated to proposing and utilizing metaheuristic methodologies to serve the purpose of large-scale EVs integration. We presented in chapter three of this dissertation an effective hybridization of two powerful, nature-inspired metaheuristic techniques: particle swarm optimization and applied physics optimization. To test the hybrid algorithm's effectiveness and robustness, we applied it to one of the most famous power system optimization problems:

the optimal reactive power dispatch (ORPD) problem. The obtained results show that combining the two techniques' searching strategies yields superior performance verified by solving single and multiobjective ORPD problems considering three IEEE tests systems: IEEE 30, IEEE 57, and IEEE 118 bus test systems. Furthermore, the obtained results show the superiority of the hybrid algorithm in comparison with previously reported literature. We have now confirmed that this metaheuristic hybridization could be effectively utilized to optimally solve microgrid optimization and control problems considering PV systems and EVs charging stations, presented in chapter four of this dissertation.

In Chapter four, the hybrid APOPSO algorithm discussed in chapter three was integrated with a vector decoupled algorithm to optimally manage hybrid microgrid operation and ensure smooth frequency levels and prevent voltage deficiency problems via utilization of the PV system and EVs charging station. Specifically, the developed metaheuristic-based vector-decoupled algorithm was deployed to balance the AC-DC microgrid operation with the incorporation of a bidirectional interlinking converter. The AC side of the microgrid is connected to synchronous generators and portable AC loads. On the other hand, the microgrid's DC side is connected to the PV system and EVs charging station. The vector-decoupled control parameters of the bidirectional converter are tuned via the hybrid algorithm. The results show that the developed algorithm successfully balanced the voltage and frequency levels considering severe microgrid operation, such as during islanding conditions considering high-pulsed demands condition and high PV power production variation. The developed methodology is verified in a state-of-the-art hardware-in-the-loop testbed. The results show the robustness and effectiveness of the developed algorithm in managing the real and reactive power exchange between the AC and DC parts of the microgrid within safe and acceptable voltage and frequency levels.

Chapter five presents dynamical modeling of different testing scenarios for large-scale EVs integration on the power distribution network. This chapter aimed to build a dynamic model in the powerful OpenDSS software of the Electric Power Research Institute (EPRI) and study uncoordinated hourly EVs charging and discharging activities on the distribution grid. To achieve this purpose, the mathematical formulation of EVs was built in the model, incorporated with 24-hour real-life data representing the load demand of a Southern California power utility. Furthermore, the IEEE 34 bus system was integrated into the model, considering its transmission line parameters and transformer connectivity. Four testing scenarios that consider no coordination or management strategies to the EVs integration were developed for 24 hours to measure the impact of large-scale EVs integration on the distribution system's hourly operation. The results show the level of congestion the EVs would accumulate on the test system, with voltage level as an indicator for the system's operation. Detailed results and analysis are provided in chapter five, which shows the need to coordinate EVs' activities on the power grid properly.

Also, we aim in this dissertation to facilitate the integration of EVs on the electrical infrastructure via safe and reliable arrival of the EVs into the charging stations. Therefore, we propose in chapter six a real-time, metadata-driven routing optimization that aims to minimize the EVs' energy consumption. The developed routing algorithm is based on evaluating Q-values through the Double Deep Q-Network (DDQN) algorithm to train the electric vehicle as an agent that aims to choose actions corresponding to the best-obtained Q-values. This assessment aims to extend the vehicle's driving range by choosing optimal routes that reduce the energy required to reach a destination. Additionally, we model the energy consumption on the road via MCM to properly model the traveling paths according to input parameters and learning strategy. The learning experience is supported with real-time data retrieved from Google's API platform that serves as the source for input information, feeding

the agent with real-time status of roads. Two experiments were conducted to verify the developed routing algorithm, considering two real-life routes of similar length, but at locations that exhibit different geographic characteristics. Both of the experiments were set at a specific time and date, assuming limited SoC of the EV's battery. Additionally, we considered the EV journey to be at continuous states, and the transitional probabilities are updated throughout as the agent considers real-time data absorbed into the framework from the Google Maps Platform. The simulation was conducted in the Python environment with real-life input information from Google's API. The results show that the energy consumption following the developed framework's implementation got considerably lower than when following the main routes developed by Google Maps for each journey. Specifically, the obtained results show that, in both simulation scenarios, the EV can reach its intended destination with lower energy than the main route developed by Google Maps, by 5.89% and 11.82%. The reason for such differences in the reported results is the significant temporal and spatial differences at each location, which influence energy consumption.

It is of importance in this dissertation to model the economic structure of large-scale integration of EVs. Chapter seven developed a dynamic pricing structure based on the demand-supply curve function to manage the billing strategy of EVs charging during peak demand hours. Specifically, the developed strategy updates the energy prices to be composed of two fractions: retail energy price that follows ToU rates and is directed to regular demands, and congested energy price is directed for billing EVs charging events during timeslots of peak demands. The developed structure is implemented in a hierarchal multi-agent architecture and is incorporated with an optimal energy management system that aims to provide a cost-efficient microgrid operation. The optimization problem's inputs are day-ahead PV forecast and stochastic EVs energy levels and connectivity times prediction models based on a discrete-time Markov chain. Besides, a predictive model of daily load demand is also presented based on adaptive Artificial Neural Network (ANN). The models were develop

based on historical data for Miami Dade County, South Florida. We presented the case that the developed pricing scheme performs better than some of the previously published centralized approaches through simulations. Specifically, allocating the congested price fraction for EVs owners who opt to charge their vehicles during congested timeslots achieves overall energy billing savings for non-EV owners. Furthermore, this contributes to better charging strategies assuming that many EVs owners would prefer to delay charging to timeslots when there is no grid congestion. However, a more-precise model was developed in chapter eight to manage the charging and discharging coordination of EVs per the grid's operation, incorporating monetary compensation for EVs who opt to charge their vehicles in other timeslots, considering the voltage and reactive power constraints on the electrical system.

In Chapter eight, a two-stage optimization strategy was developed to solve the voltage-reactive power (VVO) control problem considering large-scale EVs' integration to an unbalanced distribution network. At the first stage, we developed decomposing the distribution grid into optimal partitions based on the modularity index algorithm concept that was discussed in chapter two. Specifically, we developed a smart algorithm called community-based detection particle swarm optimization (CBDPSO) to dissect the distribution grid into partitions based on their voltage sensitivity values with respect to active and reactive power, respectively. Upon clustering the grid, the second stage formulates a centralized optimization problem solved by mixed-integer linear programming (MILP). The MILP solves to obtain feasible, economic results while satisfying the operational needs and constraints of the unbalanced three-phase PDN. Linear approximation of the equalities and inequalities of the electrical system was performed to solve the optimization model correctly using the available commercial optimization software. Moreover, large-scale integration of EVs was modeled to ensure proper operation of the distribution network. The VVO control problem in Chapter eight includes accounting for energy not served due to grid's congestion,

deployment of reactive compensation devices with a goal of their relaxation to ensure economical operation and extend its lifespan, and effective participation of PV inverters via active power curtailment and reactive power support. Four case testing were modeled in this chapter that incorporated different scenarios, considering the IEEE 123 bus system. The obtained results indicate reaching optimal economic gains while maintaining the system's voltage regulation within permissible limits. Furthermore, the solution indicates lower active power curtailment of the PV system and zero energy demand curtailment for the PEVs, which means each partition in the PDN was able to meet its demand even during peak hours, including for the PEVs connection requests.

In chapter nine, we developed a tri-level, hierarchical energy management coordination considering that aims to optimally manage the electric network considering large-scale integration of the PEVs. The main concept that this framework is based on utilizing the concept of microeconomics in accurately establishing energy price signals via updating the inverse-demand curve of the system to reflect the system's current generation availability and scarcity as well as the system's overloading condition. Such representation of the pricing signals have successfully influenced the charging behaviors of hundreds of PEVs as simulation results have shown in chapter nine. Moreover, the tri-level energy optimization problem took into account various operational and policy constraints that are imposed on the real-life operation of the system. Such constraints including line and transformer overloading, renewable energy portfolio (RPS) requirement, carbon emission requirement, and PEVs charging and discharging limitations due to the system's condition. The formulation of the developed framework was achieved by MIQP representation, and KKT approximation was performed to ensure accurate implementation of the electrical energy system's constraints, where there is a need to account for its non-linearity nature. The IEEE 123 bus system was used to test the developed tri-level framework. Furthermore, we assumed three microgrid entities that are directly connected to the system operator at its upper-level, and charging

stations run by aggregators at its lower-level. The reason behind such dissection lies in the results obtained in chapter eight, where optimal decomposition of the system into partitions based on their voltage, active and reactive power limits have been performed. Finally, results have showed that successful implementation of the developed framework led to influencing the charging behavior of hundreds of the PEVs owners to delay their charging requirements as a result of the dynamic energy price signals that are issued based on the system's timely operation. Additionally, the results show the optimal exchange of energy between different microgrids to support their overall operation and reduce their overall cost incurred from their generation units.

10.2 Recommendation for Future Work

The implementation of the concept of smart grid is far from being close to implementation, as humanity has still long way to cross before reaching a smarter and cleaner grid. On research level, there are still many work lay ahead us to achieve our goals in fighting the climate change crises. Many of these research efforts should be directed towards the field of electric vehicles, as EVs are seen as the intersection points between the two major emitters of GHG emissions. Future work should focus on the newly introduced methodologies that is based on machine-learning applications, reinforcement-learning, and metaheuristic-based research, as these methodologies are still in the beginning in developing smart and useful mathematical algorithms that serve the purpose not only in the EVs' field and electrical engineering technologies, but also in many other fields in life. Many of these methodologies should be investigated to solve various problem related to the EVs industry, such as estimating the arrival/departure and driving patterns of PEVs owners, accurately assessing energy price signals that reflect the timely updated operation of the power grid, and achieving reliable and economic operation of the grid giving the system's various barriers and constraints.

List of References

1. Conference of the Parties, Adoption of the Paris Agreement, Dec. 12, 2015 U.N. Doc. FCCC/CP/2015/L.9/Rev/1 (Dec. 12, 2015). Retrieved from https://unfccc.int/resource/docs/2015/cop21/eng/l09r01.pdf
2. Kyoto Protocol to the United Nations Framework Convention on Climate Change, Dec. 10, 1997 37 I.L.M. 22 (1998); 2303 U.N.T.S. 148; U.N. Doc FCCC/CP/1997/7/Add. Retrieved from https://unfccc.int/process-and-meetings/the-kyoto-protocol/history-of-the-kyoto-protocol/text-of-the-kyoto-protocol
3. 430-R-21-001, E. P. A. (2021). DRAFT INVENTORY OF US GREENHOUSE GAS EMISSIONS AND SINKS. The United States Environmental Protection Agency. Retrieved from https://www.epa.gov/sites/production/files/2021-02/documents/us-ghg-inventory-2021-main-text.pdf
4. Le Quéré, C., Jackson, R. B., Jones, M. W., Smith, A. J., Abernethy, S., Andrew, R. M., ... & Peters, G. P. (2020). Temporary reduction in daily global CO 2 emissions during the COVID-19 forced confinement. Nature Climate Change, 10(7), 647-653.
5. IEEE Standards Coordinating Committee 21, ‘‘IEEE guide for design, operation, and integration of distributed resource island systems with electric power systems,’’ IEEE Std 1547.4TM-2011, July 20, 2011.
6. Wu, Q.H.; Ma, J.T. Power system optimal reactive power dispatch using evolutionary programming. *IEEE Trans. Power Syst.* **1995**, *10*, 1243–1249
7. Belegundu, A.D.; Chandrupatla, T.R. Optimization Concepts and Applications in Engineering; Chapter 3; Prentice Hall: Upper Saddle River, NJ, USA, 1999.
8. Shoults, R.R.; Sun, D.T. Optimal power flow based upon P-Q decomposition. IEEE Trans. Power Appar. Syst. 1982, 101, 397–405.
9. Chen, C.R.; Lee, H.S.; Tsai, W. Optimal Reactive Power Planning Using Genetic Algorithm. In Proceedings of the IEEE International Conference on Systems, Man and Cybernetics, Taipei, Taiwan, 8–11 October 2006; Volume 6, pp. 5275–5279.
10. Subbaraj, P.; Rajnarayanan, P.N. Optimal reactive power dispatch using self-adaptive real coded genetic algorithm. Electr. Power Syst. Res. 2009, 79, 374–381.
11. Le, D.A.; Vo, D.N. Optimal reactive power dispatch by pseudo-gradient guided patiicle swarm optimization. In Proceedings of the 2012 10th International Power &

Energy Conference (IPEC), Ho Chi Minh City, Vietnam, 12–14 December 2012; pp. 7–12.

12. Yoshida, H.; Kawata, K.; Fukuyama, Y.; Takayama, S.; Nakanishi, Y. A particle swarm optimization for reactive power and voltage control considering voltage security assessment. *IEEE Trans. Power Syst.* 2000, *15*, 1232–1239.
13. Singh, R.P.; Mukherjee, V.; Ghosal, S.P. Optimal reactive power dispatch by particle swarm optimization with an aging leader and challengers. *Appl. Soft Comput.* **2015**, *2*, 298–309.
14. Liu, Z.F.; Ge, S.Y.; Yu, Y.X. Optimal reactive power dispatch using chaotic particle swarm optimization algorithm. *Dianli Xitong Zidonghua (Autom. Electr. Power Syst.)* **2005**, *29*, 53–57.
15. El Ela, A.A.; Abido, M.A.; Spea, S.R. Differential evolution algorithm for optimal reactive power dispatch. Electr. Power Syst. Res. 2011, 81, 458–464.
16. Yutian, L.; Li, M. Reactive Power Optimization based on Tabu Search Approach. Autom. Electr. Power Syst. 2000.
17. Lu, F.C.; Hsu, Y.Y. Reactive power/voltage control in a distribution substation using dynamic programming. IEE Proc. Gener. Transm. Distrib. 1995, 142, 639–645
18. Khazali, A.H.; Kalantar, M. Optimal reactive power dispatch based on harmony search algorithm. Int. J. Electr. Power Energy Syst. 2011, 33, 684–692.
19. Duman, S.; Sönmez, Y.; Güvenç, U.; Yörükeren, N. Optimal reactive power dispatch using a gravitational search algorithm. *IET Gener. Transm. Distrib.* **2012**, *6*, 563–576.
20. Niknam, T.; Narimani, M.R.; Azizipanah-Abarghooee, R.; Bahmani-Firouzi, B. Multi objective optimal reactive power dispatch and voltage control: A new opposition-based self-adaptive modified gravitational search algorithm. *IEEE Syst. J.* **2013**, *7*, 742–753.
21. Sulaiman, M.H.; Mustaffa, Z.; Mohamed, M.R.; Aliman, O. Using the gray wolf optimizer for solving optimal reactive power dispatch problem. Appl. Soft Comput. 2015, 32, 286–292.
22. Kennedy, J.; Eberhart, R. Particle Swarm Optimization. In Proceedings of the IEEE International Conference on Neural Networks, Perth, WA, Australia, 27 November–1 December 1995; pp. 1942–1948, doi:10.1109/ICNN.1995.488968.

23. Spears, W.M.; Gordon, D.F. Using artificial physics to control agents. In Proceedings of the 1999 International Conference on Information Intelligence and Systems (Cat. No. PR00446), Bethesda, MD, USA, 31 October–3 November 1999; pp. 281–288
24. Zhan, X.; Xiang, T.; Chen, H.; Zhou, B.; Yang, Z. Vulnerability assessment and reconfiguration of microgrid through search vector artificial physics optimization algorithm. Int. J. Electr. Power Energy Syst. 2014, 62, 679–688, ISSN 0142-0615, doi:10.1016/j.ijepes.2014.05.024.
25. Teeparthi, K.; Kumar, D.V. Dynamic Power System Security Analysis Using a Hybrid PSO-APO Algorithm. Eng. Technol. Appl. Sci. Res. 2017, 7, 2124–2131.
26. Aljohani, T. M., Ebrahim, A. F., & Mohammed, O. (2020). Hybrid Microgrid Energy Management and Control Based on Metaheuristic-Driven Vector-Decoupled Algorithm Considering Intermittent Renewable Sources and Electric Vehicles Charging Lot. Energies, 13(13), 3423.
27. Wu, D., Tang, F., Dragicevic, T., Vasquez, J. C., & Guerrero, J. M. (2014). A control architecture to coordinate renewable energy sources and energy storage systems in islanded microgrids. IEEE Transactions on Smart Grid, 6(3), 1156-1166
28. Lasseter, R. H., & Paigi, P. (2004, June). Microgrid: A conceptual solution. In 2004 IEEE 35th Annual Power Electronics Specialists Conference (IEEE Cat. No. 04CH37551) (Vol. 6, pp. 4285-4290). IEEE
29. Hatziargyriou, N., Asano, H., Iravani, R., & Marnay, C. (2007). Microgrids. IEEE power and energy magazine, 5(4), 78-94
30. Karavas, C. S., Kyriakarakos, G., Arvanitis, K. G., & Papadakis, G. (2015). A multi-agent decentralized energy management system based on distributed intelligence for the design and control of autonomous polygeneration microgrids. *Energy Conversion and Management*, *103*, 166-179
31. Rocabert, J., Luna, A., Blaabjerg, F., & Rodriguez, P. (2012). Control of power converters in AC microgrids. IEEE transactions on power electronics, 27(11), 4734-4749
32. Farahat, M. A., Metwally, H. M. B., & Mohamed, A. A. E. (2012). Optimal choice and design of different topologies of DC–DC converter used in PV systems, at different climatic conditions in Egypt. Renewable Energy, 43, 393-402.
33. Lee, J. P., Min, B. D., Kim, T. J., Yoo, D. W., & Yoo, J. Y. (2008). A novel topology for photovoltaic DC/DC full-bridge converter with flat efficiency under wide PV

module voltage and load range. IEEE Transactions on Industrial Electronics, 55(7), 2655-2663

34. Wang, T., O'Neill, D., & Kamath, H. (2015). Dynamic control and optimization of distributed energy resources in a microgrid. *IEEE transactions on smart grid*, *6*(6), 2884-2894.
35. Aljohani, T.M., Saad, A.& Mohammed, O (2020, June). On the Real-Time Modeling of Voltage Drop and Grid Congestion Due to the Presence of Electric Vehicles on Residential Feeders. In 2020 IEEE International Conference on Environment and Electrical Engineering and 2020 IEEE Industrial and Commercial Power Systems Europe (EEEIC/I&CPS Europe). IEEE.
36. Aljohani, T.; Beshir, M. Distribution System Reliability Analysis for Smart Grid Applications. Smart Grid Renew. Energy 2017, 8, 240–251, doi:10.4236/sgre.2017.87016.
37. Aljohani, T.; Beshir, M. Matlab Code to Assess the Reliability of the Smart Power Distribution System Using Monte Carlo Simulation. J. Power Energy Eng. 2017, 5, 30–44, doi:10.4236/jpee.2017.58003.
38. Han, S., Han, S. H., & Sezaki, K. (2010, January). Design of an optimal aggregator for vehicle-to-grid regulation service. In 2010 Innovative Smart Grid Technologies (ISGT) (pp. 1-8). IEEE.
39. Islam, M. M., Zhong, X., Sun, Z., Xiong, H., & Hu, W. (2019). Real-time frequency regulation using aggregated electric vehicles in smart grid. Computers & Industrial Engineering, 134, 11-26.
40. Yang, J., Zeng, Z., Tang, Y., Yan, J., He, H., & Wu, Y. (2015). Load frequency control in isolated micro-grids with electrical vehicles based on multivariable generalized predictive theory. *Energies*, *8*(3), 2145-2164
41. Ou, X., Zhang, X., Zhang, X., & Zhang, Q. (2013). Life cycle GHG of NG-based fuel and electric vehicle in China. *Energies*, *6*(5), 2644-2662
42. Aljohani, T.M, and Alzahrani, G. "Life Cycle Assessment to Study the Impact of the Regional Grid Mix and Temperature Differences on the GHG Emissions of Battery Electric and Conventional Vehicles," 2019 SoutheastCon, Huntsville, AL, USA, 2019, pp. 1-9
43. M. F. Shaaban, Y. M. Atwa, and E. F. El-Saadany, "PEVs modeling and impacts mitigation in distribution networks," IEEE Trans. Power Syst., vol. 28, no. 2, pp. 1122–1131, May 2013.

44. The International Energy Agency (IEA). Global EV Outlook: Toward Cross-Modal Electrification. 2018. Available online: https://webstore.iea.org/global-ev-outlook-2018 (accessed on 11 August 2018).
45. McDermott, T.E.; Dugan, R.C. Distributed generation impact on reliability and power quality indices. In Proceedings of the Rural Electric Power Conference, Colorado Springs, CO, USA, 5–7 May 2002; Volume D3, pp. 1–7.
46. Trichakis, P.; Taylor, P.C.; Lyons, P.F.; Hair, R. Predicting the technical impacts of high levels of small-scale embedded generators on low-voltage networks. IET Renew. Power Gener. 2008, 2, 249–262. [CrossRef]
47. Hadley, S.W. Impact of Plug-In Hybrid Vehicles on the Electric Grid; Technical report ORNL/TM-2006/554; Oak Ridge National Laboratory: Oak Ridge, TN, USA, 2006.
48. Denholm, P.; Short, W. An Evaluation of Utility System Impacts and Benefits of Optimally Dispatched Plug-In Hybrid Electric Vehicles; Technical report; National Renewable Energy Laboratory: Golden, CO, USA, 2006.
49. Kersting, W.H. Distribution System Modeling and Analysis; CRC: Boca Raton, FL, USA, 2002.
50. IEEE 34 Bus Test Feeder. Available online: http://ewh.ieee.org/soc/pes/dsacom/testfeeders/ (accessed on 17 May 2018).
51. Williams, B.D.; Kurani, K.S. Commercializing light-duty plugin/plug-out hydrogen-fuel-cell vehicles: 'Mobile Electricity' technologies and opportunities. J. Power Sources 2007, 166, 549–566. [CrossRef]
52. Tomic, J.; Kempton, W. Using fleets of electric-drive vehicles for grid support. J. Power Sources 2007, 168, 459–468. [CrossRef]
53. Aljohani, T.M. The Impact of EPA's New Developed Limits on the U.S. Power Industry. Int. J. Electr. Energy 2014, 2, 343–347.
54. Miceli, R.; Viola, F. Designing a Sustainable University Recharge Area for Electric Vehicles: Technical and Economic Analysis. Energies 2017, 10, 1604. [CrossRef]
55. Ul-Haq, A.; Cecati, C.; Al-Ammar, E.A. Modeling of a Photovoltaic-Powered Electric Vehicle Charging Station with Vehicle-to-Grid Implementation. Energies 2017, 10, 4. [CrossRef]
56. Olivella-Rosell, P.; Villafafila-Robles, R.; Sumper, A.; Bergas-Jané, J. Probabilistic Agent-Based Model of Electric Vehicle Charging Demand to Analyse the Impact on Distribution Networks. Energies 2015, 8, 4160–4187. [CrossRef]

57. Yang, J.; Hao, W.; Chen, L.; Chen, J.; Jin, J.; Wang, F. Risk Assessment of Distribution Networks Considering the Charging-Discharging Behaviors of Electric Vehicles. Energies 2016, 9, 560.
58. Elsayad, N.; Moradisizkoohi, H.; Mohammed, O. Design and Implementation of a New Transformerless Bidirectional DC-DC Converter with Wide Conversion Ratios. IEEE Trans. Ind. Electron. 2018.
59. Van Hasselt, H., Guez, A., & Silver, D. (2016, March). Deep reinforcement learning with double q-learning. In Thirtieth AAAI Conf. Artif. Intell.
60. Hasselt, H.V. (2010). Double Q-learning. In Advances in Neural Information Processing Systems (pp. 2613–2621).
61. Watkins, C. J., & Dayan, P. (1992). Q-learning. Machine learning, 8(3-4), 279-292.
62. Mnih, V., Kavukcuoglu, K., Silver, D., Graves, A., Antonoglou, I., Wierstra, D., & Riedmiller, M. (2013). Playing atari with deep reinforcement learning. arXiv preprint arXiv:1312.5602.
63. Valogianni, K., Ketter, W., Collins, J., & Zhdanov, D. (2014, June). Effective management of electric vehicle storage using smart charging. In Twenty-Eighth AAAI Conference on Artificial Intelligence.
64. Liu, T., Zou, Y., Liu, D., & Sun, F. (2015). Reinforcement learning of adaptive energy management with transition probability for a hybrid electric tracked vehicle. IEEE Transactions on Industrial Electronics, 62(12), 7837-7846.
65. Qi, X., Wu, G., Boriboonsomsin, K., Barth, M. J., & Gonder, J. (2016). Data-driven reinforcement learning–based real-time energy management system for plug-in hybrid electric vehicles. Transportation Research Record, 2572(1), 1-8.
66. Wang, H., Huang, T., Liao, X., Abu-Rub, H., & Chen, G. (2016). Reinforcement learning in energy trading game among smart microgrids. IEEE Transactions on Industrial Electronics, 63(8), 5109-5119.
67. Kim, B. G., Zhang, Y., Van Der Schaar, M., & Lee, J. W. (2015). Dynamic pricing and energy consumption scheduling with reinforcement learning. IEEE Transactions on Smart Grid, 7(5), 2187-2198.
68. Foruzan, E., Soh, L. K., & Asgarpoor, S. (2018). Reinforcement learning approach for optimal distributed energy management in a microgrid. IEEE Transactions on Power Systems, 33(5), 5749-5758.

69. Liu, T., Hu, X., Li, S. E., & Cao, D. (2017). Reinforcement learning optimized look-ahead energy management of a parallel hybrid electric vehicle. IEEE/ASME Transactions on Mechatronics, 22(4), 1497-1507.
70. Sallab, A. E., Abdou, M., Perot, E., & Yogamani, S. (2017). Deep reinforcement learning framework for autonomous driving. Electronic Imaging, 2017(19), 70-76.
71. Karbasioun, M. M., Lambadaris, I., Shaikhet, G., & Kranakis, E. (2014, November). Optimal charging strategies for electrical vehicles under real time pricing. In 2014 IEEE International Conference on Smart Grid Communications (SmartGridComm) (pp. 746-751). IEEE.
72. Tang, D., & Wang, P. (2015). Probabilistic modeling of nodal charging demand based on spatial-temporal dynamics of moving electric vehicles. IEEE Transactions on Smart Grid, 7(2), 627-636.
73. Beom, H. R., & Cho, H. S. (1995). A sensor-based navigation for a mobile robot using fuzzy logic and reinforcement learning. IEEE transactions on Systems, Man, and Cybernetics, 25(3), 464-477.
74. Hasegawa, Y., Fukuda, T., & Shimojima, K. (1999). Self-scaling reinforcement learning for fuzzy logic controller-applications to motion control of two-link brachiation robot. IEEE Transactions on Industrial Electronics, 46(6), 1123-1131.
75. Oh, S. Y., Lee, J. H., & Choi, D. H. (2000). A new reinforcement learning vehicle control architecture for vision-based road following. IEEE Transactions on Vehicular Technology, 49(3), 997-1005.
76. Barrett, E., Howley, E., & Duggan, J. (2013). Applying reinforcement learning towards automating resource allocation and application scalability in the cloud. Concurrency and Computation: Practice and Experience, 25(12), 1656-1674.
77. Rafiee, G., Dlay, S. S., & Woo, W. L. (2010, July). A review of content-based image retrieval. In 2010 7th International Symposium on Communication Systems, Networks & Digital Signal Processing (CSNDSP 2010) (pp. 775-779). IEEE.
78. Asada, M., Noda, S., Tawaratsumida, S., & Hosoda, K. (1995, May). Vision-based reinforcement learning for purposive behavior acquisition. In Proceedings of 1995 IEEE International Conference on Robotics and Automation (Vol. 1, pp. 146-153). IEEE.
79. Bonarini, A. (2001). Evolutionary learning, reinforcement learning, and fuzzy rules for knowledge acquisition in agent-based systems. Proceedings of the IEEE, 89(9), 1334-1346.

80. Liu, W., Qin, G., He, Y., & Jiang, F. (2017). Distributed cooperative reinforcement learning-based traffic signal control that integrates V2X networks' dynamic clustering. IEEE transactions on vehicular technology, 66(10), 8667-8681.
81. Huang, X., Yuan, T., Qiao, G., & Ren, Y. (2018). Deep reinforcement learning for multimedia traffic control in software defined networking. IEEE Network, 32(6), 35-41.
82. Ortiz, A., Al-Shatri, H., Li, X., Weber, T., & Klein, A. (2016, May). Reinforcement learning for energy harvesting point-to-point communications. In 2016 IEEE International Conference on Communications (ICC) (pp. 1-6). IEEE.
83. Luong, N. C., Hoang, D. T., Gong, S., Niyato, D., Wang, P., Liang, Y. C., & Kim, D. I. (2019). Applications of deep reinforcement learning in communications and networking: A survey. IEEE Communications Surveys & Tutorials, 21(4), 3133-3174.
84. Johnson, J. D., Li, J., & Chen, Z. (2000). Reinforcement Learning: An Introduction-RS Sutton, AG Barto, MIT Press, Cambridge, MA 1998, 322 pp. ISBN 0-262-19398-1. Neurocomputing, 35(1-4), 205-206.
85. Mohamed, A., & Mohammed, O. (2013). Real-time energy management scheme for hybrid renewable energy systems in smart grid applications. Electric Power Systems Research, 96, 133-143.
86. Salehi, V., Mohamed, A., & Mohammed, O. A. (2012, October). Implementation of real-time optimal power flow management system on hybrid AC/DC smart microgrid. In *2012 IEEE Industry Applications Society Annual Meeting* (pp. 1-8). IEEE
87. Kuznetsova, E., Li, Y. F., Ruiz, C., Zio, E., Ault, G., & Bell, K. (2013). Reinforcement learning for microgrid energy management. *Energy*, *59*, 133-146
88. Yoon, S. G., & Kang, S. G. (2017). Economic microgrid planning algorithm with electric vehicle charging demands. *Energies*, *10*(10), 1487
89. Shekari, T., Golshannavaz, S., & Aminifar, F. (2016). Techno-economic collaboration of PEV fleets in energy management of microgrids. *IEEE Transactions on Power Systems*, *32*(5), 3833-3841
90. López, M. A., Martin, S., Aguado, J. A., & de la Torre, S. (2011, December). Optimal microgrid operation with electric vehicles. In *2011 2nd IEEE PES International Conference and Exhibition on Innovative Smart Grid Technologies* (pp. 1-8). IEEE
91. Fan, Z. (2012). A distributed demand response algorithm and its application to PHEV charging in smart grids. IEEE Transactions on Smart Grid, 3(3), 1280-1290.

92. Erol-Kantarci, M., & Hussein, T. M. (2010, October). Prediction-based charging of PHEVs from the smart grid with dynamic pricing. In IEEE Local Computer Network Conference (pp. 1032-1039). IEEE.
93. Azzouz, M. A., Shaaban, M. F., & El-Saadany, E. F. (2015). Real-time optimal voltage regulation for distribution networks incorporating high penetration of PEVs. IEEE Transactions on Power Systems, 30(6), 3234-3245.
94. T. Senjyu, Y. Miyazato, A. Yona, N. Urasaki, and T. Funabashi, "Optimal distribution voltage control and coordination with distributed generation," IEEE Trans. Power Del., vol. 23, no. 2, pp. 1236–1242, Apr. 2008.
95. S. Deshmukh, B. Natarajan, and A. Pahwa, "Voltage/VAR control in distribution networks via reactive power injection through distributed generators," IEEE Trans. Smart Grid, vol. 3, no. 3, pp. 1226–1234, Sep. 2012.
96. Y. P. Agalgaonkar, B. C. Pal, and R. A. Jabr, "Distribution voltage control considering the impact of PV generation on tap changers and autonomous regulators," IEEE Trans. Power Syst., vol. 29, no. 1, pp. 182–192, Jan. 2014.
97. Manbachi, M., Farhangi, H., Palizban, A., & Arzanpour, S. (2016). A novel Volt-VAR Optimization engine for smart distribution networks utilizing Vehicle to Grid dispatch. International Journal of Electrical Power & Energy Systems, 74, 238-251.
98. Nedić, A., Olshevsky, A., & Rabbat, M. G. (2018). Network topology and communication-computation tradeoffs in decentralized optimization. Proceedings of the IEEE, 106(5), 953-976.
99. Quirós-Tortós, J., Sánchez-García, R., Brodzki, J., Bialek, J., & Terzija, V. (2014). Constrained spectral clustering-based methodology for intentional controlled islanding of large-scale power systems. IET Generation, Transmission & Distribution, 9(1), 31-42.
100. Jiang, T., Bai, L., Jia, H., & Li, F. (2016). Spectral clustering-based partitioning of volt/VAR control areas in bulk power systems. IET Generation, Transmission & Distribution, 11(5), 1126-1133.
101. Baran, M. E., & El-Markabi, I. M. (2007). A multiagent-based dispatching scheme for distributed generators for voltage support on distribution feeders. IEEE Transactions on power systems, 22(1), 52-59.
102. Elkhatib, M. E., El-Shatshat, R., & Salama, M. M. (2011). Novel coordinated voltage control for smart distribution networks with DG. IEEE transactions on smart grid, 2(4), 598-605.

103. Aljohani, T.; Mohammed, O. Modeling the Impact of the Vehicle-to-Grid Services on the Hourly Operation of the Power Distribution Grid. Designs 2018, 2, 55.
104. Hadley, S. W. (2006). Impact of plug-in hybrid vehicles on the electric grid. ORNL Report, (October).
105. Collins, M. M., & Mader, G. H. (1983). The timing of EV recharging and its effect on utilities. IEEE Transactions on Vehicular Technology, 32(1), 90-97.
106. Hajimiragha, A. H., Canizares, C. A., Fowler, M. W., Moazeni, S., & Elkamel, A. (2011). A robust optimization approach for planning the transition to plug-in hybrid electric vehicles. IEEE Transactions on Power Systems, 26(4), 2264-2274.
107. Hu, J., You, S., Lind, M., & Østergaard, J. (2013). Coordinated charging of electric vehicles for congestion prevention in the distribution grid. IEEE Transactions on Smart Grid, 5(2), 703-711
108. Gunter, S. J., Afridi, K. K., & Perreault, D. J. (2013). Optimal design of grid-connected PEV charging systems with integrated distributed resources. IEEE Transactions on Smart Grid, 4(2), 956-967.
109. Girvan, M., & Newman, M. E. (2002). Community structure in social and biological networks. Proceedings of the national academy of sciences, 99(12), 7821-7826
110. Newman, M. E. (2006). Modularity and community structure in networks. Proceedings of the national academy of sciences, 103(23), 8577-8582
111. Resources. IEEE PES AMPS DSAS Test Feeder Working Group. Retrieved from https://site.ieee.org/pes-testfeeders/resources/
112. Huang, G.M.; Nair, N.K.C. Detection of dynamic voltage collapse. IEEE Power Eng. Soc. Summer Meet. 2002, 3, 1284–1289.
113. Durairaj, S.; Kannan, P.S. Improved genetic algorithm approach for multi-objective contingency constrained reactive power planning. In Proceedings of the 2005 Annual IEEE India Conference-Indicon, Chennai, India, 11–13 December 2005; pp. 510–515.
114. Xie, L.; Zeng, J.; Cui, Z. General framework of artificial physics optimization algorithm. In Proceedings of the 2009 World Congress on Nature & Biologically Inspired Computing (NaBIC), Coimbatore, India, 9–11 December 2009; pp. 1321–1326.
115. Talbi, E.G. Metaheuristics: From Design to Implementation; John Wiley & Sons: Hoboken, NJ, USA, 2009; Volume 74.
116. Talbi, E.G. A taxonomy of hybrid metaheuristics. J. Heuristics 2002, 8, 541–564.

117. Illinois Center for a Smarter Electric Grid (ICSEG). Available online: https://icseg.iti.illinois.edu/ieee-30-bus-system/ (accessed on February 25th, 2019).
118. The IEEE 57-Bus Test System. Illinois Center for a Smarter Electric Grid (ICSEG). Available online: https://icseg.iti.illinois.edu/ieee-57-bus-system/ (accessed on February 25th, 2019).
119. The IEEE 118-Bus Test System. Available online: http://labs.ece.uw.edu/pstca/pf118/pg_tca118bus.htm (accessed on February 25th, 2019).
120. Lee, K.Y.; Park, Y.M.; Ortiz, J.L. Optimal real and reactive power dispatch. Electr. Power Syst. Res. 1984, 7, 201–212.
121. Lee, K.Y.; Park, Y.M.; Ortiz, J.L. A united approach to optimal real and reactive power dispatch. IEEE Trans. Power Appar. Syst. 1985, 104, 1147–1153.
122. Ayan, K.; Kılıc, U. Artificial bee colony algorithm solution for optimal reactive power flow. Appl. Soft Comput. 2012, 12, 1477–1482.
123. Mahadevan, K.; Kannan, P.S. Comprehensive learning particle swarm optimization for reactive power dispatch. Appl. Soft Comput. 2010, 10, 641–652.
124. Basu, M. Multi-objective optimal reactive power dispatch using multi-objective differential evolution. Int. J. Electr. Power Energy Syst. 2010, 82, 213–224.
125. Mukherjee, A.; Mukherjee, V. Solution of optimal reactive power dispatch by chaotic krill herd algorithm. IET Gener. Transm. Distrib. 2015, 9, 2351–2362.
126. Aljohani, T.M. The flywheel energy storage system: A conceptual study, design, and applications in modern power systems. Int. J. Electr. Energy 2014, 2, 146–153, doi:10.12720/ijoee.2.2.146-153.
127. Salehi, V., Mohamed, A., Mazloomzadeh, A., & Mohammed, O. A. (2012). Laboratory-based smart power system, part I: Design and system development. IEEE Transactions on Smart Grid, 3(3), 1394-14046
128. Ahmed. F. Ebrahim, S. M. W. Ahmed, S. E. Elmasry and O. A. Mohammed, "Implementation of a PV emulator using programmable DC power supply," SoutheastCon 2015, Fort Lauderdale, FL, 2015, pp. 1-7.
129. Ghareeb, A. T., Mohamed, A. A., & Mohammed, O. A. (2013, July). DC microgrids and distribution systems: An overview. In 2013 IEEE Power & Energy Society General Meeting (pp. 1-5). IEEE

130. S. Bacha, D. Picault, B. Burger, I. Etxeberria-Otadui and J. Martins, "Photovoltaics in Microgrids: An Overview of Grid Integration and Energy Management Aspects," in IEEE Industrial Electronics Magazine, vol. 9, no. 1, pp. 33-46, March 2015.
131. Hussein, K. H., Muta, I., Hoshino, T., & Osakada, M. (1995). Maximum photovoltaic power tracking: an algorithm for rapidly changing atmospheric conditions. IEE Proceedings-Generation, Transmission and Distribution, 142(1), 59-64.
132. Liu, X., & Lopes, L. A. (2004, June). An improved perturbation and observation maximum power point tracking algorithm for PV arrays. In 2004 IEEE 35th Annual Power Electronics Specialists Conference (IEEE Cat. No. 04CH37551) (Vol. 3, pp. 2005-2010). IEEE
133. Elsayed, A., Ebrahim, A. F., Mohammed, H., & Mohammed, O. A. (2015, April). Design and implementation of AC/DC active power load emulator. In SoutheastCon 2015 (pp. 1-5). IEEE
134. Aljohani, T. M., Ebrahim, A. F., & Mohammed, O. (2019). Single and multiobjective optimal reactive power dispatch based on hybrid artificial physics–particle swarm optimization. Energies, 12(12), 2333.
135. Aljohani, T.M.; Ebrahim, A.; Mohammed, O. Dynamic Real-Time Pricing Structure for Electric Vehicle Charging Considering Stochastic Microgrids Energy Management System. In Proceedings of the 2020 IEEE International Conference on Environment and Electrical Engineering and 2020 IEEE Industrial and Commercial Power Systems Europe (EEEIC/I&CPS Europe), Madrid, Spain, 9–12 June 2020.
136. Willis, H.L.; Scott, W.G. Distributed Power Generation. Planning and Evaluation; Marcel Dekker: New York, NY, USA, 2000.
137. Borlease, S. Smart Grids: Infrastructure, Technology and Solutions; CRC Press: Boca Raton, FL, USA, 2013.
138. The International Energy Agency (IEA). Global EV Outlook: Toward Cross-Modal Electrification. 2018. Available online: https://webstore.iea.org/global-ev-outlook-2018 (accessed on 11 August 2018).
139. “Smart Grid Resource Center > Simulation Tool – OpenDSS.” EPRI, smartgrid.epri.com/SimulationTool.aspx.
140. Florida Public Service Commission (2018). Statistics of the Florida UtilityIndustry. Retrieved from

http://www.psc.state.fl.us/Files/PDF/Publications/Reports/Electricgas/Statistics/2017.pdf

141. State of Florida End-use Energy Consumption 2018Estimates. U.S. Energy Information Administration - EIA - IndependentStatistics and Analysis. Retrieved fromhttps://www.eia.gov/beta/states/states/fl/overview`

142. Nair, A., Srinivasan, P., Blackwell, S., Alcicek, C., Fearon, R., De Maria, A., ... & Silver, D. (2015). Massively parallel methods for deep reinforcement learning. arXiv preprint arXiv:1507.04296.

143. G. Cybenko "Approximations by superpositions of sigmoidal functions Math. Control Signals. Syst., 2 (4) (1989), pp. 303-314

144. Kurt Hornik "Approximation capabilities of multilayer feedforward networks Neural Netw., 4 (2) (1991), pp. 251-257

145. G.E. Hinton, S. Osindero, Y.W. Teh "A fast learning algorithm for deep belief nets" (PDF) Neural Comput, 18 (7) (2006), pp. 1527-1554

146. Froyland, G. (2001). Extracting dynamical behavior via Markov models. In Nonlinear dynamics and statistics (pp. 281-321). Birkhäuser, Boston, MA.

147. J.G. Kemeny and J.L. Snell. Finite Markov Chains. Van Nostrand, Princeton, NJ, USA, 1960.

148. Maia, R., Silva, M., Araújo, R., & Nunes, U. (2011, June). Electric vehicle simulator for energy consumption studies in electric mobility systems. In 2011 IEEE Forum on Integrated and Sustainable Transportation Systems (pp. 227-232). IEEE.

149. Schlote, A., Crisostomi, E., Kirkland, S., & Shorten, R. (2012). Traffic modelling framework for electric vehicles. International Journal of Control, 85(7), 880-897.

150. Crisostomi, E., Kirkland, S., Schlote, A., & Shorten, R. (2011). Markov chain based emissions models: A precursor for green control. In Green IT: Technologies and applications (pp. 381-400). Springer, Berlin, Heidelberg.

151. Apostolaki-Iosifidou, E., Codani, P., & Kempton, W. (2017). Measurement of power loss during electric vehicle charging and discharging. Energy, 127, 730-742.

152. Tamar, A., Wu, Y., Thomas, G., Levine, S., & Abbeel, P. (2016). Value iteration networks. arXiv preprint arXiv:1602.02867.

153. Gold, S. (1997, January). A PSPICE macromodel for lithium-ion batteries. In The Twelfth Annual Battery Conference on Applications and Advances (pp. 215-222). IEEE.

154. Kroeze, R. C., & Krein, P. T. (2008, June). Electrical battery model for use in dynamic electric vehicle simulations. In 2008 IEEE Power Electronics Specialists Conference (pp. 1336-1342). IEEE.

155. Chen, M., & Rincon-Mora, G. A. (2006). Accurate electrical battery model capable of predicting runtime and IV performance. IEEE transactions on energy conversion, 21(2), 504-511.

156. Schweighofer, B., Raab, K. M., & Brasseur, G. (2003). Modeling of high power automotive batteries by the use of an automated test system. IEEE transactions on instrumentation and measurement, 52(4), 1087-1091.

157. Gao, L., Liu, S., & Dougal, R. A. (2002). Dynamic lithium-ion battery model for system simulation. IEEE transactions on components and packaging technologies, 25(3), 495-505.

158. Sun, C., Moura, S. J., Hu, X., Hedrick, J. K., & Sun, F. (2014). Dynamic traffic feedback data enabled energy management in plug-in hybrid electric vehicles. IEEE Transactions on Control Systems Technology, 23(3), 1075-1086.

159. Tran, M., Banister, D., Bishop, J. D., & McCulloch, M. D. (2012). Realizing the electric-vehicle revolution. Nature climate change, 2(5), 328-333.

160. Lew, D., Milligan, M., Jordan, G., Freeman, L., Miller, N., Clark, K., & Piwko, R. (2009). How do wind and solar power affect grid operations: The western wind and solar integration study (NREL/CP-550-46517). National Renewable Energy Lab.(NREL), Golden, CO (United States

161. Jones, L. E. (2017). Renewable energy integration: practical management of variability, uncertainty, and flexibility in power grids. Academic press

162. Atia, R., & Yamada, N. (2016). Sizing and analysis of renewable energy and battery systems in residential microgrids. IEEE Transactions on Smart Grid, 7(3), 1204-1213

163. Gnann, T., Klingler, A. L., & Kühnbach, M. (2018). The load shift potential of plug-in electric vehicles with different amounts of charging infrastructure. Journal of Power Sources, 390, 20-29

164. Hidrue, M. K., Parsons, G. R., Kempton, W., & Gardner, M. P. (2011). Willingness to pay for electric vehicles and their attributes. Resource and energy economics, 33(3), 686-705

165. Soares FJ, Lopes JAP, Almeida PMR. A Monte Carlo method to evaluate electric vehicles impacts in distribution networks. In: IEEE Conference on Innovative

Technologies for an Efficient and Reliable Electricity Supply (CITRES), Waltham, USA; 2010.

166. Shepero, M., & Munkhammar, J. (2018). Spatial Markov chain model for electric vehicle charging in cities using geographical information system (GIS) data. Applied Energy, 231, 1089-1099

167. Wang, M., Liang, H., Zhang, R., Deng, R., & Shen, X. (2014). Mobility-aware coordinated charging for electric vehicles in VANET-enhanced smart grid. IEEE Journal on Selected Areas in Communications, 32(7), 1344-1360

168. Office of Policy Planning, Florida Department of Transportation (2013). 2009 National Household Travel Survey Florida Data Analysis. Retrieved from https://fdotwww.blob.core.windows.net/sitefinity/docs/default-source/content/planning/trends/special/nhts.pdf?sfvrsn=b8c0d79c_0

169. William AM, Martin AM. Travel estimation techniques for urban planning Transport Research Board National Research Council, U.S., NCHRP 365 Rep. B8-29. 6; 1998. Retrieved from http://onlinepubs.trb.org/onlinepubs/nchrp/nchrp_rpt_365.pdf

170. Yilmaz, M., & Krein, P. T. (2012). Review of battery charger topologies, charging power levels, and infrastructure for plug-in electric and hybrid vehicles. IEEE transactions on Power Electronics, 28(5), 2151-2169

171. Orr, J. A., Emanuel, A. E., & Oberg, K. W. (1982). Current harmonics generated by a cluster of electric vehicle battery chargers. IEEE Transactions on Power Apparatus and Systems, (3), 691-700.

172. Mohamed, A., Salehi, V., Ma, T., & Mohammed, O. (2013). Real-time energy management algorithm for plug-in hybrid electric vehicle charging parks involving sustainable energy. IEEE Transactions on Sustainable Energy, 5(2), 577-586

173. Florida Public Service Commission (2019). Statistics of the Florida Utility Industry. Retrieved from http://www.psc.state.fl.us/Files/PDF/Publications/Reports/Electricgas/Statistics/2018.pdf

174. K. Levenberg, A method for the solution of certain problems in least squares, Quarterly of Applied Mathematics, 5, 164–168, 1944.

175. Basterrech, S., Mohammed, S., Rubino, G., & Soliman, M. (2011). Levenberg—Marquardt Training Algorithms for Random Neural Networks. The computer journal, 54(1), 125-135

176. National Renewable Energy Laboratory. PVWatts Calculator. Retrieved from https://pvwatts.nrel.gov/

177. Determination of the Historical Solar Resource for any Latitude – Longitude location in Florida," Dr. Charles J. Cromer, PhD, P.E., 3 June 2011, Florida Solar Energy Center, Cocoa, FL.

178. Chadès, I., Chapron, G., Cros, M. J., Garcia, F., & Sabbadin, R. (2014). MDPtoolbox: a multi-platform toolbox to solve stochastic dynamic programming problems. Ecography, 37(9), 916-920

179. Liang, X., Li, X., Lu, R., Lin, X., & Shen, X. (2013). UDP: Usage-based dynamic pricing with privacy preservation for smart grid. IEEE Transactions on Smart Grid, 4(1), 141-150

180. Yamin, H., Al-Agtash, S., & Shahidehpour, M. (2004). Security-constrained optimal generation scheduling for GENCOs. IEEE Transactions on power systems, 19(3), 1365-1372

181. Knezović, K., Soroudi, A., Keane, A., & Marinelli, M. (2017). Robust multi-objective PQ scheduling for electric vehicles in flexible unbalanced distribution grids. IET Generation, Transmission & Distribution, 11(16), 4031-4040.

182. Knezović, K., & Marinelli, M. (2016). Phase-wise enhanced voltage support from electric vehicles in a Danish low-voltage distribution grid. Electric Power Systems Research, 140, 274-283.

183. Newman, M. E. (2004). Fast algorithm for detecting community structure in networks. Physical review E, 69(6), 066133.

184. Ferreira, R. S., Borges, C. L. T., & Pereira, M. V. (2014). A flexible mixed-integer linear programming approach to the AC optimal power flow in distribution systems. IEEE Transactions on Power Systems, 29(5), 2447-2459.

185. Franco, J. F., Rider, M. J., Lavorato, M., & Romero, R. (2013). A mixed-integer LP model for the optimal allocation of voltage regulators and capacitors in radial distribution systems. International Journal of Electrical Power & Energy Systems, 48, 123-130.

186. Wu, W., Tian, Z., & Zhang, B. (2016). An exact linearization method for OLTC of transformer in branch flow model. IEEE Transactions on Power Systems, 32(3), 2475-2476.

187. Pereira, M. V., Granville, S., Fampa, M. H., Dix, R., & Barroso, L. A. (2005). Strategic bidding under uncertainty: a binary expansion approach. IEEE Transactions on Power Systems, 20(1), 180-188.

188. Dong, J., Xue, Y., Kuruganti, T., Sharma, I., Nutaro, J., Olama, M., ... & Bowen, J. W. (2018, February). Operational impacts of high penetration solar power on a real-world distribution feeder. In 2018 IEEE Power & Energy Society Innovative Smart Grid Technologies Conference (ISGT) (pp. 1-5). IEEE.

189. Lofberg, J. (2004, September). YALMIP: A toolbox for modeling and optimization in MATLAB. In 2004 IEEE international conference on robotics and automation (IEEE Cat. No. 04CH37508) (pp. 284-289). IEEE.

190. Cplex, I. I. (2009). V12. 1: User's Manual for CPLEX. International Business Machines Corporation, 46(53), 157.

191. IEEE 123 Node Test Case. (2019, October 16). Retrieved July 07, 2020, from https://xendee.com/ieee-123-node-test-case/.

192. Kersting, W.H., "Radial distribution test feeders," Power Engineering Society Winter Meeting, 2001. IEEE, vol.2, no., pp.908,912 vol.2, 2001doi: 10.1109/PESW.2001.916993.

193. Bayram, I. S., Abdallah, M., & Qaraqe, K. (2014, May). Providing QoS guarantees to multiple classes of EVs under deterministic grid power. In 2014 IEEE International Energy Conference (ENERGYCON) (pp. 1403-1408). IEEE.

194. Ahmadian, A., Sedghi, M., Mohammadi-ivatloo, B., Elkamel, A., Golkar, M. A., & Fowler, M. (2017). Cost-benefit analysis of V2G implementation in distribution networks considering PEVs battery degradation. IEEE Transactions on Sustainable Energy, 9(2), 961-970.

195. Ma, Z., Zou, S., & Liu, X. (2015). A distributed charging coordination for large-scale plug-in electric vehicles considering battery degradation cost. IEEE Transactions on Control Systems Technology, 23(5), 2044-2052.

196. Quaschning, V. (n.d.). Specific carbon dioxide emissions of various fuels. Retrieved January 03, 2021, from https://www.volker-quaschning.de/datserv/CO2-spez/index_e.php

197. Matsumura, T., & Yamagishi, A. (2017). Long-run welfare effect of energy conservation regulation. Economics Letters, 154, 64-68.

198. Penkovskii, A., Stennikov, V., Mednikova, E., & Postnikov, I. (2018). Search for a market equilibrium of Cournot-Nash in the competitive heat market. Energy, 161, 193-201.
199. Gurobi Optimization Inc., “Gurobi optimizer reference manual,” 2016. [Online]. Available: http://www.gurobi.com
200. Meindl, B., & Templ, M. (2012). Analysis of commercial and free and open source solvers for linear optimization problems. Eurostat and Statistics Netherlands within the project ESSnet on common tools and harmonised methodology for SDC in the ESS, 20.
201. Aljohani, T.M. Saad, A. Mohammed, O. (2021). *A Tri-Level Hierarchical Energy Management with Large-Scale Penetration of Electric Vehicles*. "Manuscript submitted for publication"

Appendix A: Hardware Setup for Chapter 4

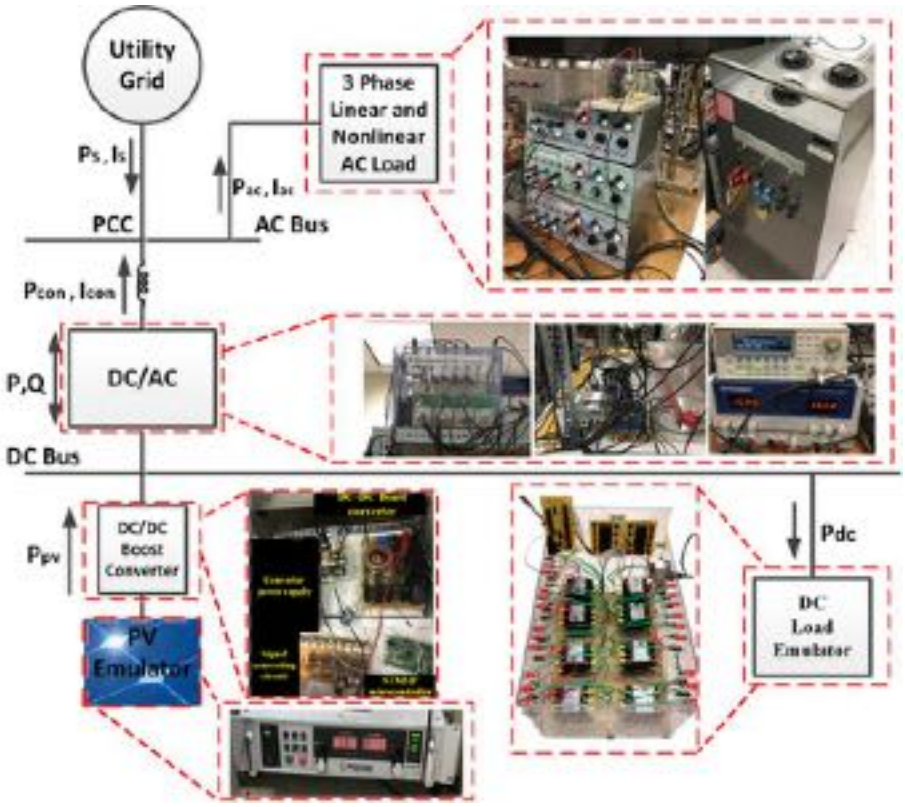

Fig.A.1. Experimental setup block diagram

To investigate the feasibility of the developed metaheuristic-based vector-decoupled algorithm for the energy management and control of hybrid microgrids considering electric vehicles charging stations, a hardware setup has been established, as depicted in Fig. A.1. It has been implemented in the power system testbed at the Energy System Research Laboratory, Florida International University. The testbed is composed of AC and DC parts connected through an AC-DC converter. The DC part is represented with a DC bus, with its voltage set at 380 V. Additionally, a DC-load emulator is integrated to model the load of the DC side while a PV emulator is integrated to represent a PV system. The PV emulator model is the XR SERIES DC power supply, which is offered by the MAGNA-POWER ELECTRONICS. This PV emulator is programmed to simulate the PV I-V characteristics, and is connected to the DC bus via a DC-DC boost converter to extract the maximum power

generated by the PV system. The mathematical modeling behind the PV system and the converter MPPT controller are modeled in MATLAB/SIMULINK environment and are executed with the DSpace 1104 real-time interface. In addition, battery packs that resemble the electric vehicles are connected to the DC bus, equipped with a signal converter circuit and a microcontroller. Furthermore, the battery packs are coupled with the AC part via the bidirectional DC-AC converter, as figures A.2 and A.3 show. The DC load emulator is composed of of eight resistors with different values as follows: 1 Ω, 5 Ω, 10 Ω, 20 Ω, 30 Ω, 40 Ω, 50 Ω, and 60 Ω. In addition to these load resistor combinations, eight controlled switches are utilized to restructure the topology. This allow obtaining different load patterns by the manipulation of the values of the equivalent load resistors. The main concept of the operation is based on sending control signals to the switches to change their states (on/off). By changing their states, the equivalent load resistance accordingly change. The control commands are generated from a load profile generator developed in the LabVIEW environment. The control commands are transferred through the PCI 6025E card to a circuit. This circuit is based on TEXAS INSTRUMENT inverting buffer module sn7406n. This module contains six inverters with open collector output. The RMS values for the voltage in the AC zone is set to 208 V. The AC bus is connected to the utility grid at PCC. Also, different load models were designed to represent the AC load pattern. One of the passive loads built has a switching capacity of 10 levels parallel of resistive loads from 300-W to 3-kW power in steps of 300-W at a nominal voltage that can be switched to emulate various load patterns. The parameters of the main components of the hardware setup are given in Table A.1. The controller is programmed based on the developed modified vector decoupling control. This control technique enables the microgrid's grid-tie converter to act as DSTATCOM to maintain the power quality at the bus of connection in the best condition. By counteracting the unbalance and harmonics problems with the help of the smart integration of microgrid. It is worth to mention that the controller provides harmonic mitigation and power factor

correction at the PCC. The controller is verified in MATLAB/SIMULINK for simulation purposes.

TABLE A.1. The parameter of the experimental setup

Component	Parameter	Specification
Boost Converter	power rating	2500 W
	IGBT module	SKM100GAL12T4
	switching frequency	5 kHz
	LBC, RLBC	6 mH, 0.21Ω
Bidirectional AC/DC Converter	power rating	1800 W
	IGBT module	SK45GB063
	switching frequency	10.89 kHz
AC Filter	L AF, RLAF	12 mH, 0.31 Ω

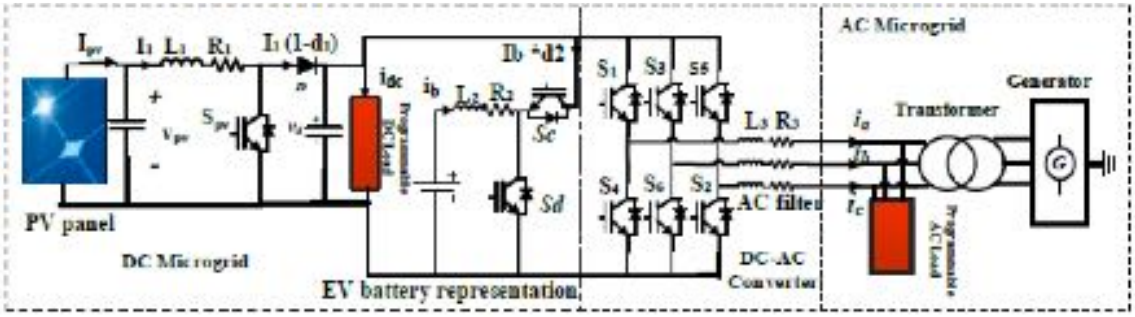

Figure A-2 Schematic illustration of the hybrid microgrid circuit in the setup

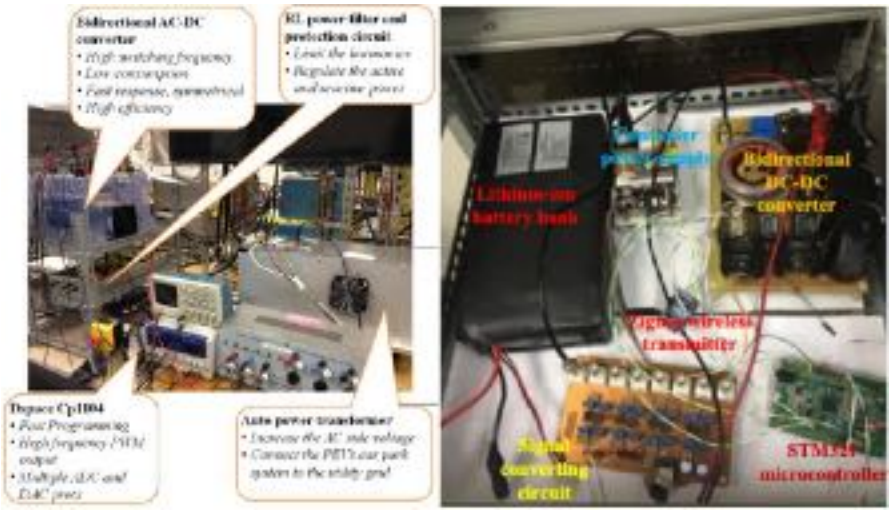

Figure A-3 Hardware-in-the-loop equipment at the testbed

Vita

VITA

TAWFIQ MASAD ALJOHANI

Pembroke Pines, Florida, United States of America

Email: taljo005@fiu.edu

Education

- Bachelor of Science Degree in Electrical Engineering (Power & Machines) 2004-2009
- Electrical and Computer Department.
- Faculty of Engineering, King Abdul Aziz University, Jeddah, Saudi Arabia.
- GPA: 3.99/5 (3.04/4, WES).

- Master of Science Degree in Electrical Power Systems Engineering [January 2012 – May 2014].
- Viterbi School of Engineering, University of Southern California, Los Angeles, CA, USA.
- GPA: 3.81/4

- Master of Science Degree in Green Technologies [January 2016 – Expected December 2017].
- Viterbi School of Engineering, University of Southern California, Los Angeles, CA, USA. GPA:
- 3.61/4

- Graduate Certificate in System Architecture and Engineering [December 2017]
- For taking five graduate courses in the department of system architecture and engineering.
- Can be applied as a master's degree in case of taking two additional graduate courses in the area.
- GPA: 3.74/4

- PhD in Electrical Engineering [2018 ~2021]
- Florida International University, Miami, Florida, USA.
- Expected graduation: Spring 2019 or Fall 2018.
- GPA: 3.54/4

- Strong technical background in power and machines engineering. Outstanding
- quantitative, analytical, problem solving and programming skills. Excellent
- researcher and presenter.
- Excellent oral and written communication skills.

- Member of IEEE.
- Member of IEEE Power & Energy.

Selected Publications

1. Aljohani, T. M., Ebrahim, A., & Mohammed, O. (2021). Real-Time metadata-driven routing optimization for electric vehicle energy consumption minimization using deep reinforcement learning and Markov chain model. Electric Power Systems Research, 192, 106962.
2. Aljohani, T. M., Saad, A., & Mohammed, O. A Two-Stage Optimization Strategy for Solving the VVO Problem Considering High Penetration of Plug-in Electric Vehicles to Unbalanced Distribution Networks. Accepted in IEEE Transactions in Industry Applications.
3. Aljohani, T. M., Ebrahim, A. F., & Mohammed, O. (2020). Hybrid Microgrid Energy Management and Control Based on Metaheuristic-Driven Vector-Decoupled Algorithm Considering Intermittent Renewable Sources and Electric Vehicles Charging Lot. Energies, 13(13), 3423.
4. Aljohani, T. M., Ebrahim, A. F., & Mohammed, O. (2019). Single and multiobjective optimal reactive power dispatch based on hybrid artificial physics–particle swarm optimization. Energies, 12(12), 2333.
5. Aljohani, T., Ebrahim, A., & Mohammed, O. (2020, June). Dynamic Real-Time Pricing Structure for Electric Vehicle Charging Considering Stochastic Microgrids Energy Management System. In 2020 IEEE International Conference on Environment and Electrical Engineering and 2020 IEEE Industrial and Commercial Power Systems Europe (EEEIC/I&CPS Europe) (pp. 1-8). IEEE.
6. Aljohani, T.M., Beshir, M.J. “Distribution System Reliability Analysis for Smart Grid Applications”. International Journal of Distributed Energy Resources and Smart Grid, March 2016.